Majd Ahmad

Dynamic Behavior of Soil Under Irregular Loading Patterns

Doctoral Dissertation

Supervisor:
Professor Dr. Richard P. Ray PhD
Department of Structural and Geotechnical Engineering
Faculty of Architecture, Civil Engineering and Transport Sciences
Széchenyi István University

Multidisciplinary Doctoral School of Engineering Sciences
Széchenyi István University

Győr, Hungary
2024

Acknowledgments

My deepest thanks go to my supervisor, Richard Ray, for his guidance, mentorship, and support throughout my PhD program. His expertise, feedback, and encouragement have been critical to my academic success, and I am grateful for the opportunity to have worked under his guidance.

I would like to express my heartfelt appreciation to my family for their unconditional love and support throughout my academic journey. Although they are not physically present with me, their constant encouragement and belief in me have been my guiding light and source of strength.

My parents, Maan Ahmad and Wafaa Zaidan, have been my role models and inspiration, instilling in me the value of education and hard work from a young age. Their support and belief in me have been my driving force, and I am honored to have made them proud.

My siblings, Yara and Hadi, have been my pillars of strength and support, cheering me on from afar and always believing in me. Their love and encouragement have been instrumental in helping me achieve this milestone.

I would like to express my deepest gratitude to my wife, Sofia Suarez, for her unwavering love, support, and encouragement throughout my PhD journey. Her faith in me, her patience, and her constant belief in my abilities have been a source of motivation, and I am blessed to have her as my partner in life.

I would also like to thank all the faculty members, colleagues, and friends who have supported and encouraged me along the way. Their insights, feedback, and encouragement have been invaluable, and I am honored to have had the opportunity to learn and grow alongside such a remarkable community.

Summary

This PhD dissertation focuses on exploring the dynamic behavior of dry sand when subjected to cyclic and irregular loading patterns. The increasing demand of a more detailed assessment of material dynamic properties and the interactions between soil, foundation, and structure requires a better understanding of the dynamic behavior of both soil and structure. By advancing our knowledge of the influence of irregular loading patterns on the dynamic properties of soils, new advanced models can predict how a site might respond to different earthquake time histories.

We conducted laboratory tests on selected granular soils in Hungary using the combined Resonant Column-Torsional Simple Shear Device (RC-TOSS). The testing equipment can be deemed as one-of-a-kind globally as it has the ability to conduct both types of tests on a single hollow cylinder soil specimen. We designed the testing program to investigate the effect of the loading cycles on the dynamic properties. After exceeding the cyclic threshold, an increase in the shear modulus with the increasing number of cycles for dry or drained sand under cyclic loading is called “cyclic hardening in stiffness”. Available soil models such as Ramberg-Osgood and Hardin-Drnevich coupled with the Masing criteria simulate the dynamic shear stress-shear strain curves of soil without considering the stiffening behavior. In this study, these models are evaluated through the 3D Finite Element (FE) model created to simulate the TOSS test. Our lab testing and data analysis further improved and extended these models to capture the stiffening behavior resulting from the cyclic loading. VBA subroutines are generated in MS Excel for an instant analysis of the tests results. The least square method applied through the solver in Excel finds the models constants that best fit the curves obtained from the TOSS test.

The FE model further examines the effect of nonuniformity of the soil samples. This is achieved by assigning a simple Tresca model to the elements with varying properties. An iterative method using solver in Excel and Midas finds a discrete distribution of the yield stresses of the elements that has a collective behavior that matches the results obtained from the TOSS test. This model with the discrete distribution of elements can investigate the nonuniform samples with inclusions and voids.

Osszefogl

A doktori értekezés célja a ciklikus és szabálytalan terhelési mintázatoknak kitett száraz homok dinamikus viselkedésének kutatása. Az anyagok dinamikus tulajdonságainak, valamint a talaj, az alapozás és a szerkezet közötti kölcsönhatásának részletesebb megismerésének növekvő igénye megkívánja mind a talaj, mind a szerkezet dinamikus viselkedésének jobb megértését. Továbbá a szabálytalan terhelési mintázatok hatásának elemzése révén új, fejlett modellek segítségével előre lehet jelezni, hogy egyes területek várhatóan hogyan reagálnak különböző földrengésekre.

A kombinált Rezonanciás Oszlop-Torziós Egyszerű Nyíróberendezés (RC-TOSS) segítségével Magyarországon elforduló válogatott szemcsés talajmintákon végeztem laboratóriumi kísérleteket. A felhasznált tesztelési berendezés világszerte egyedülállónak tekinthető, mivel egyetlen henger alakú talajmintán képes elvégezni mindkét típusú vizsgálatot. A tesztprogramot úgy terveztük meg, hogy első sorban a terhelési ciklusok hatását vizsgáljuk meg a dinamikus tulajdonságokra. A ciklusok küszöbértékének túllépését követően a száraz vagy drénezett homok esetében a ciklikus terhelés alatt a ciklusok számának növekedésével járó fokozatosan növekvő nyíró modulust a " ciklikus merevség felkeményedésének" nevezzük. A szakirodalomban fellelhető talajmodellek, mint például a Ramberg-Osgood és a Hardin-Drnevich modell, alkalmasak a Masing-kritériummal kombinálva a talaj dinamikus nyírófeszültség-nyíródeformáció görbéinek szimulálására anélkül, hogy figyelembe vennék a merevség változásának hatását. Ebben a tanulmányban ezeket a modelleket a TOSS tesztek szimulációjára létrehozott 3D Véges Elem (FE) modelleken keresztül értékeljük. A laboratóriumban elvégzett tesztek és azok elemzése alapján továbbfejlesztettük és kiterjesztettük ezeket a modelleket annak érdekében, hogy rögzítsük a ciklikus terhelésből származó merevség megváltozását. Továbbá létrehoztunk az MS Excel szoftverben egy VBA approgramot, mellyel lehetséges a teszteredmények azonnali és közvetlen elemzése. A legkisebb négyzetek módszerét alkalmazva az Excelben található Solver segítségével megadtuk az egyes modellekhez tartozó és a TOSS tesztek során kapott görbékhez legjobban illeszkedő állandókat.

A Véges Elem (FE) modell segítségével figyelembe vettük továbbá a talajminták egyenetlenségét. Ennek megvalósításához egy egyszerű Tresca-modellt rendeltünk a változó tulajdonságú elemekhez. Az Excelben található Solver és a Midas segítségével így egy iteratív módszerrel diszkrét eloszlást készítettünk az elemek folyási feszültségéhez, amelyek kollektív viselkedése legjobban illeszkedik a TOSS teszten kapott eredményekhez. Ez a modell a diszkrét elemeloszlással képes vizsgálni az egyenetlen mintákat a bennük található hézagokkal együtt.

Contents:

Chapter 1
Introduction

1.1 Background

In engineering practice, static loading produces most of the actions considered in geotechnical design. However, as structures have evolved and material costs have significantly increased, a more advanced approach has required engineers to consider structures subjected to dynamic loading. Designers can no longer assume quasi-static behavior for dynamic conditions and apply overly generous safety factors. Newer designs demand a more detailed assessment of material dynamic properties and the interactions between soil, foundation, and structure. Newer designs require a better understanding of the dynamic behavior of both soil and structure.

The response of structures to dynamic loading is directly related to the response of soil beneath and around it. Therefore, many researchers in the past few decades focused on studying the behavior of soils subjected to dynamic loading. When earthquake waves propagate through the soil, they often pass upward through layers that usually become less stiff (lower modulus) as they approach the surface. The reduction is generally due to decreasing confining stresses in the soil, directly reducing its stiffness and strength. A consequence of the stiffness reduction is that the propagating waves refract to a more vertical path. The propagating waves travel vertically at many building locations, with most of their energy carried by shear waves. The surface ground motion consists of two horizontal (N-S and E-W) and one vertical component. Structures can usually withstand the vertical component even with only a static design due to the high factor of safety used to support the static load. However, structures are more susceptible to horizontal motion since they are innately less capable of resisting it. The ground motion in most earthquake-related design problems derives from the horizontal shaking of vertically propagating shear waves.

A site response analysis is one of the most common tasks in geotechnical earthquake engineering, which aims to determine the response of the soil deposit to the motion of the bedrock immediately beneath it. The transfer functions used in equivalent linear site response analysis require knowing two significant dynamic soil properties (the shear modulus G, and the damping ratio D) representing the soil's shear stiffness and energy dissipation, respectively. Even though practicing engineers employ the equivalent linear approach, it assumes that dynamic soil properties remain constant throughout the computational reach for the duration

of the earthquake. This assumption may oversimplify the nonlinearity of soil behavior. Laboratory and large-scale models have demonstrated that shear stiffness decreases, and the damping ratio increases with increasing shear strain, even at low strain levels. Integrating the equation of motion over small time steps overcomes the problems from this approximation. Advanced constitutive models can predict the soil's dynamic nonlinear behavior and provide a basis for an accurate nonlinear time history analysis. Several models, such as the Hyperbolic, Ramberg-Osgood, Hardin-Drnevich, and Iwan-type models, can predict the cyclic shear stress-shear strain behavior.

The variation of *G* and *D* in a soil profile over time during an earthquake impacts the structural demands on the surface in several ways. Structures resonate in horizontal motions at various frequencies, depending on the size, configuration, and materials used. While those resonant frequencies may be far different from the resonance of the soil profile, they may change during a seismic event. As the soil changes *G* while shaking, due to shear strain effects, the profile may produce loading frequencies near the structural resonance and produce higher structural demands in terms of both loading and deformation. Since the soil profile constantly changes its stiffness during an earthquake, predicting the final loading conditions on the structure is very complex. Most of the previous researchers focused on studying the behavior of soil subjected to cyclic loading, while few directed their attention toward irregular loading patterns. This leads to the fact that available soil models do not always perform well in simulating the soil behavior under such loads, especially for an extended time and a high number of cycles where the influence of stiffening or softening becomes evident.

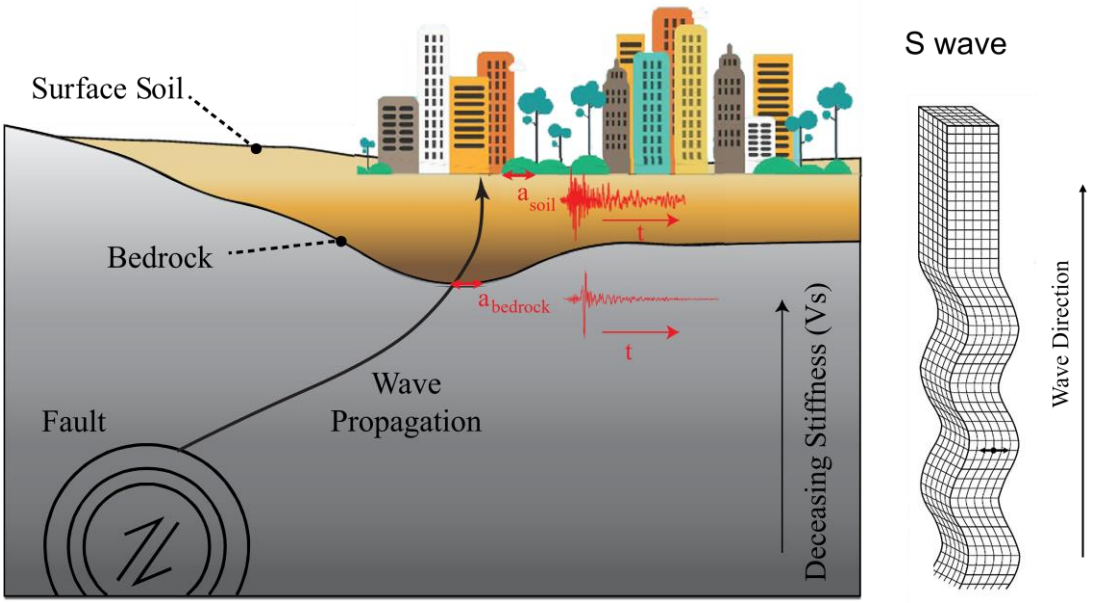

Figure 1-1 Propagation of shear waves in layered medium and the ground response (a_{soil}) based on acceleration record measurements at the bedrock ($a_{bedrock}$).

1.2 Objectives of the research

This study determines whether soil models can accurately predict the behavior of soils subjected to cyclic and irregular load histories. Additionally, the study aims to compare different soil models to determine their effectiveness in finite element software for problems with similar types of loading, such as the vibration of machine foundations, train loadings, and earthquake time histories. The research will extend the capabilities of existing soil models to include behavior under irregular loading. The improved models should consider changes in stiffness and damping due to cyclic loading.

Laboratory tests were conducted on selected granular soils in Hungary using the combined Resonant Column-Torsional Simple Shear Device (RC-TOSS). Prof. Ray at the University of Michigan (Ray, 1984) built the original device, then Ray and Szilvagyi (Szilvágyi, 2017) added further improvements at the Geotechnical Laboratory of Széchenyi István University. MS Excel spreadsheets and programs provided test execution, data acquisition, and curve fitting. Midas GTS NX software performed nonlinear finite element modeling of the soil specimens to verify behavior and explore complex scenarios.

By advancing our knowledge of the influence of irregular loading patterns on the dynamic properties of soils, new advanced models can predict how a site might respond to different earthquake time histories. The site response may apply to deterministic or probabilistic seismic hazard analysis. Such analysis will also impact the response of a proposed structure built on that site, leading to more accurate results and design.

Material properties derived from laboratory soil tests often assume that the property is uniform throughout the specimen. This assumption may hold true for some exceptional soils but is obviously false for many others. This study presents a method of modeling inherently non-uniform soil specimens to study the effect of nonuniformity and the presence of rigid inclusions. Finite element software, Midas GTS NX, will represent the soil specimen with elements having a simple elasto-plastic Tresca material model whose properties vary throughout the sample. The method will match computed behavior to behavior obtained from the RC-TOSS laboratory tests.

1.3 Organization of dissertation

A thorough literature review presents the state-of-the-art methods and practices for analyzing and measuring soil behavior under dynamic cyclic and irregular loading. The following

sections address laboratory testing, data interpretation, modeling approaches, evaluation of soil models, and a discussion of the findings.

Chapter 2 contains the literature review, explaining the most used parameters to define the dynamic behavior of soils and the methods to measure them. Then the theory behind the RC-TOSS device in measuring the shear modulus and damping ratio follows along with the effects of different parameters on the dynamic properties of dry sand. The final paragraphs review the most widely used soil models, and criteria to capture the behavior of soil subjected to cyclic and irregular loading patterns.

Chapter 3 describes the RC-TOSS device and other equipment used in this study. Other descriptions include sample preparation methods for dense and loose samples, methods of analyzing and interpreting raw data by Visual Basic for Application (VBA) in Excel, and the subroutines to analyze the cyclic and irregular tests.

Chapter 4 includes the numerical modeling and analysis in Midas GTS NX FEM software. The model created to simulate the TOSS test validates the Ramberg-Osgood and Hardin-Drnevich soil models' ability to simulate the specimen behavior when subjected to irregular loading patterns. Moreover, the FE model produces a numerical study of random material properties within a soil specimen using Tresca elasto-plastic elements in the model. Different scenarios evaluate the effects of randomly varying properties and inclusions/voids.

Chapter 5 presents the tested soils' laboratory testing program and properties, the measured dynamic shear modulus, and damping ratio graphs. The Steady State Vibration method (SSV) and the Free Vibration Decay method (FVD) for measuring damping are compared to the damping calculated from the hysteresis loops acquired in the TOSS test. The final section presents the effect of the number of cycles and the stiffening behavior on the Masing criteria used in modeling the dynamic behavior of soil. The suggested modifications to the models are discussed.

A summary of the findings and thesis statements are given in Chapter 6.

Annex A contains the laboratory test results, while Annex B lists VBA codes for data analysis. Furthermore, the device calibrations performed during this study are recorded in Annex C.

Chapter 2
Literature Review

2.1 Dynamic behavior of soils

As mentioned, the most critical parameters determining soil behavior under dynamic loads are the dynamic shear modulus (G) and the damping ratio (D). These two parameters appear in many dynamic geotechnical problems related to earthquakes and machine foundations. Researchers have investigated ways to develop and enhance instruments that precisely measure G and D and explored how various loading factors impact these properties (Ahmad & Ray, 2023).

2.1.1 Dynamic shear modulus

The shear modulus (G) represents the shear stiffness of the soil. G possesses its maximum value at very low strain levels ($<10^{-4}$%). Figure 2-1 shows the small strain or maximum shear modulus (G_{max}). At this strain level, the soil exhibits an elastic behavior with no permanent microstructural changes taking place in the soil. G_{max} depends on the shear wave velocity (V_s) passing through the soil and the density (ρ) by the following equation:

$$G_{max} = \rho * V_s^2 \qquad \text{Equation 2-1}$$

This equation determines the maximum shear modulus of soil layers in the field by applying in-situ methods that measure V_s (e.g., the cross-hole or down-hole test, the seismic cone penetration test (SCPT) and the spectral/multichannel analysis of surface waves (S/MASW)). Furthermore, many studies have established empirical correlations from extensive laboratory testing data to estimate G_{max} as a function of the void ratio and mean effective stress. The most commonly utilized equations are the ones introduced by (Hardin & Richart, 1963), (Hardin & Black, 1966), and most recently by (Wichtmann, et al., 2015). Nevertheless, despite the potential advantages of these correlations, they can have a significant degree of variability and may not always offer an adequate representation of actual stiffness. Therefore, engineers should not solely depend on them in all situations. Nowadays, more reliable laboratory testing methods simulate (to an acceptable level) the shear loading conditions in the field, such as the resonant column and bender element tests. The dynamic testing methods corresponding to different strain levels appear in Figure 2-2.

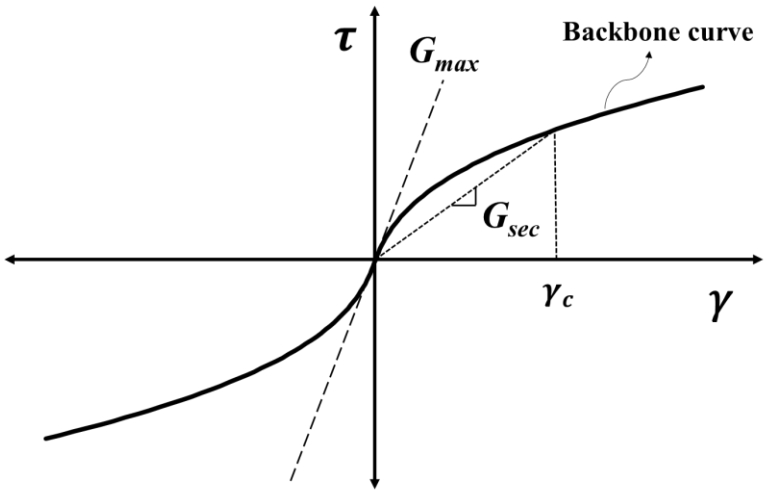

Figure 2-1 Shear stress-shear strain backbone curve.

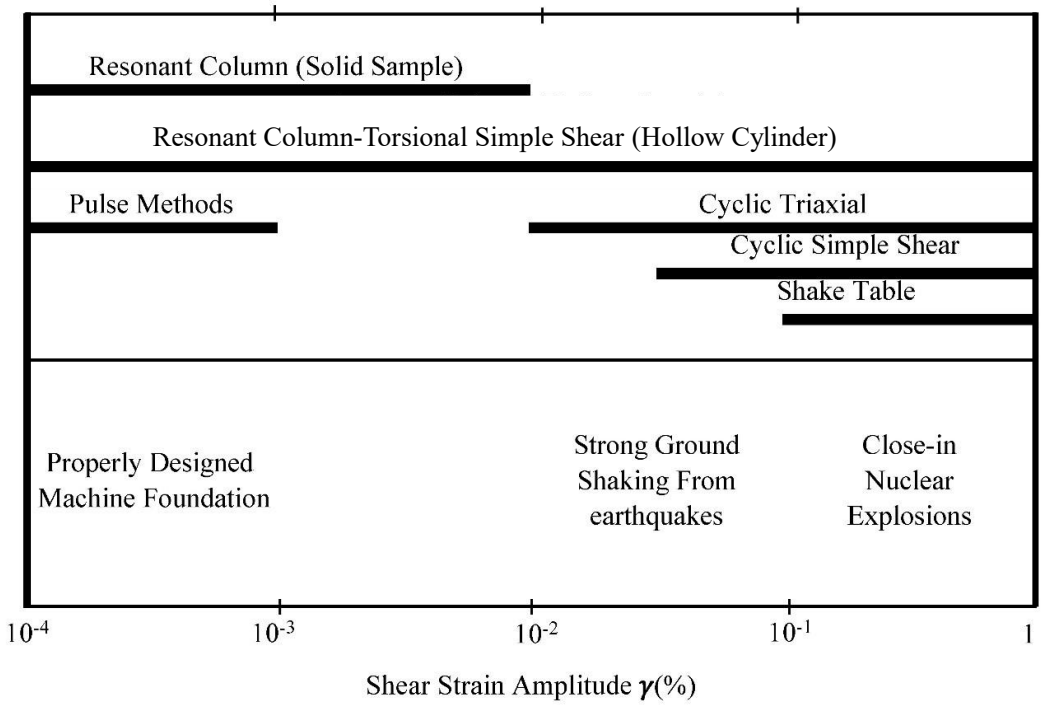

Figure 2-2 Dynamic testing methods corresponding to different strain levels, modified from (Woods, 1978).

Once the shear strains in soils exceed a certain threshold level, the separation or slippage of intergranular contacts causes the behavior of the soil to become nonlinear, and the stiffness starts degrading until it reaches 5-10% of its original maximum stiffness at high strain levels. A modulus reduction curve represents this effect where the shear modulus decreases with increasing shear strain, as shown in Figure 2-3. (Vucetic, 1994) defined two

types of shear strain thresholds based on extensive cyclic laboratory data. The values of these thresholds depend on the soil type. The linear threshold (γ_{tl}) is the strain at which the ratio of the modulus to maximum modulus (G/G_{max}) is 0.99, and before this threshold, the soil behaves elastically. Beyond this limit, the soil first behaves as a slightly elastoplastic material (nonlinear but still elastic) where permanent changes are negligible. Later, the strains increase to a second threshold, defined as the volumetric threshold shearing strain (γ_{tv}), after which the soil microstructure undergoes an irreversible alteration, resulting in a permanent change in the stiffness of the soil. Investigations by (Anderson, 1979) (Ladd, 1982), and (Georgiannou, et al., 1991) show that γ_{tv} corresponds to a range of G_{sec}/G_{max} between 0.60 and 0.85.

The secant shear modulus (G_{sec}) represents the ratio between the shear stress and shear strain at each loading step on the backbone curve (Figure 2-1), which refers to the one-way loading shear stress-shear strain curve. In other words, it is the slope of the line that connects the origin with the point along the backbone curve corresponding to (γ_c). For cyclic loading, the reduction in stiffness disappears after each turning point due to the re-engagement and interlocking of previously slipped contacts between particles in the opposite direction. Naturally, if loading resumes back in this direction, elastic contacts will once again be lost, and stiffness will start degrading as before. Due to this nonlinearity and recovery of stiffness around load reversals, the stress-strain path forms a hysteresis loop, as presented in Figure 2-4a. The slope of the line that connects the endpoints of the hysteresis loop represents the "average" shear stiffness of the soil, hence the secant shear modulus.

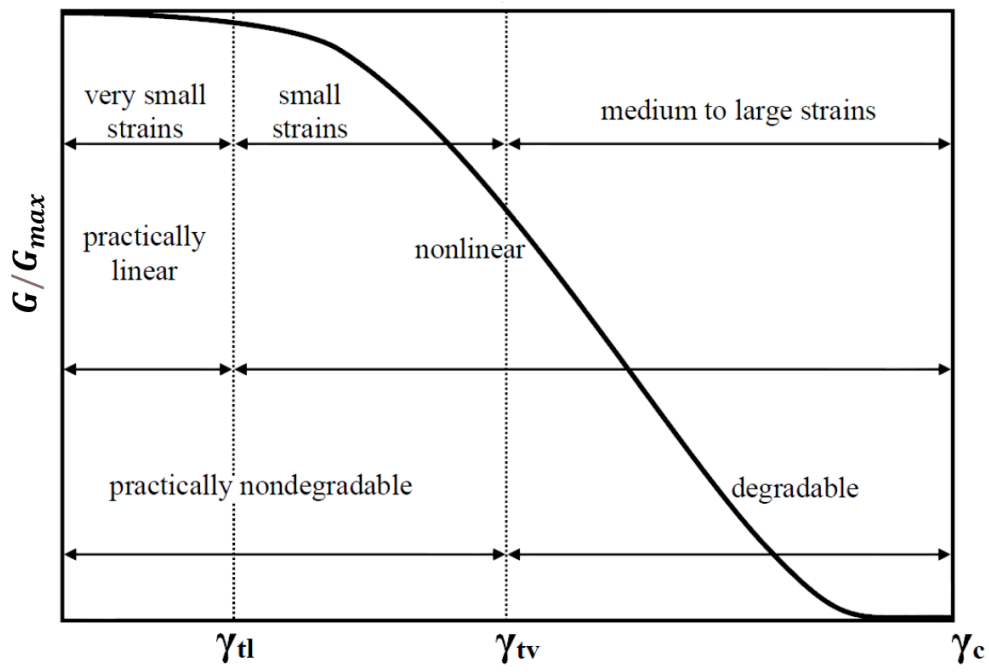

Figure 2-3 Secant shear modulus degradation curve due to increasing shear strain (Vucetic, 1994).

2.1.2 Damping ratio:

The Damping ratio is an important dynamic property of soil. It represents the energy dissipation when waves propagate through the soil layers.

There are several types of damping in materials. However, we are only concerned with hysteretic and viscous damping in soil. These two types of damping occur due to different mechanisms. Hysteretic damping is independent of the vibration frequency and proportional to the displacement, while viscous damping changes with frequency and is directly proportional to the velocity.

During cyclic loading in soil, the damping behavior can be very complicated, and damping results from two main mechanisms, fluid flow loss and inelastic friction loss (White, 1983). Soils dissipate energy even at very small strain levels (Kramer, 1996). At such strain levels where the soil is behaving elastically and no hysteretic loop will form, the fluids in the voids are responsible for the damping (Kokusho, 1987), which is an indicator that fluid energy loss is the dominant mechanism in small strain damping in soil (viscous damping). On the other hand, when exceeding the linear threshold (γ_{tl}), where the behavior becomes nonlinear, the stress-strain curves exhibit a hysteresis loop as the soil is cyclically loaded. Beyond this threshold, hysteretic damping increases with the strain level (Figure 2-4b) and most of the energy dissipation is due to inelastic friction which is independent of the frequency of the vibration. Therefore, the nature of damping is hysteretic and viscous damping can be neglected (Hardin, 1965), (Dobry, 1970).

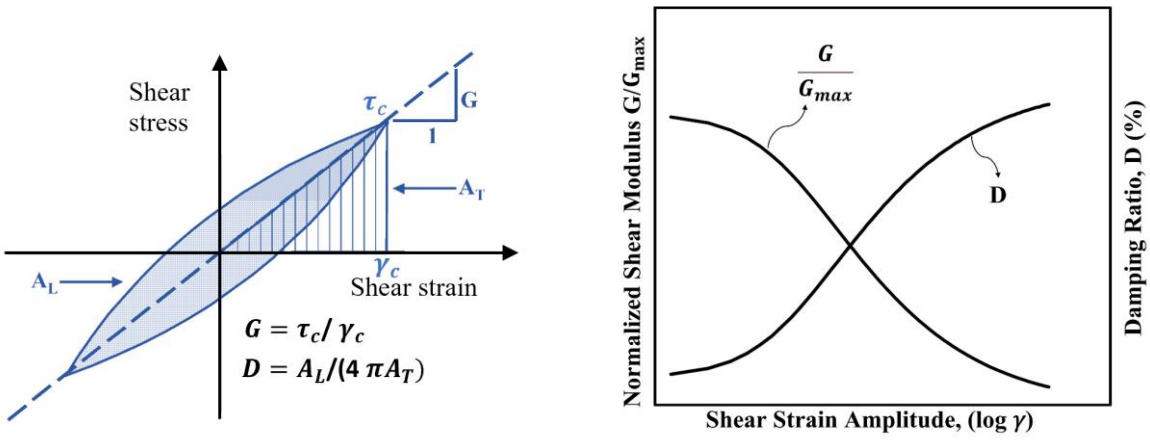

(a) A hysteresis loop and calculation of the secant shear modulus and damping ratio. *(b) Increase of damping ratio with the strain rate.*

Figure 2-4 The secant shear modulus and damping ratio.

Even though damping in the soil is known to be hysteretic, equivalent viscous damping often replaces it in most analyses due to mathematical simplicity. Viscous damping provides a very straightforward representation in dynamic analysis because it is linearly proportional to

the velocity. Many geotechnical and structural dynamic problems approximate single and multi-degree-of-freedom systems with a viscous dashpot where damping force results:

$$F = C\dot{u} \quad \text{Equation 2-2}$$

Where C = viscous damping coefficient, and $\dot{u}$ = particle velocity.

"The equivalent viscous damping is determined in such a manner as to yield the same dissipation of energy per cycle as that produced by the actual damping mechanism" (Bae, 2007). The damping ratio, *D*, represents the energy absorbed in one vibration cycle divided by the potential energy at maximum displacement in that cycle (Richart, et al., 1970). The equivalent damping ratio (D) due to hysteretic damping results from the following equation:

$$D = \frac{A_{\mathrm{L}}}{4\pi * A_{\mathrm{T}}} \quad \text{Equation 2-3}$$

Where: A_L= the area of the entire hysteresis loop (Figure 2-4a)

A_T= the triangular area bounded by the secant modulus line at the point of maximum strain (Ishihara, 1996).

Small strain damping ratio (D_{min}) often defies accurate measurement due to many factors, such as equipment damping and environmental noise. Therefore, D_{min} varies over a broader range when measured by the resonant column method.

(Xu, et al., 2021) presented a new method for measuring D_{min} in the torsional shear test. The method examines the phase shift between the stress and strain signals and requires two calculation steps. The first step fits the sinusoidal time series of stress and strain signals to equations and determines the phase angle for both signals. The difference between θ_1 and θ_2 is the phase shift used for calculating the hysteretic material damping ratio. The Fourier transform method accurately computes the strain amplitudes by allowing the filtration of the signal's frequency components. This method only applies to the elastic strain range of the material damping ratio (10^{-5}–10^{-4}%), where it shows accurate and consistent results.

(Drnevich, et al., 1978) described two methods to measure the damping ratio in the RC test: (1) the Steady-State Vibration method (SSV) and (2) the Free Vibration Decay method (FVD). The SSV method measures the input energy (current through coils) at resonance. The more input energy required to maintain a strain level translates to a higher damping value. However, the device cannot maintain precise resonance at high strain levels, and the decay method produces more reliable results over a short period (10 seconds) (Ray, 1984). In the decay method, the power disconnects from the coils, allowing the sample to behave as a damped, freely vibrating system (Figure 2-5). The recorded decaying response then determines damping via the following equation:

$$\delta = \frac{1}{N} * \ln \frac{Z_1}{Z_{1+N}} = \frac{2\pi D}{\sqrt{1 - D^2}} \quad \text{Equation 2-4}$$

Where δ = logarithmic decrement, N = number of cycles, Z_1 = first amplitude, Z_{1+N} = amplitude after N cycles, and D = damping ratio.

For small values of the damping ratio as found in soil, $\sqrt{1 - D^2}$ can be approximated to 1, and the damping expression can be determined as follows:

$$D = \frac{\delta}{2\pi} = \frac{1}{2N\pi} * \ln \frac{Z_1}{Z_{1+N}} \quad \text{Equation 2-5}$$

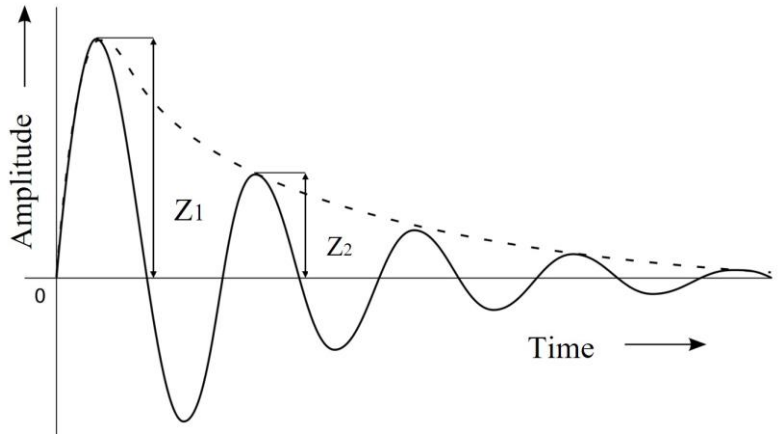

Figure 2-5 the decaying response in RC test.

According to (Ray, 1984), *N* should be small when driving at high amplitude because a larger *N* would introduce strain effects due to a drop in amplitude by a factor of three over the measurement interval. (ASTM D4015, 1992) suggests the use of fewer than 10 cycles. The research by (Gabryś, et al., 2018) on the RC apparatus agrees with these regulations. Furthermore, a recent study by (Mog & Anbazhagan, 2022) examined the effect of the number of successive cycles (*N*) used in calculating the damping ratio using the (GCTS) resonant column apparatus. When measuring up to 10 cycles, they reported an increase in the damping ratio when increasing the number of cycles. Nevertheless, after 10 cycles, the damping ratio diminishes for higher numbers of cycles in the measurements (i.e., for 20, 30, and 50 cycles). Due to the considerable scatter in the damping ratio measurements determined by this method, estimates should use two or three successive cycles to calculate the damping ratio in the RC test.

The SSV method for calculating the damping ratio is also called the half-power bandwidth method. It initially determined a structure's modal damping ratio ξ from the width of the peaks in its frequency response function, and it may apply to soil in the RC test. In this method, the width of the frequency response curve near the resonance determines the loga-

rithmic decrement (δ). The half-power bandwidth ($\Delta\omega$) is the width of the peak where the magnitude of the frequency response function is $1/\sqrt{2}$ multiplied by the peak value (Chopra , 2007). The following equation calculates δ:

$$\delta = \frac{\pi(f_2^2 - f_1^2)}{2f_n^2} * \sqrt{\frac{P^2}{P_{max}^2 - P^2}} \frac{\sqrt{1-2D^2}}{1-D^2} \qquad \text{Equation 2-6}$$

Where, f_1 and f_2 = frequencies below and above the resonance where the strain amplitude = P, P_{max} = maximum amplitude (or resonant amplitude), f_n = resonant frequency (Figure 2-6), and D = damping ratio of the material.

When the damping is small and the amplitude $P = \frac{P_{max}}{\sqrt{2}}$, Equation 2-6 can be written as:

$$\delta \cong \frac{\pi(f_2 - f_1)}{f_n} \qquad \text{Equation 2-7}$$

Then, the damping ratio becomes:

$$D \cong \frac{(f_2 - f_1)}{2f_n} \qquad \text{Equation 2-8}$$

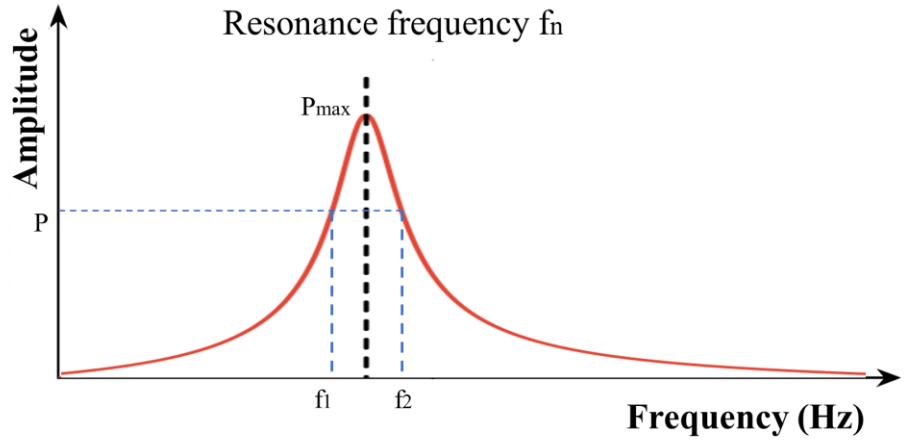

Figure 2-6 Resonant frequency in RC test.

The scatter (from an average value) of the damping ratio measured using the SSV method and FVD method with two successive cycles can reach 15% (of the average) at strain levels less than 0.005% (Mog & Anbazhagan, 2022) and even higher (up to 50% of the average) when the number of successive cycles is higher (3, 7, and 10 cycles). The ambient noise during the RC test may cause this difference (Meng, 2003), and/or the number of applied cycles (higher for SSV). Several authors suggested relying on SSV (half- power bandwidth) to determine the damping ratio within a very small shear strain range where the frequency response curve is still symmetrical. The frequency response curve becomes non-symmetric at

higher strain levels (>0.005%), and measurement accuracy is uncertain. Therefore, the FVD method better estimates the damping ratio at high strains (Senetakis, et al., 2015), (Facciorusso, 2020).

2.2 Shear modulus in RC-TOSS testing

The resonant column test uses a high-accuracy accelerometer to acquire readings at very small strains (10^{-4}%). At these strain levels, the shear modulus behaves as linear elastic (G_{max}). The relationship between acceleration, velocity and displacement experiencing harmonic motion produces accuracy at such low strain values. Differentiating the expression for simple harmonic displacement (u) produces expressions for velocity ($\dot{u}$) and acceleration ($\ddot{u}$):

$$u(t) = A\sin(\omega t) \quad \text{Equation 2-9}$$

$$\dot{u}(t) = \frac{du}{dt} = \omega A\cos(\omega t) \quad \text{Equation 2-10}$$

$$\ddot{u}(t) = \frac{d^2u}{dt^2} = -\omega^2 A\sin(\omega t) = -\omega^2 \mathrm{u} \quad \text{Equation 2-11}$$

Where, A = the displacement amplitude, ω = the circular frequency, t = time.

The two vital elements in resonant column testing are the accelerometer's sensitivity and the range of typical resonant frequencies produced by the device. A high-quality piezoelectric accelerometer produces about 300 millivolts/g. A high-grade digital voltmeter can easily measure up to 0.1 millivolt AC, translating to acceleration as < 0.01 g. The same meter could also detect frequencies/periods of dynamic signals with four- or five-digit accuracy. Typical resonant frequencies would range from $200 < \omega_n < 500$ rad/s. The frequency range is a significant advantage in producing small strains. Knowing that the specimen length L = 0.14m, and at resonance, for a natural circular frequency ω_n = 400 (rad/sec), and acceleration $\ddot{u}$ = 0.025 (m/sec^2). From Equation 2-11, the displacement u=1.56e^{-7}m, and the shear strain is calculated as follows:

$$\gamma = \frac{u}{L} = \frac{1.56 * 10^{-7}}{0.14} = 1.12 * 10^{-6}\ \mathrm{mm/mm} \quad \text{Equation 2-12}$$

Based on the wave propagation theory in rods, the resonant column test applies a torsional oscillation on the top of the specimen. The testing procedure follows the standard designated ASTM D4015-81. However, the standard does not include sample preparation for a hollow cylinder specimen. Therefore, this dissertation describes the device and testing procedure. (Ishimoto & Iida, 1936) developed the first resonant column testing system. Hollow cylindrical samples produced more uniform shear strains within the cross-section of the spec-

imen (Hardin & Drnevich, 1972), (Sherif & Ishibashi, 1976), and (Iwasaki & Tatsuoka, 1977). More history of the RC test is presented by (Woods, 1978). The device today can consistently measure stiffness at small-to-intermediate (up to 10^{-1}%) strain levels, making it one of the most used laboratory devices for measuring the dynamic behavior of soil.

The fixed-free configuration oscillates the soil specimen at the top end while it fixes the base. The driving frequency gradually increases to find resonance, and the accelerometer measures the specimen's response. The frequency that maximizes the response amplitude is the first-mode fundamental frequency of the sample (resonant frequency). By using the wave equation and theory of elasticity and considering the fixed-free configuration of the device, the governing equation becomes.

$$\frac{I}{I_0} = \frac{\omega_n L}{Vs} \tan\frac{(\omega_n L)}{Vs} = \beta\tan\beta \qquad \text{Equation 2-13}$$

Where: I = the sample polar moment of inertia, I_0 = the free end mass polar moment of inertia, V_s = the shear wave velocity in the sample, ω_n = resonant frequency in torsion, L = the length of the sample.

The specimen's geometry and mass determine the value for I, and I_0 comes from calibrating the drive head (steel top ring, magnets, and mounting plate) using the three-wire pendulum method, so β can be computed. Subsequently, we can relate the resonant frequency to the shear wave velocity:

$$V_s = \frac{\omega_n L}{\beta} = \frac{2\pi f_n L}{\beta} \qquad \text{Equation 2-14}$$

The measured shear wave velocity and specimen mass density produce the shear modulus via Equation 2-1.

The torsional simple shear test applies torque to the specimen using a drive system of two magnets and four coils. The current flowing through the coils relates directly to the magnitude of torque. Calibration relating current flow to torque using a specimen rod of known stiffness provides the proper conversion factor. Proximitors, mounted near the specimen's top, measure displacements that translate to rotation (θ) at the top of the specimen. For the fixed-free configuration, the rotation (θ) varies linearly with the height of the measuring point in the specimen, starting from zero at the bottom and ending with the maximum value at the top. In our device, the shear strain relates to top rotation via the following equation:

$$\gamma = \frac{r * \theta_{\max}}{h} \qquad \text{Equation 2-15}$$

Where θ_{max} = the rotation (Equation 2-16), h = height of the cross-section of interest. r = the radial distance between the specimen axis and the calculated point.

$$\theta_{max} = \frac{x}{R} = \frac{x_A}{l_A} \qquad \text{Equation 2-16}$$

Where: x = arc length where a point at the edge of the specimen rotates, R = radius of the specimen, x_A = displacement of the attached accelerometer, l_A = radial offset of the accelerometer from the specimen axis.

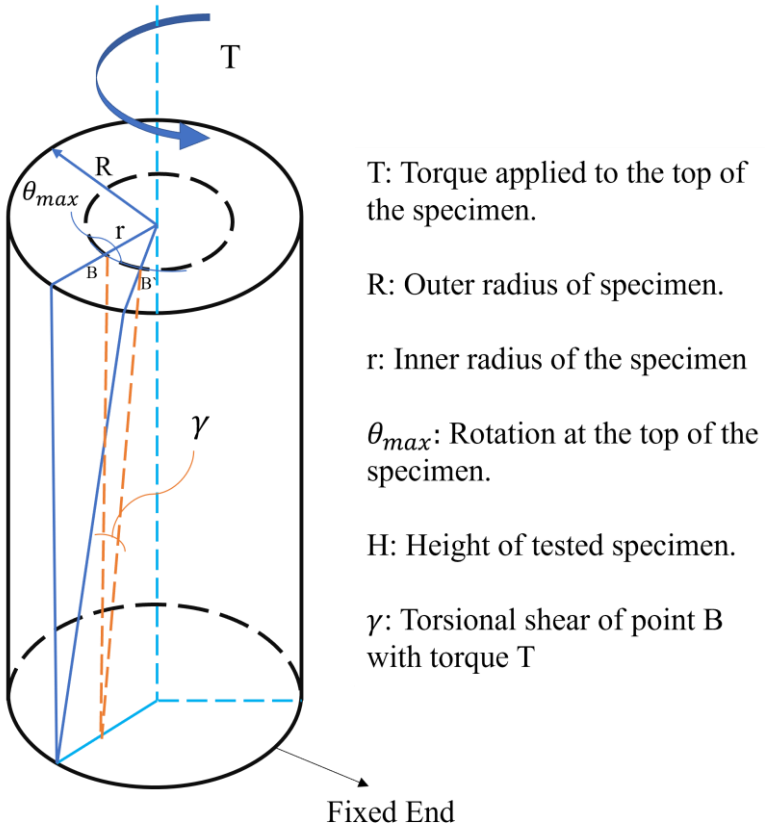

Figure 2-7 Diagram of the concept for torsional strain in a fixed-free hollow cylinder specimen.

Torsional testing produces stress-strain hysteresis loops characterized by secant shear modulus, as described in Figure 2-4a. The device can run both cyclic and irregular loading histories. However, cyclic tests provide more consistent information to study the influence of different parameters on the dynamic properties of soils (shear modulus and damping ratio).

2.3 Factors affecting the dynamic behavior of soil.

Many researchers have assessed the effects of different soil properties on the dynamic behavior of soil. Some factors did not affect behavior, while others influenced behavior significantly and were included in empirical equations to calculate the shear modulus and damping ratio. (Hardin & Drnevich, 1972) divided the factors that influence the dynamic behavior

of soil into three categories: very important, less important, and relatively unimportant. For dry sand (the soil tested in this investigation), the strain amplitude, effective confining pressure, and void ratio significantly influence dynamic properties. The degree of saturation, the over-consolidation ratio, and loading frequency contribute very little to behavior. However, for other soils, saturation, OCR, and other parameters may significantly influence G_{max}, G, and D. They considered that the number of loading cycles did not influence the shear modulus of sand. (Hardin & Drnevich, 1972). However, the TOSS tests in this study show a rather substantial effect. The following sections present the impact of these parameters on sand behavior.

2.3.1 Strain amplitude:

As shown before, the shear modulus decreases, and the damping ratio increases with increasing strain amplitude due to the nonlinear behavior of soil after exceeding the linear threshold (γ_{tl}) (Anderson, 1979), (Ladd, 1982), (Ray, 1984), (Georgiannou, et al., 1991). The shear modulus degradation curve (Figure 2-3) presents this effect.

2.3.2 Magnitude of the effective confining pressure

(Hardin & Richart, 1963) studied the influence of effective confining pressure through a laboratory testing program. They found that the shear modulus increases, and the damping ratio decreases with increasing effective mean principal stress. In a following study on clean sand by (Hardin & Drnevich, 1972), they concluded that for very small strain amplitudes, the modulus (G_{max}) varies with the 0.5 power of mean effective principal stress. For larger strains, the modulus depends on soil strength with a variation approximately equal to the 1.0 power. Later studies also confirmed this observation, such as (Saxena & Reddy, 1989) (Fioravante, 2000) (Hoque & Tatsuoka, 2004) ; (Chaudhary, et al., 2004) (Wichtmann & Triantafyllidis, 2004), where the power (n) in Equation 2-17 ranged between 0.45 and 0.62.

A recent study by (Mog & Anbazhagan, 2022) on the RC device agrees with the previous studies, where the damping ratio decreased with increasing confining pressure due to the higher contact between the particles, decreasing the attenuation of the propagating wave.

2.3.3 Duration of the effective confinement pressure

(Stokoe & Richart, 1973) conducted laboratory and field tests to find the effect of the duration of confining stress on the shear modulus under low-strain conditions. (Darendeli,

2001) confirmed their results, where G increased with time at each applied confining pressures during testing, as shown in Figure 2-8. However, this effect was marginal for sandy soils at confining pressures lower than 200 KPa. In our study, the confining pressure does not exceed 98 KPa, eliminating the need to consider this effect. Darendeli also found that D_{min} decreases as the specimen consolidates at a given confining pressure, as illustrated in Figure 2-9b. Note that both increase linearly with the log of time.

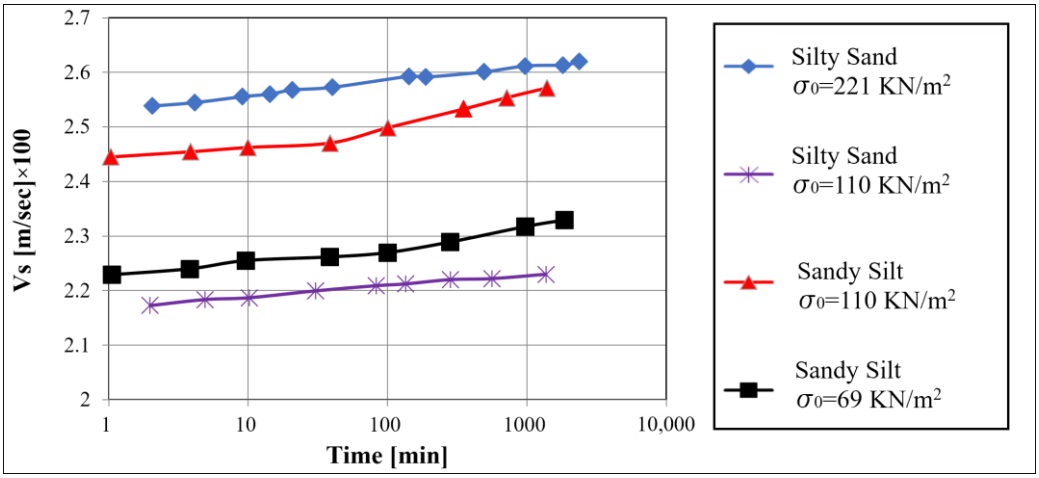

Figure 2-8 Shear wave velocity increase with time of confinement (Stokoe & Richart, 1973).

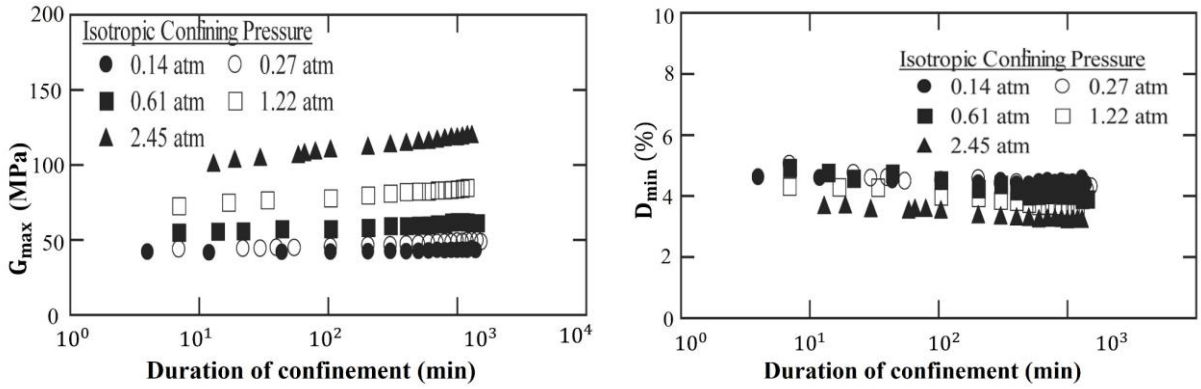

(a) increase of shear velocity and modulus. *(b) Decrease of minimum damping ratio.*

Figure 2-9 Effect of the increasing time of confinement (Darendeli, 2001).

2.3.4 Number of loading cycle

(Afifi & Woods, 1971), (Anderson & Richart, 1976), (Alarcon-Guzman, et al., 1989), and (Kim, et al., 1991) observed that the number of cycles does not affect the shear modulus below the elastic threshold strain, usually in the range of 0.001 % to 0.01 %. Thus, the value of G_{max} is considered independent of the time of vibration.

After exceeding the cyclic threshold, most studies reported an increase in the shear modulus with the increasing number of cycles for dry or drained sand under cyclic loading,

which is called "cyclic hardening in stiffness." Nevertheless, the studies have not entirely agreed on the degree of this effect, whether slight or significant. (Silver & Seed, 1971) reported that the increase is significant for the first 10 cycles followed by a relatively small change. For (Sherif & Ishibashi, 1976) the increase in the shear modulus reached up to 28% at the 25th cycle and then leveled off. Several factors influence the cyclic hardening in stiffness; fabric reorientation, particle relocation, and an increase in contact area (Ray, 1984). The highest increase in the shear modulus was reported by (Ray, 1984) of about 5% per logarithmic loading cycle. (Ray & Woods, 1988) obtained similar results from their RC-TOSS tests, where the increase was up to 120% of the initial value at a given strain level, and the increase was proportional to Log *N* (number of cycles). They also reported that the damping ratio could drop to 50% of its initial value after 200 cycles. More investigation about this effect appears in Chapter 5.

Several authors found a decrease in damping with the number of cycles, such as (Silver & Seed, 1971), (Edil & Luh, 1978), and (Kokusho, 1987). The RC-TOSS tests conducted by (Ray & Woods, 1988) showed a more pronounced reduction in damping ratio at a higher strain and a continuous decrease in damping on a Glacier Way Silt specimen after 30,000 cycles without an indication of leveling off.

(Cherian & Kumar, 2016) conducted resonant column tests on sand specimens with relative densities of 61 and 85% at confining stresses of 300 and 500 KPa to study the effect of vibration cycles on the dynamic properties. After 1000, 10,000, and 50,000 cycles at different strain levels, the measurements showed no effect below a certain threshold (shear strain between 0.0024 and 0.0044%). However, at higher strain levels, additional cycles caused an increase in the strain magnitude, causing a decrease in shear modulus and an increase in damping ratio. The strongest influence occurred at a confining stress of 300 KPa, a relative density of about 61%, and a shear strain amplitude of 0.03%. After 50,000 cycles, they produced an increase in shear strain of 34%, leading to an 8% decrease in the shear modulus and a 10% increase in the damping ratio.

Another study on the pre-vibration effect on the dynamic properties of dry Toyoura sand was carried out by (Yang, et al., 2019). They improved their Energy Injecting Virtual Mass (EIVM) resonant column system (Mark II) to reduce the time needed to reach a steady-state vibration. The system achieved a steady state after 12 equivalent cycles minimizing the disturbance to the specimen. The air pluviation method made cylindrical specimens at 38mm in diameter and 81 mm in height to achieve a relative density of 65%. Different sets of tests received pre-vibrations of 0.001, 0.005, 0.02, and 0.05% for 100-100,000 cycles and confin-

ing stresses of 25-500 KPa. The test results showed that the elastic threshold strain was about 10^{-2} %, where the pre-vibration did not affect the soil's dynamic properties. Less than a 5% decrease in the maximum shear modulus occurred when the specimen was pre-vibrated at a strain up to 0.02% for 100,000 cycles. Pre-vibrations of less than 10,000 cycles produced a marginal decrease. This pattern inverted when the pre-vibration increased to 0.05%, as the maximum shear modulus increased by 10% with the number of cycles (=100,000). The trend appears in Figure 2-10. Furthermore, the study shows a negligible effect of the confining pressure on the influence of pre-vibration (less than 3%).

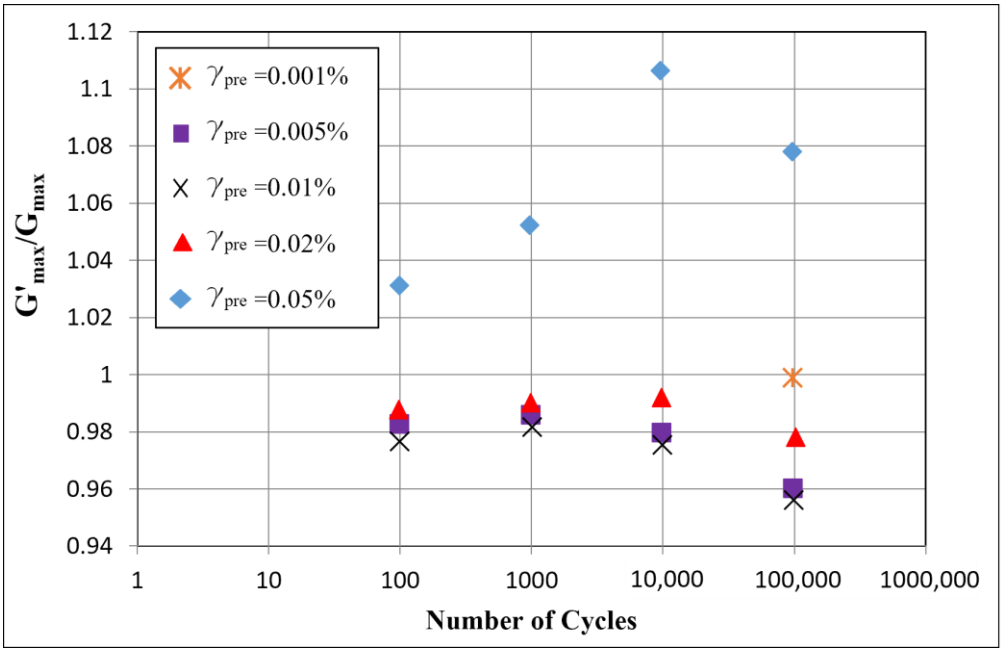

Figure 2-10 Effect of pre-vibration on G_{max} for confining stress of 100 KPa (Yang, et al., 2019).

2.3.5 Loading frequency

(Hardin, 1965) and (Hardin & Black, 1966) conducted precise static torsional and resonant column tests. They observe that the frequency had no influence on the low-strain shear modulus (G_{max}). As a result, static and dynamic tests produce identical G_{max} due to the elastic behavior of the soils at very small strain levels.

At higher strain levels, strain-rate effects become more evident. Stiffness increases with higher strain rates (RC-TOSS) when compared to monotonic static tests with low strain rates as reported by (Dobry & Vucetic, 1987) and (Tatsuoka & Shibuya, 1992). The cyclic torsional test is usually conducted at frequencies between 0.1-1 Hz, while in the resonant column test, the resonant frequency ranges from 30-200 Hz. (Ray & Woods, 1988) concluded that the two tests are interchangeable, provided that the cyclic effects have no significant impact. Nevertheless, (Tatsuoka, et al., 1979) and (Lo Presti, et al., 1997) found that the trend in a

monotonic test is different (shear strain rate of 0.01% per minute). It produces lower shear stiffness for a specific strain level, so the G/G_{max}-γ curve should be evaluated separately for monotonic and cyclic loading conditions.

According to (Darendeli, 2001), the loading frequency above 1Hz significantly affects sandy clay's minimum damping ratio (D_{min}), as it can increase by 100% over a log-cycle increase in excitation frequency. However, studies show that the damping of sand is independent of the frequency.

2.3.6 Void ratio:

Soil void ratio is a fundamental property that significantly affects the maximum shear modulus (G_{max}). The shear wave velocity decreased linearly with the increasing void ratio in the study by (Hardin & Richart, 1963). Since the 1990s, researchers have introduced different empirical correlations for G_{max} as a function of the void ratio (F(e)) for different types of soils by fitting equations to laboratory test results, as described in Equation 2-17. All studies confirmed that the small-strain shear modulus decreased with an increased void ratio.

Most correlations represent the maximum shear modulus as a function of the void ratio and confining stress as follows:

$$G_{\max} = A\mathrm{F}(e)\left(\frac{\acute{p}}{p_{\mathrm{atm}}}\right)^{n} \qquad \text{Equation 2-17}$$

$$\mathrm{F}(e) = \frac{(a-e)^2}{1+e} \qquad \text{Equation 2-18}$$

Where A, a, and n are experimentally determined coefficients and are called intrinsic (state-independent) parameters and are associated with small-strain stiffness (Carraro, et al., 2009), $\acute{p}$ equals the mean effective stress in [KPa], p_{atm} is the atmospheric pressure [KPa], and F(e) is the function of void ratio, which varies from researcher to researcher (Qian, et al., 1991); (Kagawa, 1992); (Qian, et al., 1993); (Guha, 1995); (Baig, et al., 1997); (Simonini & Cola, 2000); (Fam, et al., 2002); (Kallioglou, et al., 2008). The parameters proposed by studies on sand are summarized in Table 1.

The most recent empirical equation is given by (Wichtmann, et al., 2015) as a result of their extensive laboratory testing, and it depends on the uniformity coefficient (C_U) and the percentage of fine particles (FC). The parameters A, a, and n in Equation 2-17 for sands with non-cohesive fines (for FC < 10%) are as follows:

$$G_{\max} = A\frac{(a-e)^2}{1+e}\ p'^{n}\ p_{atm}^{1-n} \quad \text{Equation 2-19}$$

$$a = 1.94\exp(-0.066Cu)\exp(0.065FC) \quad \text{Equation 2-20}$$

$$n = 0.4\,C_u^{0.18}[1 + 0.116\ln(1+FC)] \quad \text{Equation 2-21}$$

$$A = (1563 + 3.130.4\,C_u^{2.98})0.5[\exp(-0.03FC^{1.1}) + \exp(-0.28FC^{0.85})] \quad \text{Equation 2-22}$$

Table 1 Correlations for small strain shear modulus G_{max} of sand using Equation 2-17. G_{max} is in [MPa], p' in [KPa], and p_{atm} = 1 atm).

Soil Tested	D_{50} [mm]	C_U [-]	A [-]	F(e) [-]	n [-]	Reference
Ottawa sand No. 20–30	0.72	1.20	69	$\frac{(2.17-e)^2}{1+e}$	0.5	(Hardin & Richart, 1963)
Ticino sand (subangular)	0.54	1.50	71	$\frac{(2.27-e)^2}{1+e}$	0.43	(Lo Presti, et al., 1993)
Toyoura sand (subangular)	0.22	1.35	72	$e^{-1.3}$	0.45	(Lo Presti, et al., 1993)
Quiou carbonate sand	0.75	4.40	71	$e^{-1.3}$	0.62	(Lo Presti, et al., 1993)
Kenya carbonate sand	0.13	1.86	101–129	$e^{-0.8}$	0.45–0.52	(Fioravante, 2000)
Ticino sand (subangular)	0.55	1.66	79–90	$e^{-0.8}$	0.43–0.48	(Fioravante, 2000)
Hostun sand (angular)	0.31	1.94	80	$\frac{(2.17-e)^2}{1+e}$	0.47	(Hoque & Tatsuoka, 2000)
H.River sand (subangular)	0.27	1.67	72–81	$\frac{(2.17-e)^2}{1+e}$	0.50–0.52	(Kuwano & Jardine, 2002)
Glass ballotini (spheres)	0.27	1.28	64–69	$\frac{(2.17-e)^2}{1+e}$	0.55–0.56	(Kuwano & Jardine, 2002)
Silica sand (subangular)	0.20	1.10	80	$\frac{(2.17-e)^2}{1+e}$	0.5	(Kallioglou, et al., 2003)
Silica sand (subangular)	0.20	1.70	62	$\frac{(2.17-e)^2}{1+e}$	0.5	(Kallioglou, et al., 2003)
Silica sand (subangular)	0.20	1.10	62	$\frac{(2.17-e)^2}{1+e}$	0.5	(Kallioglou, et al., 2003)
Silica sand (angular)	0.32	2.80	48	$\frac{(2.17-e)^2}{1+e}$	0.5	(Kallioglou, et al., 2003)
Toyoura sand (subangular)	0.16	1.46	71–87	$\frac{(2.17-e)^2}{1+e}$	0.41–0.51	(Hoque & Tatsuoka, 2004)
Toyoura sand (subangular)	0.19	1.56	84–104	$\frac{(2.17-e)^2}{1+e}$	0.50–0.57	(Chaudhary, et al., 2004)
Ticino sand (subangular)	0.50	1.33	61–64	$\frac{(2.17-e)^2}{1+e}$	0.44–0.53	(Hoque & Tatsuoka, 2004)
Silica sand	0.55	1.80	275	$\frac{(2.17-e)^2}{1+e}$	0.42	(Wichtmann & Triantafyllidis, 2004)
SLB sand (subround)	0.62	1.11	82–130	$\frac{(2.17-e)^2}{1+e}$	0.44–0.53	(Hoque & Tatsuoka, 2004)
Natural quartz sand	0.27–1.33	1.34–2.76	$-5.88C_u+57.1$	$e^{-0.28Cu-0.98}$	0.47	(Senetakis, et al., 2012)
Quarry sand	0.16–2	2–2.5	$-9.54C_u+78.1$	$e^{-0.28Cu-0.98}$	0.63	(Senetakis, et al., 2012)
Volcanic sand	0.23–1.6	1.53–4.18	$-3.04C_u+52$	$e^{-0.28Cu-0.98}$	0.55	(Senetakis, et al., 2012)
Blue sand	1.01–1.94	1.41–8.22	$84C_u^{-0.14}\rho^{0.68}$	$e^{-1.29}$	$0.5C_u^{0.12}(0.23\rho + 0.59)$	(Payan, et al., 2016)
Danube Sand	0.107–0.424	2.06–9.85	62	$\frac{(2.17-e)^2}{1+e}$	0.45	(Szilvágyi, et al., 2017)

The void ratio did not affect the modulus degradation curve G/G_{max} (Iwasaki, et al., 1978) based on RC-TOSS test results on Toyoura sand. Researchers have attempted to find a correlation between void ratio and strain-dependent shear modulus, such as (Oztoprak & Bolton, 2013), who evaluated 454 tests on 60 soils from 65 reference studies. As a result, they modified Equation 2-17 and suggested a different void ratio function for strain-dependent stiffness:

$$G(\gamma) = \frac{A(\gamma)p_{\text{atm}}}{(1+e)^3}\left(\frac{\acute{p}}{p_{\text{atm}}}\right)^{n(\gamma)} \qquad \text{Equation 2-23}$$

where $A(\gamma)$ and $n(\gamma)$ are strain dependent parameters, given in Figure 2-11.

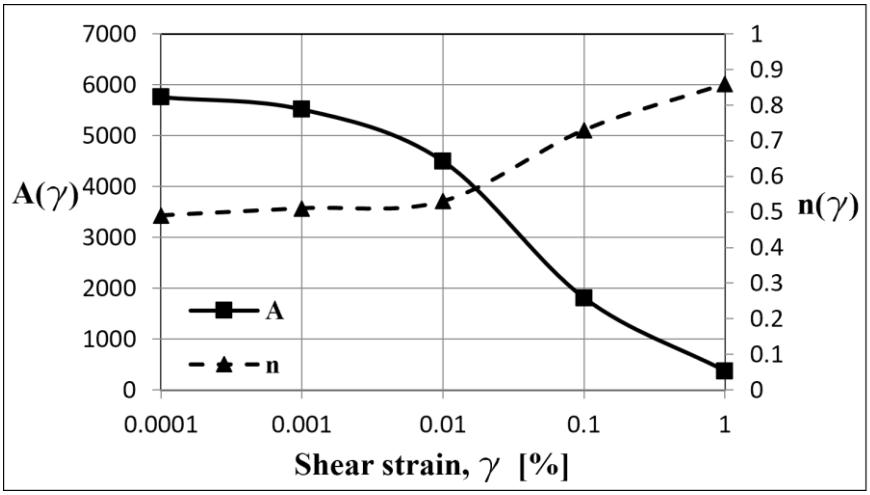

Figure 2-11 Coefficients for Equation 2-23 after (Oztoprak & Bolton, 2013).

This equation has a relatively large scatter indicating the difficulty of obtaining a correlation for the strain-dependent shear stiffness that would be reliable for a wide variety of granular soils. Therefore, a different approach can model the dynamic behavior of soil at larger strain levels.

(Szilvágyi, 2017) compared his measurement data on Danube sand to the correlations proposed by (Carraro, et al., 2009), (Biarez & Hicher, 1994), (Wichtmann & Triantafyllidis, 2009), (Wichtmann, et al., 2015), and (Oztoprak & Bolton, 2013). The fit was excellent for (Carraro, et al., 2009), as 75% of the measured G_{max} values fell within the range of ±15%. Furthermore, 87% of the data points were within the range of ±20%. The correlation provided by (Biarez & Hicher, 1994) produced satisfactory outcomes for the soils examined. Among the 69 measured G_{max} values, approximately 72% were found to fall within the ±15% range using this correlation. Moreover, around 84% of the data points were within the ±20% range. The correlation for clean sands (Wichtmann & Triantafyllidis, 2009) tends to over-predict many measured results. A total of 47% of the data points lie within the ±15% margin, and

60% of data points lie within the ±20% margin. In contrast, the correlation provided for sands containing non-plastic fines by (Wichtmann, et al., 2015) underestimates the G_{max} of soils with low content of plastic fines (up to 7.6%). The accuracy of the correlation is similar to the previous equations, with approximately 51% of the data points falling within the ±15% margin and around 63% within the ±20% margin. However, it should be noted that these equations underestimate G_{max} in certain cases by more than 35%. The correlations provided by (Oztoprak & Bolton, 2013) tended to overestimate the majority of the measured results. However, the estimated values still fell within the range of ±100%, which was also observed by the researchers for a significant portion of the collected data.

2.3.7 Effect of sample disturbance

In a study by (Szilvágyi, et al., 2017), in-situ and laboratory tests were conducted to measure the shear wave velocity for soils in Budapest, Hungary, to use it for 1D ground response analysis. They compared shear wave velocity values obtained using RC and TOSS measurements to the multichannel analysis of surface waves (MASW) and seismic cone penetration tests (SCPT). The shear modulus obtained from the laboratory measurements provided a lower bound for the in-situ tests, as shown in Figure 2-12. The author justifies this difference because the field void ratio (state of compaction) and stress state are not certain. Two later studies agreed with these findings (Rocha, et al., 2021) and (Fernandes, et al., 2023). In both studies, in-situ seismic dilatometer Marchetti test (SDMT) measurements showed a higher G_{max} than those obtained from the RC test by 17% to 46% in (Rocha, et al., 2021) and by 8% to 35% in (Fernandes, et al., 2023). The decrease in the shear modulus defined in the laboratory can be a cause of the effect of soil suction or disturbance during sample preparation.

(Lashin, et al., 2021) compared resonant column small strain shear modulus measurements with the stiffness obtained using the piezoelectric ring-actuator technique (P-RAT). This device recorded the shear wave velocity of the soil based on the transmission of a mechanical signal through the soil specimen with source and receiver transducers during the oedometer test. The testing program included tests on sand specimens prepared using the wet-tamping method with different void ratios and confining pressures. The results demonstrated higher values for the shear wave velocities measured by the RC tests compared to the P-RAT, especially for loose samples. The authors attributed this overestimation to the discrepancy between the assumption of the linear elastic behavior of soil and natural soil behavior. The

study recommends using the P-RAT technique to study the small strain stiffness of soil due to its higher accuracy.

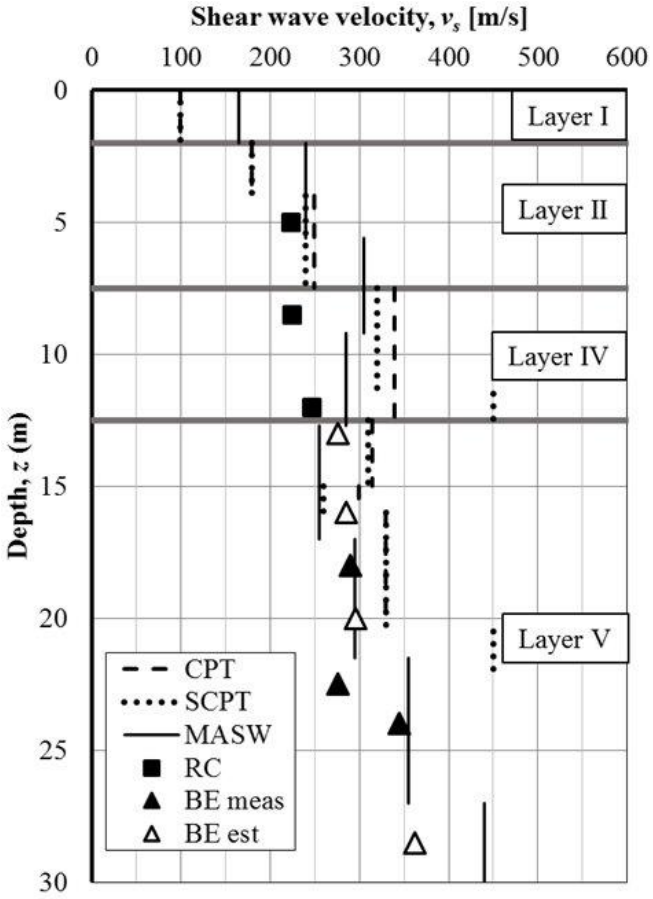

Figure 2-12 Comparison of measured shear wave velocity values (Szilvágyi, et al., 2017).

2.3.8 Temperature effect

(Yu, et al., 2017) used a special resonant column apparatus to study the dynamic behavior of frozen silt soils, where a cooling bath (Thermo Scientific HAAKE Bath) controlled the specimen temperature to ±0.01 °C. The sample was compacted, placed in a chloroprene rubber membrane, saturated, and confined in silicon oil. The study showed that the stiffness and damping ratio remained constant with temperature until −1.4 °C. The properties started to increase considerably until -3 °C (sensitive range), and at colder temperatures, the change was gradual (insensitive stage). The maximum shear modulus for the frozen soil was much higher than at ambient temperature. Shear modulus degradation curves reached lower values at low temperatures when compared to soils at ambient temperatures. For instance, at a strain level of 10^{-3}%, the value of G/G_{max} was 40% for a sample tested at a temperature of -15 °C whereas it was 90% for a sample tested at room temperature. However, the damping ratio continued increasing as the temperature dropped for strains of 10^{-6} to 5×10^{-4}, as shown in Table 2 and

Figure 2-13. The authors suggested temperature correction coefficients based on the RC tests to modify the dynamic properties and account for freezing effects.

Table 2 Parameters of the frozen silt modulus ratio and damping ratio curves at different temperatures (Yu, et al., 2017)

Temperature [°C]	G_{max} **[MPa]**	γ_r **[%]**	D_{max} **[-]**	n **[-]**
−15	1539.2	6.312×10−5	0.073	0.42
−10	1467.4	6.670×10−5	0.078	0.36
−5	1341.8	7.520×10−5	0.106	0.44
−3	1238.4	9.354×10−5	0.116	0.36
Room temperature (15 °C to 25 °C)	64.2	6.602×10−4	0.183	0.60

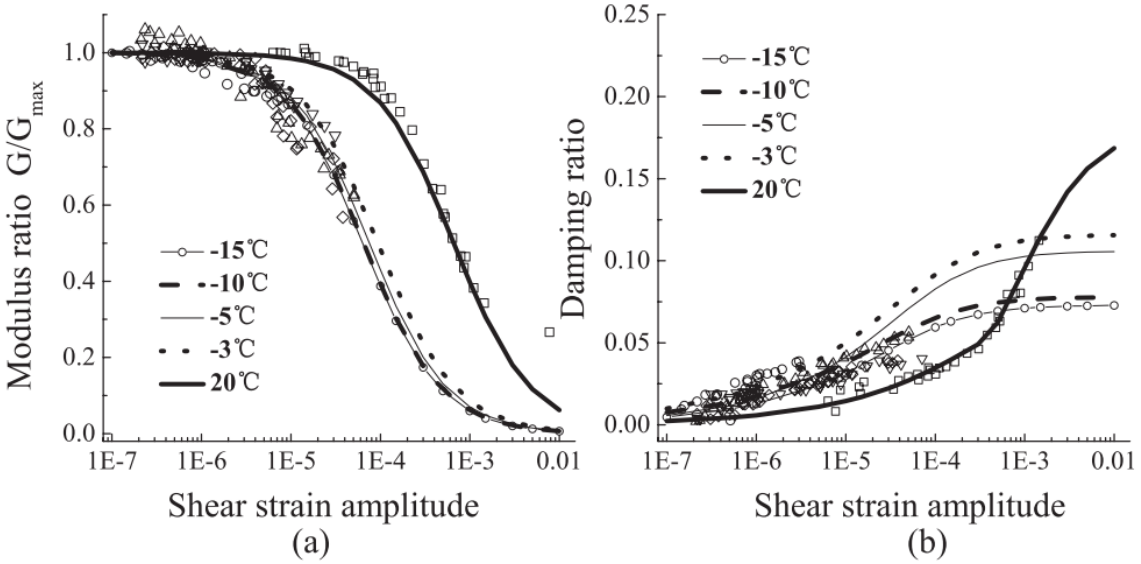

Figure 2-13 Temperature effect: (a) Modulus ratio (b) Damping ratio (Yu, et al., 2017).

2.4 Soil models

2.4.1 Irregular loading and Masing criteria

A simple soil model can easily simulate soils' nonlinear monotonic shear stress-shear strain behavior. However, predicting such behavior for reversible strains and irregular load histories requires introducing more rules that dictate the path followed by the shear stress-shear strain curve when generating the hysteresis loops.

(Masing, 1926) investigated the behavior of brass under cyclic loading and introduced two rules that are sufficient to describe regular, symmetric cyclic loading and could be applied to soils, as discussed by (Pyke, 1979):

1. The shear modulus in unloading is equal to the initial tangent modulus for the initial loading curve (Figure 2-14).

2. The unloading and reloading curve duplicate the initial curve, except that its scale increases by a factor of two in both directions. The variables τ and γ in the formulation are replaced by $(\tau - \tau_i)/2$ and $(\gamma - \gamma_i)/2$ (Figure 2-14).

Note that these two rules are insufficient to describe the soil behavior if the loading is more general or irregular (not symmetrical or periodic). (Jennings, 1965) presented a general nonlinear hysteretic force-deflection relation for a one-degree-of-freedom structure to study the earthquake response of a yielding structure, and he extended the criteria by adding two additional rules as follows:

3. Unloading and reloading curves should follow the initial curve if the condition exceeds the previous maximum shear strain.

4. If the current loading or unloading curve intersects a previous one, it should follow the previous curve.

Most researchers cite these four rules as the extended Masing criteria, which were first used for soil by (Constantopoulos , et al., 1973) and (Finn, et al., 1977) and today extend to soil models that formerly described only monotonic behavior. Figure 2-14 illustrates an example using the Ramberg-Osgood model.

As mentioned by (Valera , et al., 1978), the two added rules require that the model keeps track of previous paths in both directions. Programmed turnaround coordinates use a last in-first out (LIFO) sequence to determine when the stress-strain curve applies rule (4).

Figure 2-15b illustrates the discussion by (Pyke, 1979), where he shows the stress-strain curve transitioning from point 4 as a turnaround to point 2. The transition occurs at point 3. Upon reloading from point 4, the solution suggested by (Rosenblueth & Herrera, 1964) and that proposed by (Jennings, 1965) would follow path A. On the other hand, if the dashed curve 0-1 is the greatest previous reloading curve, it would follow stress path B.

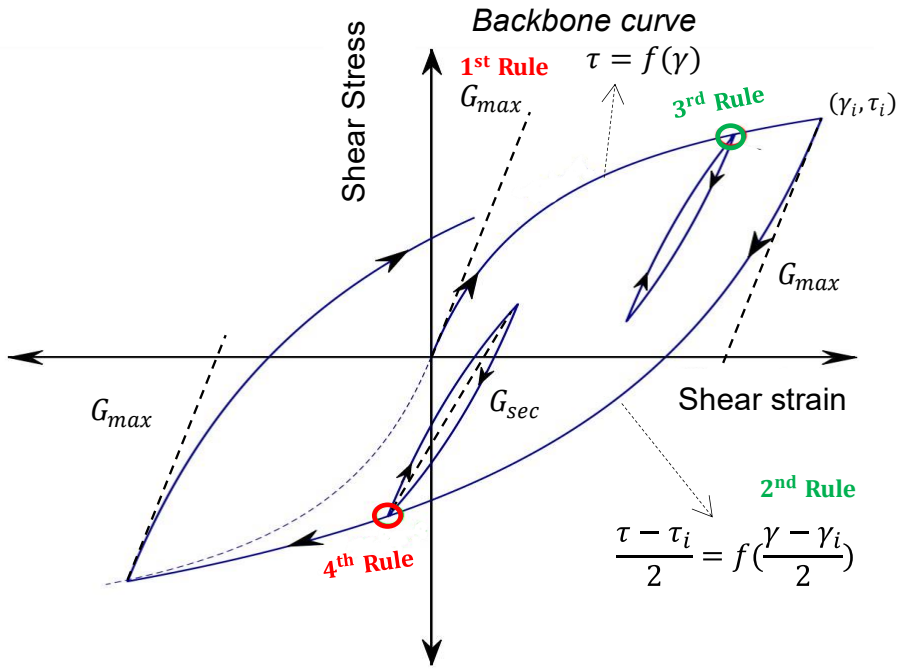

Figure 2-14 Masing criteria.

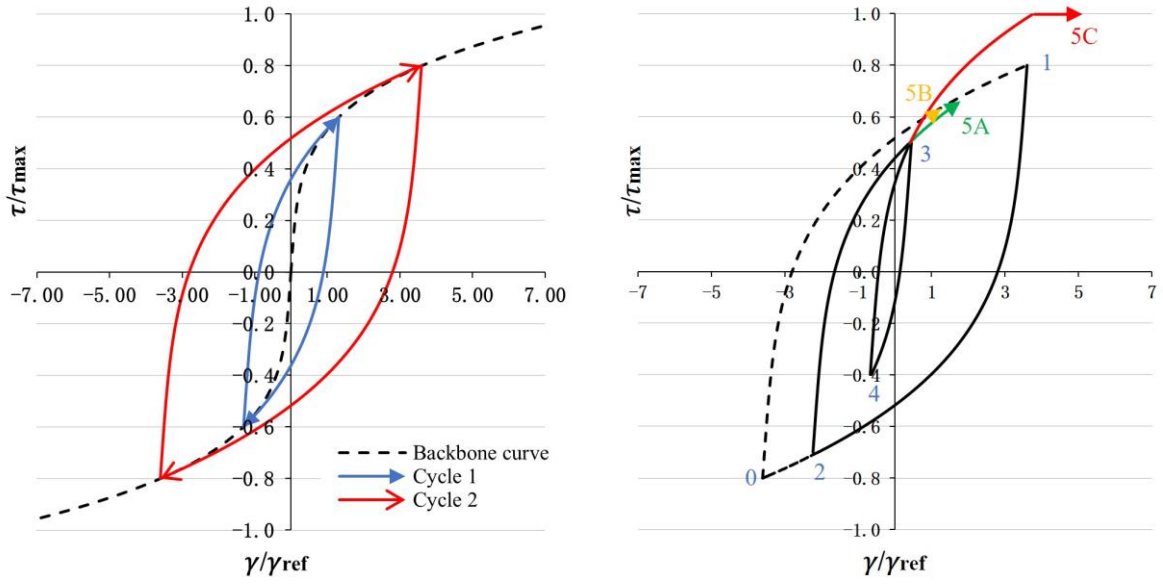

(a) Symmetric. *(b) Irregular loading with Pyke's discussion.*

Figure 2-15 Hysteresis loops according to the extended Masing rules using the Ramberg-Osgood model after (Pyke, 1979).

2.4.2 Modified Ramberg-Osgood model:

(Ramberg & Osgood, 1943) proposed a model with three parameters describing the stress-strain curves of aluminum-alloy stainless-steel and carbon-steel sheets to consider the gradual transition from the straight elastic line for low loads toward the horizontal line characterizing plastic behavior. (Jennings, 1965) used this model to describe the hysteretic curves

for the steady-state response of yielding structures as a relationship between displacement and restoring force. Then, this model was first used for soil by (Faccioli, et al., 1973) to describe the stress-strain nonlinear behavior of the soil under simple shear in their one-dimensional wave propagation model to study the seismic response in Managua. The form today differs from the original, and the model used for soil in geotechnical earthquake engineering was demonstrated by (Streeter, et al., 1974) shown in Equation 2-24. This equation has been widely used in several studies, e.g. (Ray & Woods, 1988) (Benz, 2006) (Szilvágyi, 2017). The formulation used for the shear stress-shear strain relation follows:

$$\gamma = \frac{\tau}{G_{\max}}\left(1+\alpha\left|\frac{\tau}{C\,\tau_{\max}}\right|^{R-1}\right) \qquad \text{Equation 2-24}$$

Where: γ is the shear strain, τ is the shear stress, $G_{\max}$ is the small strain shear modulus, $\tau_{\max}$ is the maximum shear strength (usually from triaxial tests), α, C, and R are the curve-fitting constants.

It is a straightforward calculation to obtain shear strains from shear stresses. However, it is more difficult to invert the formulation. Different methods can solve this problem, including the Newton-Raphson method.

The secant shear modulus, as defined by the ratio between the shear stress and shear strain at any strain level, can be expressed in the RO model as follows:

$$G_{\text{sec}} = \frac{\tau}{\gamma} = \frac{G_{\max}}{\left(1+\alpha\left|\frac{\tau}{C\,\tau_{\max}}\right|^{R-1}\right)} \qquad \text{Equation 2-25}$$

The following equation gives the tangent shear modulus:

$$G_{\tan} = \frac{\partial\tau}{\partial\gamma} = \frac{G_{\max}}{\left(1+\alpha R\left|\frac{\tau}{C\,\tau_{\max}}\right|^{R-1}\right)} \qquad \text{Equation 2-26}$$

Subsequently, Equations 2-27 and 2-28 produce shear moduli degradation for secant and tangent shear modulus, respectively. Note that the secant shear modulus is always higher than the tangent modulus at any given strain, as shown in Figure 2-16.

$$\frac{G_{\text{sec}}}{G_{\max}} = \frac{1}{1+\alpha\left|\frac{\tau}{C\,\tau_{\max}}\right|^{R-1}} \qquad \text{Equation 2-27}$$

$$\frac{G_{tan}}{G_{\max}} = \frac{1}{\left(1+\alpha R\left|\frac{\tau}{C\,\tau_{\max}}\right|^{R-1}\right)} \qquad \text{Equation 2-28}$$

It is common to use a log scale to plot strains on the horizontal axis to see the soil behavior more clearly. Researchers may express strain either in percent (%) or (mm/mm), and

the modulus may reduce significantly below its maximum value at relatively low strain levels ($\gamma = 0.001$).

Equation 2-24 has a dimensionless form by introducing a reference shear strain γ_{ref} at $\tau_{\max}$ shear stress as follows:

$$\frac{\gamma}{\gamma_{\text{ref}}} = \frac{\tau}{\tau_{\max}}\left(1+\alpha\left|\frac{\tau}{C\,\tau_{\max}}\right|^{R-1}\right) \qquad \text{Equation 2-29}$$

$$\gamma_{\text{ref}} = \frac{\tau_{\max}}{G_{\max}} \qquad \text{Equation 2-30}$$

The maximum shear stress is typically assumed to equal the Mohr-Coulomb failure envelope strength with effective stress properties, as shown in Figure 2-17. Based on the diagram, the maximum shear strength is:

$$\tau_{\max} = \left(\frac{c'}{\tan\varphi'} + \sigma_0'\right)\sin\varphi'\cos\varphi' \qquad \text{Equation 2-31}$$

$$\tau_{\max} = \sqrt{\left(\left(\frac{1+K_0}{2}\right)\sigma_v'\sin\varphi' + c'\cos\varphi'\right)^2 - \left(\left(\frac{1-K_0}{2}\right)\sigma_v'\right)^2} \qquad \text{Equation 2-32}$$

Equation 2-32 applies to the isotropic confining conditions often produced in laboratory tests. Equation 2-32 represents anisotropic (K_0) conditions in the field. The dimensionless form (Equation 2-29) applies to the soil at any depth. Changes in $\tau_{\max}$ automatically resolve the soil's depth effects (confining stress). Normalizing the curves produces one standard curve for similar soils.

When considering loading reversals, the formulation becomes slightly more complex. The most straightforward approach uses the Masing formulation and substitutes into the equations $\frac{\gamma-\gamma_i}{2}$ for γ, and $\frac{\tau-\tau_i}{2}$ for τ; then the formulation becomes:

$$\frac{\gamma-\gamma_i}{2} = \frac{\frac{\tau-\tau_i}{2}}{G_{\max}}\left[1+\alpha\left|\frac{\frac{\tau-\tau_i}{2}}{C\tau_{\max}}\right|^{R-1}\right] \qquad \text{Equation 2-33}$$

Where γ_i and τ_i equal the shear strain and shear stress at the last turning point.

The same substitution occurs in formulations for G_{sec} and $G_{\tan}$ (Equation 2-27 and Equation 2-28). This approach will produce a hysteresis loop with reversals, as shown in Figure 2-14. The figure illustrates some other important properties as well. At every reversal point, the stress-strain curve starts with a stiffness of $G_{\max}$. The line labeled G_{sec} shows an example of computing the secant modulus for a hysteresis loop (Figure 2-14).

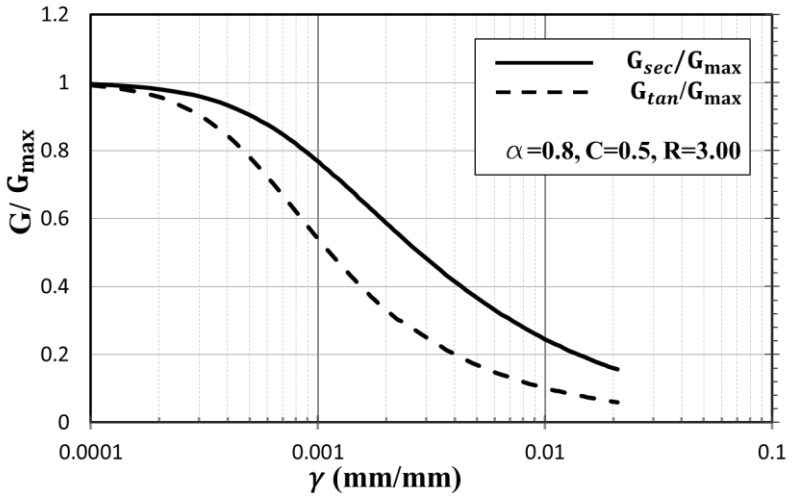

Figure 2-16 Normalized secant and tangent modulus vs. strain obtained with the Ramberg-Osgood model.

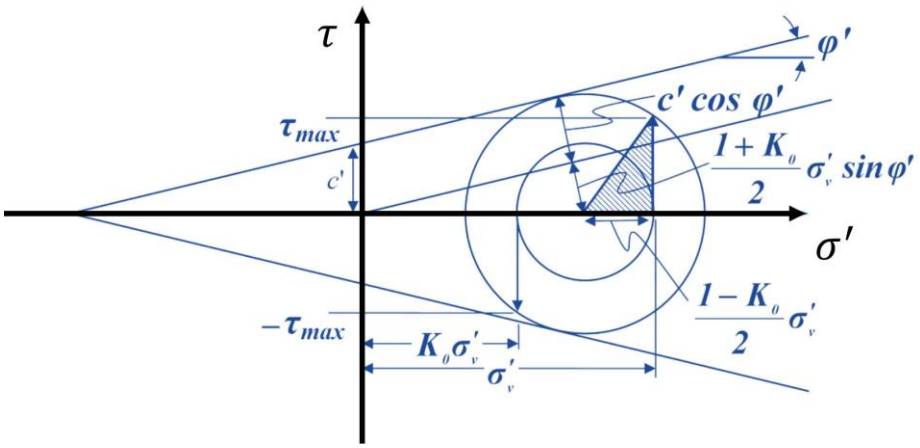

Figure 2-17 Mohr diagram for maximum shear stress.

Damping in Ramberg-Osgood model is calculated by integrating along the stress axis. Given the differential element shown in Figure 2-18, it has a width of $d\tau$ and a length of $(\gamma_2 - \gamma_1)$.

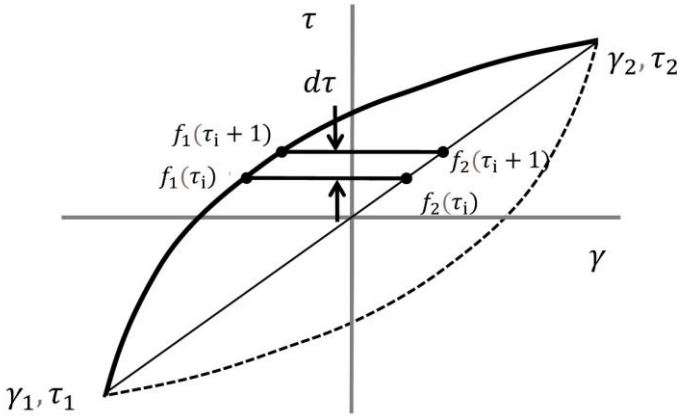

Figure 2-18 Integration element for half a loop in RO model.

We can integrate this expression from τ_1 to τ_2. The two functions can be written as:

$$f_1(\tau) = \gamma = 2\left\{\frac{\tau-\tau_1}{2G_{\max}}\left[1+\alpha\left|\frac{\tau-\tau_1}{2C\tau_{\max}}\right|^{R-1}\right]\right\}+\gamma_1 \quad \text{Equation 2-34}$$

If $a=\frac{1}{G_{\max}}$, $b=\frac{a}{(2C\tau_{\max})^{R-1}}$ then $f_1(\tau)=a(\tau-\tau_1)+ab(\tau-\tau_1)^R+\gamma_1$

$$f_2(\tau)=\frac{(\tau-\tau_1)(\gamma_2-\gamma_1)}{(\tau_2-\tau_1)}+\gamma_1 \quad \text{Equation 2-35}$$

$$if\ c=\frac{(\gamma_2-\gamma_1)}{(\tau_2-\tau_1)}\ then\ f_2(\tau)=c(\tau-\tau_1)+\gamma_1$$

Then, the integration can be written as:

$$\int_{\tau_1}^{\tau_2} f_2(\tau)-f_1(\tau)d\tau=\int(c-a)\,(\tau-\tau_1)d\tau-\int b\,(\tau-\tau_1)^R d \quad \text{Equation 2-36}$$

The final formula resulting from the integration is given by:

$$A_{\text{half loop}}=\frac{(c-a)(\tau_2-\tau_1)^2}{2}+\frac{b(\tau_2-\tau_1)^{R-1}}{R+1} \quad \text{Equation 2-37}$$

Subsequently, from the definition of the damping ratio, it is calculated by using the following equation:

$$D=\frac{A_{\text{loop}}}{4*\pi*A_{\text{triangle}}}=\frac{2*A_{\text{half loop}}}{4*\pi*\left(\frac{A_{\text{lower triangle}}+A_{\text{upper triangle}}}{2}\right)} \quad \text{Equation 2-38}$$

Midas uses a different form of the Ramberg-Osgood equation with two curve fitting constants instead of three. In the initial loading, it moves along the following skeleton curve (MIDAS Information Technology Co., 2014).

$$G_0\gamma=\tau\left(1+\alpha|\tau|^{\beta}\right) \quad \text{Equation 2-39}$$

Where G_0 is the Initial stiffness (shear modulus), α and β are the model parameters given by:

$$\alpha=\left(\frac{2}{\gamma_r G_0}\right)^{\beta}\quad,\qquad \beta=\frac{2\pi h_{\max}}{2-\pi h_{\max}} \quad \text{Equation 2-40}$$

γ_r is the reference shear strain, and $h_{\max}$ is the maximum damping constant. For unloading and reloading, the hysteresis curve is as follows:

$$G_0\left(\frac{\gamma\mp\gamma_i}{2}\right)=\left(\frac{\tau\mp\tau_i}{2}\right)\left(1+\alpha\left(\frac{\tau\mp\tau_i}{2}\right)^{\beta}\right) \quad \text{Equation 2-41}$$

Where γ_i and τ_i are the shear strain and stress values at the turnaround point.

Considering the uniaxial condition, the hysteresis curve is expressed as follows:

$$E_0\varepsilon = \sigma + \alpha|\sigma|^{\beta}\sigma \quad \text{Equation 2-42}$$

In 3D conditions, the formula divides into hydrostatic and deviatoric (shearing) components. The formula becomes a 3D expression:

$$E_0\varepsilon_{\mathrm{dev}} = (1+\nu)\sigma_{\mathrm{dev}} + \frac{3}{2}\alpha\sigma_{\mathrm{eq}}^{\beta}\sigma_{dev} \quad \text{Equation 2-43}$$

Where E_0 is the initial stiffness and σ_{eq} is the Von Mises stress.

If the equivalent deviatoric strain $\varepsilon_{\mathrm{eq}} = \sqrt{\frac{2}{3}\varepsilon_{\mathrm{dev}}:\varepsilon_{\mathrm{dev}}}$, it is expressed as follows:

$$E_0\varepsilon_{\mathrm{dev}} = \frac{2}{3}(1+\nu)\sigma_{\mathrm{dev}} + \alpha\sigma_{\mathrm{eq}}^{\beta}\sigma_{\mathrm{dev}} \quad \text{Equation 2-44}$$

The following equation calculates the tangent stiffness:

$$\frac{\partial\sigma_{\mathrm{eq}}}{\partial\varepsilon_{\mathrm{eq}}} = \frac{E_0}{\frac{2}{3}(1+\nu) + (\beta+1)\alpha\sigma_{\mathrm{eq}}^{\beta}} \quad \text{Equation 2-45}$$

The Poisson's ratio ν is assumed to be a constant regardless of the stress state, and Equation 2-45 provides the equivalent elastic modulus. The 3D stiffness matrix uses the equivalent elastic modulus as follows:

$$D = \frac{\bar{E}}{(1+\nu)(1-2\nu)}\begin{bmatrix} 1-\nu & \nu & \nu & 0 & 0 & 0 \\ \nu & 1-\nu & \nu & 0 & 0 & 0 \\ \nu & \nu & 1-\nu & 0 & 0 & 0 \\ 0 & 0 & 0 & \frac{1-2\nu}{2} & 0 & 0 \\ 0 & 0 & 0 & 0 & \frac{1-2\nu}{2} & 0 \\ 0 & 0 & 0 & 0 & 0 & \frac{1-2\nu}{2} \end{bmatrix} \quad \text{Equation 2-46}$$

2.4.3 The Hyperbolic Model

A hyperbolic equation was proposed by (Hardin & Drnevich, 1972) as a simple nonlinear relationship between the shear stress and strain (Figure 2-19a). The first iteration took the following form:

$$\tau = \frac{\gamma}{\frac{1}{G_{\max}} + \frac{\gamma}{\tau_{\max}}} \quad \text{Equation 2-47}$$

However, they noticed that the soil behavior deviated from a simple hyperbolic curve, depending on the soil type and properties, as shown in Figure 2-19b. Therefore, they introduced a modified hyperbolic strain to the equation to fit the curve with the soil behavior by distorting the strain axis scale. The modified hyperbolic strain is expressed by:

$$\gamma_{\mathrm{h}} = \frac{\gamma}{\gamma_{\mathrm{r}}}\left[1 + a * \exp\left(-b\left(\frac{\gamma}{\gamma_{\mathrm{r}}}\right)\right)\right] \quad \text{Equation 2-48}$$

where “a” and “b” are coefficients that adjust the shape of the stress-strain curve.

The equation used today in Midas for the modified Hardin-Drnevich model, coupled with the Masing criteria for hysteresis loops, follows:

$$\tau = \frac{G_0 \gamma}{1 + \left|\frac{\gamma}{\gamma_r}\right|} \quad \text{Equation 2-49}$$

Where G_0 is the initial shear modulus and γ_r is the reference shear strain.

The same method as in the RO model modifies the hysteretic curve from the skeleton curve in HD as follows:

$$\tau - \tau_1 = \frac{G_{0(}\gamma - \gamma_1)}{1 + \left|\frac{\gamma - \gamma_1}{2\gamma_r}\right|} \quad \text{Equation 2-50}$$

In this form, a least squares regression technique adjusts the reference strain to fit the model to laboratory test results.

By dividing both sides of Equation 2-49 by γ, the shear modulus (G) is obtained:

$$G = \frac{G_0}{1 + \left|\frac{\gamma}{\gamma_r}\right|} \quad \text{Equation 2-51}$$

The modulus reduction curve follows by rearranging Equation 2-51 to obtain:

$$\frac{G}{G_0} = \frac{1}{1 + \left|\frac{\gamma}{\gamma_r}\right|} \quad \text{Equation 2-52}$$

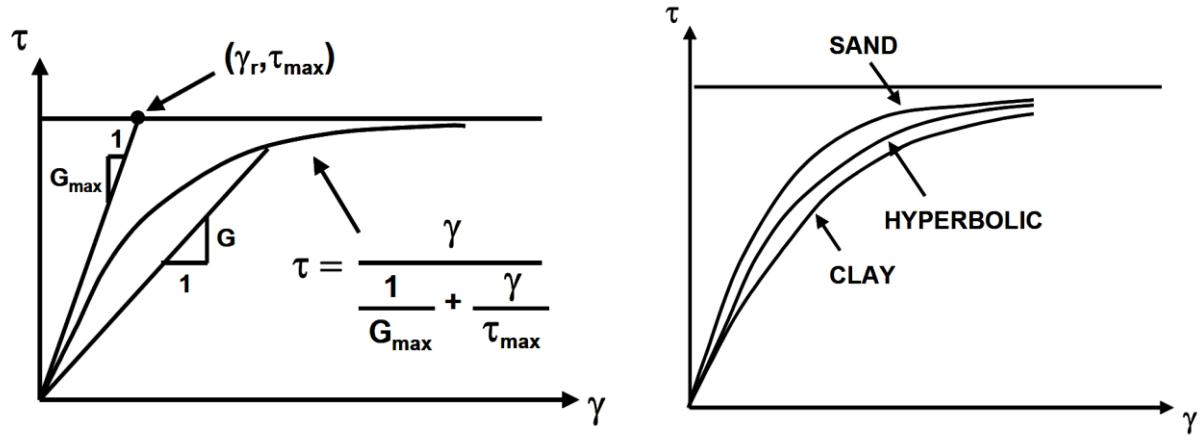

(a) Hyperbolic soil model proposed by Hardin and Drnevich (1972).

(b) The deviation from a hyperbole depending on soil type.

Figure 2-19 Hyperbolic model.

Hardin and Drnevich (1972b) also proposed an approximate shape for the material damping curve as:

$$\frac{D}{D_{\max}} = \frac{\frac{\gamma}{\gamma_r}}{1+\frac{\gamma}{\gamma_r}} \qquad \text{Equation 2-53}$$

Where D_{max} is the maximum damping ratio, depending on soil type, confining pressure, number of load cycles, and loading frequency.

(Matasovic & Vucetic, 1993) introduced a curvature coefficient, a, into the normalized modulus reduction curve for a better fit with the measured data as follows:

$$\frac{G}{G_{\max}} = \frac{1}{1+\left(\frac{\gamma}{\gamma_r}\right)^a} \qquad \text{Equation 2-54}$$

(Darendeli, 2001) also incorporated the coefficient, but he defined the reference shear strain γ_r as the strain amplitude when the shear modulus reduces to one-half of G_{max}. He suggested measuring this value from laboratory tests when G/G_{max} is around 0.5. An example is shown in Figure 2-20 of the normalized modulus reduction curve using Equation 2-54 for $\gamma_r = 0.03\%$ and a=0.9.

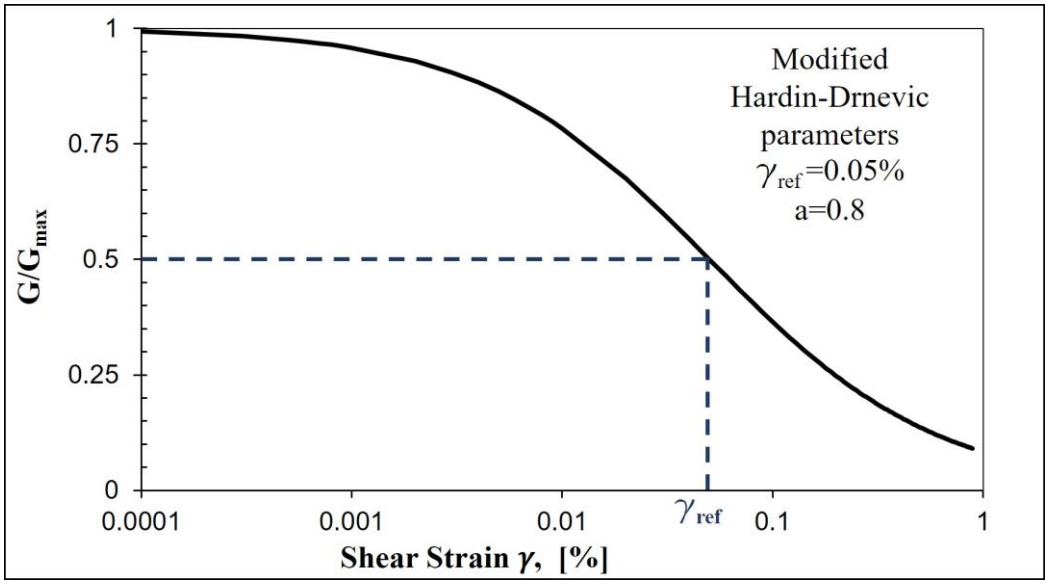

Figure 2-20 Normalized modulus reduction curve (of a silty sand at 1 atm effective confining pressure) represented using a modified hyperbolic model (Darendeli 2001).

Chapter 3
RC-TOSS Device

In the previous chapter, we discussed the techniques and formulas employed to calculate the dynamic shear modulus and damping ratio and the outcomes obtained from the RC-TOSS examination. This chapter describes more details about the used testing device and procedure.

3.1 Device

The device used in this study is the combined Resonant Column-Torsional Simple Shear Device (RC-TOSS). It was first designed and built by Prof. Richard Ray at Michigan University in the 1980s based on ideas gathered from early designs such as (Hall & Richart, 1963); (Hardin & Music, 1965); (Drnevich, 1967); (Isenhower, 1979) as well as a few new developed features. The device design process, transducers, signal conditioning, data acquisition, and test control are presented in his dissertation (Ray, 1984). The device was rebuilt in Győr at the Geotechnical Laboratory of the Department of Structural and Geotechnical Engineering at Széchenyi István University for the Ph.D. study of Zsolt Szilvágyi between 2013 and 2017. Improvements to the device produced higher torque and a broader strain range. Comprehensive descriptions of the apparatus appear in (Ray, 1984) and (Szilvágyi, 2017), and this section includes a further summary for a better understanding of the results and discussion presented later.

The RC-TOSS equipment uses a fixed-free configuration. A rigid, massive steel plate anchors the device's base, holding a measurement post and drive coil supports. The device applies torsion to the top of a cylindrical specimen with an inner diameter D_i = 4.0 cm, an outer diameter D_o = 6.0 cm and a length of 14 cm. The torsion is applied using a set of two permanent magnets and four electric coils. The inner and outer molds fit securely with the membranes against the inner and outer diameters of the base assembly. A porous, sintered bronze ring provides a rough surface for the contact between the device and specimen, allowing saturation and pore water movement. The top assembly moves freely where the specimen connects to the drive head through a retainer, plug, and ring. Two permanent neodymium magnets, attached to the drive head, pass freely through four drive coils. The independently mounted coils adjust to any minor variations in specimen dimensions and are slightly elongated to allow for vertical settlement of the specimen. Inner and outer neoprene membranes cov-

er the specimen allowing for external pressure or internal vacuum confinement. Vacuum confinement provided a more convenient means to apply isotropic stress but limited the maximum magnitude to about 98 KPa. External pressure using a confining chamber could increase stress levels to about 300 kPa.

The RC test requires displacement measurements with very high accuracy at very low amplitude (γ=10^{-4}%), provided by an accelerometer mounted on the drive head and connected to a multimeter and oscilloscope, providing dynamic amplitude and frequency data. Two proximitors mounted on the measurement post measured rotational displacement for the TOSS test. Since the proximitors measured the air gap between themselves and a metal target, they did not touch or impede the motion of the drive head. The RC portion of the test required free movement. The measurement post also held a linear variable differential transformer (LVDT) that measured the vertical settlement of the drive head (and specimen). The LVDT connection allowed for a spring counterbalance to neutralize the vertical load of the drive head. The spring eliminated any anisotropic confinement effects due to the drive head's weight on the sample. A 500-watt DC power amplifier controlled the current passing through the coils that drove the device. Operating in a current-controlled mode allowed for better torque control since current and torque were directly proportional, allowing the device to deliver the same stress when the drive coils heated up.

A hollow cylindrical specimen reduces the high variation in strain distribution across the radius of a specimen. Shear strains varied about 20% above and below average, much more uniform than strains in a solid specimen.

The device could create different stress ratios (σ_1/σ_3) and static shear stress or strain (τ_{static}, γ_{static}) during a test by applying a static offset DC voltage before performing the resonant column test.

The data acquisition system and MS Excel VBA macros performed test control and data gathering tasks during the TOSS test. The device could perform RC and TOSS tests on the same specimen, allowing for any combination of RC, cyclic, and irregular load history tests on a single specimen. The Excel-VBA software also performed data reduction, analysis, and presentation following test completion.

The RC test is highly accurate, measuring small to medium strain levels between 10^{-4}% and 10^{-2}%. The TOSS test is more suitable for studying the dynamic behavior under medium to large strains ranging from 10^{-2}% to 1%.

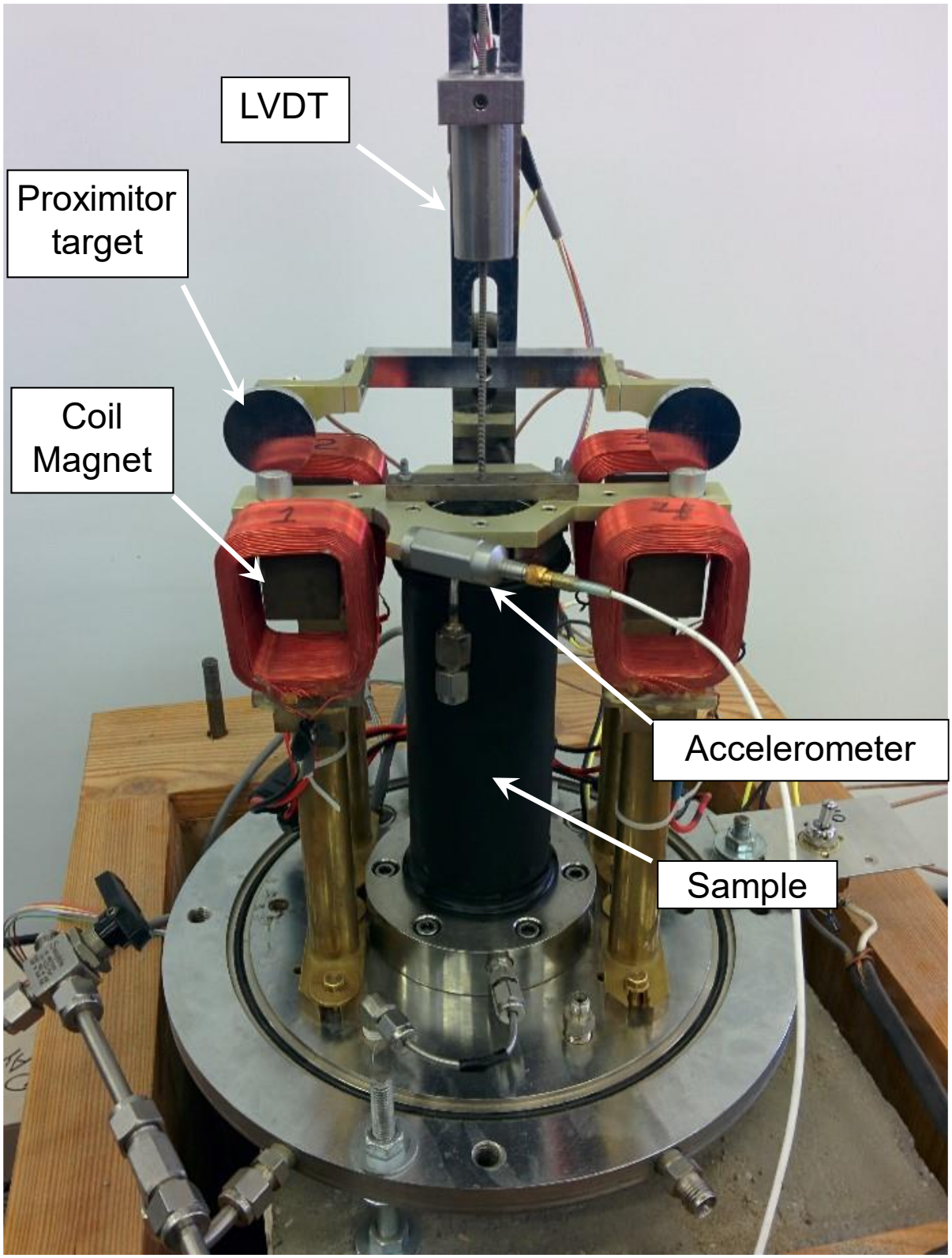

Figure 3-1 Combined Resonant Column – Torsional Shear Device (RC-TOSS) at the Geotechnical Laboratory of Széchenyi István University.

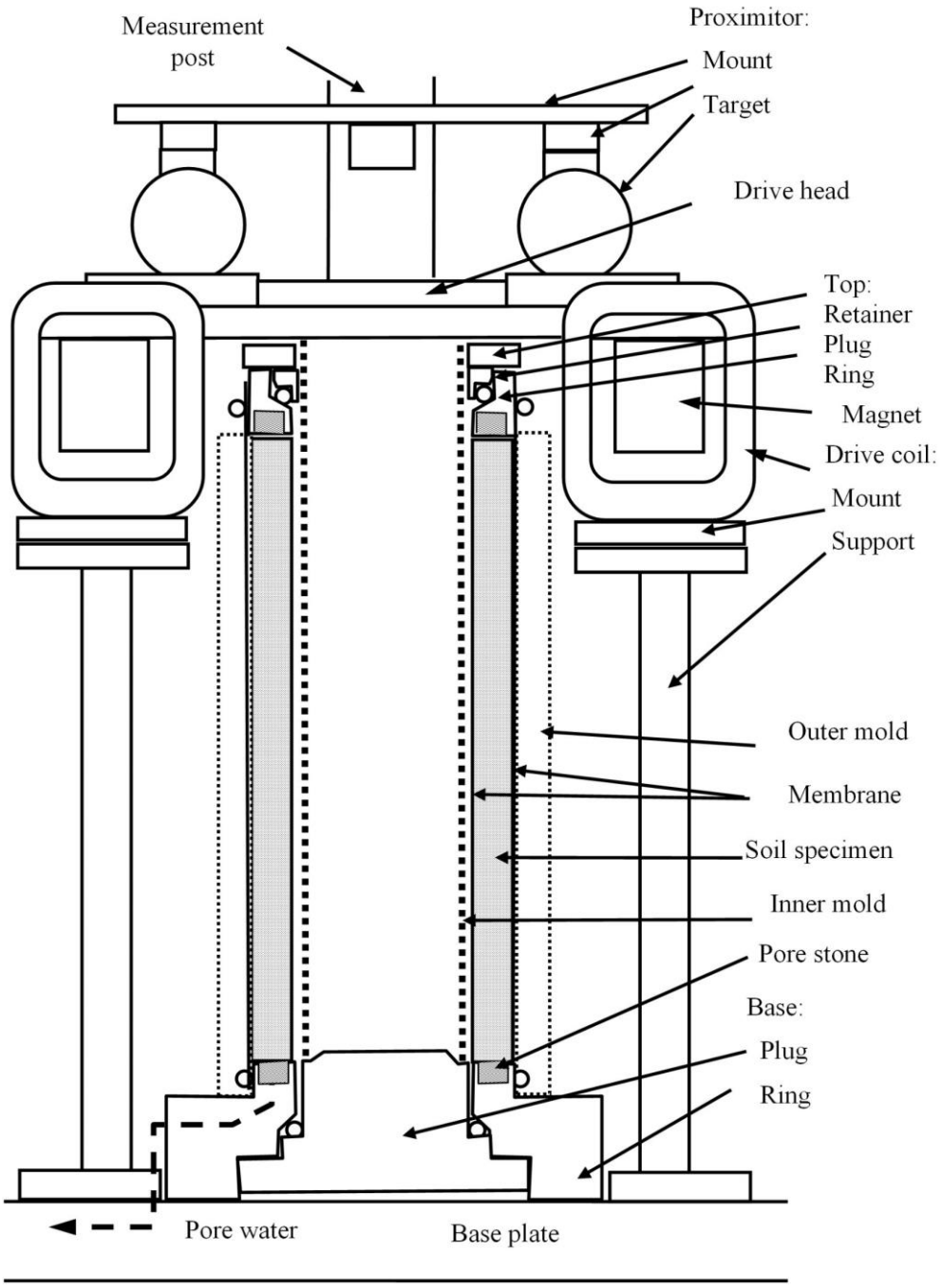

Figure 3-2 Cross section of RC-TOSS testing device.

3.2 Sample preparation

The sample preparation method depends on the required initial density of the soil. The inner and outer molds with membranes and O-rings are assembled and placed on the device base ring. A vacuum, applied to the outer mold, holds the outer membrane open. Soil specimen placement then follows. The dry pluviation method creates a dense specimen. Dry soil, poured slowly from a controlled height, falls and collides with the soil below, generating a dense condition. The height of the fall controlled the specimen's density. A hollow cylinder

specimen required a 50 cm cone to direct the falling soil outward into the space between inner and outer molds. An outer tube, matching the specimen's outer diameter, also directed the soil. For the tested soils in this study, the dry pluviation method achieved samples with relative densities that ranged between 0.72 and 0.80.

On the other hand, to prepare samples in a loose state, the method to produce the maximum void ratio of the soil is employed: the dry filling-tamping method, where a glass funnel with a 14 cm spout deposits the dry soil into the mold. To create a bulking effect on a uniform loose specimen, we start with the spout touching the base ring and then carefully raise the spout constantly and move it around to touch the surface of the soil gently. A slightly denser condition is accomplished by softly tapping the mold 10-15 times.

After the sample is in place, the top ring covers the soil, and the outer membrane is pulled over it and fastened in position with an O-ring. The plug and retainer on the top ring seal the inner membrane. The vacuum then applies vacuum confinement (~97 KPa) when it transfers to the pore pressure port. The sample can now stand independently, and the inner mold is removed. The drive system attaches to the top ring before removing the outer mold. The coils are adjusted around the magnets to provide sufficient space. Subsequently, all the transducers and sensors can be mounted in place (accelerometer, proximitors, and LVDT), and the connections to the power supply, amplifier, multimeter, and oscilloscope are checked. The sample is then ready to be tested, and different sequences of resonant-column and cyclic and irregular torsional simple shear tests can be performed, depending on the purpose of the study.

3.3 Data acquisition and interpretation

A national instrument PCI-6221 (37-pin) data acquisition card provided testing control. The A/D D/A board samples 16 bits through 16-channel inputs (or 8-channel differential input) and outputs signals on two channels. Since the input/output channels convert voltages directly, no further integer processing is needed. After it acquires and converts a voltage, the Excel-VBA code stores and manipulates the data within a spreadsheet (xlsm format). The connections to the data acquisition board appear in Figure 3-3.

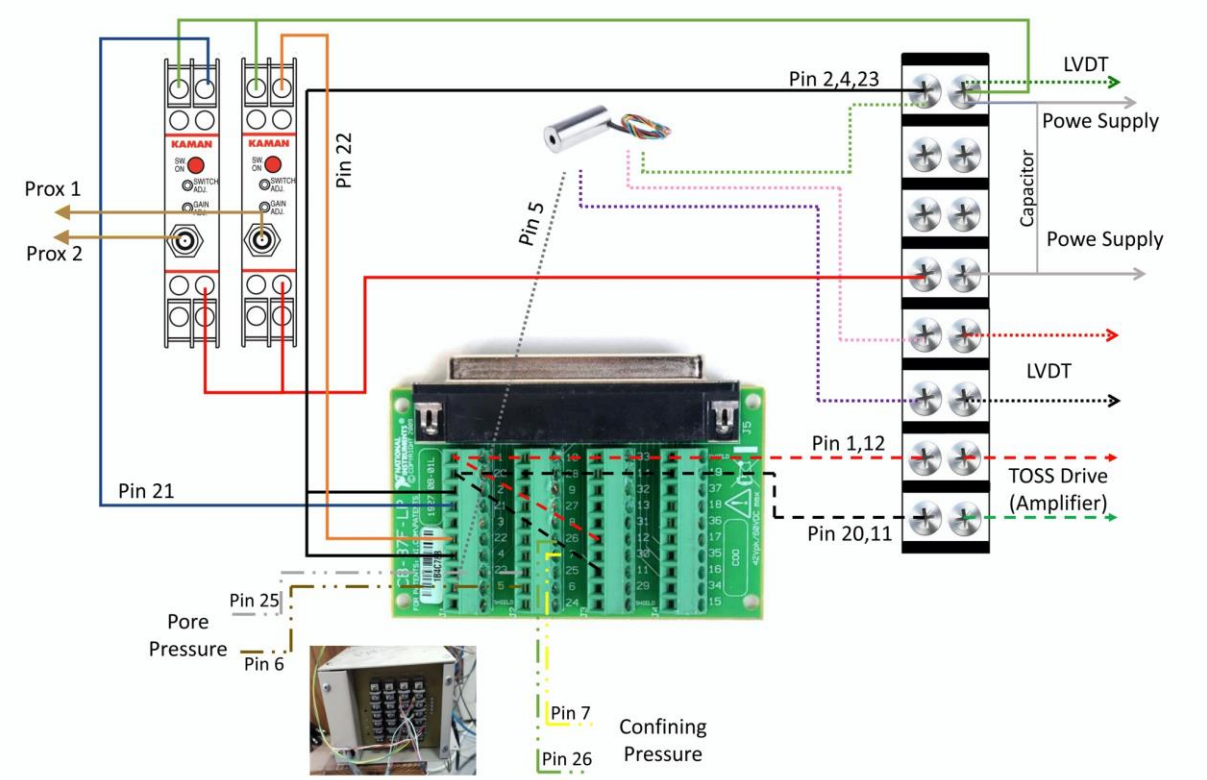

Figure 3-3 Illustration of the connections in the data acquisition system.

A typical sequence starts with a low amplitude resonant column test, followed by a cyclic TOSS test at a low shear stress level (10 kPa). The resonant column test establishes a baseline G_{max} for the testing sequence, and the TOSS test may produce slight hysteresis. The next stages follow with a low-strain RC test and a TOSS stage at higher shear stress (~20, 30, 40 kPa). The RC test provides a reference point for each increasing TOSS stage. The TOSS stage may also contain irregular loading history.

After sample preparation, the operator enters sample dimensions and other data in the proper Excel worksheet. RC testing requires connecting the DC amplifier to a sinewave generator, while TOSS testing uses the analog output channel programmed by the VBA code. For RC testing, the accelerometer mounted on the free end of the sample measures tangential acceleration and frequency. The output voltage passes through a digital voltmeter that measures the signal's AC voltage (amplitude) and period (frequency) and an oscilloscope that allows the operator to watch acceleration levels as he varies the input frequency. By manually adjusting the frequency, the operator can find the first resonance of the specimen. The operator records the accelerometer resonant output voltage and period in the RC worksheet. It converts the readings to shear strain amplitude, shear wave velocity, and shear modulus. The operator may then record the accelerometer signal and shut off power to the coils, causing the vibration to decay. Resonance occurs at a different frequency for each amplitude (strain level). The

amplitude is measured and recorded in (Volts RMS), which then can be converted to displacement and strain using the appropriate accelerometer calibration factors in the Excel spreadsheet. The shear modulus is then calculated from the obtained first-mode resonance at each strain amplitude and the modulus degradation curve is plotted.

At resonance, the operator records the frequency and amplitude, then cuts power and records the decaying response on a storage oscilloscope. The logarithmic decrement and the half-power bandwidth methods appear as VBA subroutines in the spreadsheet. The bandwidth method records the frequency when the response amplitude equals 0.707 times the resonance amplitude on both sides of the curve. Damping results from the calculations are discussed in Section 2.1.2. An example of the recorded and interpreted data of a resonant column test appears in Figure 3-4.

For running a TOSS test, the amplifier should output current control, and then the operator can choose either a stress- or strain-controlled test. Subsequently, depending on the purpose of the study, the operator chooses a cyclic or irregular loading history. Peak testing amplitude applies to either type of test (maximum stress in KPa for stress-controlled tests or maximum strain in % for strain-controlled tests). The number of cycles can vary up to 65000. However, the effect of the number of cycles is relatively small after 25-75 cycles, depending on the amplitude, and 200 cycles is a typical choice. The operator also enters how many cycles to record and each cycle number. For cyclic tests, each data cycle consists of 200 readings. For irregular history tests, every point is a loading point and a data point (up to 10000 total). The input sheet appears in Figure 3-5.

The LVDT, pressure transducers, and proximitors signals are acquired and converted by the A/D D/A board and recorded to the computer during the test. The gaps between the proximitors and their targets produce a voltage ranging between 0-10 Volts. This voltage is transferred to distance based on the calibration procedure using a depth meter explained in (Ray, 1984). The rotation (θ) of the top of the specimen is then calculated:

$$\theta = \frac{(Prox_{1\text{out}} - Prox_{2\text{out}})}{d} \qquad \text{Equation 3-1}$$

Where *d* is the distance between the proximitors (142.6 mm in this device).

The strain results from Equation 2-15 by substituting the radius with the average radius for a hollow cylinder given by:

$$R_{\text{ave}} = \frac{2(R_{\text{out}}^3 - R_{\text{in}}^3)}{3(R_{\text{out}}^2 - R_{\text{in}}^2)} \qquad \text{Equation 3-2}$$

Sample			
Sand- BME-Paks III-6-D-7.5			
Inside Dia	Outside Dia	Length	
(cm)	(cm)	(cm)	
3.9878	5.9944	13.68	Meas 1
3.9878	5.9944	13.68	Meas 2
3.9878	5.9944	13.68	Meas 3
3.9878	5.9944	13.6800	Average

Sample Weight		Water Content	Initial Confining Stress		
Wet	Dry	W/C			
(gms)	(gms)	(%)	(kPa)		
350.00	350.00	0.0000	97.00		
Unit Weight	Unit Weight	Specific Weight	Void ratio	Strength Parameters	
Wet	Dry	Gs	e	c or c'	φ or φ'
(gm/cm^3)	(gm/cm^3)	-	-	(kPa)	(deg)
1.6263	1.6263	2.65	0.63	0.00	34.00

Sample X-sec	Sample Volume	Mass Polar Moment of Inertia, J	Drive Head Mass Polar Moment of Intertia, Jo	Beta
(cm^2)	(cm^3)	(gm-cm^2)	(gm-cm^2)	
15.7317	215.2103	2267.7979	41735.49	0.23

Start of Confinement			2022/ 10/ 25. 11:58			Start of Testing		2022/ 10/ 25. 12:30					Logarethmic Decrement Method				Half-bandwidth Method			
		Date Time	Elapsed	Period	Freq	Vs	G	Accel Volts	Accel Disp	Strain	G/Gmax	gam/gamref	Z	Z+1	N	D	Fr	F1	F2	D
		(clock)	(hr:min:sec)	(msec)	(rad/sec)	(m/sec)	(kPa)	(volts rms)	(cm s-a)	(% s-a)					cycles	(%)	volts rms	(msec)	(msec)	(%)
Conf Pres (kPa)		2022/ 10/ 25. 12:30		16.00	392.70	232.59	87984	0.00380	1.14E-04	4.52E-04	100.0%	9.25E-03			1					
96		2022/ 10/ 25. 12:33	0:35:00	16.20	387.85	229.72	85825	0.00620	1.91E-04	7.55E-04	97.5%	1.55E-02			1					
Taumax		2022/ 10/ 25. 12:40	0:42:00	16.30	385.47	228.31	84775	0.00920	2.87E-04	1.13E-03	96.4%	2.32E-02	0.02	0.00988	3	2.35	61.35	59.60	63.80	3.42
43		2022/ 10/ 25. 12:47	0:49:00	16.50	380.80	225.55	82732	0.01800	5.76E-04	2.27E-03	94.0%	4.66E-02	0.03	0.02091	1	3.53	60.606	59.70	63.90	3.47
Gmax		2022/ 10/ 25. 12:55	0:57:00	16.80	374.00	221.52	79804	0.03000	9.95E-04	3.93E-03	90.7%	8.05E-02	0.02	0.00923	3	3.73	59.524	57.30	61.50	3.53
87984		2022/ 10/ 25. 13:02	1:04:00	17.30	363.19	215.12	75258	0.04700	1.65E-03	6.53E-03	85.5%	1.34E-01	0.07	0.04977	1	4.72	57.803	55.30	60.80	4.76
Gam Ref		2022/ 10/ 25. 13:10	1:12:00	17.80	352.99	209.07	71089	0.07100	2.64E-03	1.04E-02	80.8%	2.14E-01	0.07	0.03777	2	5.11	56.18	52.80	59.80	6.23
4.88E-04		2022/ 10/ 25. 13:16	1:18:00	18.60	337.81	200.08	65105	0.09800	3.98E-03	1.57E-02	74.0%	3.22E-01	0.09	0.05495	1	7.38	53.763	51.40	59.00	7.07
		2022/ 10/ 25. 13:45	1:47:00	18.60	337.81	200.08	65105	0.10200	4.15E-03	1.64E-02	74.0%	3.36E-01	0.13	0.08965	1	6.13	53.763	49.60	60.50	10.14
		2022/ 10/ 25. 13:54	1:56:00	19.20	327.25	193.83	61100	0.14700	6.37E-03	2.52E-02	69.4%	5.15E-01	0.21	0.04815	3	7.73	52.083	44.50	56.30	11.33
		2022/ 10/ 25. 14:10	2:12:00	20.20	311.05	184.23	55200	0.20000	9.59E-03	3.79E-02	62.7%	7.76E-01	0.13	0.06857	1	9.60	49.505	41.80	52.50	10.81
		2022/ 10/ 25. 14:20	2:22:00	23.30	269.66	159.72	41489	0.25700	1.64E-02	6.48E-02	47.2%	1.33E+00	0.18	0.09387	1	10.03	42.918	36.40	48.20	13.75
		2022/ 10/ 25. 14:26	2:28:00	25.00	251.33	148.86	36038	0.32000	2.35E-02	9.28E-02	41.0%	1.90E+00	0.09	0.04588	1	10.37	40	34.50	45.50	13.75
		2022/ 10/ 25. 14:35	2:37:00	25.50	246.40	145.94	34639	0.35000	2.67E-02	1.06E-01	39.4%	2.16E+00								

Figure 3-4 RC test sheet.

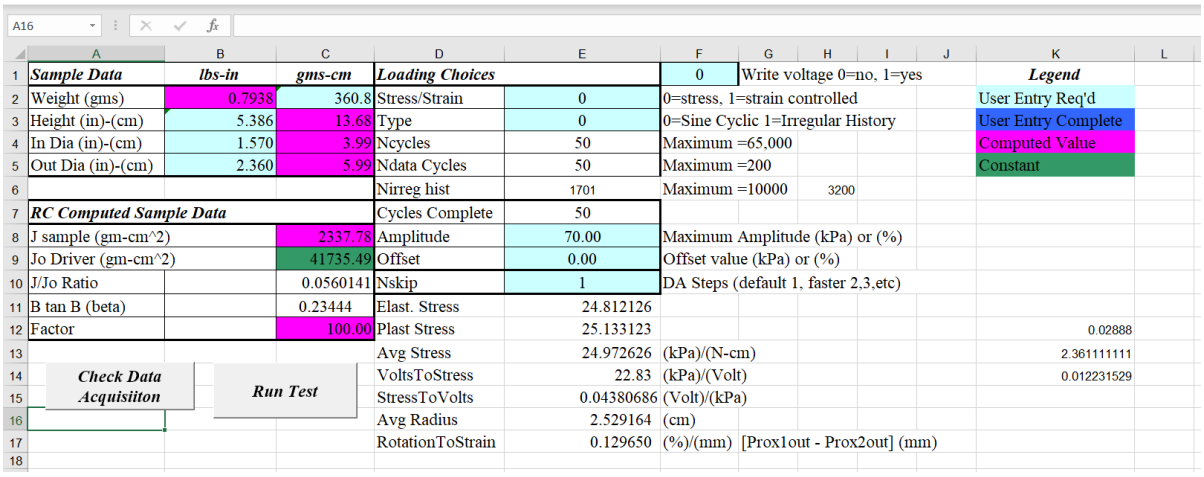

	A	B	C	D	E	F	G	H	I	J	K	L
1	***Sample Data***	***lbs-in***	***gms-cm***	***Loading Choices***		0	Write voltage 0=no, 1=yes				***Legend***	
2	Weight (gms)	0.7938	360.8	Stress/Strain	0	0=stress, 1=strain controlled					User Entry Req'd	
3	Height (in)-(cm)	5.386	13.68	Type	0	0=Sine Cyclic 1=Irregular History					User Entry Complete	
4	In Dia (in)-(cm)	1.570	3.99	Ncycles	50	Maximum =65,000					Computed Value	
5	Out Dia (in)-(cm)	2.360	5.99	Ndata Cycles	50	Maximum =200					Constant	
6				Nirreg hist	1701	Maximum =10000	3200					
7	***RC Computed Sample Data***			Cycles Complete	50							
8	J sample (gm-cm^2)		2337.78	Amplitude	70.00	Maximum Amplitude (kPa) or (%)						
9	Jo Driver (gm-cm^2)		41735.49	Offset	0.00	Offset value (kPa) or (%)						
10	J/Jo Ratio		0.0560141	Nskip	1	DA Steps (default 1, faster 2,3,etc)						
11	B tan B (beta)		0.23444	Elast. Stress	24.812126							
12	Factor		100.00	Plast Stress	25.133123						0.02888	
13				Avg Stress	24.972626	(kPa)/(N-cm)					2.361111111	
14	***Check Data Acquisiiton***		***Run Test***	VoltsToStress	22.83	(kPa)/(Volt)					0.012231529	
15				StressToVolts	0.04380686	(Volt)/(kPa)						
16				Avg Radius	2.529164	(cm)						
17				RotationToStrain	0.129650	(%)/(mm)	[Prox1out - Prox2out] (mm)					
18												

Figure 3-5 RC-TOSS sample and test data.

All the calculations are programmed in VBA in the test spreadsheet. The test results will appear in 6 columns for each cycle (stresses, strains, vertical displacements, and proximitors data shown in Volts just in case further analysis is needed). A separate spreadsheet performs raw data interpretation using subroutines and functions in VBA. The worksheet plots shear stress-strain curves and calculates secant shear modulus and damping ratio. Damping calculations use the area of a hysteresis loop and a numerical integration approach described in Figure 2-18. The final results include the shear modulus degradation curve and the change in damping ratio with the strain level.

The worksheet records shear stresses and strains in two columns for irregular TOSS tests. Before this research, no programs could process this data because all previous studies had focused on cyclic TOSS tests. Analyzing the data manually was challenging and time-consuming since it required identifying the turning points and separating the cycles before calculating any properties. As a result, Excel VBA subroutines could automate the analysis. The new subroutines extracted all the required parameters within seconds after reading the raw data to the analysis Excel sheet in columns A and B, as shown in Figure 3-6.

The analysis identified the hysteresis loops and their turning points and stored them in arrays for further analysis. Furthermore, the code plotted loops on a chart sheet using different colors for each loop for easier identification of the path followed by shear stress-shear strain, as shown in Figure 3-7.

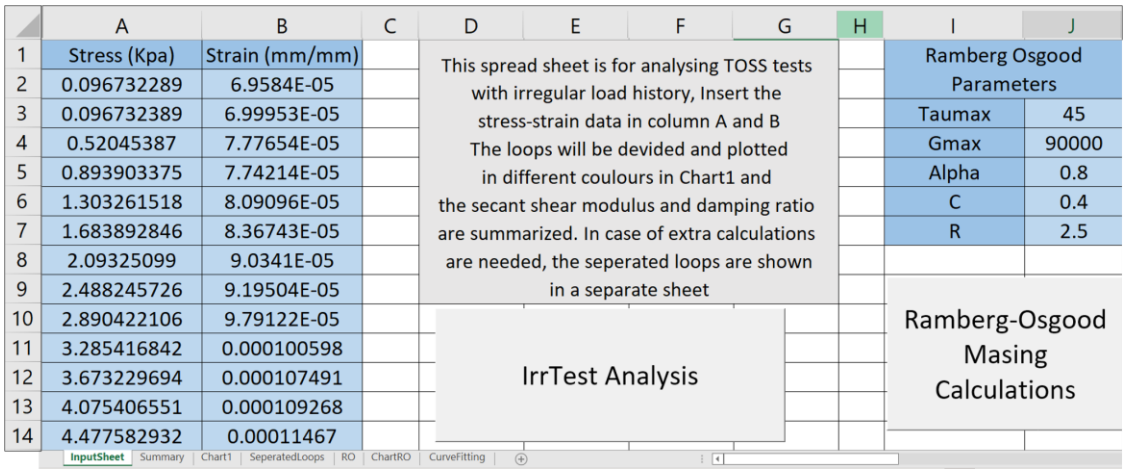

Figure 3-6 Input sheet where raw data is inserted in columns A and B.

The dynamic properties are then calculated and summarized in each test's "summary" section. Having obtained the turning points, the worksheet computed the secant modulus from the following equation.

$$G_{\text{sec}} = \frac{\tau_2 - \tau_2}{\gamma_2 - \gamma_1} \qquad \text{Equation 3-3}$$

Where, τ_2, τ_1 are the stresses and γ_2, γ_1 are the strains at turning points 1 and 2.

On the other hand, calculating the damping ratio is more complicated. First, the equation of the line that connects the two ends of the loops is determined from the following equation.

$$\gamma = \frac{(\tau - \tau_1)}{(\tau_2 - \tau_1)}(\gamma_2 - \gamma_1) + \gamma_1 \qquad \text{Equation 3-4}$$

The next step involves dividing the area between the line and the loop (equivalent to half a cycle) into extremely small sections, allowing us to consider them trapezoids, as illustrated in Figure 2-18. The code then computes the cumulative sum of the area of every trapezoid to find the total area. The area is multiplied by 2 to get the area of a complete cycle (A_L). For obtaining the area of the triangle (A_T), we use a function "AvgStrainEnergy" that computes average strain energy when the ends of a hysteresis loop are not symmetric. It draws a line from one end to the other and transfers the origin to the midpoint of the line. This is because the strain γ does not go through zero anymore. The following equation gives the function.

$$A_T = \frac{A * B}{2} \qquad \text{Equation 3-5}$$

Where:

$$A = \left|\frac{\tau_1 - \tau_2}{2}\right| \qquad \text{Equation 3-6}$$

$$B = \left|\frac{\gamma_1 - \gamma_2}{2}\right| \quad \text{Equation 3-7}$$

Subsequently, the damping ratio for each loop results from Equation 2-3, and they appear in Figure 3-8.

The R-O model accurately predicts soil behavior under irregular loading conditions when coupled with the Masing criteria. First, functions are created for the one-way and two-way loadings in Equation 2-24 and Equation 2-33, respectively. Applying these equations already satisfies the first two Masing criteria. The least squares method allows for the determination of best-fit parameters. Excel solver will minimize the sum of the square differences between the RO and test data curves.

After finding the required parameters, they are inserted in the input sheet in cells J3 to J7. Pushing the "Ramberg-Osgood Masing calculation" button starts the subroutine for this analysis. It continues from the separated loops from the previous subroutine with the predetermined number of loops and turning points. Equation 2-24 determines the strains for the first skeleton curve, and the maximum strain remains in variable "gammamax." Equation 2-33 generates the reloading curve data points for comparison to the maximum strain. Whenever the reloading value exceeds the maximum, the curve follows Equation 2-24 again to satisfy the third Masing criteria.

In order to satisfy the fourth Masing criteria, we need to know which turning points (τ_i, γ_i) to use for the RO two-way equation. First, the latest turning point is applied to calculate the strain, then this data point is compared to curves based on all the previous turning points, and if there is an intersection with a previous curve, the equation will switch its turning point. The method to track previous turning points uses a counter variable (k) representing the previous loop's number. This variable decreases every time the curve intersects with a previous one. The method to determine the occurrence of an intersection follows:

When the absolute value of the difference between the stresses is below a specific value (e.g., 0.4) and the absolute value of the difference between the strains is below a tolerance (of 0.00125*γ) then there is an intersection detected, and the previous turning point (k) replaces the newer one for the next calculated strain.

After calculating the strains for all the data points in the load history, the subroutine plots the shear stress- shear strain curves. The results of the same loading history in Figure 3-7 using the Ramberg-Osgood model parameters in the input sheet in Figure 3-6 appear in Figure 3-9

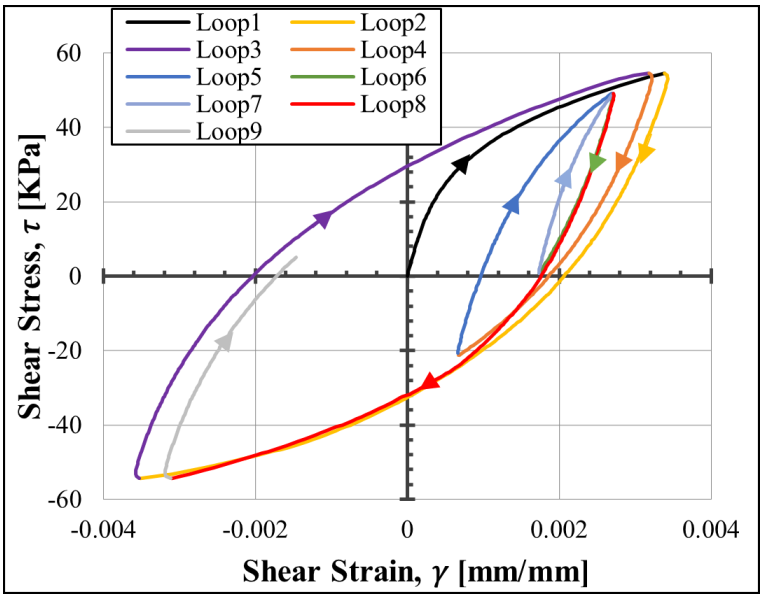

Figure 3-7 Shear stress-strain curve with separated loops of an irregular TOSS test.

Irregular TOSS Test							
Loop	**Stress**	**Strain**	**Gsec**	**Strain p-p**	**HL area**	**AVGstrain**	**Damping**
#	Kpa	mm/mm	KPa	mm/mm	mm2		%
1	54.62	0.00338648	16128.97	0.00339	0.04028	0.0231	27.73
2	-54.31	-0.003517372	15778.21	-0.00690	0.17321	0.0940	29.33
3	54.61	0.003177295	16270.09	0.00669	0.14206	0.0912	24.81
4	-21.30	0.000680345	30402.38	-0.00250	0.02852	0.0237	19.16
5	49.10	0.002694401	34955.08	0.00201	0.02096	0.0177	18.82
6	0.67	0.001737023	50586.52	-0.00096	0.00437	0.0058	12.01
7	49.12	0.002714246	49582.50	0.00098	0.00510	0.0059	13.73
8	-54.31	-0.003102516	17782.04	-0.00582	0.13748	0.0752	29.09
9	5.08	-0.001464384	36256.61	0.00164	0.01479	0.0122	19.35

Figure 3-8 The summary of the results spreadsheet for irregular TOSS tests.

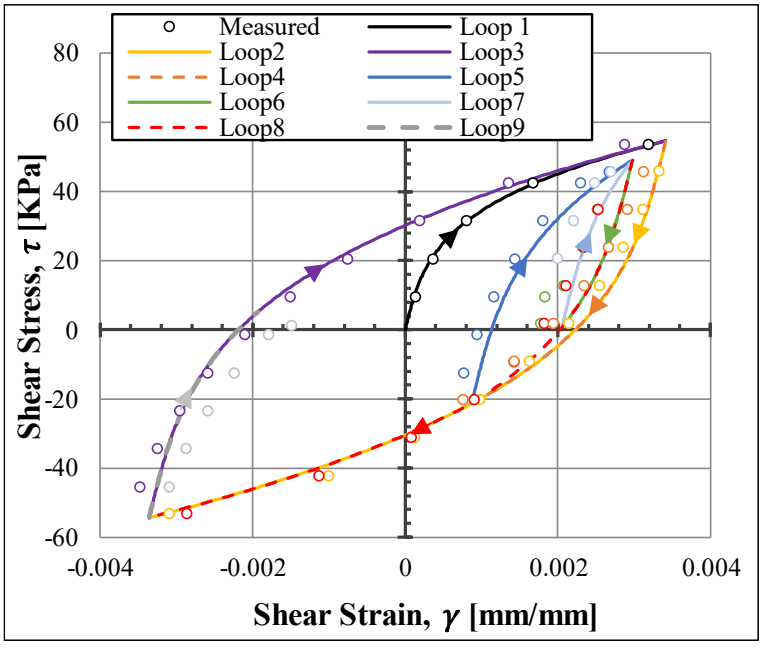

Figure 3-9 Shear stress-strain curve with separated loops.

Chapter 4
Numerical Modeling and Random Distribution

4.1 Model in Midas GTS NX

The progressive development in computer technology, accompanied by the increasing speed of processing complex calculations, allowed numerical modeling for easier and faster calibration of models for further use in realistic and much more complicated geotechnical problems. The numerical modeling in this study was conducted using the Finite Element (FEM) software Midas GTS NX. This software can create 2D and 3D models for advanced geotechnical analysis. The software integrates several advanced soil models such as the Hardening Soil Small Strain (HSS), Cam Clay, Ramberg-Osgood, and Hardin-Drnevich. This variety allows it to model and solve complicated geotechnical problems, including groundwater seepage, consolidation, soil and rock stability, dynamic vibration, and soil-structure interaction.

An accurate 3D axisymmetric model with a cylindrical coordinate system will simulate the TOSS test conditions because the torsional load is out-of-plane. A 2D or extended 2.5D axisymmetric model is not sufficient for this task. A similar model was created previously by (Szilvágyi 2017). However, that model focused on studying the small-strain stiffness of soils and verified the software's capability to model the TOSS test under static loading conditions. Moreover, some computational difficulties occurred during analysis, but the models developed in this study overcame those problems. This research concentrated mainly on predicting the dynamic behavior of soils under irregular and more complicated loading patterns, which is unique for this study (Ahmad & Ray, 2021).

The cylindrical element coordinate system provided the best basis for modeling. The model simulates the TOSS test; consequently, it consists of a 1 cm thick hollow cylinder with the exact dimensions of the tested soil specimen. The mesh elements used in the model are hexahedral with high order; each element has 20 nodes with the dimensions shown in Figure 4-1b in mm.

4032 elements comprise this model, pinned at the bottom surface and connected at the top nodes via rigid links to a central node which is allowed to move along and rotate around the vertical axis. External loading consists of either prescribed rotation or applied moment to this central node, which will simulate the torsional load applied in the TOSS test. The model produced no stress irregularities at the base after the confining stress stage.

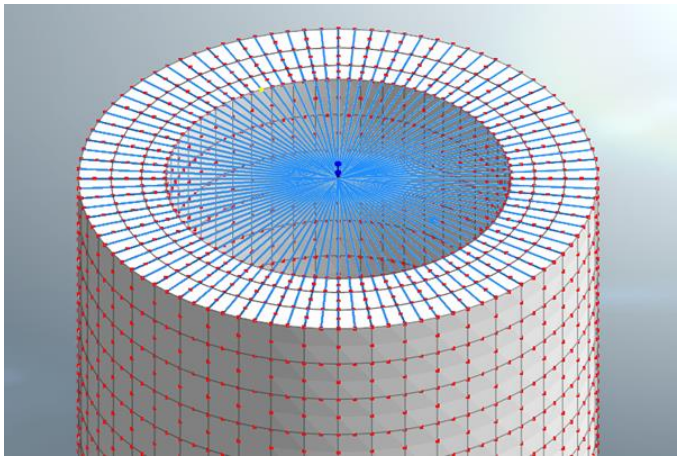

(a) Elements and nodes.

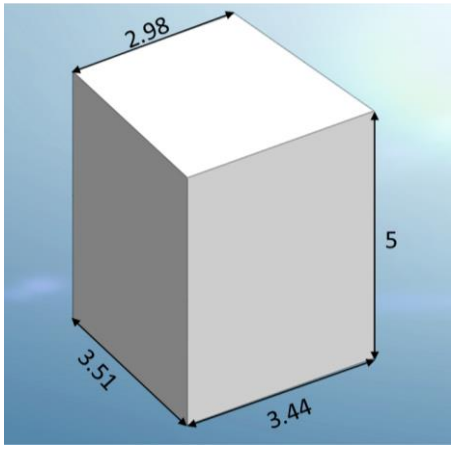

(b) Dimensions of the middle element.

Figure 4-1 Finite element mesh of soil sample.

The analysis proceeds in (construction) stages to simulate the test conditions. It starts by applying a confining stress of 96 KPa on the free surface of the elements. Afterward, the dynamic material model (R-O or H-D) activates for all the elements, and the torsional loading stage begins. The prescribed rotation around the vertical axis was assigned a time-varying function to convert the loading from static to dynamic.

4.2 Model calibration

Two material models provided a basis for comparison in predicting the dynamic behavior of soils. The Ramberg-Osgood and Hardin-Drnevich models provide an excellent basis for comparing laboratory data under cyclic and irregular loading conditions. Midas fully supports both models so they may represent laboratory and field conditions. Both have Masing conditions coded into their behavior, simplifying computations for complex loading conditions. An irregular TOSS test on dry sand provided data for calibrating the models' parameters. The time history applied to the model is scaled to a maximum shear stress of 40 KPa.

The time-varying function is similar to the load history in the TOSS test with a maximum rotation of 0.00338 radians, which will cause an average shear strain in the θ-Z direction of 0.00067 mm/mm. The improved nonlinear Solver did not require additional loading steps near turning points. Implementing the full Newton-Raphson method for all time steps required only 5-10 iterations compared to over 50 from the previous Solver.

The solver tool in Excel provided a means to find the optimum combinations of curve-fitting constants for the Ramberg-Osgood and Hardin-Drnevich soil models (Equation 2-24 and Equation 2-49) with the test data. The same method determined the Midas reference

strain for the R-O equation (Equation 2-39). The curves for R-O, H-D, and Test Data appear in Figure 4-2. The calculated model parameters are shown in

Table 3.

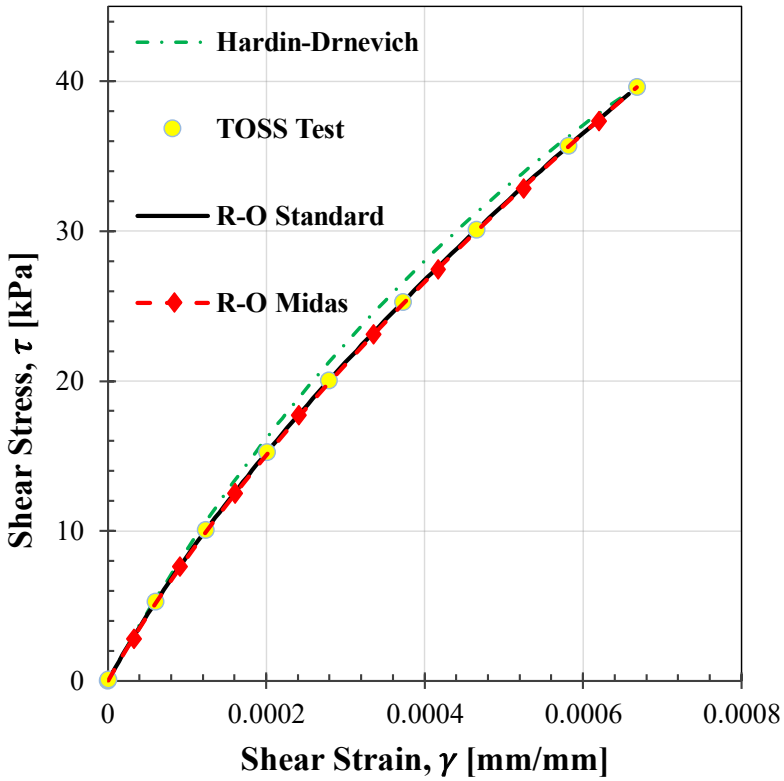

Figure 4-2 Curve fitting between the soil model and the TOSS test data (monotonic one-way curve).

Table 3 Material model parameters used in this study.

Parameter		**Conventional Ramberg-Osgood**	**Midas Ramberg-Osgood**	**Hardin-Drnevich**	**Unit**
Initial dynamic shear modulus	G_0	95500	95500	95500	KPa
Max. shear stress	τ_{max}	44.17	-	-	KPa
Reference shear strain	γ_r	0.000462	0.00148	0.0011	mm/mm
Curve fitting constants	α	1	0.0267	-	-
	C	1.55	-	-	-
	R	1.9	-	-	-
	β	-	0.8508	-	-
Max. damping constant	h_{max}	-	0.19	-	%
Dry density	γ_d	17	17	17	KN/m^3
Poisson ratio	ν	0.3	0.3	0.3	-

After the first stage, an isotropic confining stress of 96 KPa surrounds the specimen. As a result, stresses in the model specimen exhibited identical magnitudes in all the elements and all directions with no noticeable irregularities, even with the pinned bottom surface.

The load history duration is 0.801 seconds, with time increments of 0.001 seconds, which results in 801 total time steps for each analysis. Figure 4-3 shows the distribution of shear stresses and strains along the radius of the specimen at the final increment. As expected, similar behavior occurs for both the R-O and H-D soil models, where the strain distribution is uniform along the height of the specimen and increases with radial distance. The hollow cylindrical specimen produces a more even distribution of stress and strain along the radius of the sample.

The average solid stresses and strains in the θ-Z direction (S-YZ, E-YZ) for three elements (inner, middle, and outer) were compared to the shear stress-strain curves from the TOSS test for both material models. Moreover, the dynamic shear modulus was calculated from these curves and compared to the shear modulus degradation curves obtained from the RC-TOSS tests.

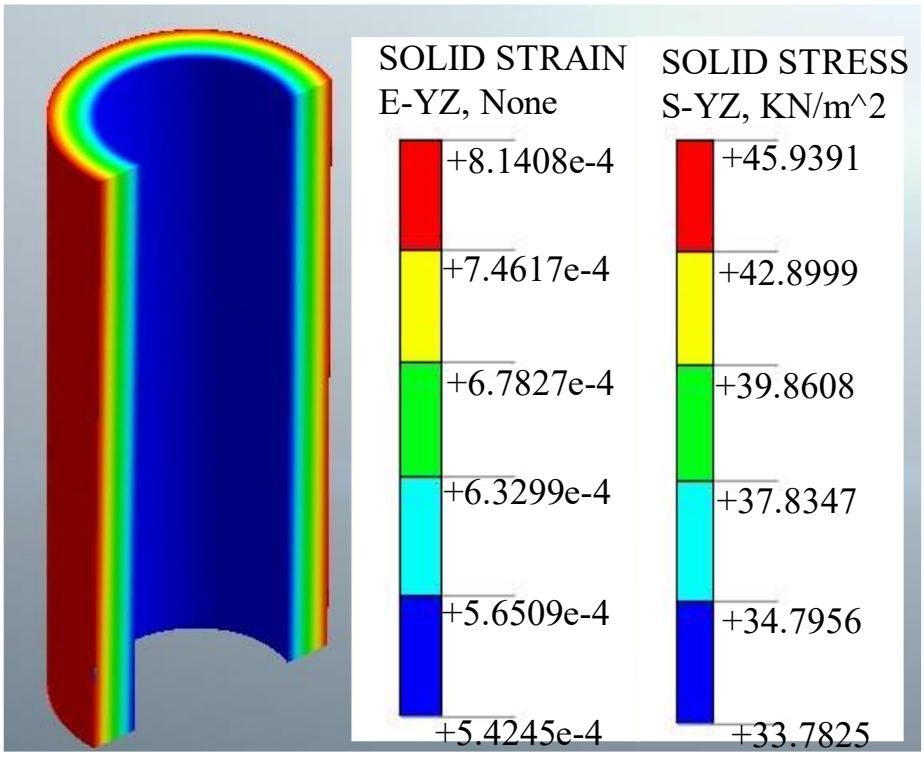

Figure 4-3 Shear stresses and strains distribution along the radius (R-O model).

Figure 4-4 shows a good fit between the test data and the curves obtained from FEM calculations on Midas using the Ramberg-Osgood model. However, the Hardin-Drnevich model produced a lower quality fit when using the parameters from

Table 3, as seen in Figure 4-5. The calculated values would drift even further from the test data at higher stress levels when using the conventional hyperbolic Hardin-Drnevich formula.

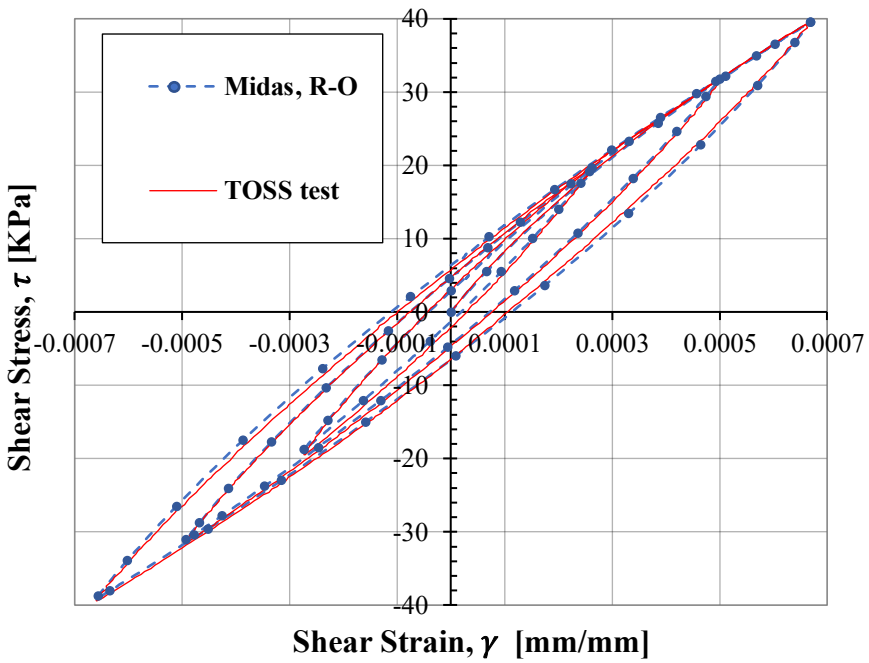

Figure 4-4 Shear stress-strain curve from Midas using Ramberg-Osgood model.

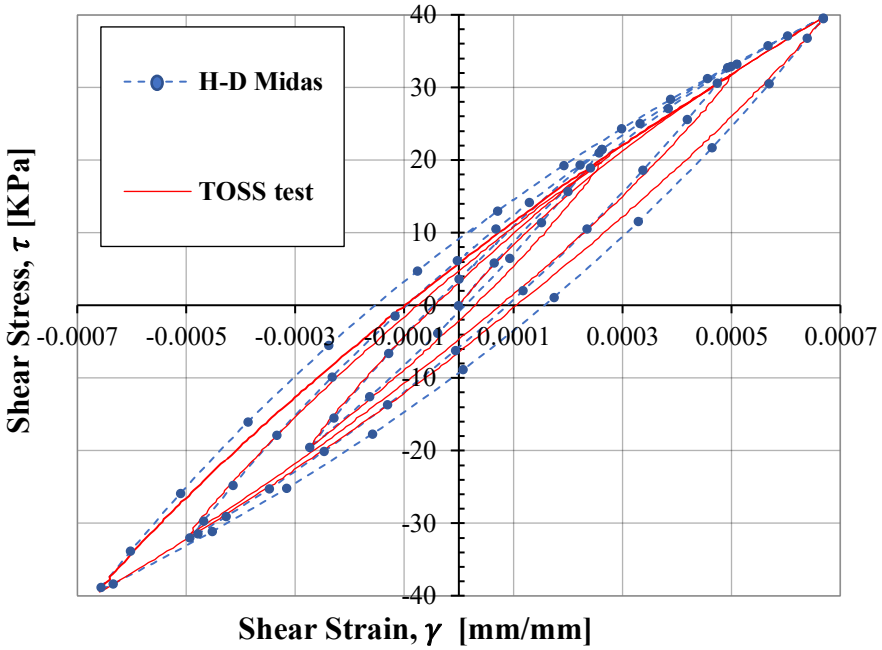

Figure 4-5 Shear stress-strain curve from Midas using Hardin-Drnevich model.

Figure 4-6 shows how both models predict the shear modulus in the FEM calculations in Midas. The Ramberg-Osgood shear modulus degradation curve followed Equation 2-27, and matches perfectly with the FEM R-O calculations in Midas. They show very good agreement with the RC and TOSS tests. The modulus reduction curve for the Hardin-Drnevich model obtained from one-way loading curve resulted from Midas analysis. The resulting curve tracks higher than the lab values until it reaches a strain value of 0.057%, dropping below the TOSS test curve.

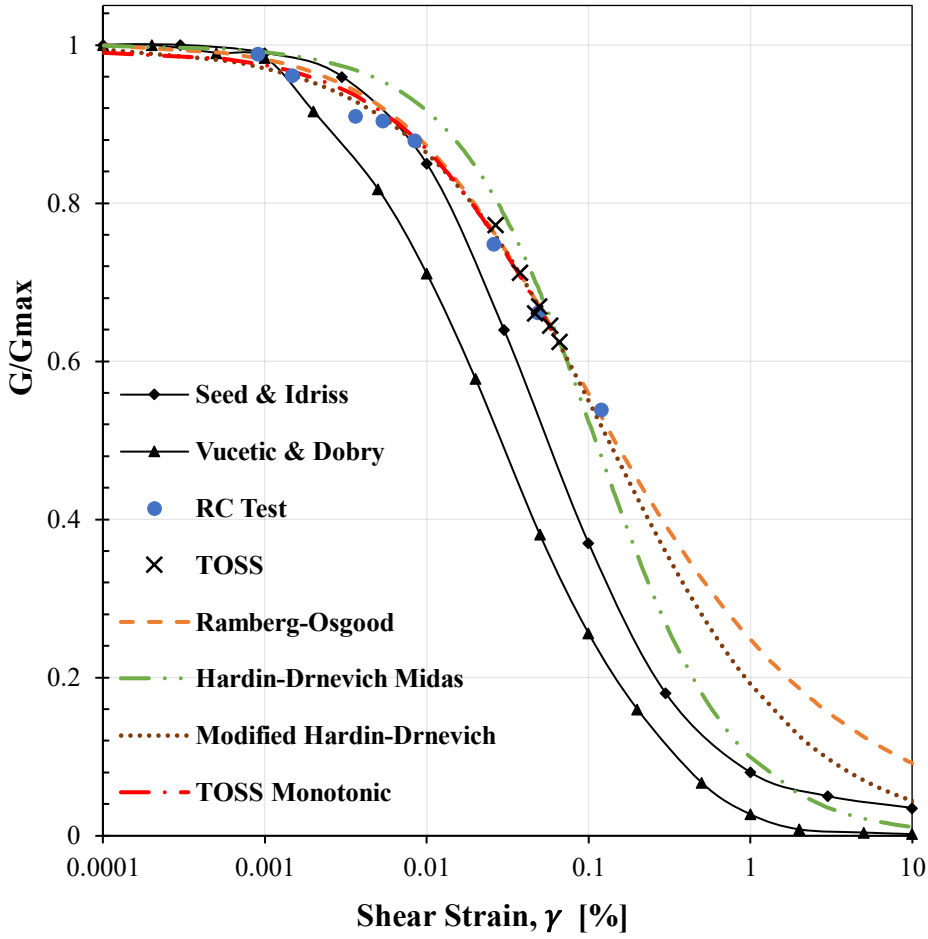

Figure 4-6 Shear modulus degradation curves comparison.

(Darendeli, 2001) suggested modifying the hyperbolic model to better represent the normalized modulus reduction curve by integrating a curvature coefficient (a) into the equation. Since the RO model uses a parameter (a), the Darendeli coefficient will be denoted (m) in this study. The Darendeli modification can be applied to the hyperbolic equation by Hardin and Drnevich for better prediction of the hysteresis behavior of soils as follows:

$$\tau = \frac{G_0(\gamma - \gamma_1)}{1 + \left|\frac{\gamma - \gamma_1}{2\gamma_r}\right|^m} + \tau_1 \qquad \text{Equation 4-1}$$

By using the same method as before (least squares), the values of the reference strain: γ_r=0.00132 mm/mm, and the curvature coefficient: m=0.7129, give a much better fit to the testing data for both the stress-strain curve (Figure 4-7) and the modulus degradation curve (Figure 4-6) than the conventional Hardin-Drnevich model.

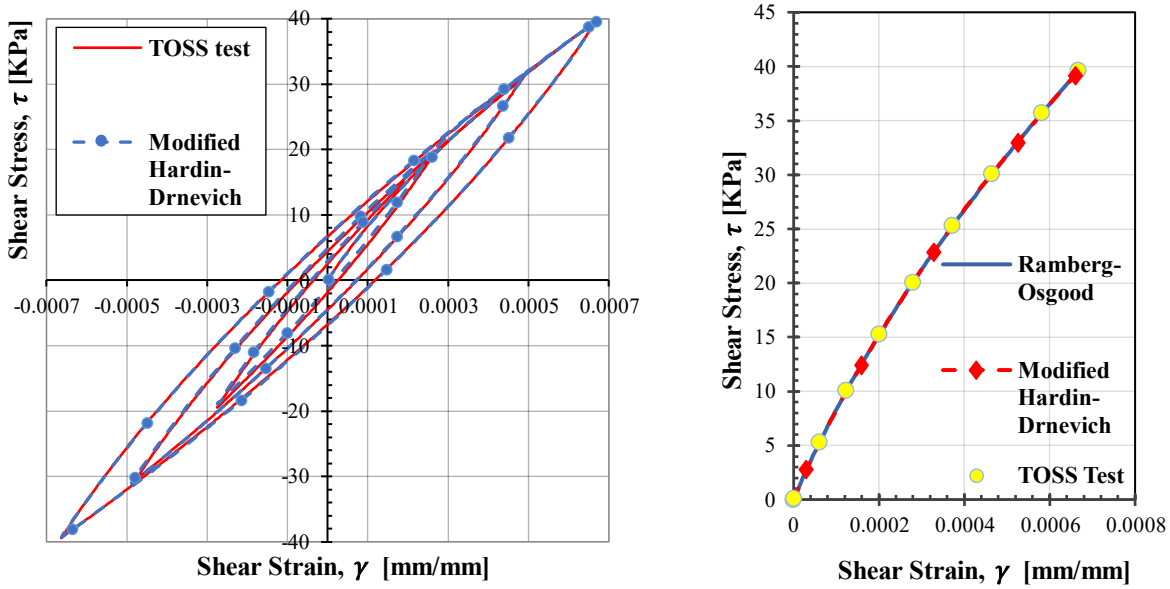

(a) Shear stress-Strain hysteresis behavior *(b) Shear stress-Strain one way*

Figure 4-7 Modified Hardin-Drnevich model.

4.3 Numerical Study of Random Material Properties Within a Soil Specimen

Material properties derived from laboratory soil tests often assume that the property is uniform throughout the specimen. This uniformity may hold true for some exceptional soils but is obviously false for many others. We have been performing cyclic and irregular torsional simple shear (TOSS) tests on hollow cylinder samples for decades and were intrigued by how to model inherently nonuniform specimens. As an added corollary, we wanted to understand the influence of imperfections (voids, inclusions) on the measured stress-strain behavior in these tests. In this section, we examine two general classes of problems: (a) nonuniform specimens with random distributions of material properties within the specimen, and (b) nonuniform specimens with inclusions or voids. Finite element modeling was performed on a TOSS specimen (D_i =4cm, D_o =6cm, L=14cm) using a set of over 500 different elastoplastic material properties within the specimen. We examined various distributions (Normal, Log-normal, Bimodal) of stiffness and strength properties. The results were plotted as torque vs. twist curves since those values directly result from TOSS laboratory tests before being converted (with assumptions of uniformity) to shear stress-shear strain hysteresis. The Bimodal distributions represented soils with distinct hard and soft zones. Additionally, distributions with some degree of spatial correlation were also examined (Ahmad & Ray, 2021).

In a paper written in 1926, Masing discussed the behavior of a brass specimen undergoing loading and unloading. His underlying premise about modeling the stress-strain response

of the specimen was that it behaved as a collection of elasto-plastic elements loaded to their yield point at slightly different times during the test. The collective behavior resulted in the load-deformation curve in Figure 4-8a where location *l* is the onset of yielding. He believed the specimen did not fail suddenly because the stresses along the specimen cross-section were not uniform, and therefore, some failed while others were still undergoing elastic loading. The gradual transition from fully elastic condition to (nearly) fully plastic could be seen by observing the normalized tangent modulus versus strain shown in red in Figure 4-8b. Such a curve now represents soil behavior under small-strain conditions as a modulus reduction curve where G/G_{max} would replace the parameter "**a**" along the y-axis.

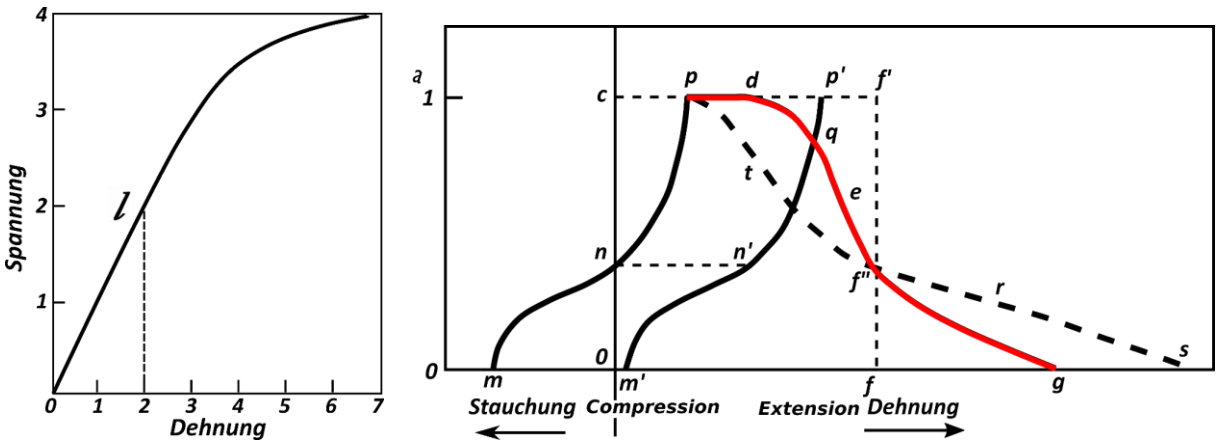

(a) Stress-strain curve. *(b) Modulus reduction curve (red).*

Figure 4-8 Nonlinear stress-strain curve and tangent modulus reduction curve redrawn from Masing (1926).

Masing's idea prompted a numerical study where various simple elasto-plastic material properties were assigned throughout a specimen to generate nonlinear stress-strain behavior. The purpose was to understand better the impacts of various simple material properties on the collective behavior of a soil specimen.

The simple elasto-plastic model used extensively in this study is the one developed by Tresca. It has an elastic modulus, Poisson's ratio, and a yield value (1D), yield line (2D), or, more generally, yield surface (3D). The yield surface is a hexagonal-shaped tube centered along the hydrostatic axis. The behavior in torsional shear would follow a path along the deviatoric plane shown in Figure 4-9.

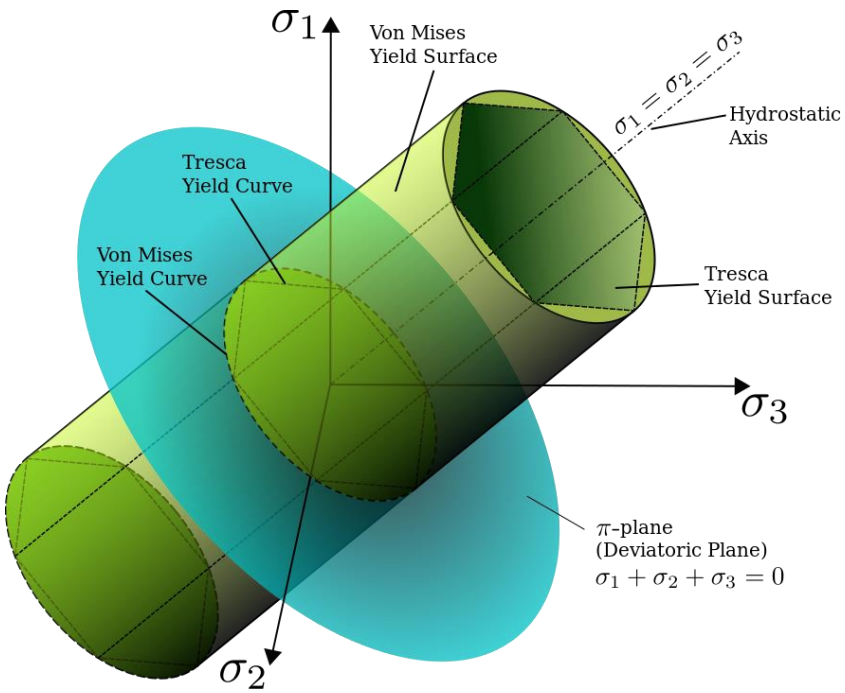

Figure 4-9 Tresca and Von Mises failure surfaces.

The same 3D model in Midas that consists of 4032 quadratic hexahedral elements and 20,689 nodes served as the baseline configuration. We specified 512 different elasto-plastic materials in the original model to create random properties. The Midas program could export the mesh and materials to a text file (.fpn) identical to a (.csv) format file and easily imported into Excel. The program could produce material properties having a prescribed statistical distribution and then place them randomly throughout the model. The randomized model could then be imported back into Midas. A workflow chart and example of randomized elements from Excel appear in Figure 4-10. One should note that step (4) could generate a normal distribution of yield stresses and moduli based on the prescribed mean and standard deviations for that material. There could also be up to ten different distributions of Tresca materials, each with its mean and standard deviation values for yield and modulus. The only requirement was that the total number of possible property combinations (yield stress and modulus) had to be 512. At this stage, log-normal and random (flat histogram) distributions could also be created. For step (5), the 512 properties created from step (4) were distributed throughout the specimen with even randomness, creating a specimen with a normal distribution of properties. The property map shown (step 5) is the inner "cylinder" of the finite element mesh laid out flat so that we can visually inspect the distribution of properties. Each cell has a property number from 1 to 512 and a corresponding color. The middle and outer cylinders were mapped similarly.

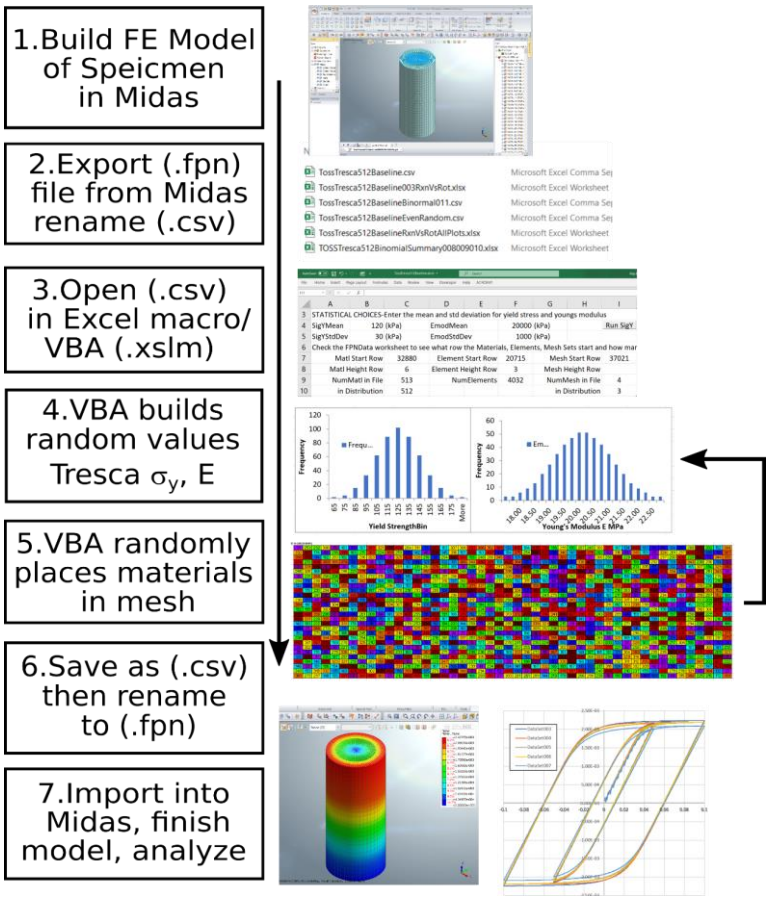

Figure 4-10 workflow for analysis the randomized material model.

Once the randomized mesh was imported into Midas, the remaining analysis parameters were input. Boundary conditions were added at the base as pinned nodes representing the experimental apparatus's fixed base. The top of the specimen was connected to a series of rigid links. These links crossed the top of the mesh along every diameter, connecting nodes on opposite sides, a total of 529 nodes. The links were all connected to a single node at the center where a single moment (M_z) or prescribed rotation (ϕ_z) was applied. This arrangement provided a uniform rotation along the top of the specimen throughout the test. Generally, a rotation was prescribed since it was more likely to remain stable as the specimen approached total yield.

Since Tresca material strength is independent of confining stress, there was no need to simulate confinement during the analysis. The prescribed rotation was entered as a static displacement; however, the final load condition was a time-varying static load. The time function was often a sine wave with a duration of 1.25 cycles, simulating initial (one-way) loading and then one complete cycle to produce a hysteresis loop. The time function was set to a slow speed to avoid any inertial effects; however, the analysis type was set to nonlinear time history since it was the most convenient way to model the loading process.

Analysis options were set to seek convergence via normalized load, deflection, and work parameters below 1.0e-03, 1.0e-03, and 1.0e-06, respectively. The solution method used a full Newton Raphson stiffness update scheme, allowing for line search. The maximum number of iterations for a single loading step was set to 50, and the loading history was set to 1200 steps for the 1.25 cycle excursion.

4.3.1 Preliminary analysis cases and results

The initial analyses were performed to verify that the Tresca material model was performing in a way we understood. As a verification, three realizations with different Tresca σ_y and E values were analyzed, and centrally located element stress-strain data was extracted. The results in Figure 4-11 showed what we expected: in pure rotational shear: a) the stiffness was equal to the shear modulus G, where:

$$G = \frac{E}{2(1+\nu)} \qquad \text{Equation 4-2}$$

and b) the yield stress in pure shear was equal to one-half the Tresca yield. Since $\upsilon = 0.3$ for all tests, G and E were related by a factor of 2.6. The linear portions of Figure 4-11a illustrate the concept.

An initial set of analyses investigated the behavior of the test specimen with random distributions of properties. Table 4 lists the series of configurations where modulus, yield stress, and the nature of distributions are varied. The analysis number indicates normal distribution (N), log-normal distributions (LN), bimodal normal even split (BE), and bimodal normal with offset (BO). All distributions started with a population of 512 materials. The normal distributions required values of mean and standard deviation for E and σ_y. The log-normal distributions required much higher values for standard deviation, and the reader should note the drastic differences in standard deviation between the two sets. The whole purpose of using log-normal distributions is to account for the extensive degree of variability in geotechnical material properties one may find. The even bi-modal normal distributions were two distributions of 256 values with two mean values and two standard deviations. Both distributions were randomly spread over the element mesh, as no soil layers or zones separated them. The offset bi-modal normal distributions were two distributions with different populations that summed up to 512. The overall mean remained unchanged (σ_y = 120 kPa, E=20000 kPa). The placement of all elements in this set was also entirely random.

Reaction moment vs. rotation plots appear for each group in Figure 4-12 and Figure 4-13. Figure 4-12 shows the reaction moment vs. rotation for specimens with normal and log

normal distributions of E and σ_y. Test numbers correspond to the conditions listed in Table 4. The first characteristic is the "wobbly" path of the initial loading curve. The wobble is not a numerical oscillation but demonstrates the effect of different elements reaching yield and perhaps unloading/reloading over short intervals as the main body of the specimen continues to twist. The unloading/reloading bursts were verified by viewing the plastic states of all elements during the entire loading history. We recorded animations of each test, and they proved to be quite remarkable. Since every test was a prescribed rotation between 0.1 and -0.1 radians, the plots all match along the horizontal axis.

Table 4 Material conditions, random distributions, loading conditions.

Analysis Number	Number of Materials	Yield Stress, σ_y [kPa]		Tresca Modulus E [kPa]	
		Mean	Std Dev	Mean	Std Dev
N-01	512	120	30	20000	1000
N-02	512	120	20	20000	1000
N-03	512	120	20	20000	5000
LN-01	512	120	60	20000	10000
LN-02	512	120	120	20000	20000
LN-03	512	120	240	20000	40000
BE-01	256 256	80 160	20 20	10000 30000	2000 5000
BE-02	256 256	80 160	20 20	16000 24000	2000 2000
BE-03	256 256	60 180	20 20	14000 26000	2000 2000
BO-01	384 128	80 240	20 20	14000 38000	2000 2000
BO-02	435 77	80 346	20 20	14000 53900	2000 2000
BO-03	486 26	80 868	20 20	14000 132000	2000 2000

Figure 4-12 presents a set of (a) normally distributed properties and (b) log-normally distributed properties. The effect is evident in that the log-normal paths are more smoothly curved and mimic more closely the typical behavior of soils in our torsional shear tests.

A similar effect occurs in Figure 4-13a, where the pairs of mean values separate over greater and greater distances. Analysis BE-03 has the widest separation and shows the smoothest curvature. In Figure 4-13b the bimodal concept was changed so that the stiffer, stronger component had a reduced population. However, the overall average E and σ_y remained constant. The progression is similar to the previous groups but less pronounced.

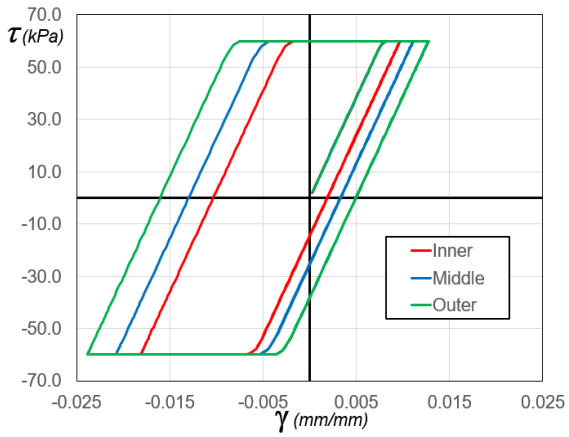

(a) Stress-strain curves for E=20000 kPa σ_y=120.

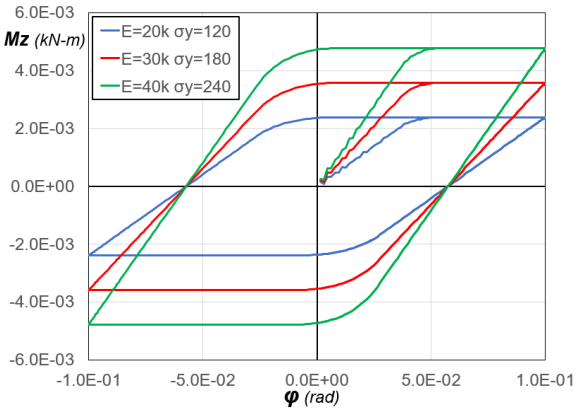

(b) Moment rotation curves for three specimens with unform properties.

Figure 4-11 Preliminary results of the model.

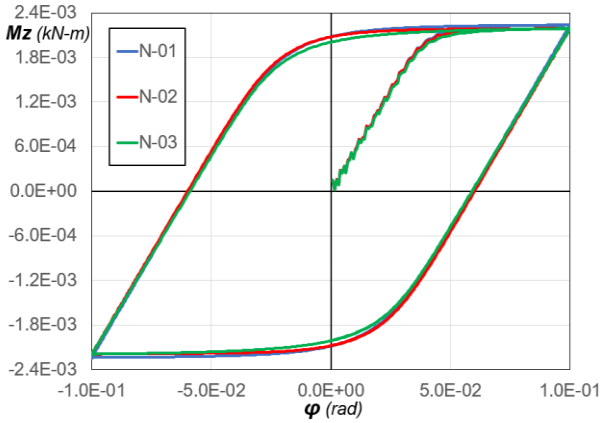

(a) Normally distributed values of E and σ_y.

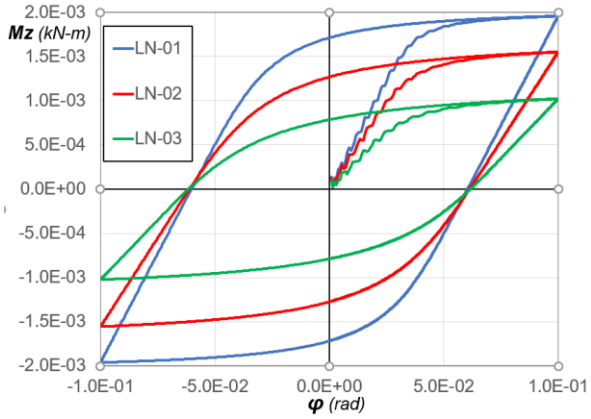

(b) Log-Normally distributed values of E and σ_y.

Figure 4-12 Reaction moment vs rotation.

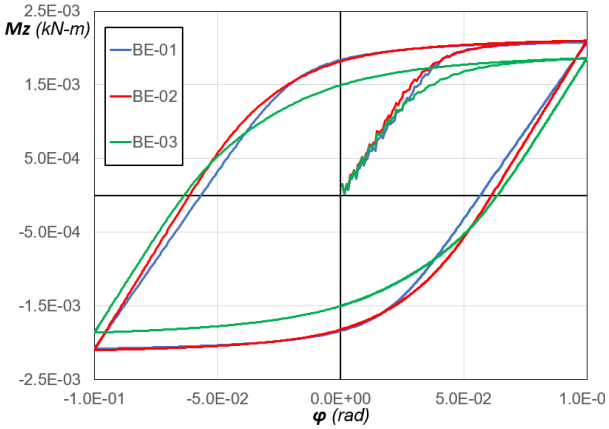

(a) Even bimodal normal distribution of values of E and σ_y.

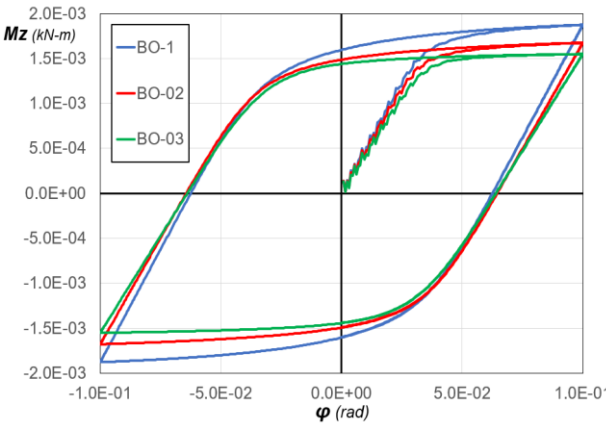

(b) Offset bimodal normal distribution of values of E and σ_y.

Figure 4-13 Reaction moment vs rotation.

After finding that a simple material model such as Tresca can generate complex soil behavior by varying the properties of the elements, and the nonlinearity becomes more evident when the variation of properties varies over a broader range (log-normal distribution). The next step in this study was to find the distribution of Tresca elements within the soil sample, which have different properties in Midas but will generate a nonlinear behavior that matches the RO model, hence the TOSS test results.

4.3.2 Masing Model

In Masing's original model, the system consists of successively yielding elements. Each element has an elasto-plastic yield behavior, which deviates from the elastic line as more and more elements yield, as shown in Figure 4-14. The plastic term of the stress-strain equation in the relative coordinates is divided by two upon unloading and reloading since the yield stresses have effectively doubled. The distribution of the yield levels depends on the material's microstructure and the cross-section's dislocation arrangement. A probability density function can describe this distribution.

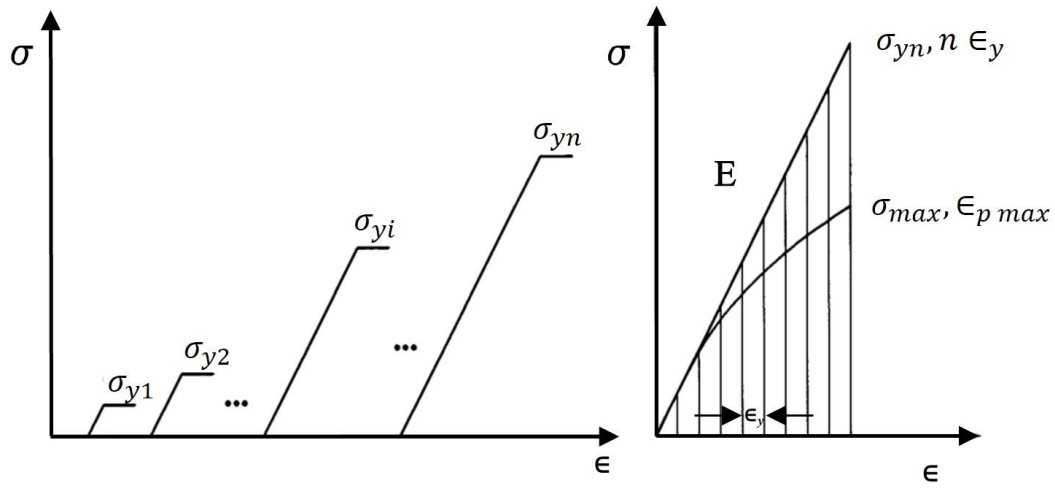

Figure 4-14 Masing elastic–plastic element yield model gives gradual departure from elastic line as more and more elements yield (Skelton, et al., 1997).

(Skelton, et al., 1997) used a discrete distribution by approximating the continuous distribution by an isosceles triangle, where the number of yielding elements increases in linear steps as the yielding stress increases. The process continues until the yield reaches a maximum value, then decreases linearly, as demonstrated in Figure 4-15 (before the arrows). If *n* is the number of yield stress levels until the apex of the triangle, then *N=2n* is the total number of yield stress levels, and the total number of elements *Z* involved in deforming up to σ_{max} is given by:

$$Z = \frac{N(N+2)}{4} \qquad \text{Equation 4-3}$$

Calculating the total stress for the entire system differs from the Iwan model because the elements do not connect in series or parallel. However, with a combination of both, thus we calculate the total shear stress for the system as follows:

$$\tau = (\sum_{i=1}^{j} G\gamma_i + \sum_{i=j+1}^{N} \tau_i)/Z \qquad \text{Equation 4-4}$$

The summation from 1 to j includes those elements that remain elastic after loading deflection γ, and the summation from j+1 to N includes all elements that slipped or yielded. If we have 100 yield stress levels (*N=100*) and a total of *Z=2550* elements, we choose the yield stress levels to match the maximum stress of $\sigma_{\max} = 100$ KPa. We can see from Figure 4-16 that using this distribution does not give control over the nonlinearity of the curvature to obtain a good fit with the Ramberg-Osgood curve that fits the testing data. Therefore, a second method may fit the two curves and determine the combination of yield stresses for the elements that give the fit between the Tresca model and the test data.

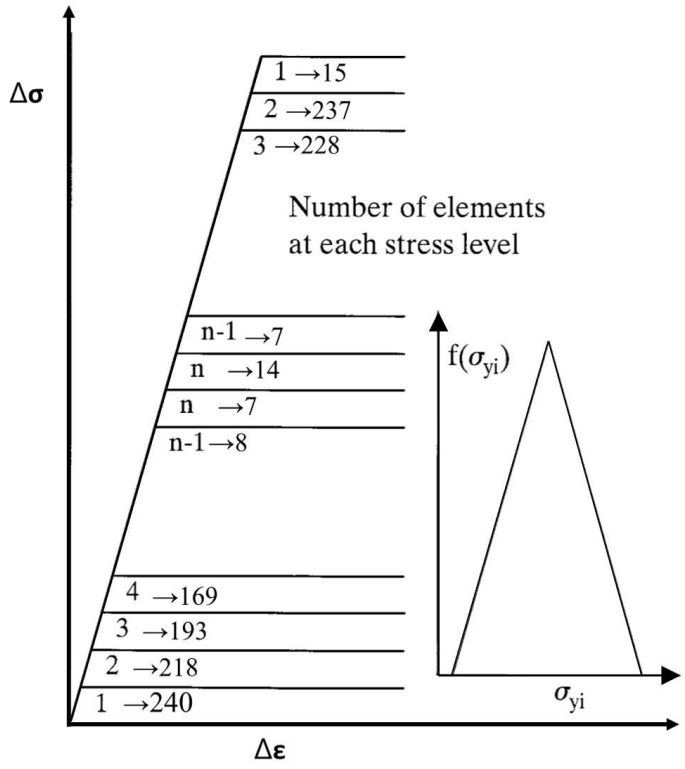

Figure 4-15 Idealization of continuous distribution function by discrete levels and elements; and after the arrows are the number of elements at each stress lever after using the solver.

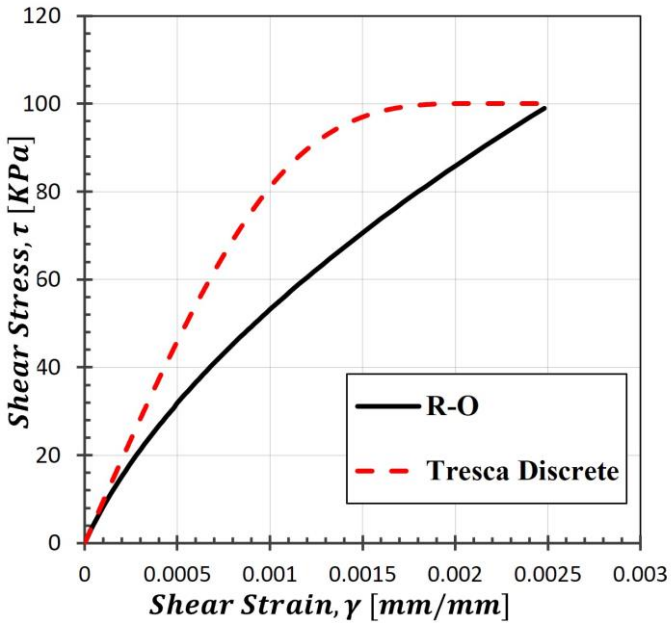

Figure 4-16 Discrete distribution fitting attempt with RO.

4.3.3 Calibration and curve fitting

In order to obtain a fit between discretely distributed Tresca elements (Equation 4-4) with the RO model, a hybrid approach used Solver in Excel and Midas analysis together (Ahmad & Ray , 2023). Only monotonic loading is applied in Midas for the calibration process to save time. First, as in the previous example, we have a constant stiffness for all the elements, knowing that the young modulus (E) is related to the shear modulus (G) and Poisson's ratio (ν) as follows:

$$E = 2 * G(1 + \nu) = 2 * 95500(1 + 0.3) = 248300\ KPa \qquad \text{Equation 4-5}$$

We start with 100 stress levels, knowing that the yield stress in pure shear equals one-half the Tresca yield. Then Solver is used in Excel (least squares method) to change the number of elements at each stress level with the constraint that the total number of elements (Z) is 4032 equals the number of elements in the model in Midas. The number of elements for some of the stress levels is shown in Figure 4-15 (after the arrows). For this initial analysis, we assumed that the strain is uniform across the specimen for all the elements (γ_i), which is not the case as observed after running the analysis on Midas with these properties. The non-uniformity of the strains at the last step appears in Figure 4-17a. This led to a shear stress-strain curve lower than the calculations shown in Figure 4-17-b. However, this run obtained an initial strain for each element (γ_i) in Midas to assign in the Excel sheet for the calculations in the next step.

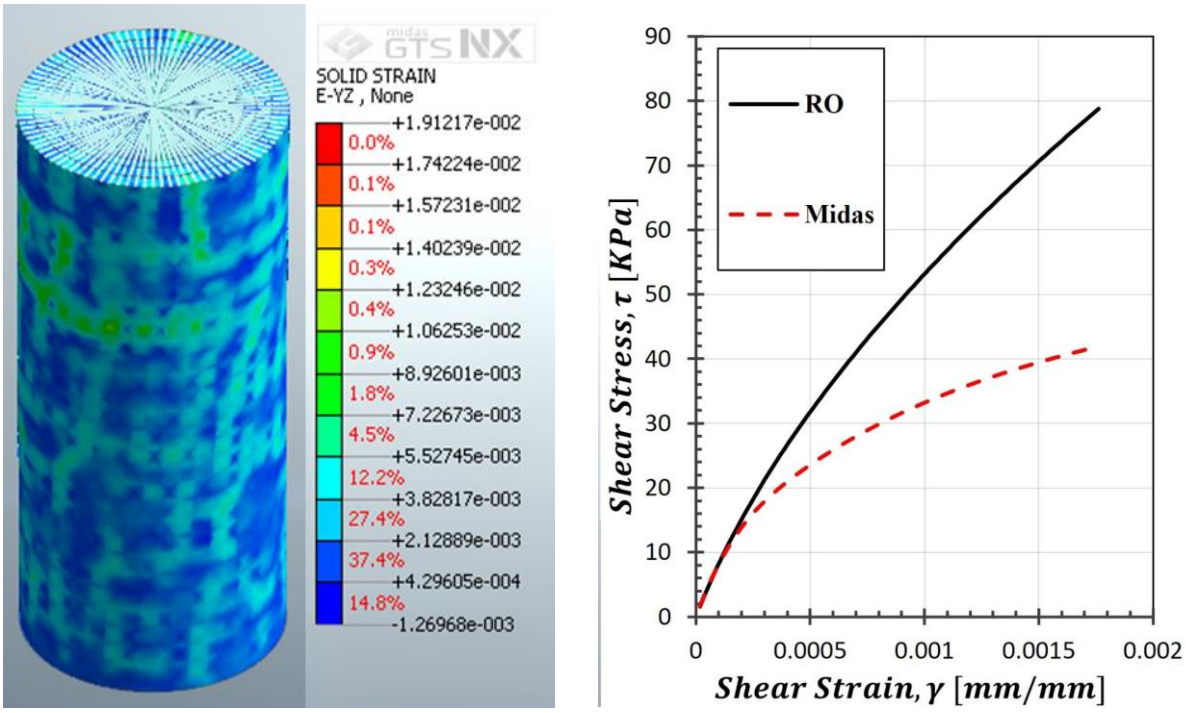

(a) Nonuniform distribution of strain. *(b) Comparison for the initial condition.*

Figure 4-17 Initial analyses results.

Based on the previous yield stress level distribution, the next step will have 4032 yield stress levels, so each of the elements has a different yield stress, and for the Tresca model calculation, each element has different strains extracted from the previous run of Midas (Figure 4-17-a). As a result, every element will have different strain steps depending on its location in the sample. However, the average of the strains for all the elements will always be the same. The Solver is used again to find a new distribution of the yield stresses in the sample to match the Tresca calculated curve with the RO curve. These properties transfer to Midas via (.fpn) file, the loading conditions are defined, and the analysis is run. The results in Midas will not match precisely with the calculations in Excel, but they will get closer (Figure 4-18). This is due to the evolution of strain distributions in the elements from the new analysis (iteration).

By repeating this process shown in Figure 4-19, each iteration will provide a distribution of the yield stresses in the sample that will produce a curve closer to the RO curve. When we find the correct distribution of strains in the sample, the Midas, RO, and Excel calculations will match after a few iterations. Seven iterations produced a match for this example.

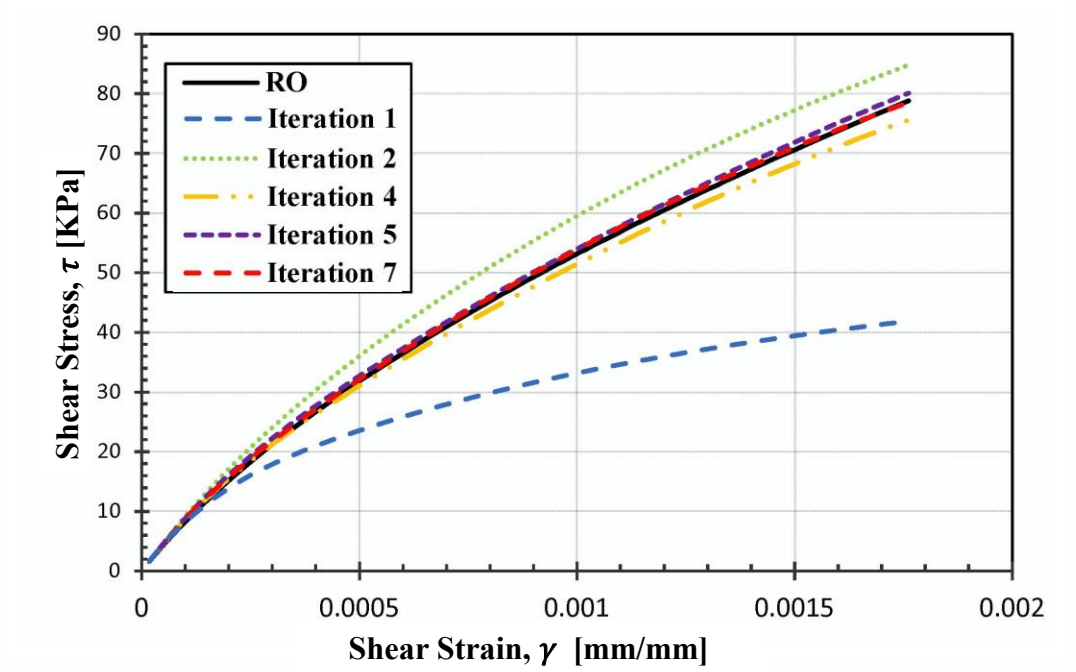

Figure 4-18 Iterations to reach a match between Tresca and RO models.

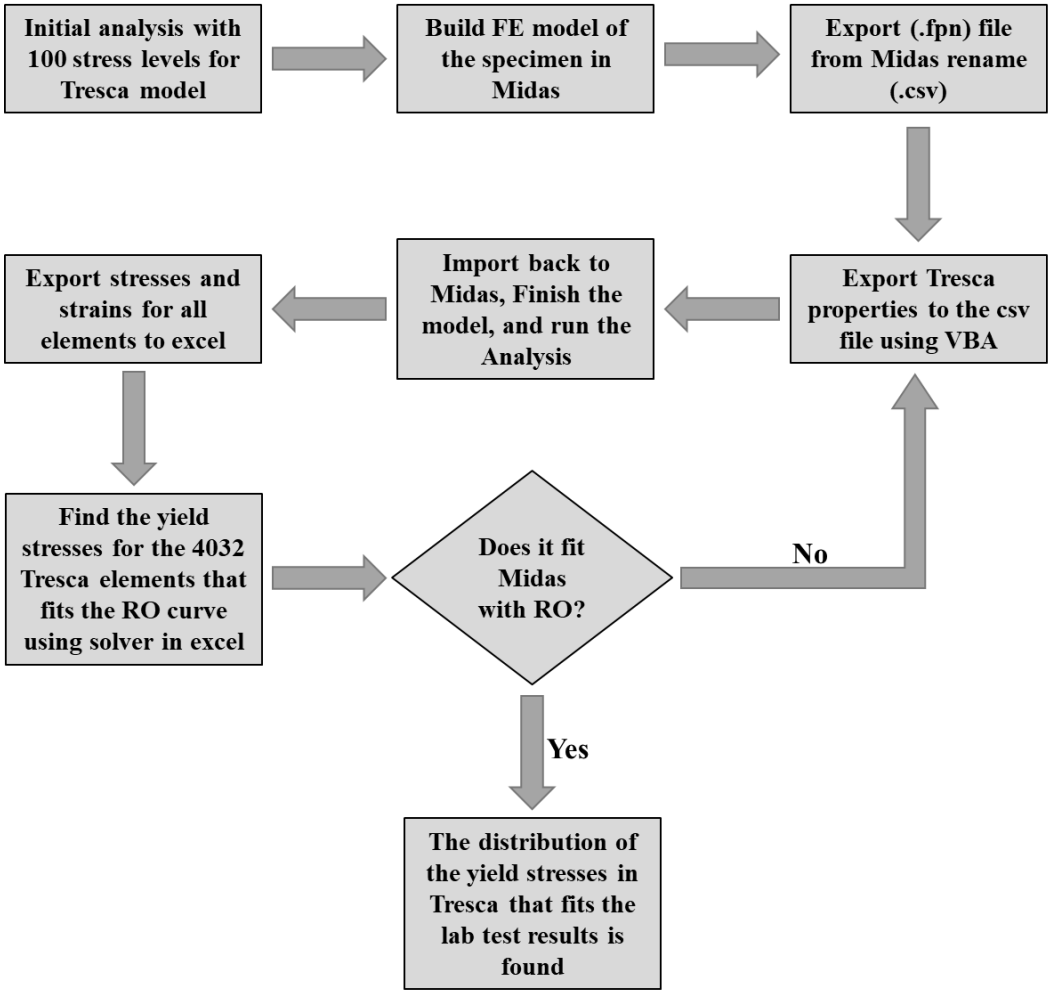

Figure 4-19 process followed for iterations to reach a match between Tresca and RO models.

As a result, we found the combination of Tresca properties that matched the shear stress-shear strain curve obtained from the RO model hence the test data. Figure 4-20 shows the fit for the cyclic loading, where a sine function produced dynamic loading conditions. This model inherently applies the two Masing criteria. A comparison made by plotting the torque-rotation curves at the center point of the rigid links also matches perfectly with the torque-rotation curve of the lab test. Figure 4-21 shows the distribution of the yield stress levels among the elements. This distribution can regenerate Tresca properties for elements in a different Midas model by knowing the number of elements in the soil layer and using Excel's "Random number generation" tool. Furthermore, different aspects of non-uniformity can be studied, such as voids and dense localities.

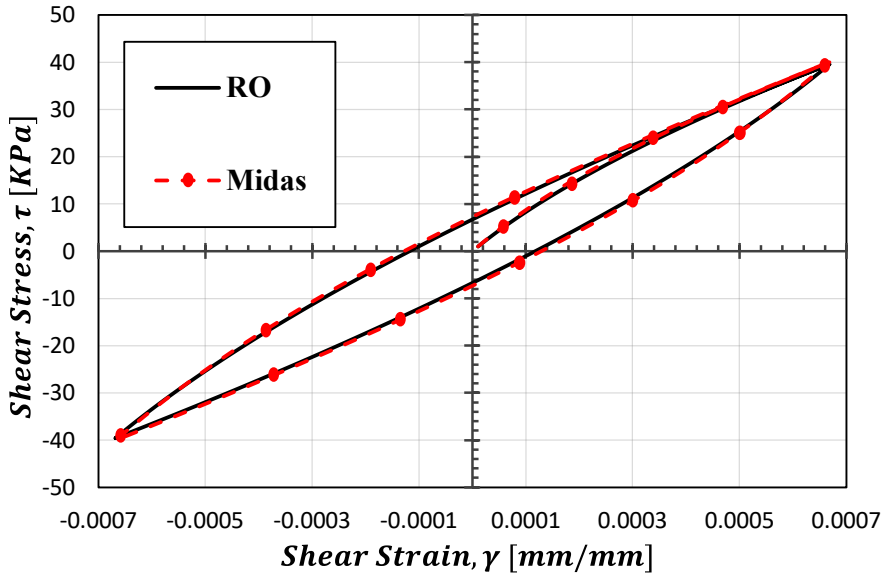

Figure 4-20 RO and Tresca match for cyclic loading.

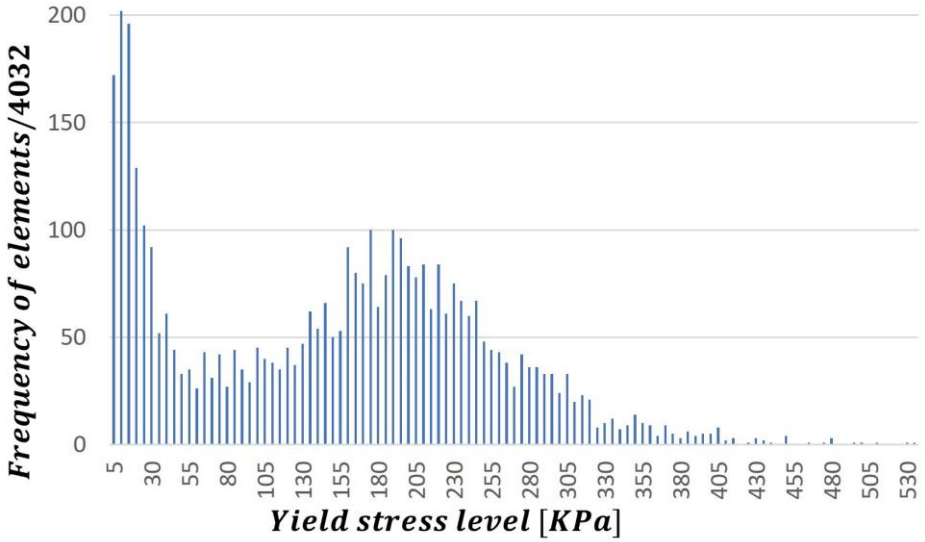

Figure 4-21 The distribution of the yield stresses in Tresca model that fits the lab testing results.

4.3.4 Effect of randomness and rigid inclusions

We investigated the effect of property distribution in the sample by shuffling them randomly to the elements and importing them to Midas, followed by an analysis. The results of 9 different random distributions of the same properties show a maximum deviation of 4.27% from the original RO shear stress-shear strain curve.

The sample preparation method for the TOSS test depends on the required initial density of the sample. The dry pluviation method achieves the dense state, while the loose state results from pouring dry soil into the sample mold with a glass funnel. However, uniformity in the sample is not assured, and dense localities can appear in random locations due to variations in forming the sample. The existence of particles of higher diameter and strength, or the bonding between the particles, may occur randomly throughout the specimen. To reproduce the effects of rigid inclusions or voids, the FEM model contained blocks of elements with linear elastic material property (rigid or soft) and a very high (or low) elastic modulus representing a rigid inclusion or void. The number of elements in this block gradually increased from one block of 3x3x3 elements (0.7% of the sample are inclusions) to two blocks of 13x13x3 elements (25% of the sample are inclusions), as shown in Figure 4-22. The shear stress-strain curves of the specimens with inclusions were compared to specimens without inclusions. Results show that stiffness increases with larger inclusions, as shown in Figure 4-23 and Table 5, and this increase is almost linear for our tested soil given by:

$$y = 1.205 * x + 4.23 \qquad \text{Equation 4-6}$$

Where y is the increase in stiffness in percent, and x is the percentage of inclusions in the sample.

The same approach studied the decrease in stiffness due to voids and deformities in the sample. Polystyrene blocks in the specimen simulated voids and reduced stiffness significantly. By giving the voids elements an elastic modulus of one-tenth of the sample (here 9.55 MPa), the stiffness decreased by 45% when 12% of the sample were voids as shown in Figure 4-24.

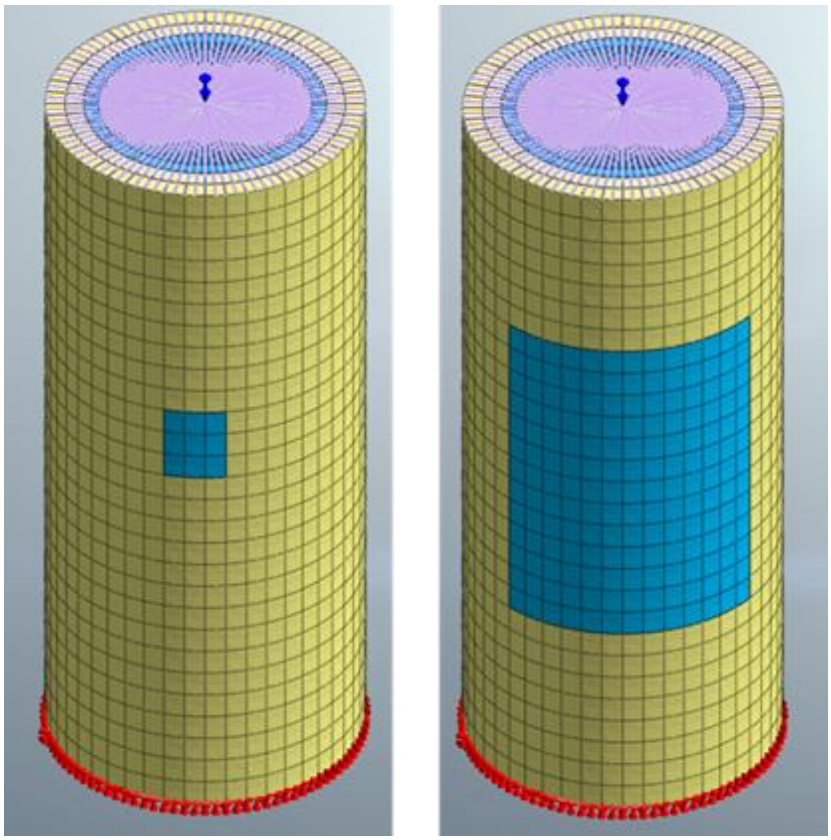

Figure 4-22 Inclusions in the specimen (the elements in blue).

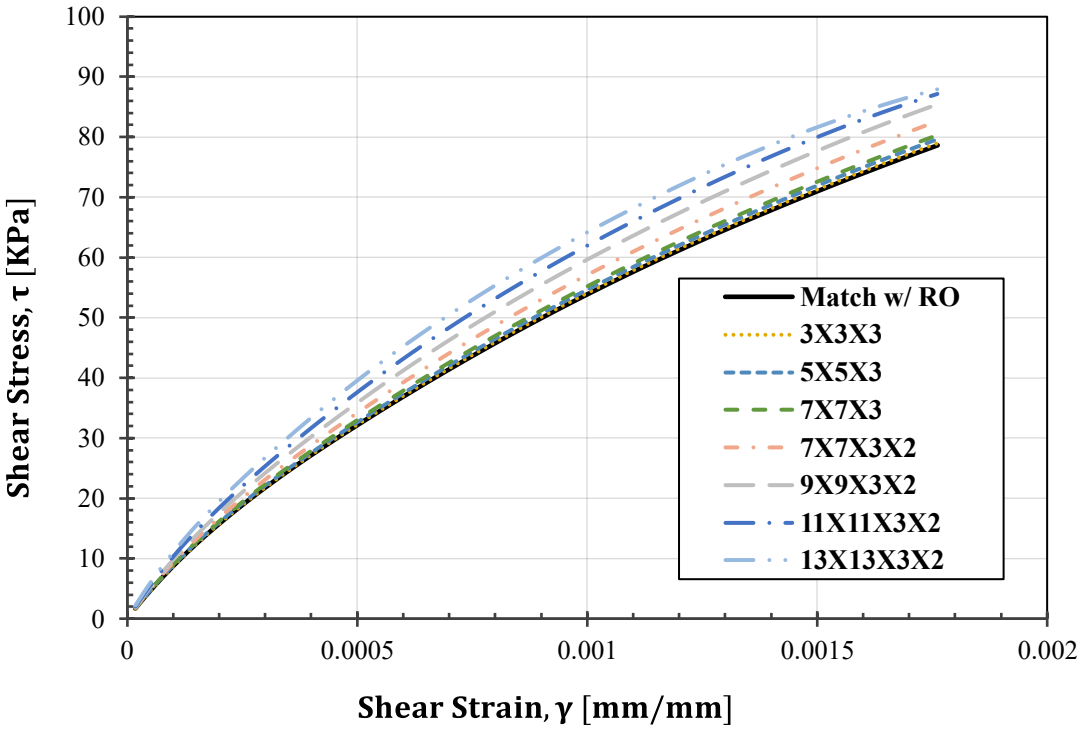

Figure 4-23 The increase in stiffness with the increasing number of inclusion elements.

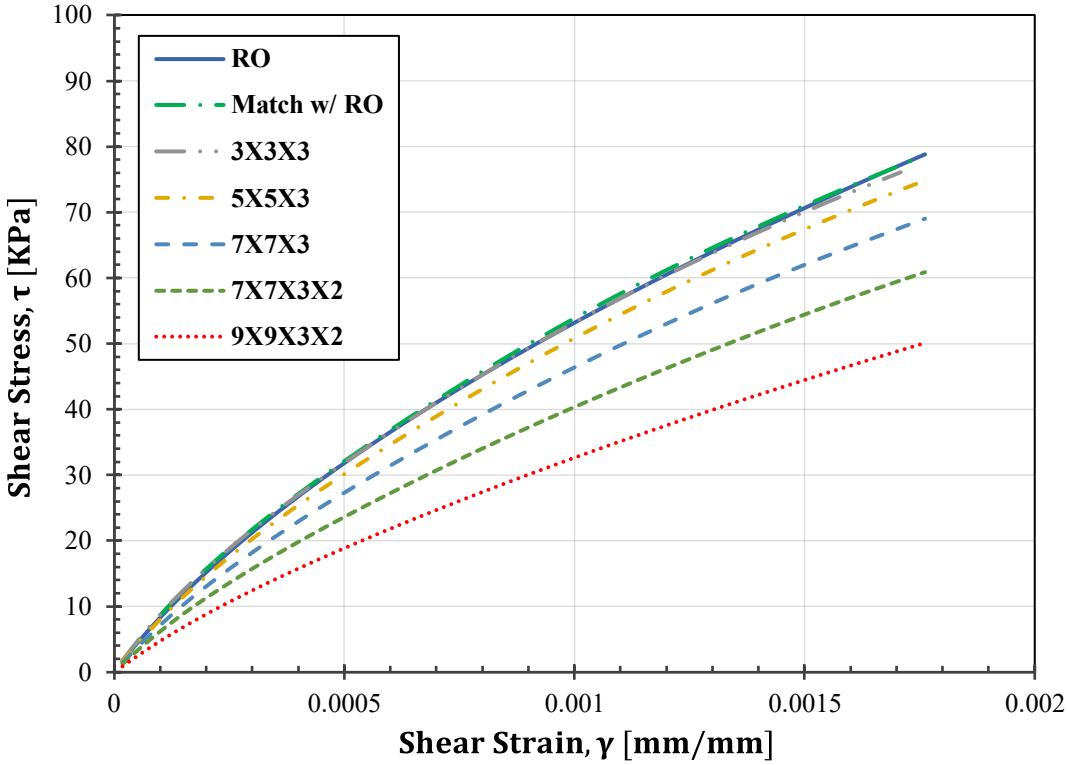

Figure 4-24 The decrease in stiffness with the increasing number of voids elements.

Table 5 The effect of inclusions and voids on the stiffness.

Number of inclusion /voids elements	Percentage of inclusions /voids [%]	Increase in stiffness with inclusions [%]	Decrease in stiffness with voids [%]
3x3x3	0.67	5.5	3.4
5x5x3	1.86	6.83	6.3
7x7x3	3.65	8.38	17
7x7x3x2	7.29	12.63	28
9x9x3x2	12.05	18.4	45
11x11x3x2	18	25.51	-
13x13x3x2	25.15	35.11	-

Chapter 5
Stiffening Behavior and the Proposed Model

As mentioned in section 2.3.4, TOSS specimens stiffen with additional loading cycles or irregular loading histories. The extent of this impact is disputed among past researchers and remains a topic of disagreement. In our tests, load cycles substantially increased stiffness, as demonstrated in Figure 5-1. Sometimes the dynamic shear modulus doubled when loaded at high levels for more than 50 cycles. Furthermore, the stiffening behavior dramatically impacts the functionality of the Masing criteria and the modeling of the nonlinear dynamic behavior of soil when subjected to irregular loading patterns. The results presented in Chapter 4 originated from irregular tests conducted after 100 cycles of loading. As a result, the effect of the number of cycles does not show in the shear stress-strain curves because the stiffening effect is marginal after around 75 cycles. That explains the excellent fit between the soil models (RO and HD) with the lab testing curves when using the Masing criteria. However, applying an irregular loading history on soil without preconditioning cycles (not cyclically loaded before), the Masing criteria predict behavior much less accurately. There would be a significant deviation from the laboratory test results, particularly when subjected to more cycles. This chapter explores how the stiffening behavior impacts the shear modulus in various situations. It also demonstrates suggested adjustments to the Masing criteria necessary to accurately predict soil behavior when subjected to cyclic or irregular loading histories (Ahmad & Ray, 2024).

5.1 Testing Program

We chose three specimens of coarse soils for this research. These samples originated from an area close to the Danube River in Hungary, specifically near Paks, and were taken from depths ranging between 5 to 15 meters using a hollow-stem auger sampler. The soils are fluvial sediments of the river with a wide variation of in-situ densities. Samples A and B contained a very low percentage of fines, while Sample C retained 21% of fines content with low plasticity.

The properties of the tested samples are detailed in .

Table 6, and particle size distribution curves are demonstrated in Figure 5-2. The samples exhibited a complex grain structure with heterogenous grain shapes varying between subangular and rounded shapes (Figure 5-3).

Two variations of TOSS tests allowed for the investigation of the impact of the number of cycles on the dynamic properties.

Table 7 shows the testing program. In tests (#1-#3-#5-#7-#9-#11), the backbone curve developed by loading the sample for only one cycle at progressively higher stress levels (5-10-15-20-25-30-35-40-45-50 KPa), and the equivalent shear modulus was found for each cycle (Figure 5-4). A second identical specimen was constructed with the same void ratio and confining stress for tests (#2-#4-#6-#8-#10-#12). However, in this case, the sample was subjected to 100 cycles of loading at every stress level. The duplicates revealed any effects of the number of cycles on specimen behavior (Figure 5-1). More tests were conducted (#13 to #20) to determine the effect of strain level on the stiffening behavior by loading the soil cyclically at the same peak-to-peak stress level but at different offsets. The FVD and SSV methods (Chapter 2) determined the damping ratio. Each test started with RC measurements to find the G_{max} and shear modulus up to a strain level below the volumetric strain threshold (γ_{tv}, typically around 0.01%) to avoid any interference of the vibrations in the RC test on the outcomes of the TOSS test. At the end of each test, RC measurements were also taken to study the effect of the cyclic loading on the maximum shear modulus. The findings are discussed in this chapter.

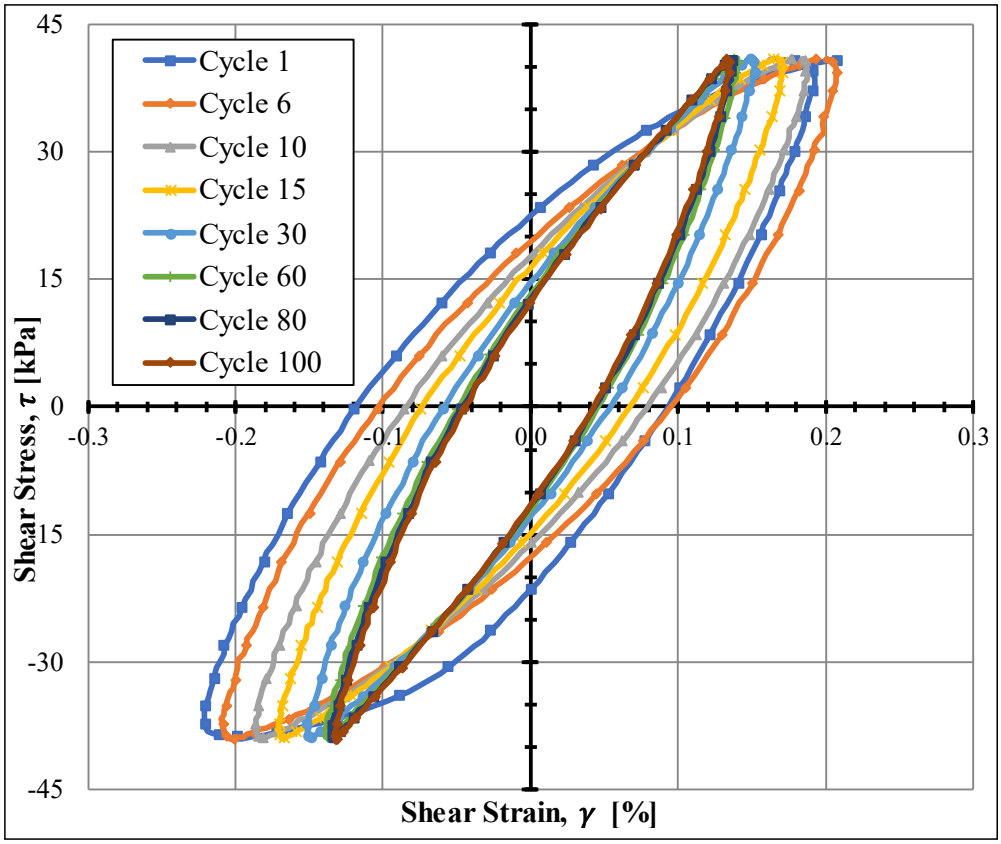

Figure 5-1 The stiffening behavior of the sample during cyclic torsional loading.

Table 6 properties of tested soil.

Sample ID	Mean particle diameter	Eff particle diameter	Uniformity coefficient	Fines content	Max void ratio	Min void ratio	Liq. limit for fines	Plastic limit for fines	Plastic index for fines
	d_{50} [mm]	d_{10} [mm]	C_u [-]	FC [%]	e_{max} [-]	e_{min} [-]	w_l [%]	w_p [%]	I_p [%]
A	0.211	0.109	2.06	7.56	0.81	0.52	-	-	-
B	0.243	0.130	2.18	5.69	0.79	0.516	-	-	-
C	0.107	0.013	9.85	21.11	0.9	0.524	30.4	19.7	10.7

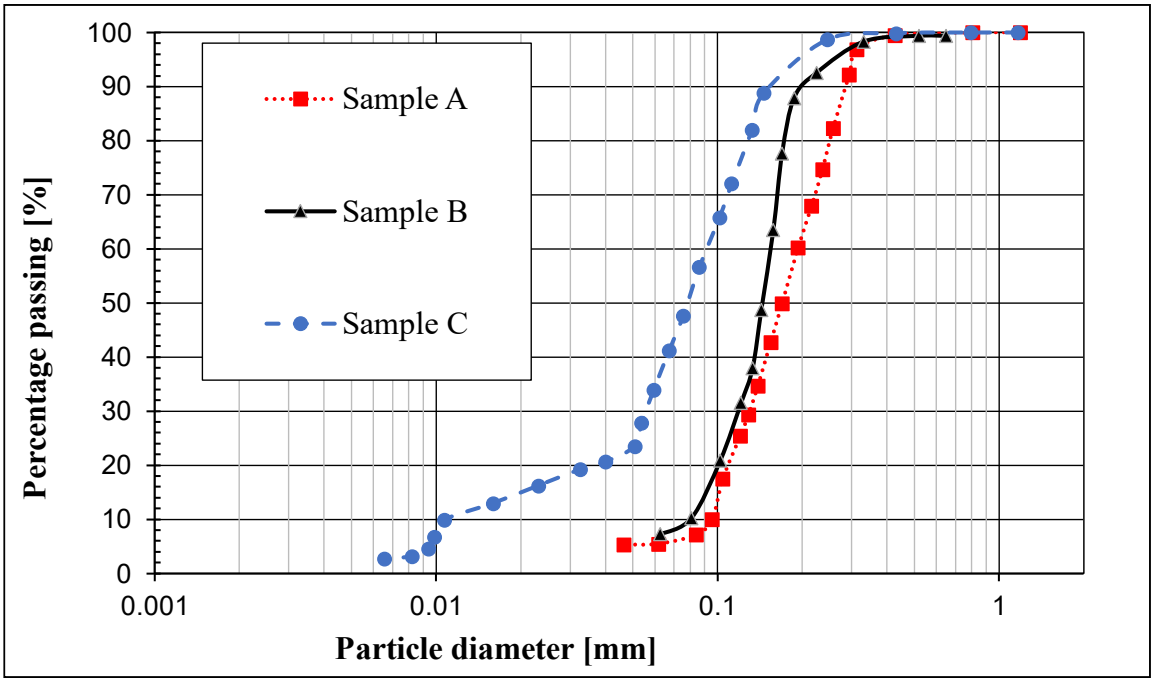

Figure 5-2 Grain size distribution curves for tested soils.

(a) Sample A *(b) Sample B* *(c) Sample C*

Figure 5-3 Particles shape of the samples (not to scale).

Table 7 Testing program.

Test number	Sample ID	Confining stress	Void ratio	Relative density	Angle of friction	Test type
#		$P`$ [KPa]	e [-]	D_r [-]	φ [°]	
1-2	A	97	0.77	0.14	31	Cyclic RC-TOSS
3-4	A	97	0.58	0.79	40	Cyclic RC-TOSS
5-6	B	96.5	0.76	0.11	35	Cyclic RC-TOSS
7-8	B	96.5	0.57	0.80	43	Cyclic RC-TOSS
9-10	C	97	0.85	0.13	31	Cyclic RC-TOSS
11-12	C	97	0.62	0.74	40	Cyclic RC-TOSS
13	A	97	0.58	0.79	40	TOSS, effect of stress offset
14	B	97	0.58	0.77	43	TOSS, effect of stress offset
15	A	96.8	0.77	0.14	31	RC, damping measurements
16	A	97	0.57	0.83	40	RC, damping measurements
17	B	97	0.73	0.22	35	RC, damping measurements
18	B	97	0.58	0.77	43	RC, damping measurements
19	C	96.6	0.85	0.13	31	RC, damping measurements
20	C	97	0.63	0.72	40	RC, damping measurements

5.2 Backbone and shear modulus curves

After obtaining the backbone curves of the tested samples from the TOSS tests (Figure 5-5), the RO model parameters that fit the curves are found after measuring the maximum shear modulus G_{max} from the RC test and computing the maximum shear stress τ_{max} from Equation 2-31. The RO model can fit to the backbone curves very well with the chosen curve fitting constants shown in

Table 8 with a coefficient of determination ($R^2>0.99$) for all the tested samples. It is evident that identical curve-fitting constants can be utilized for the same soil specimen under different conditions by changing τ_{max} and G_{max} depending on the state of the sample (angle of friction, confining stress, and void ratio). G_{max} can be determined based on RC measurements or correlations that estimate its value from the void ratio and mean effective stress. Most relevant to this study is the correlation found by (Szilvágyi, 2017) after measuring G_{max} of the Danube sand over a wide range of densities and confinement stresses.

The shear modulus degradation curves are then obtained, which show an excellent agreement between the RC and TOSS tests. The secant shear modulus and damping ratio are calculated for each cycle in the cyclic TOSS test for every stress level to analyze the effect of the number of cycles on the dynamic properties of soil. The results of one of the tests conducted on Sample A are shown in Figure 5-6, and a comparison between the shear modulus degradation curves of all the samples is demonstrated in Figure 5-7 and the normalized G/G_{max}-γ curves are illustrated in Figure 5-8.

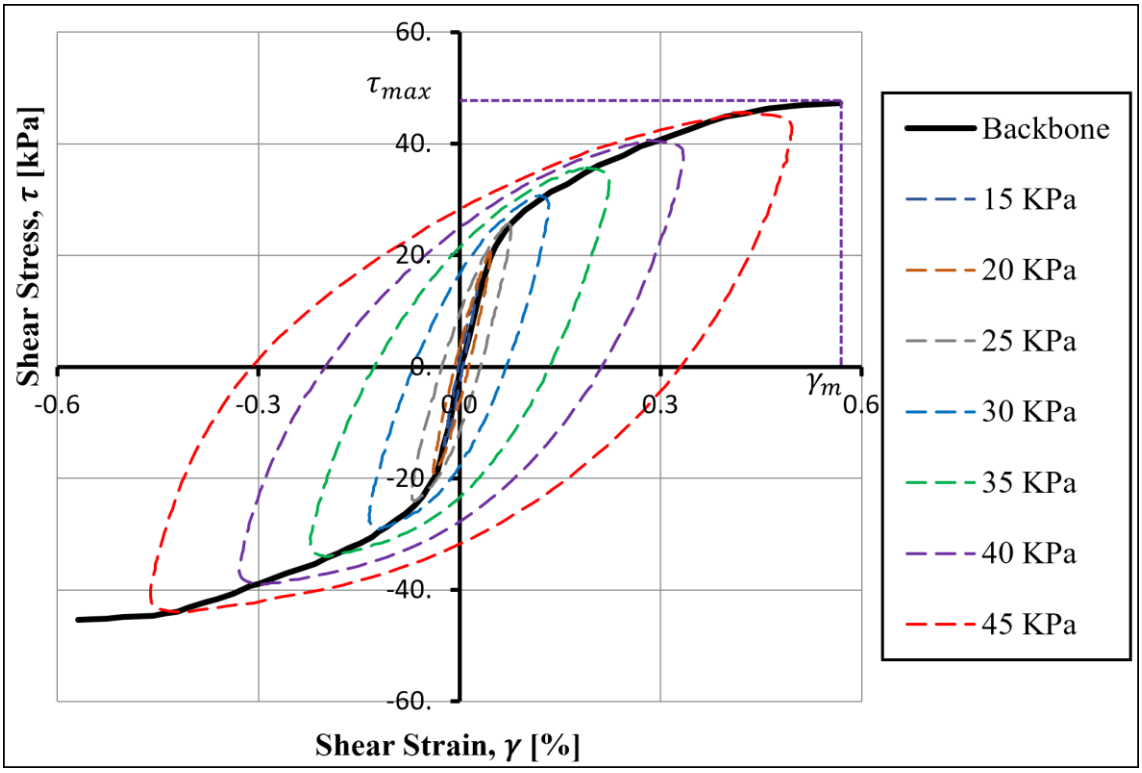

Figure 5-4 TOSS test for obtaining backbone curve (Sample B, loose state).

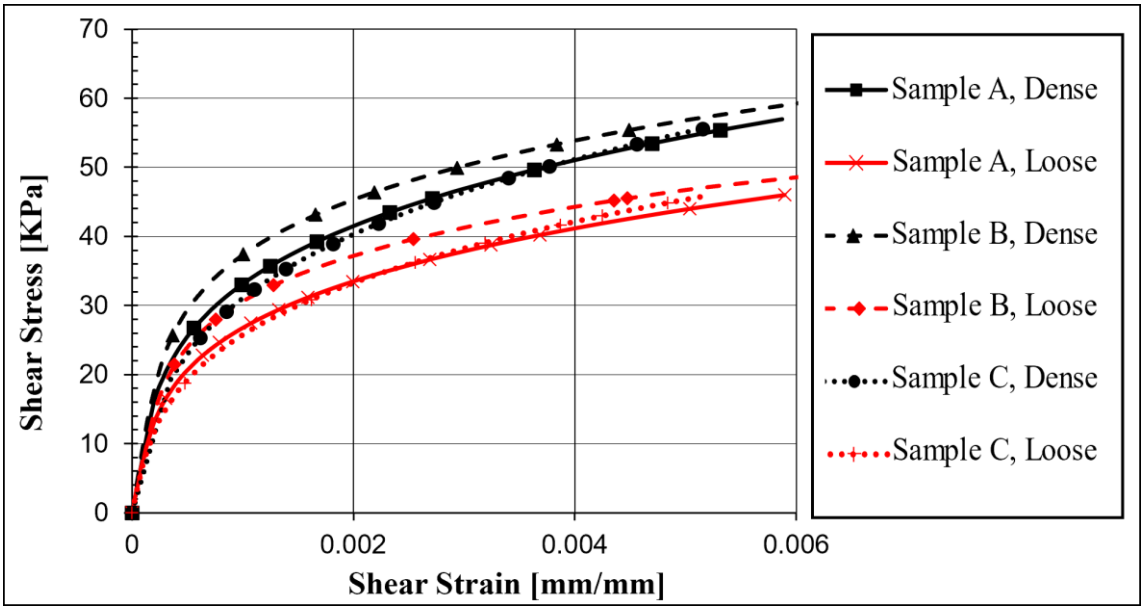

Figure 5-5 Backbone curves of the tested samples.

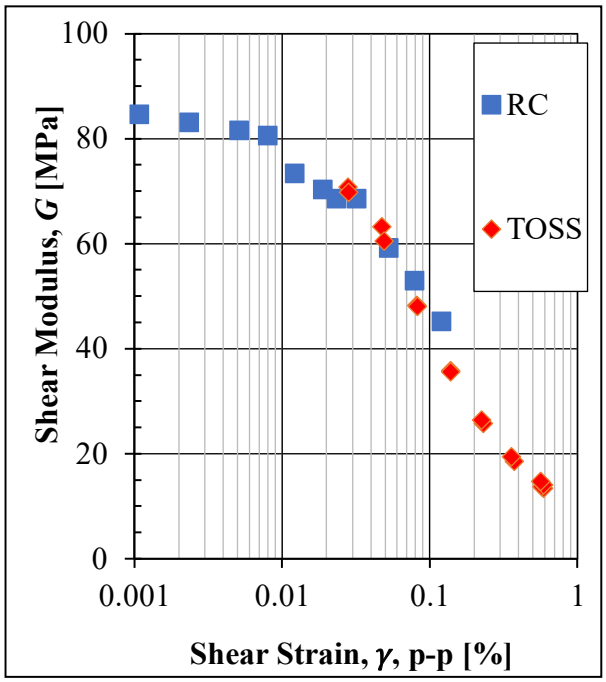

(a) Shear modulus degradation curve.

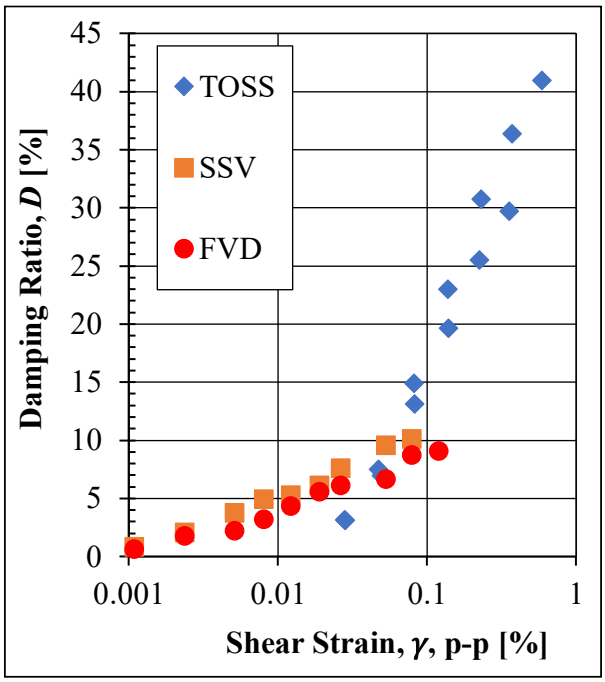

(b) Increase in damping ratio with the increasing shear strain.

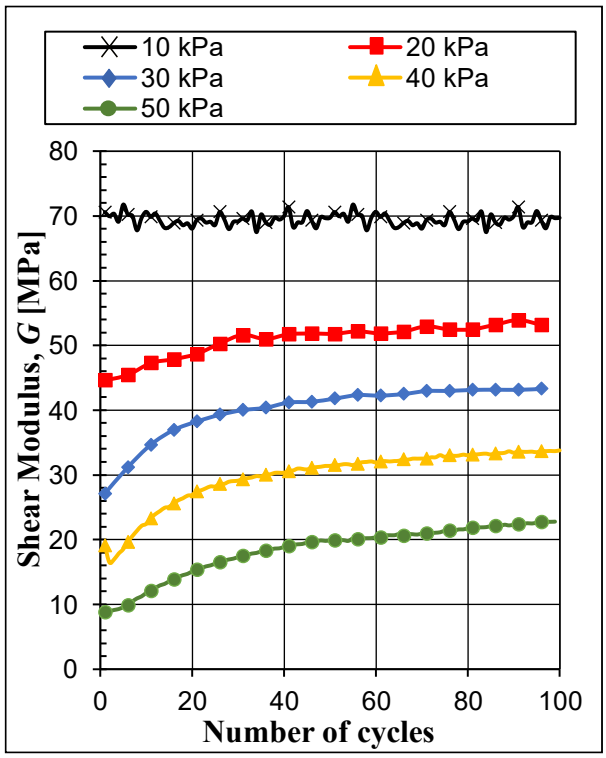

(c) Increase of shear modulus with the increasing number of cycles.

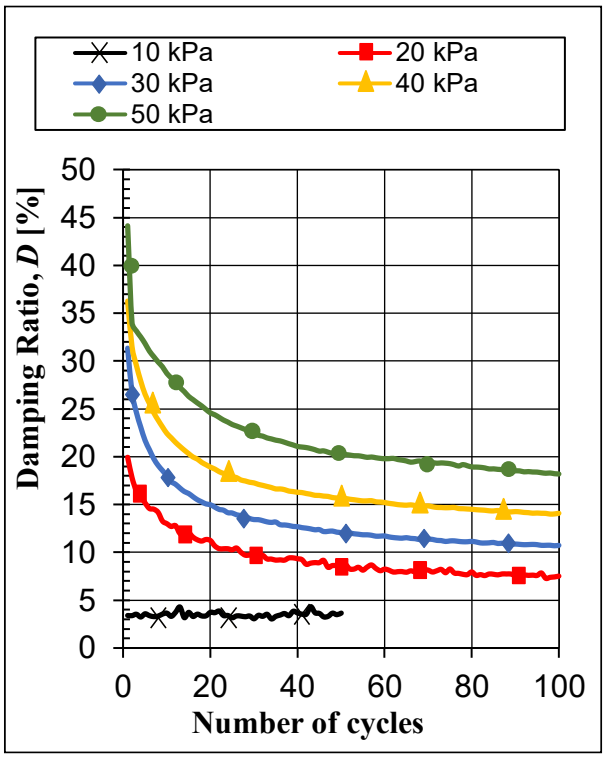

(d) Decrease of damping ratio with the increasing number of cycles.

Figure 5-6 RC-TOSS results for Sample A, loose state (Test #2).

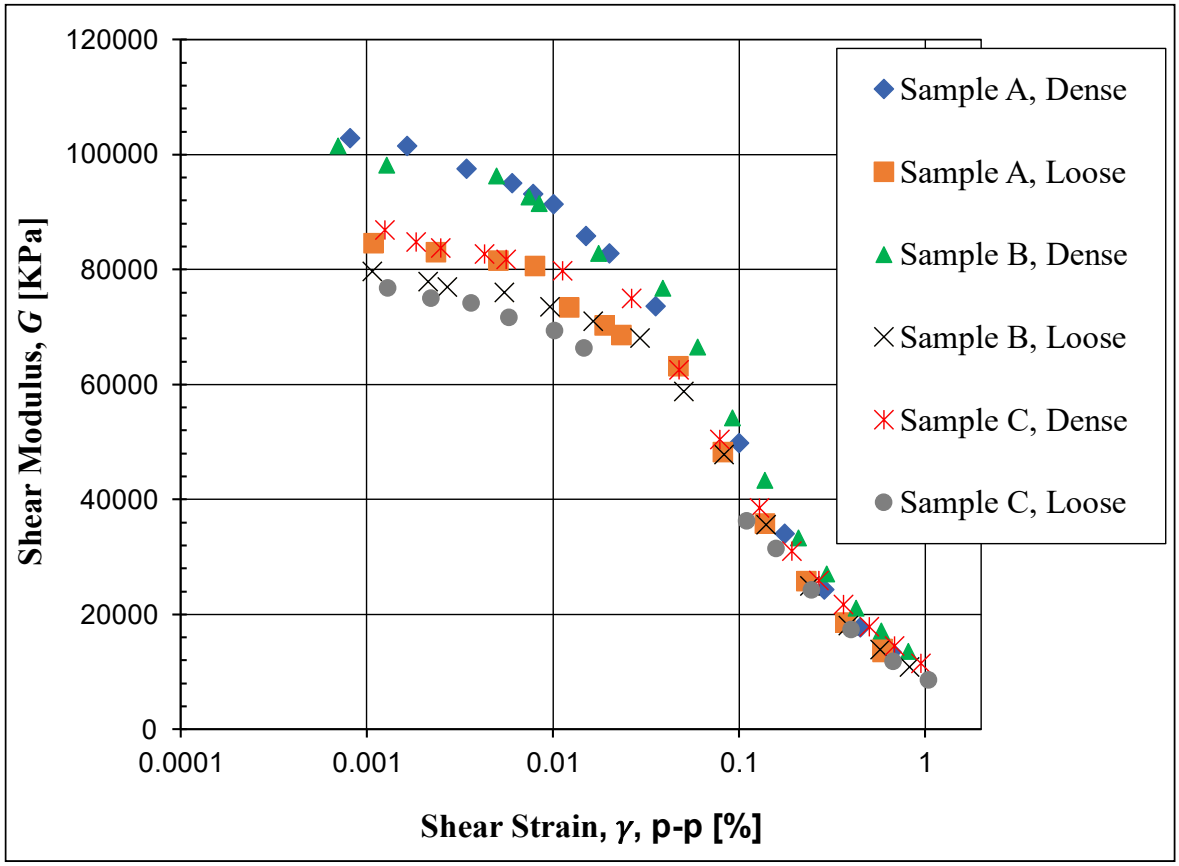

Figure 5-7 Shear modulus degradation curves.

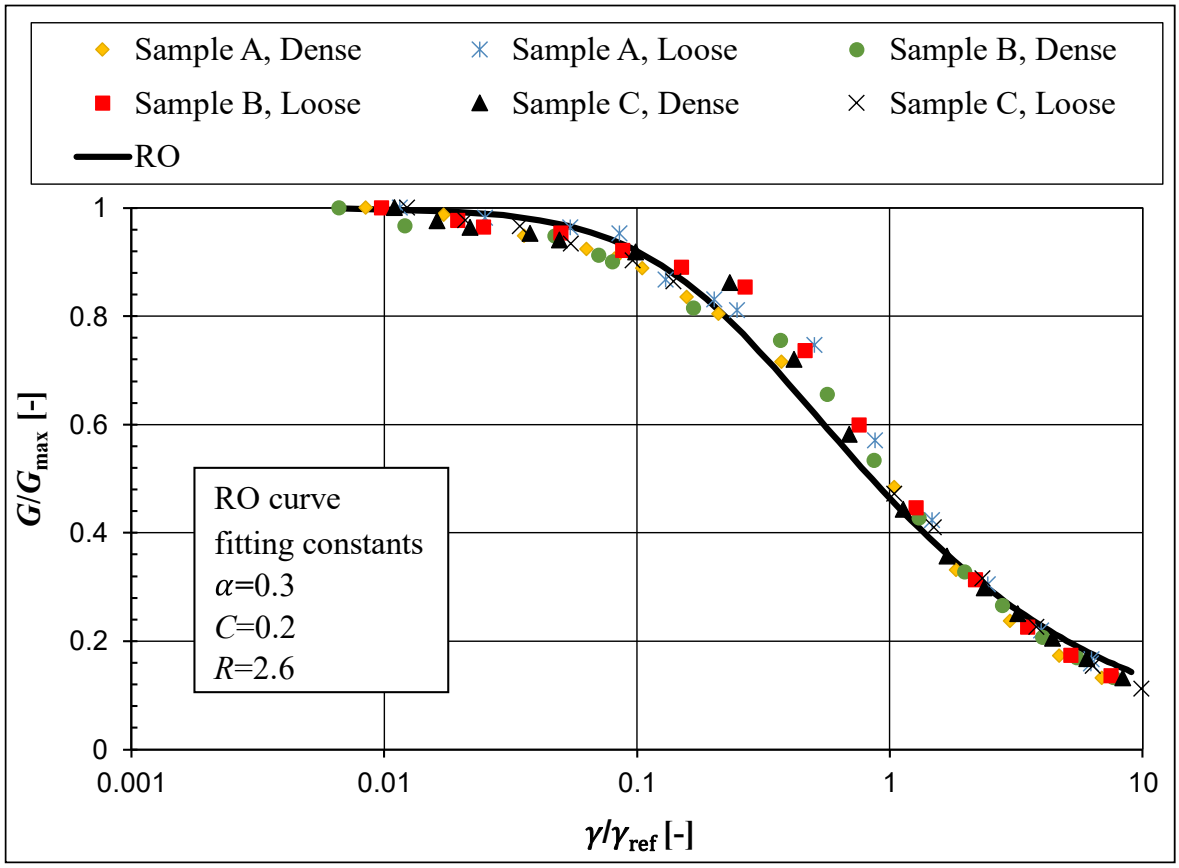

Figure 5-8 Normalized shear modulus degradation curves for all samples.

Table 8 Ramberg-Osgood parameters for the backbone curves.

Test number	**Sample ID**	**Uniformity coefficient**	**Fines content**	**Void ratio**	**Max shear modulus**	**Max shear stress**	***α***	C_b	R_b
#		C_u [-]	FC [%]	e [-]	G_{max} [MPa]	τ_{max} [KPa]	[-]	[-]	[-]
1	A	2.06	7.56	0.77	85	40	0.3	0.33	3.78
3	A	2.06	7.56	0.58	103.4	50	0.3	0.33	3.78
5	B	2.18	5.69	0.76	79.6	44	0.3	0.44	4.66
7	B	2.18	5.69	0.57	100	53	0.3	0.44	4.66
9	C	9.85	21.11	0.85	76	40	0.3	0.29	3.35
11	C	9.85	21.11	0.62	87	50	0.3	0.29	3.35

5.3 Effect of cyclic loading on the maximum shear modulus

Small-strain RC tests, performed between cyclic TOSS stages, will reveal any changes in (G_{max}) due to cyclic loading. Based on the results (Figure 2-9), G_{max} did indeed increase. The outcomes varied across the samples, with no discernable pattern or correlation to the initial G_{max} or void ratio. However, cyclic loading at higher strain levels impacted G_{max} more significantly. The cyclic loading at 0.6% strain (single amplitude) caused an increase in the maximum shear modulus by around 9 to 24% for loose samples and 5 to 15% for dense samples. Figure 5-9 shows the increase in G_{max} with the increasing stress level after applying 100 cycles.

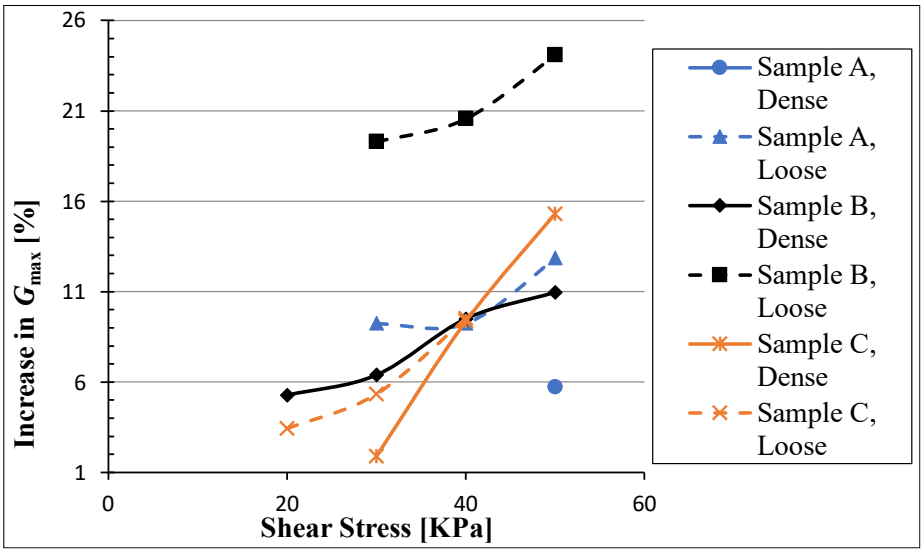

Figure 5-9 Increase of G_{max} after 100 cycles with the increasing stress level.

5.4 Cyclic stiffening behavior

The soil stiffening index (δ_G) represents the ratio of secant modulus at cycle N to cycle 1 at the same stress level.

$$\delta_G = \frac{G_N}{G_1} = \frac{\tau_c/\gamma_{cN}}{\tau_c/\gamma_{c1}} = \frac{\gamma_{cN}}{\gamma_{c1}} = t * \log(N) + 1 \qquad \text{Equation 5-1}$$

Therefore, the stiffening index δ_G, at a given stress level, is calculated as the ratio of the measured strain (γ_{cN}) of the N^{th} cycle divided by the peak strain γ_{c1} of the 1^{st} cycle obtained from the initial backbone curve at that stress level. The increase in δ_G with the increasing number of cycles for Sample A in a loose state appears in Figure 5-10. The stiffening behavior increases with the increasing stress or strain amplitude after exceeding the volumetric shear strain threshold (here at a stress level of 20 KPa).

In Equation 5-1, (t) is the slope of ($\delta_G - 1$)-log(N) plot and represents a stiffening parameter. Practically t describes the slope of the relationship:

$$t = \frac{\delta_G - 1}{\log(N)} \qquad \text{Equation 5-2}$$

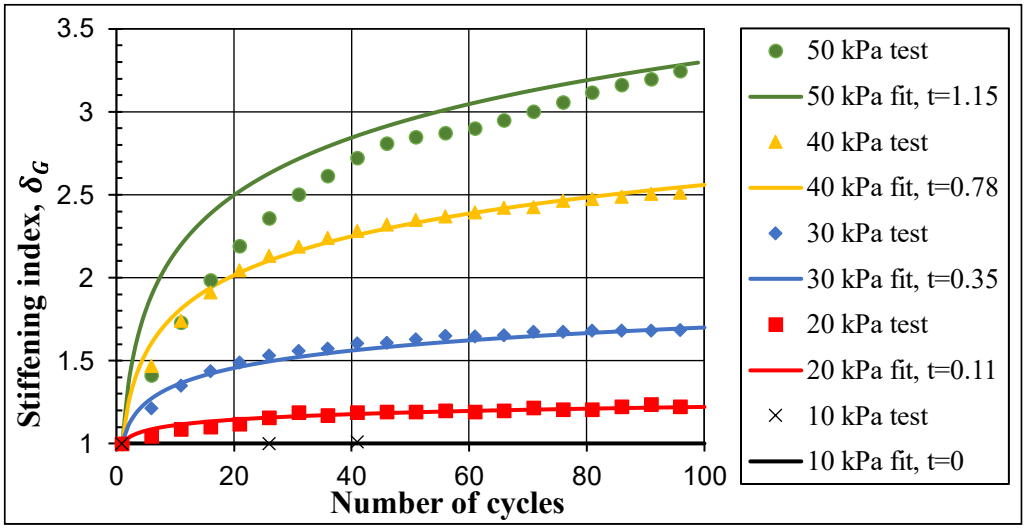

Figure 5-10 Stiffening index increase with the increasing number of cycles for Sample A, loose.

At low strain levels (below γ_{tv}) where no stiffening is experienced by the soil due to the cyclic loading, the stiffening index will take the constant value δ=1 and the stiffening parameter t=0. As the stress or strain amplitude increases, the stiffening rate also increases, leading to a rise in the value of (t). Since the tests are stress-controlled with gradually increasing stress levels of cyclic loading, loose samples will reach higher strain amplitudes than dense samples at the same stress level due to their lower initial stiffness. Therefore, the stiffening parameter (t) is always higher for loose samples at a prescribed stress level, as shown in Figure 5-11.

The stiffening parameter (t) is normalized by plotting the parameter with the normalized shear stress (τ/τ_{max}) as demonstrated in Figure 5-12. This relationship produced a good fit for all tested samples with a coefficient of determination of R^2=0.988 as follows:

$$t = 0.822\left(\frac{\tau}{\tau_{max}}\right)^2 - 0.11\frac{\tau}{\tau_{max}} - 0.024 \qquad \text{Equation 5-3}$$

Equation 5-1 and Equation 5-3 can estimate the dynamic shear modulus of dry Danube sand after any number of cycles and at any shear stress level during a torsional simple shear test.

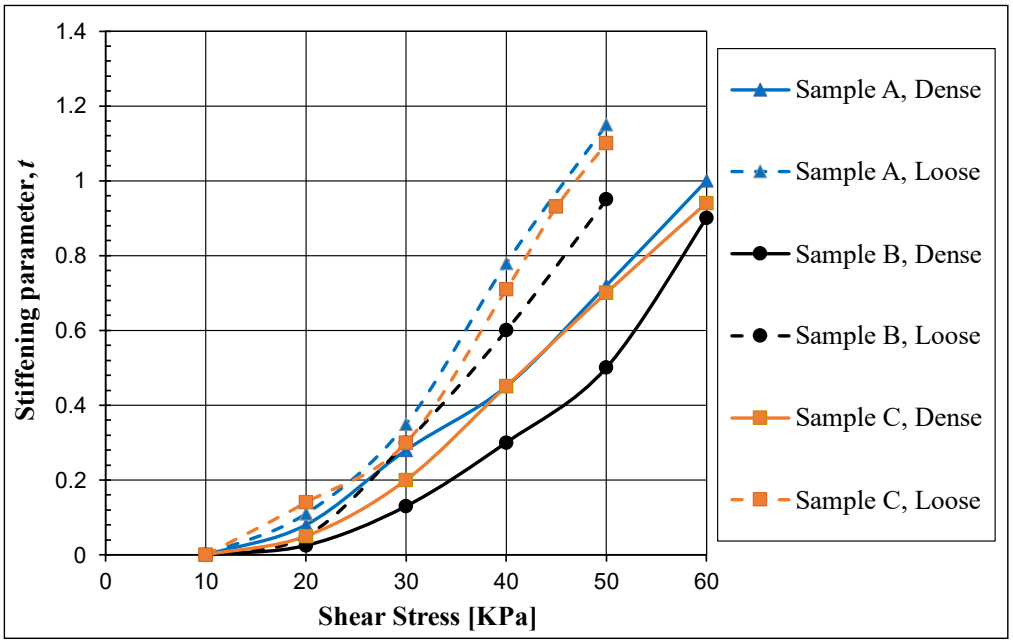

Figure 5-11 The increase in the stiffening parameter (t) with the increasing stress level.

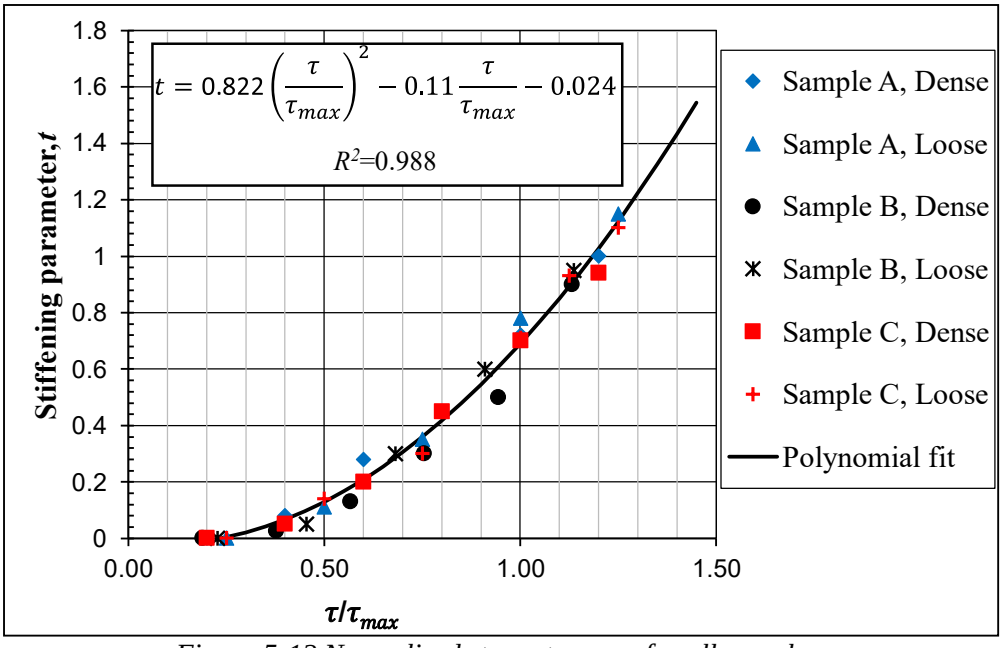

Figure 5-12 Normalized stress-t curves for all samples.

The RC-TOSS device allows for cyclic loading with loading offset. For example, a TOSS test with 30 KPa cyclic loading may include an offset stress of 10 KPa. The peak stresses of the cyclic loading in that case will be -20 KPa and 40 KPa. On the other hand, if the offset is -10, the peaks will be -40 KPa and 20 KPa. This feature allowed us to study whether stiffening behavior relates only to the peak-to-peak stress amplitude or depends on the maximum stress or strain level.

The main findings were that the cyclic loading at every peak-to-peak stress level would gradually increase G_{sec} until it reached a specific maximum value. It could not exceed that value regardless of the applied offset or the location of the loop on the strain axis. In other words, every peak-to-peak stress level has a maximum stiffening index (δ_G) no matter the number of cycles or the maximum strain amplitude. This observation provides valuable insight later in this chapter for modeling behavior with the Ramberg-Osgood model.

5.5 Damping ratio curves

5.5.1 Comparison between the three methods

The six RC tests provided a total of 115 damping measurements. This allowed for comparison with 54 data points from the TOSS test (Ahmad & Ray, 2023). Typical response curves for the SSV method appear in Figure 5-13 and Figure 5-14 for ascending strain levels. At higher strain amplitudes (above 0.1%), dynamic instability prevented precise response data from being recorded by the multimeter. For the FVD method, however, very small strain levels inhibited accurate damping measurements, and relatively accurate decay-response curves required several attempts. During the disconnection from drive coils, an electric pulse often produces a strong transient. This pulse creates noise that distorts the readings of the most critical first few cycles since damping is calculated from the first three cycles before strain levels decrease substantially. This noise did not affect the response at strain amplitudes higher than 0.005%, and the peaks could be spotted easily for the first few cycles.

Figure 5-15 compares the damping ratio measurements of the three methods. The SSV method generally provides higher damping values than the FVD method, especially at higher strain levels. At the same time, there is a closer agreement between the two methods at medium strain amplitudes (0.005%-0.03%). At higher strain amplitudes, the frequency-response curve becomes asymmetric, compromising the accuracy of the damping ratio calculations in the SSV method and causing an overestimation of their values. Such behavior also occurs

when comparing with the TOSS tests, as damping values obtained from the TOSS tests agree more with the FVD method in the RC test at the strain levels where the SSV method is questionable.

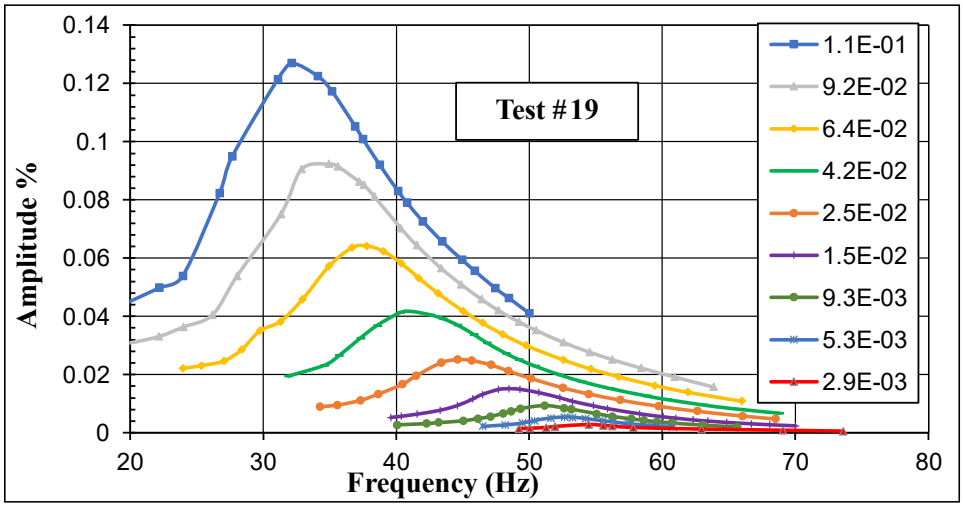

Figure 5-13 Response curves in the RC test for Sample C, loose.

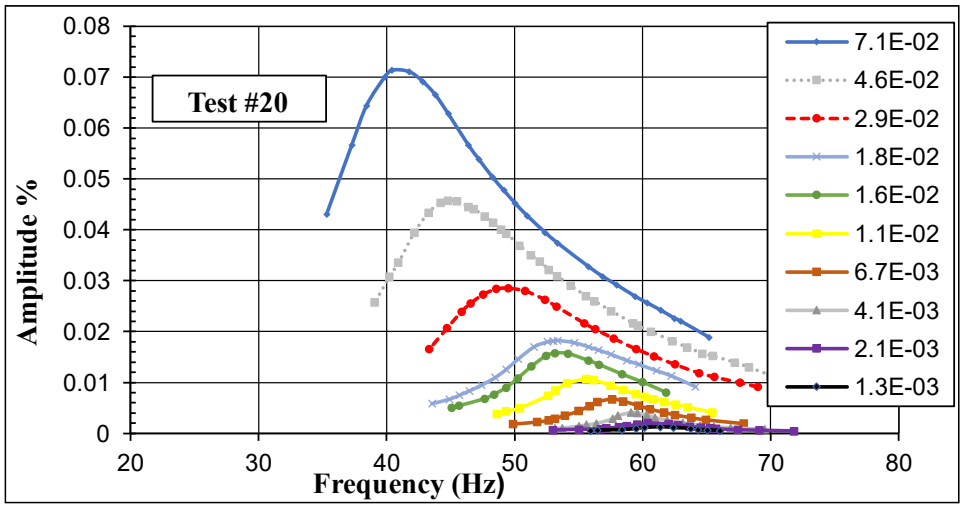

Figure 5-14 Response curves in the RC test for Sample C, dense.

Due to the nature of the TOSS test measurements and insufficient accuracy of the proximitors at very small strain amplitudes, comparisons between the RC and TOSS tests become difficult at strain levels below 0.02%. However, the two tests are in agreement, and their combined response can generate damping ratio curves for a wide range of strains.

Multiple effects and uncertainties cause the scatter seen in the damping measurements. The sources of variability include the decreasing strain amplitude with time (FVD), response curve asymmetry (SSV), and the number of cycles and stiffening behavior in the TOSS test. Such effects cause difficulties when comparing the damping ratio obtained from different methods. As a result, they produce a scatter that may exceed 40% in the data when comparing the SSV and FVD methods, as seen in Figure 5-16.

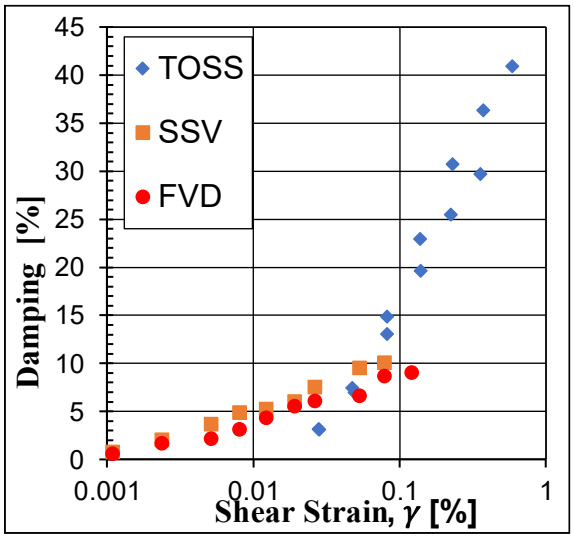

(a) Sample A, loose.

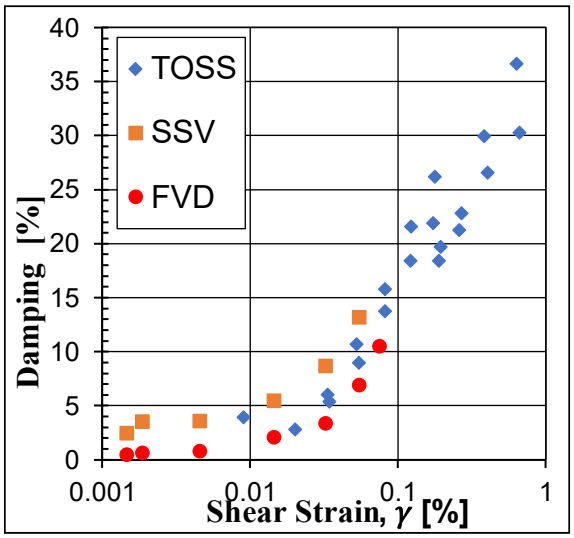

(b) Sample A, dense.

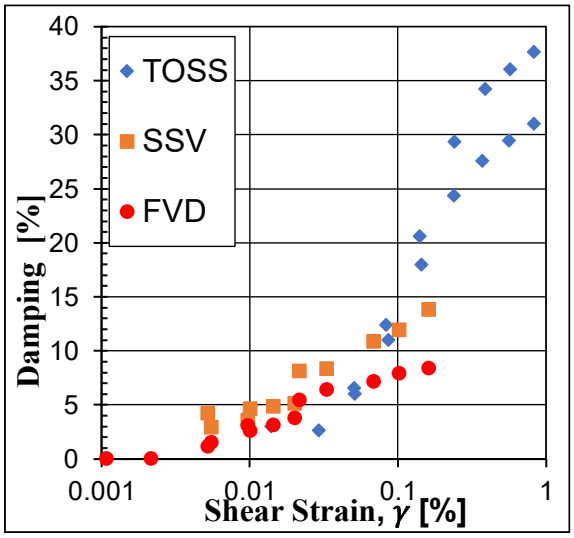

(c) Sample B, loose.

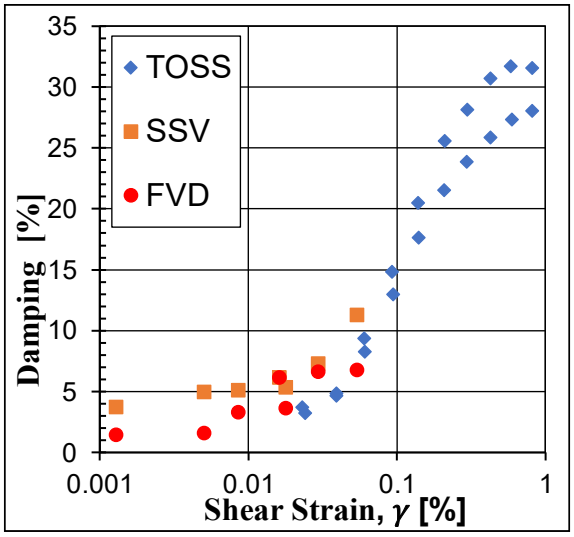

(d) Sample B, dense.

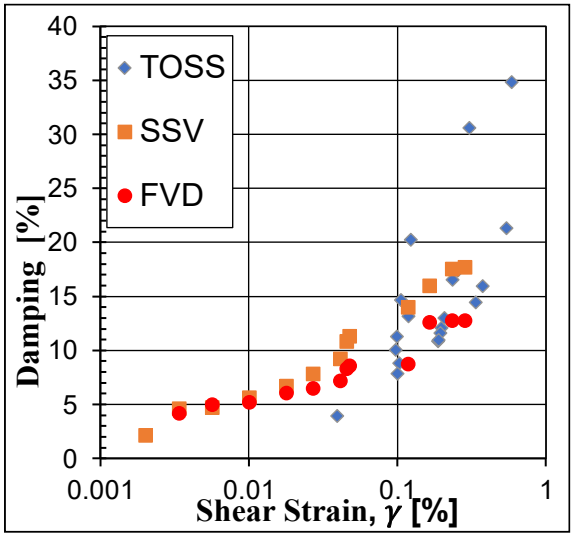

(e) Sample C, loose.

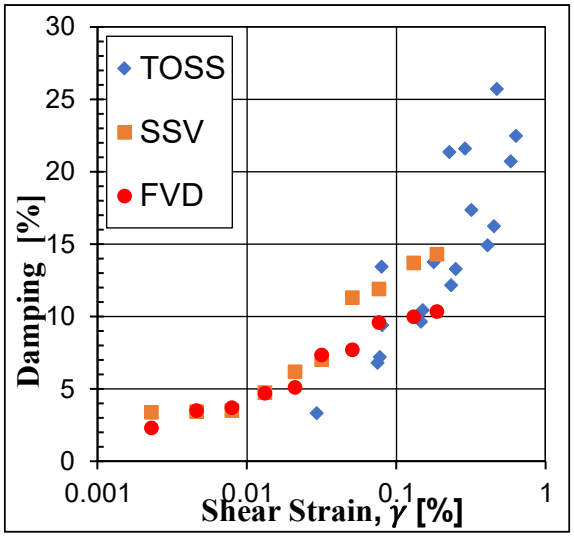

(f) Sample C, dense.

Figure 5-15 Damping results of the six tests with the three methods of calculation.

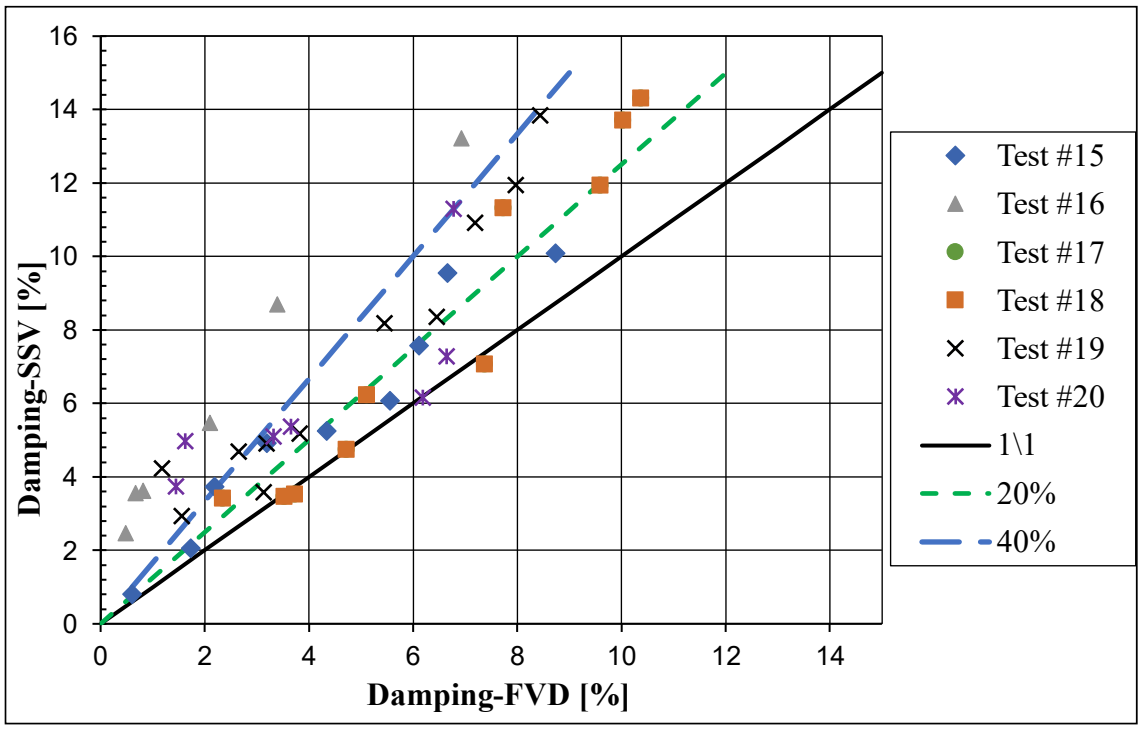

Figure 5-16 Comparison of damping between SSV and FVD for all the tests.

The best fit for all the damping ratio data points from the six tests using the three methods appears in Figure 5-17, along with a comparison with two earlier studies (Vucetic & Dobry, 1991) and (Darendeli, 2001) on dry sand.

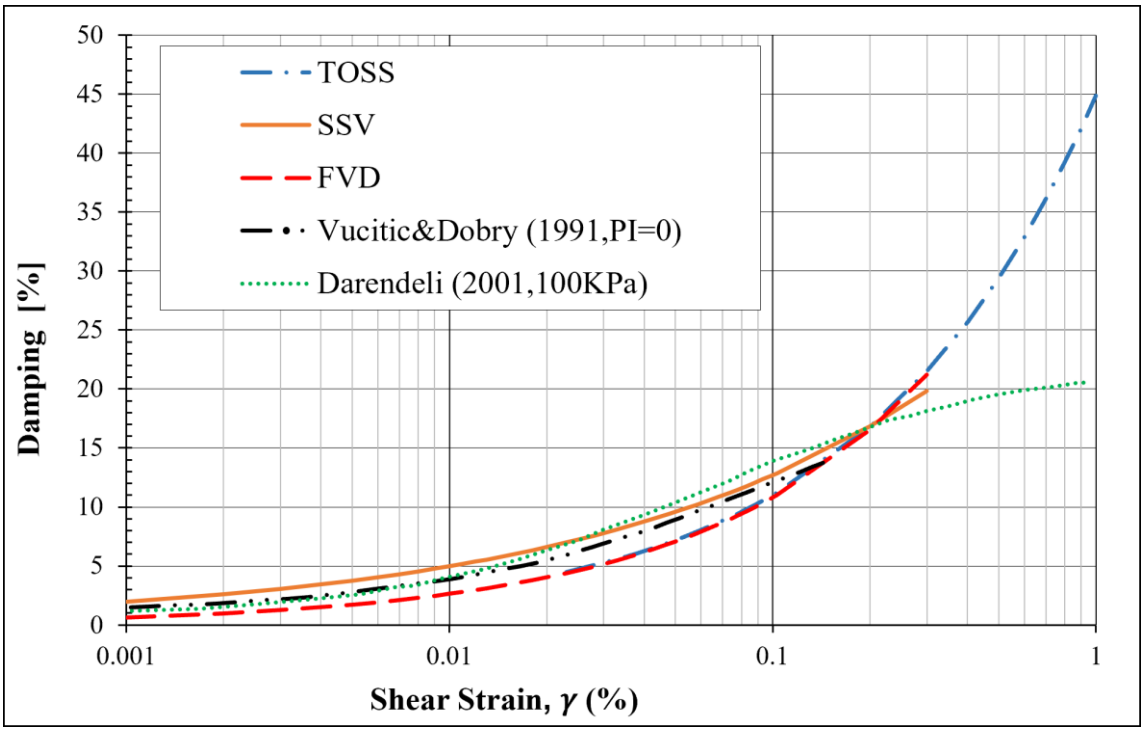

Figure 5-17 A fit of all damping data points.

5.5.2 Damping ratio correlations

To estimate the damping ratio with correlations, it is common practice to relate it with the normalized shear modulus using a second-degree polynomial of (G/G_{max}). The modified hyperbolic model based on the Hardin–Drnevich model provides an excellent presentation of the modulus-reduction curve. This model employs two curve-fitting parameters:

$$\frac{G}{G_{\max}} = \frac{1}{1 + \left(\frac{\gamma}{\gamma_r}\right)^m} \qquad \text{Equation 5-4}$$

The reference shear strain γ_r in this model is defined as the strain amplitude when the shear modulus reduces to one-half of G_{max}. The fit for all the samples is shown in Figure 5-18a for γ_r= 0.1 and m = 0.974.

After finding the correlation for the shear-modulus-degradation curve, the following equation models the damping ratio increase with increasing strain amplitude:

$$D = C_1\left(\frac{G}{G_{\max}}\right)^2 + C_2\left(\frac{G}{G_{\max}}\right) + C_3 \qquad \text{Equation 5-5}$$

where C_1, C_2, and C_3 are curve-fitting constants. The constants are found using the least square method, by minimizing the summation of the squared errors between the equation and the lab measurements. For the damping ratio measurement in this study for all tested samples, the equation becomes:

$$D = 8.5\left(\frac{G}{G_{\max}}\right)^2 - 40\left(\frac{G}{G_{\max}}\right) + 33 \qquad \text{Equation 5-6}$$

Figure 5-18b demonstrates how the equation fits the RC-TOSS damping measurements.

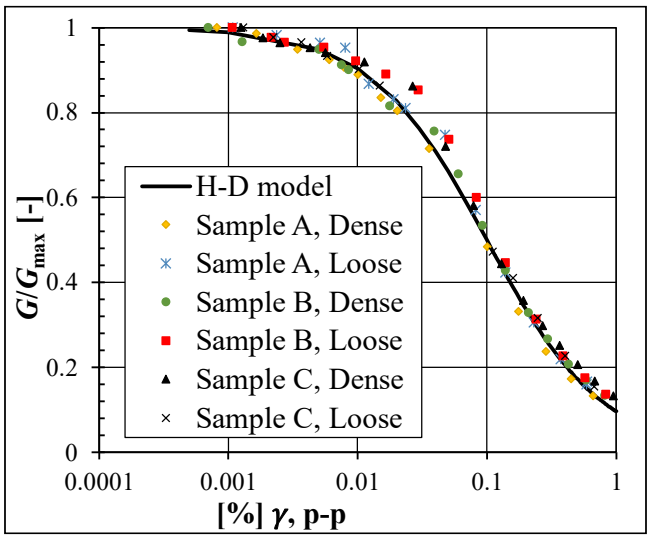

(a) Shear modulus.

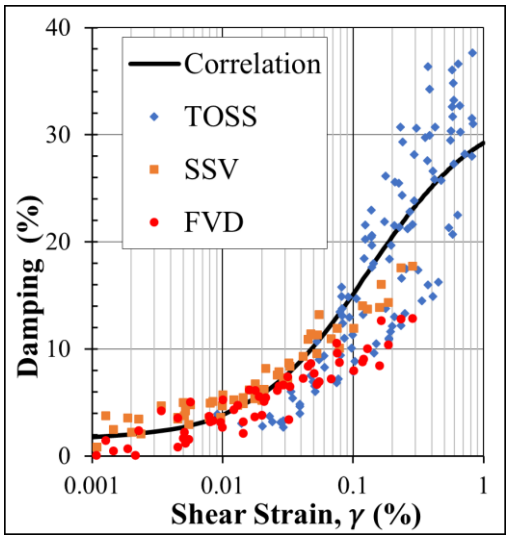

(b) Damping ratio

Figure 5-18 Shear modulus and damping ratio correlations fit with test data.

5.5.3 Effect of torsional cyclic loading on damping

As shown earlier, the area of the hysteresis loop decreases with the increasing number of cycles leading to a decrease in the damping ratio. It is difficult to estimate the rate of change for each stress level due to the sequence of the TOSS test and cyclic loading that the sample has experienced at lower stress levels. However, the higher the stress level, the higher the effect of (N) on damping up to a specific limit. Beyond this, the stress level seems to have a minor influence on the rate of decrease in the damping ratio. Specimens with a higher void ratio or lower relative density exhibit a more significant reduction in damping ratio. For instance, at stress levels of 20 KPa and 30 KPa, the damping ratio decreased by 50% and 54% after 100 cycles for a dense sample, while a loose sample decreased by 61% and 64% (Figure 5-19). D_N is the damping ratio calculated from a cyclic TOSS test at the N^{th} cycle, and D_1 is the damping ratio of the first cycle (maximum damping ratio at that stress level). Results show that $\log(D_N/D_1)$ is linearly proportional to $\log(N)$, and the slope of $\log(D_N/D_1)$-$\log(N)$ plot represents a parameter (r) that describes the rate of decrease in damping ratio with the number of cycles.

$$r = \frac{\log(D_N/D_1)}{\log(N)} \qquad \text{Equation 5-7}$$

The values of the parameter (r) also vary in a manner similar to damping ratio measurements, and it is difficult to find a pattern in the change in (r) with the increasing strain amplitude. Generally, (r) takes values between (-0.19 and -0.24) for strain amplitudes above 0.1%.

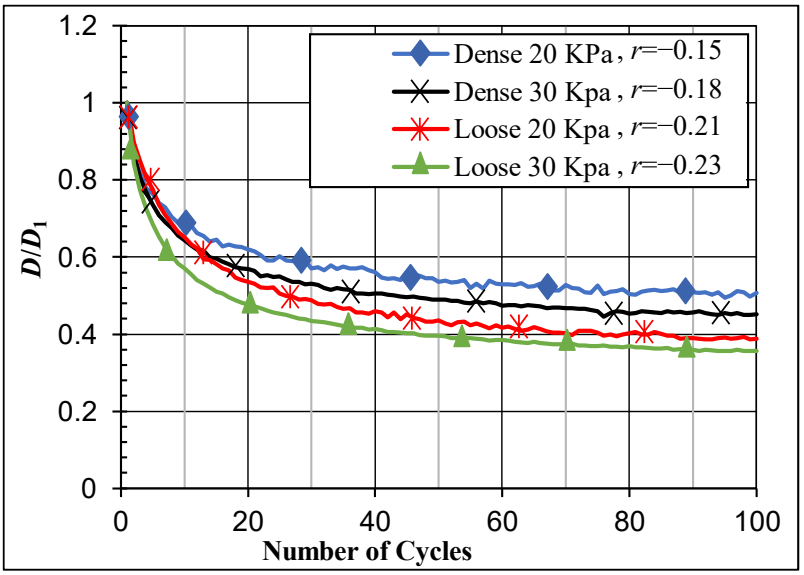

Figure 5-19 The rate of decrease in damping during cyclic loading for Sample C.

5.6 Modeling the stiffening behavior in the RO model

5.6.1 Modifications to the second Masing criterion

The second Masing criteria states that "the shape of the unloading and reloading curve is equal to the initial loading curve, except that its scale increases by a factor of two in both directions". Ignoring the impact of the stiffening behavior, the rule may be correct. However, as previously observed, applying cyclic loading causes a significant change in the size of the hysteresis loops. Some previous researchers suggested changing the scale (2) in soil models (R-O or H-D) to fit with the tests result (Idriss, et al., 1978), (Lin & Chen, 1991), and (Lo Presti, et al., 2000). Although this technique provides an improved estimate to the problem, it did not match the test outcomes in this investigation when employing the soil models, especially after a high number of cycles. The best fit resulted from custom-made VBA subroutines combining the RO model with the lab output for every separate loop in a cyclic TOSS test. We found that the curve fitting constants obtained for the backbone curve should be modified for the unloading-reloading curves for a better fit. While the value of α remained constant throughout the analysis, R and C were reduced for the unloading-reloading curves to better fit the reduced curvature observed for such curves, as demonstrated in Figure 5-20.

Furthermore, by decreasing (R) after every load reversal during cyclic tests and keeping constant values of α and C in the two-way RO equation, the stiffening behavior of the sample was captured with a better fit of the data, compared to changing the scale factor (2 in the second Masing criterion). When applying the RO model with constant curve fitting parameters for simulating the cyclic loading, the loops will always return to the same point on the shear stress-shear strain curve. However, by slightly decreasing the value of (R) after each half-cycle, the loops will start drifting from the first cycle following the stiffening behavior.

VBA codes implemented the least squares method in Excel to find the optimum value of (R) that best fits the RO model to the lab curves for each half-cycle in the shear stress-strain plot, as shown in Figure 5-21. The change of R with the number of cycles at different stress levels for Sample C, dense state is shown in Figure 5-22.

For each stress level, we can consider a parameter δ_R that represents the ratio of the curvature coefficient (R) of the n^{th} half-cycle to the curvature coefficient of the first undegraded loop (R_1) at the same stress level.

$$\delta_R = \frac{R_n}{R_1} = n^{-b} \qquad \text{Equation 5-8}$$

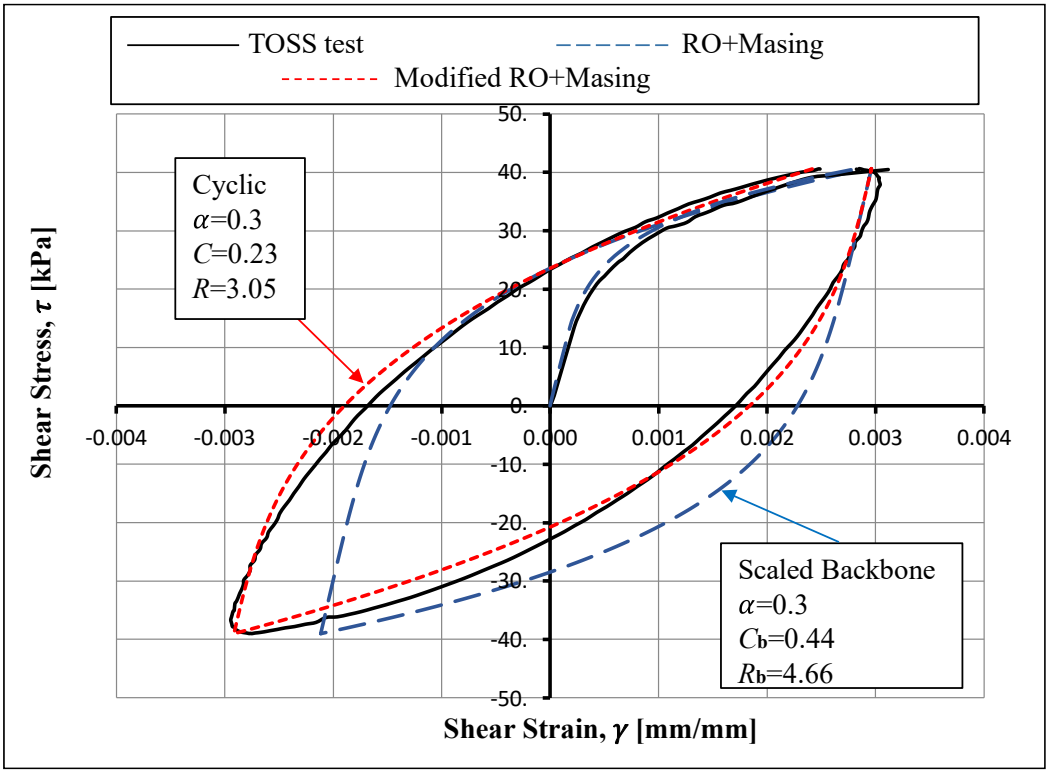

Figure 5-20 Comparison between the Masing criteria and the suggested modification for Sample B, loose, at 40 KPa, first cycle.

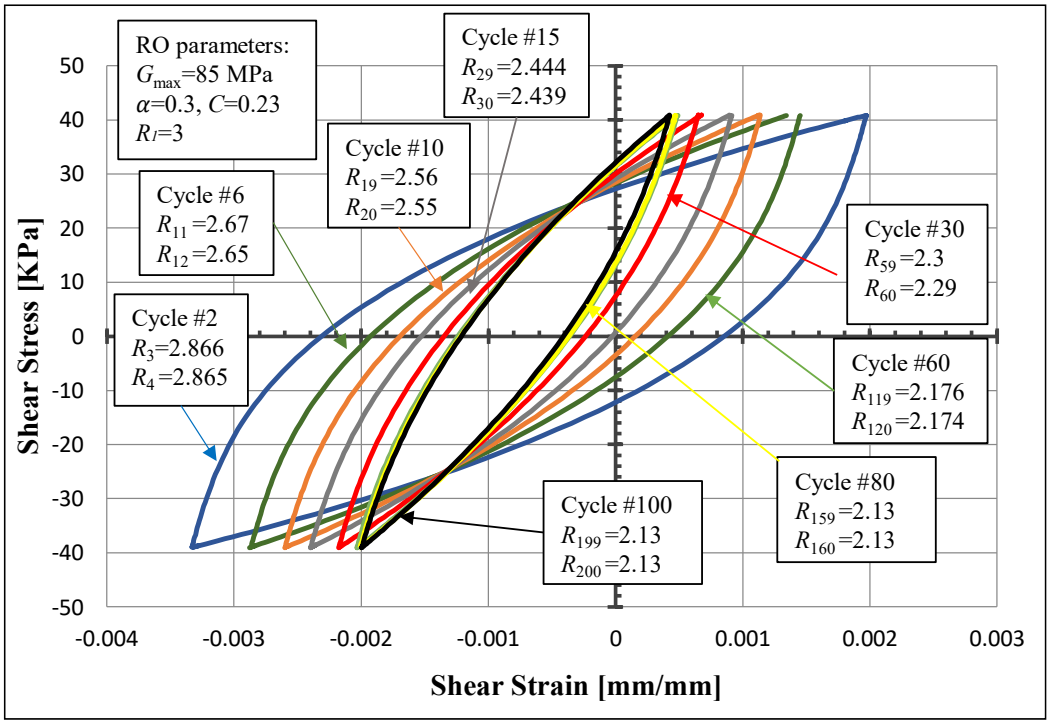

Figure 5-21 Stiffening behavior using the RO equation for Sample A, loose at 40 KPa cyclic TOSS test.

The values of R_I increased with the increasing stress level after exceeding the volumetric shear strain threshold (γ_{tv}). By conducting stress-controlled tests, we determined the relationship between the shear stress and curvature coefficient for each sample's first unloading

curve (R_1) (Figure 5-23). The relationship has a power form ($R_1 = a' * \tau^{b'}$) as shown in Table 9. Moreover, the relationship between R_1 and the shear strains can be found at any point based on the known backbone curve from the RO model (Equation 2-24). This relationship depends on the soil type and void ratio, which can be obtained separately for each test using regression analysis.

In Equation 5-8, (b) is the slope of the log(δ_R)-log(n) plot. Practically, b describes the negative slope of the relationship:

$$b = -\frac{\log(\delta_R)}{\log(n)} \qquad \text{Equation 5-9}$$

For samples A and B with very low percentages of fines, the curvature degradation parameter (b) is constant throughout the test. On the other hand, for Sample C with a fines content around 20%, the value of (b) followed the changes in cyclic loading stress level, as shown in Figure 5-24. Below the shear strain volumetric threshold (γ_{tv}), $\delta_R = 1$ where the stiffening behavior is insignificant and b=0 up to that point. Even though the value of (b) varies with the shear stress for Sample C, it does not substantially affect stiffening behavior. Setting b= *average constant* throughout the test would still yield a good approximation to the problem.

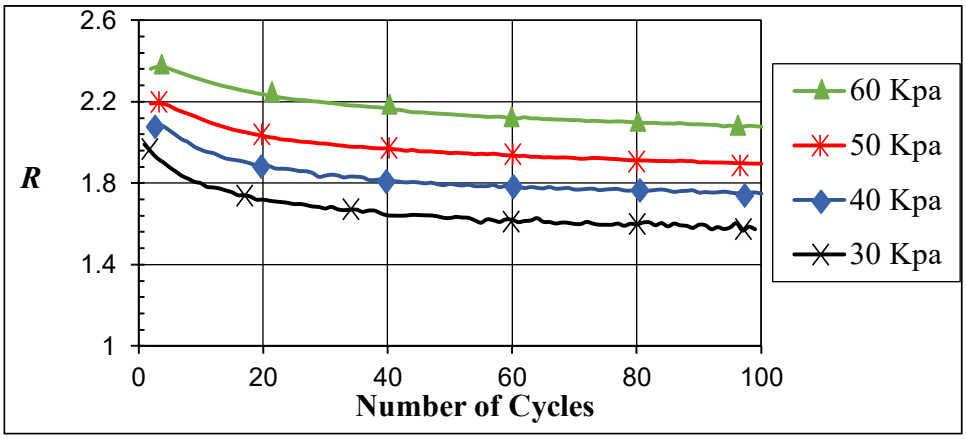

Figure 5-22 Change of R with the number of cycles at different stress levels for Sample C, dense state.

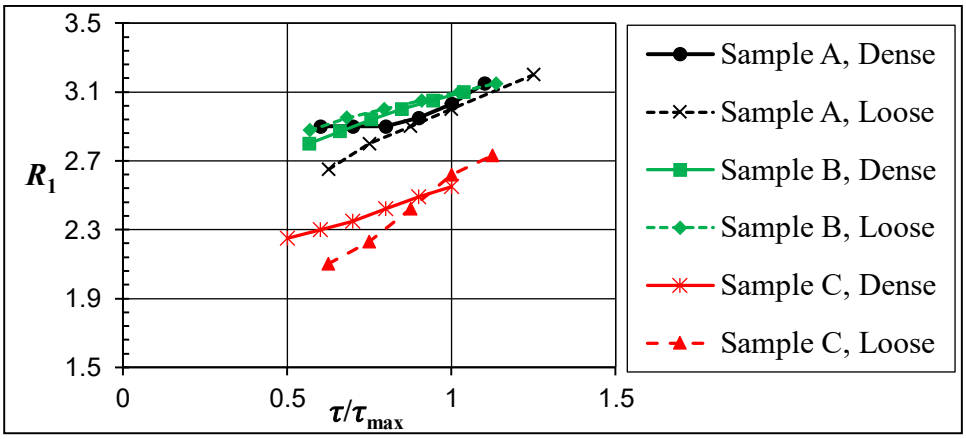

Figure 5-23 Stress normalized R_1 curves for all samples.

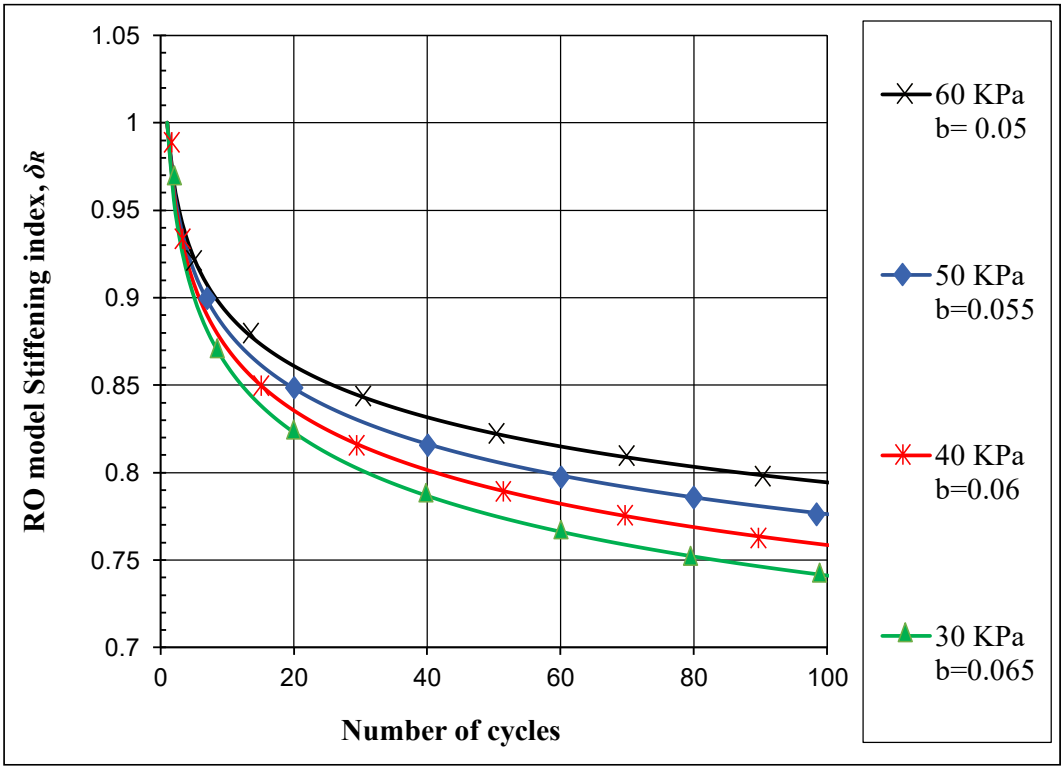

Figure 5-24 Change in RO model stiffening index (δ_R) with the number of cycles at each stress level for Sample C, Dense.

Table 9 Two-way RO model parameters for cyclic loading.

Test number	**Sample ID**	**Max shear modulus**	**Max shear stress**	α	C	R_1 *	b **
#		G_{max} [MPa]	τ_{max} [KPa]	[-]	[-]	[-]	[-]
1	A	85	40	0.3	0.23	$1.12\tau^{0.256}$	0.06
2	A	103.4	50	0.3	0.23	$1.123\tau^{0.267}$	0.06
3	B	79.6	44	0.3	0.23	$1.548\tau^{0.174}$	0.04
4	B	100	53	0.3	0.23	$1.9\tau^{0.128}$	0.055
5	C	76	40	0.3	0.15	$1.135\tau^{0.206}$	$0.08 - 0.0005\tau$
6	C	87	50	0.3	0.15	$0.463\tau^{0.467}$	0.045 for $\tau < 35$ KPa 0.06 for $\tau \geq 35$ KPa

* $\boldsymbol{\tau}$ in R_1 equations is the maximum single amplitude shear stress reached in the test in any direction.

**b=0 when $\boldsymbol{\tau < 20}$ for loose samples and when $\boldsymbol{\tau < 25}$ for dense samples.

5.6.2 Modifications to the third Masing criterion

Simulating the stiffening behavior of cyclically loaded samples leads to further complications in the Masing criteria. The third Masing criterion asserts that the unloading and reloading curves should follow the initial curve when it exceeds the previous maximum shear strain. We can apply the third rule to the maximum shear stress instead of strain in our stress-controlled tests. However, due to increased stiffness, the TOSS test results showed a considerable drift from the backbone curve during cyclic loading. In Figure 5-25, after 100 cycles of 40 KPa, we increased the shear stress to 50 KPa. If the third Masing criterion was followed, then after exceeding 40 KPa (point a), the curve would take path (A), However, this does not concur with the test results. We re-evaluated all the reloading curves after a cyclic TOSS test to overcome this problem. Based on the data, a modification to the two-way RO equation is presented. In Equation 2-33, "α" is replaced by R_1, and R is reduced to (R/1.3). The "turning point" (τ_i, γ_i) is considered as the point where the previous maximum shear stress is exceeded (point a in Figure 5-25). The curve (ab) will follow this modified equation:

$$\gamma = \frac{\tau - \tau_i}{G_{\max}}\left[1 + R_1\left|\frac{\tau - \tau_i}{2C'\tau_{\max}}\right|^{\frac{R}{1.3}-1}\right] + \gamma_i \qquad \text{Equation 5-10}$$

Where C' is a parameter that decreases with the increasing maximum reached shear stress in the test. The relationship between C' and the maximum reached shear stress can be calculated by isolating C' from Equation 5-10 and setting (τ_{m},γ_{m}) as the last measured point on the backbone curve before leveling off (point ($\tau_{\max}, \gamma_{\mathrm{m}}$) in Figure 5-4). This curve will aim to reach this point when the turning point is still on the backbone curve. Then C' is calculated for each point on the backbone curve presented as (τ_i, γ_i) in the following equation:

$$C' = \frac{\tau_{\mathrm{m}} - \tau_i}{2\tau_{\max}} * \left[\frac{\frac{G_{\max}(\gamma_{\mathrm{m}} - \gamma_i)}{|\tau_{\mathrm{m}} - \tau_i|} - 1}{R_1}\right]^{-\frac{1}{\frac{R}{1.3}-1}} \qquad \text{Equation 5-11}$$

Using Equation 5-10, after exceeding the shear stress of 40 KPa in the example given in (Figure 5-25), the curve will follow path B. The new path closely agrees with testing data. The dependency on the number of loops previously applied will be reflected on the curve by the curvature parameter (R) decrease in the equation. C' cannot have negative values. Moreover, whenever the shear stress while modeling using this method exceeds $\tau_{\max}$, C' will keep a constant positive value that is close to 0. The change in the parameter C' with the increasing maximum previously reached shear stress is shown in Figure 5-26.

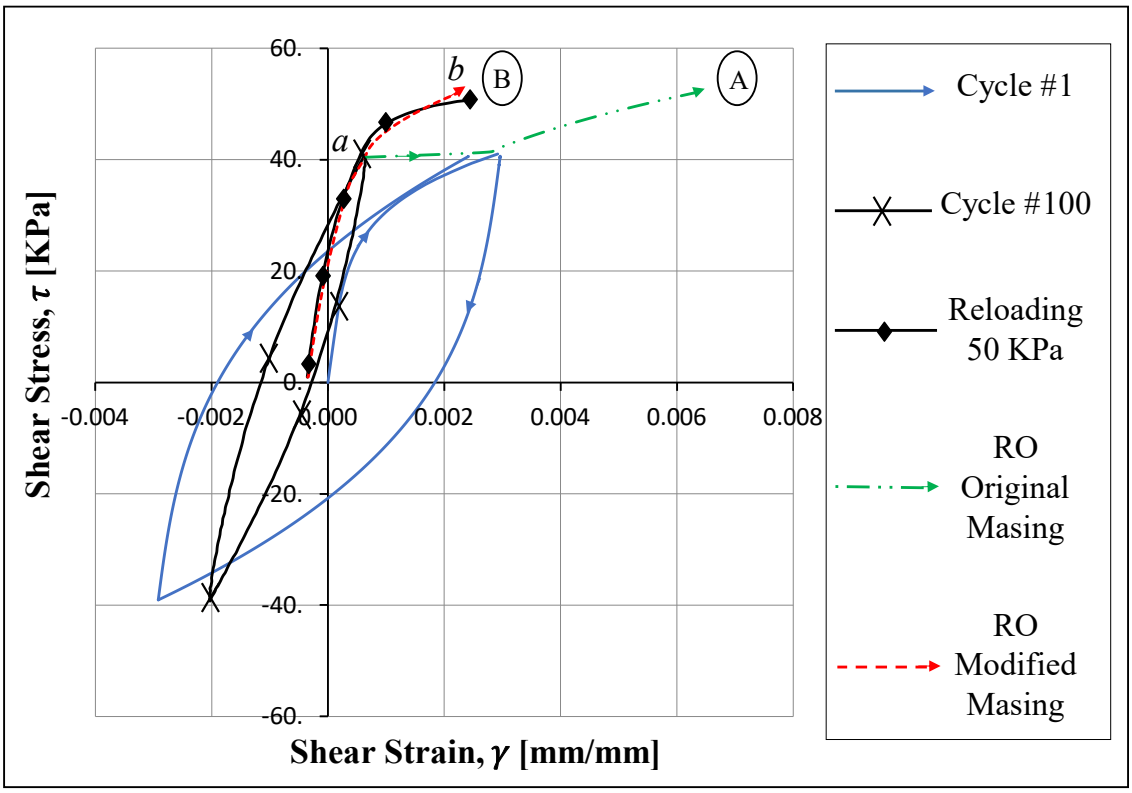

Figure 5-25 Modification to the third extended Masing criterion in RO model.

5.6.3 Previous cyclic loading effect

The stiffness of the cyclically loaded sample at any stress amplitude is affected by previous cyclic loading at a lower stress level as long as it is above the volumetric threshold. As shown in Figure 5-27, the stiffness at stress level 40 KPa increased by 55% compared to the backbone curve due to the previous 100 cycles applied at 30 KPa for a loose sample. Previous cycling also decreased the curvature parameter (R) from 3.05 to 2.8. It is challenging to study the effect of the number of previously applied cycles at lower stress levels on the stiffness because of the long time and high effort required for sample preparation and testing using the RC-TOSS device. However, here is a method to find the curvature parameter R in the RO equation based on an equivalent number of half-cycles (n_{eq}). The equivalent number of half-cycles (load reversals) depends on the peak strain amplitude when the unloading starts at a higher stress level than the previous cycle ($\gamma_n$in Figure 5-27). This method allows the prediction of the shear stress-strain curve, hence the stiffness of the sample.

After obtaining R_1 and b at each stress level for a sample, we can calculate the peak strain amplitude of each cycle from 1 to 100. By considering the strain amplitude on the backbone curve as the peak strain of the first half-cycle (γ_1), we can find a parameter δ_γ that represents the ratio of peak strain amplitude (γ) of the n^{th} half-cycle to the peak strain amplitude of the first half-cycle (γ_1) at the same stress level:

$$\delta_\gamma = \frac{\gamma_n}{\gamma_1} = n^{-k} \qquad \text{Equation 5-12}$$

The parameter (k) is the slope of the $\log(\delta_\gamma)$-$\log(n)$ plot that represents the change of the peak strain amplitude with the number of load reversals. k increases with the increasing stress level, as shown in Table 10. Note that k keeps a constant maximum value when the stress level exceeds $\tau_{\max}$.

After any sequence of cyclic loading, and when exceeding the previously reached maximum shear stress, the strain amplitude will result from Equation 5-10 before the start of the next unloading phase (curve ab in Figure 5-25) . From the strain where the unloading begins, an equivalent number of load reversals (n_{eq}) at that stress level can be calculated from the following equation:

$$n_{eq} = 10^{\frac{\log(\delta_\gamma)}{-k}} \qquad \text{Equation 5-13}$$

For instance, in a loose sample A, 100 cycles at a stress level 30 KPa were equivalent to 42 cycles at a stress level 40 KPa. The equivalent number of load reversals (half-cycles) in that case is n_{eq}=84. The curvature parameter R_n that corresponds to the calculated equivalent number of load reversals at that stress level is calculated as follows:

$$R_n = R_1 * {n_{eq}}^{-b} \qquad \text{Equation 5-14}$$

Subsequently, the cyclic loading will be restarted with $n=n_{eq}$ and the curvature coefficient $R=R_n$, will continue to diminish with the rising number of load reversals.

Table 10 Change of the parameter k with the shear stress for all samples.

Test number	**Sample ID**	**Maximum shear modulus**	**Maximum shear stress**	***k* ***
#		$G_{\max}$ [MPa]	$\tau_{\max}$ [KPa]	[-]
1	A	85	40	$0.0308e^{0.039\tau}$
2	A	103.4	50	$0.0231e^{0.052\tau}$
3	B	79.6	44	$0.001\tau + 0.13$
4	B	100	53	$0.003\tau + 0.13$
5	C	76	40	$0.0488e^{0.035\tau}$
6	C	87	50	$0.002e^{0.125\tau}$

*τ is the maximum single amplitude shear stress reached in the test in any direction.
k becomes constant when exceeding the maximum sheaar stress $\tau_{\max}$.

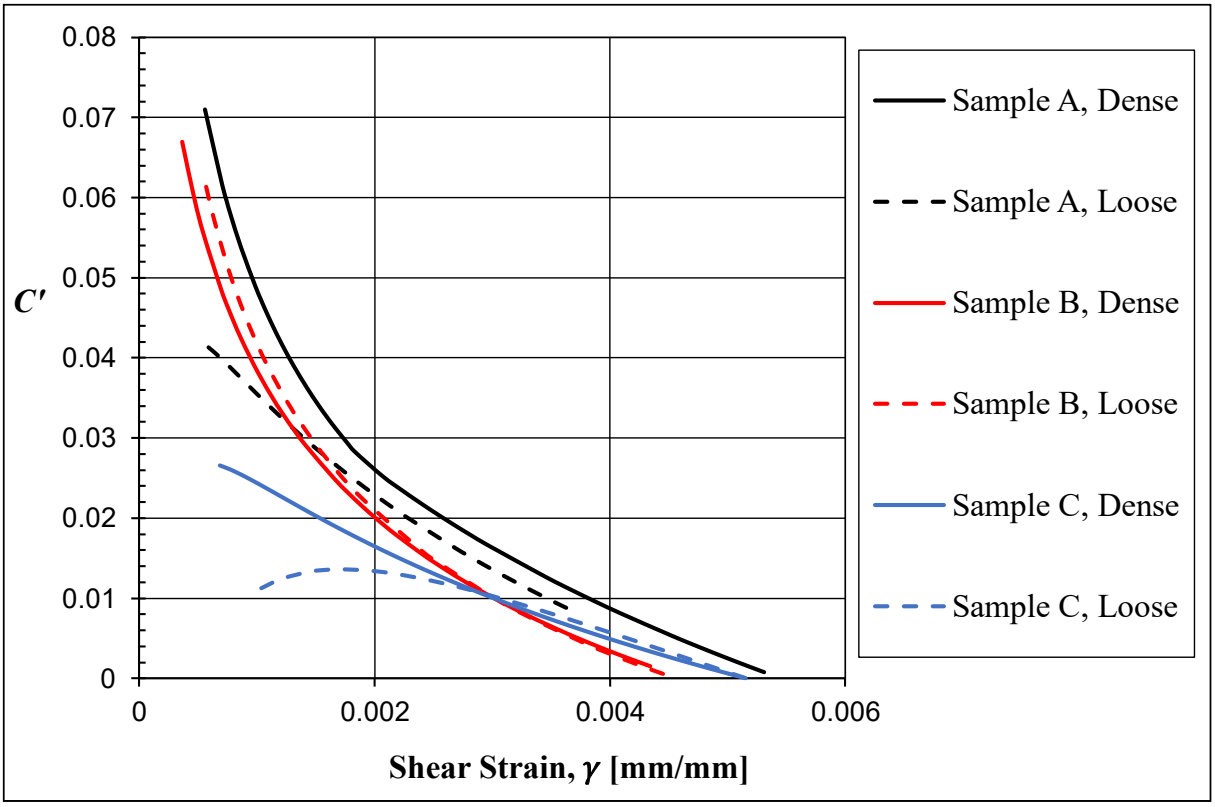

Figure 5-26 The change in the parameter C' with the increasing maximum previously reached shear stress.

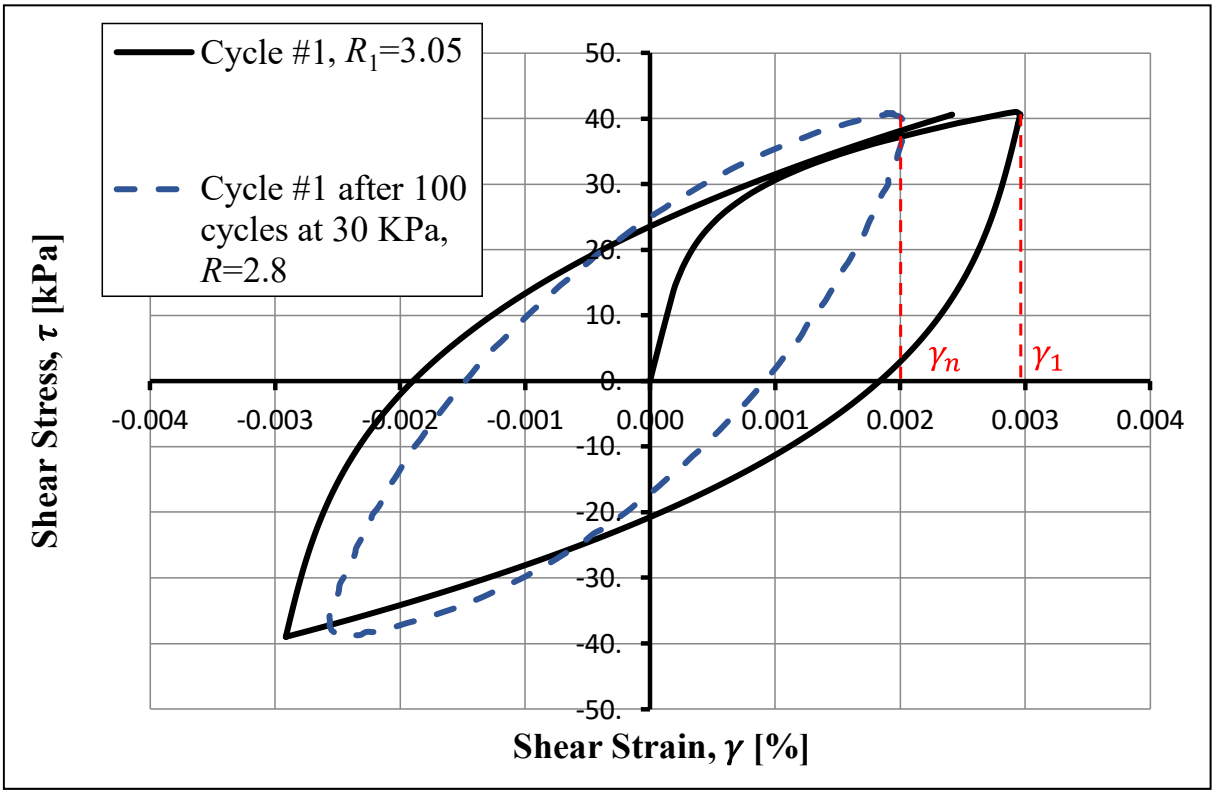

Figure 5-27 Effect of previous cyclic loading.

5.7 Modelling the stiffening behavior in HD model

The modified Hardin-Drnevich equation contains only two curve-fitting constants (γ_r, m), making it more straightforward than the Ramberg-Osgood model to simulate the behavior, especially since these parameters can be considered constant regardless of the shear strain amplitude with reasonable accuracy. The curve fitting between the TOSS test results and Equation 5-15 followed the same method described before using Excel Solver (the least square method)..

$$\tau = \frac{G_{\max(}\gamma - \gamma_i)}{1 + \left|\frac{\gamma - \gamma_i}{2\gamma_r}\right|^m} + \tau_i \qquad \text{Equation 5-15}$$

Similar to the RO model, and due to the problem discussed and shown in Figure 5-20, the parameter γ_{r_b} for the backbone curve can be higher than γ_r for the unloading-reloading curves. In order to simulate the stiffening behavior, γ_r increases with the increasing number of half-cycles (*n*) while *m* remains constant throughout the analysis.

The modified HD model calculates the stresses based on the given strain history; therefore, to study the stiffening behavior, this model is more conveniently calibrated using a strain-controlled test. However, since our device is only capable of conducting stress-controlled tests and we found that the HD model's parameters can be considered independent of the strain/stress amplitude (unlike the RO model), we can find the rate of increase in γ_r using a stress-controlled test by adjusting γ_{r_n} for each half-cycle to match the TOSS test results based on the measured shear strains.

For each stress level, we can consider a parameter δ_{γ_r} that represents the ratio of the parameter (γ_r) of the n^{th} half-cycle, to the curvature coefficient of the first half-cycle (γ_{r_1}) at the same stress level.

$$\delta_{\gamma_r} = \frac{\gamma_{r_n}}{\gamma_{r_1}} = n^f \qquad \text{Equation 5-16}$$

Where *f* is the slope of the log(δ_{γ_r})-log(*n*) plot. Practically *f* describes the slope of the relationship:

$$f = \frac{\log(\delta_{\gamma_r})}{\log(n)} \qquad \text{Equation 5-17}$$

The Hardin-Drnevich curve fitting constants and the calculated stiffening parameter *f* for all the samples are shown in Table 11. A cyclic strain-controlled test result based on the HD model considering the stiffening behavior using the parameters for Soil A in a dense state appears in Figure 5-28.

The same limitation to the third Masing criterion in the RO model described in the previous section applies to the HD model and a different equation is necessary when exceeding the previously reached maximum shear strain, as shown in Figure 5-29. The curve cannot follow the backbone curve (path A) due to stiffening behavior and higher stress levels at the same strain amplitude, instead, it should follow path B.

Figure 5-29 shows a cyclic strain-controlled test. After exceeding the maximum previously reached strain amplitude, the curve (ab) can follow the same two-way HD equation by introducing a factor (ω) that reduces G_{max} and with considering the turning point (τ_i, γ_i) to be the point where the previous maximum shear strain is exceeded (point a). Therefore, the curve in path B follows:

$$\tau = \frac{\omega G_{0(}\gamma - \gamma_i)}{1 + \left|\frac{\gamma - \gamma_i}{2\gamma_r}\right|^m} - \tau_i \qquad \text{Equation 5-18}$$

Where ω can be calculated for any strain amplitude from the backbone curve as follows:

$$\omega = \frac{(\tau_m - \tau_i) * (1 + \left|\frac{\gamma_m - \gamma_i}{2\gamma_r}\right|^m)}{G_0(\gamma_m - \gamma_i)} \qquad \text{Equation 5-19}$$

Where (τ_m, γ_m) is the last measured point on the backbone curve before leveling off (point (τ_{max}, γ_m) in Figure 5-4), which is the point that the curve will aim to reach when the turning point is still on the backbone curve. This parameter can be found from the previously calibrated curve fitting constants, and no extra curve fitting or calibrations are needed.

The same method proposed for the RO model can be exploited to find the curvature parameter γ_r in the HD equation based on an equivalent number of half-cycles that depends on the maximum stress amplitude after any previously applied cyclic loading.

After obtaining γ_{r_1} and f for each strain level in a specimen, we can find the peak stress amplitude for cycle 1 to 100 (τ_1 *to* τ_{200} in Figure 5-28). By considering the peak stress amplitude on the backbone curve as the peak stress of the first half-cycle (τ_1). We can find a parameter δ_τ that represents the ratio of peak stress amplitude of the nth half-cycle (τ_n), to the stress amplitude of the first half-cycle (τ_1) at the same strain level:

$$\delta_\tau = \frac{\tau_n}{\tau_1} = n^s \qquad \text{Equation 5-20}$$

The parameter (s) is the slope of the log(δ_τ)-log(n) plot that represents the change of the peak stress amplitude with the number of half-cycles. s increases with the increasing strain

level, as shown in Table 11. Note that s keeps a constant maximum value when the stress level exceeds τ_{max}.

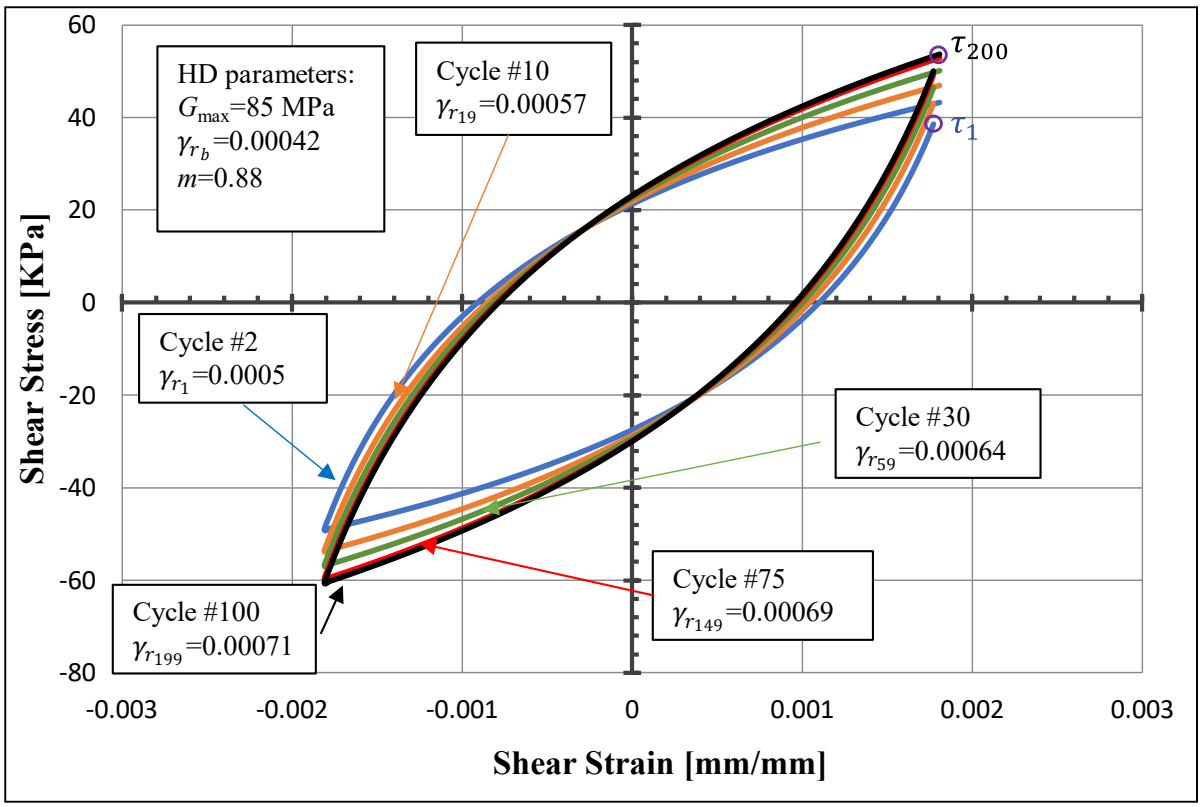

Figure 5-28 HD model stiffening behavior for a strain-controlled test.

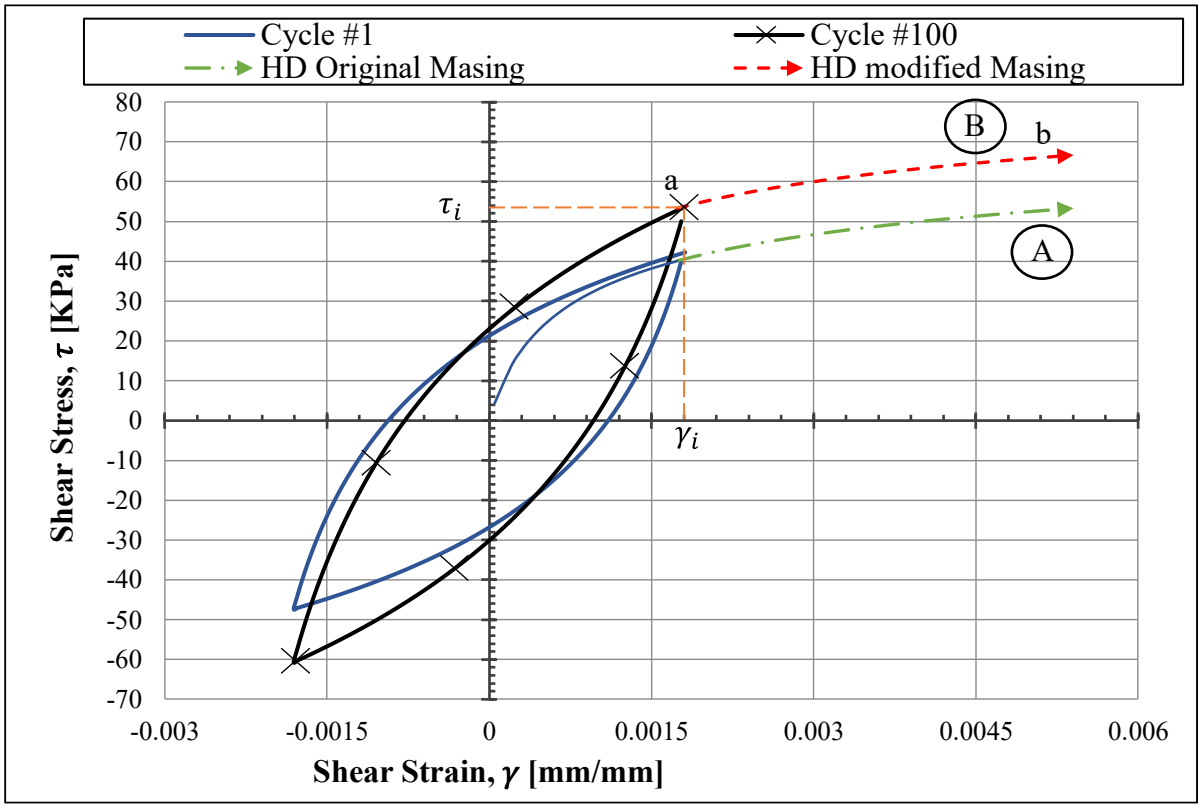

Figure 5-29 Modification to the third extended Masing criterion in HD model.

After any sequence of cyclic loading, and when the previously maximum shear strain is exceeded, the shear stresses will be calculated from Equation 5-18 before the start of the next unloading phase (curve ab in Figure 5-29). From the calculated stress at the turning point (b), an equivalent number of load reversals at that strain level can be calculated from the following equation:

$$n_{\mathrm{eq}} = 10^{\frac{\log(\delta_\tau)}{s}} \qquad \text{Equation 5-21}$$

Next, the curvature parameter γ_{r} corresponding to the calculated equivalent number of load reversals at that strain level follows:

$$\gamma_{\mathrm{r}} = \gamma_{\mathrm{r}_1} * {n_{\mathrm{eq}}}^{f} \qquad \text{Equation 5-22}$$

Table 11 Modified HD parameters for all samples.

Test number	**Sample ID**	**Maximum shear modulus**	γ_{r_b}	m	γ_r	f *	s **
#		$G_{\max}$ [MPa]	[-]	[-]	[-]	[-]	[-]
1	A	85	0.00042	0.88	0.00042	0.1	$0.18\gamma^{0.18}$
2	A	103.4	0.00042	0.88	0.00042	0.09	$0.15\gamma^{0.16}$
3	B	79.6	0.0005	0.88	0.00047	0.085	$0.09\gamma^{0.1}$
4	B	100	0.0005	0.88	0.00047	0.063	$0.114\gamma^{0.18}$
5	C	76	0.00053	0.88	0.0005	0.095	$0.24\gamma^{0.25}$
6	C	87	0.00053	0.88	0.0005	0.11	$0.29\gamma^{0.26}$

*f=0 when the shear strain is below the volumetric strain threshold.

**γ is the maximum single amplitude shear strain reached in the test.

**s is constant after exceeding a shear stress value equals to $\tau_{\max}$.

5.8 The fourth Masing criterion discussion

The irregular behavior of the sample was studied in tests #13 and #14 with the effect of stress offset on the stiffness at the same peak-to-peak shear stress amplitude. The fourth Masing criterion suggests that when the current loading or unloading curve intersects a previous one, it should follow the previous curve by taking its turning point in the soil model. This rule applies when neglecting the effect of the stiffening behavior. However, stiffening due to cyclic loading will cause the current shear stress-strain curve to intersect previous curves under

different conditions, as shown in Figure 5-30. In this test: (a) the sample was loaded for five cycles at a shear stress of 45 KPa. Then, (b) it was loaded for 30 cycles between 40 KPa and -20 KPa (~30 KPa single amplitude), which caused more stiffening in the sample. Finally, (c) when the sample was unloaded to -40 KPa, the turning point that should be used after intersecting with the curve in the fifth cycle could not be identified due to the stiffening caused by the 30 cycles that followed that fifth cycle. Thus, it would be very difficult to introduce a model that would replace the fourth Masing criterion to predict the shear stress-shear strain curve of dry sand subjected to irregular loading patterns due to stiffening behavior.

In the two tests (#13, #14), the specimen was loaded at the same peak-to-peak stress levels but with different offsets to investigate whether the stiffness depends only on the peak-to-peak stress level or location on the τ-γ plot. When we applied a peak-to-peak cyclic shear stress of 60 KPa (30 KPa single amplitude) with offsets of (+10, -10, 0) KPa for 30 cycles, we found the stiffness at a specific peak-to-peak stress always reaches a particular value regardless of the offset value. This also applies to the curvature coefficient R in the RO equation, which approaches a specific minimum value (e.g., Figure 5-23) as the number of cycles increases regardless of the previous time load history. Thus, the change in R depends on the peak-peak stress and the number of cycles. Even though we cannot precisely predict the behavior of soils under irregular (earthquake) loading patterns, we can approximate the loading history as a series of cyclic loadings that gradually increase in intensity until it reaches a maximum stress level and then decreases in intensity until it reaches zero. This would be similar to the TOSS tests performed in this research. By approximating stiffening behavior in this way, we can apply the proposed model and modify the Masing criteria to account for stiffening effects when the soil is subjected to intense irregular loading patterns.

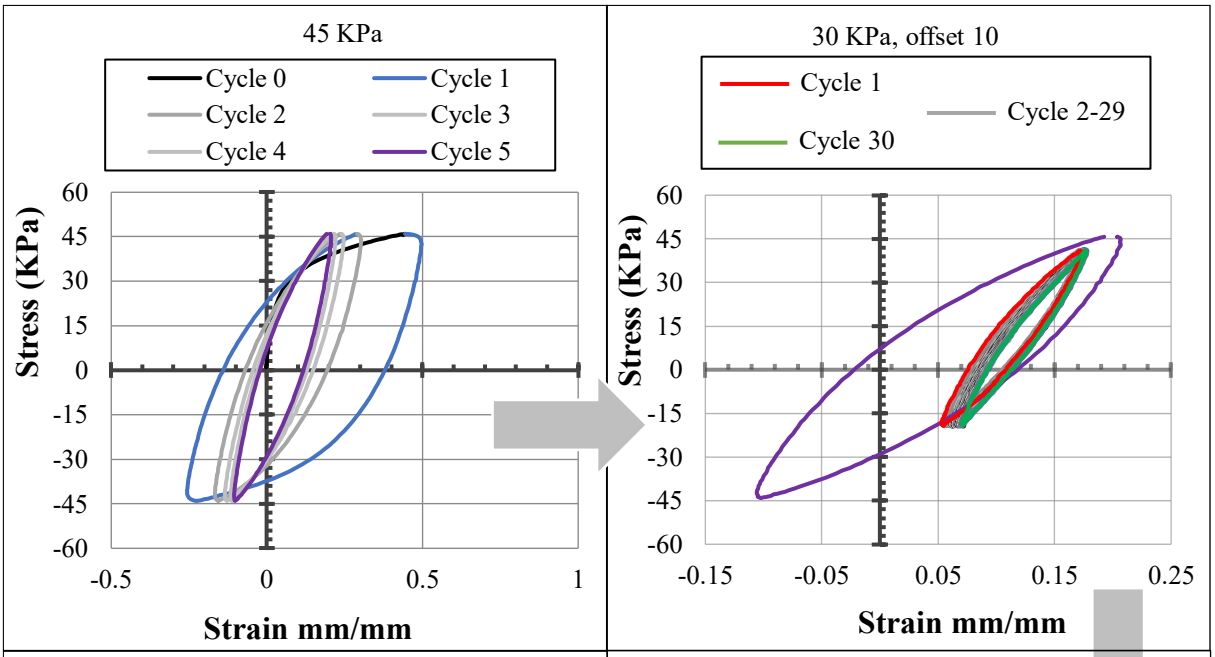

(a) Loading for 5 cycles at shear stress 45 Kpa

(b) Loading for 30 cycles between 40 KPa and -20 KPa (~30 KPa single amplitude)

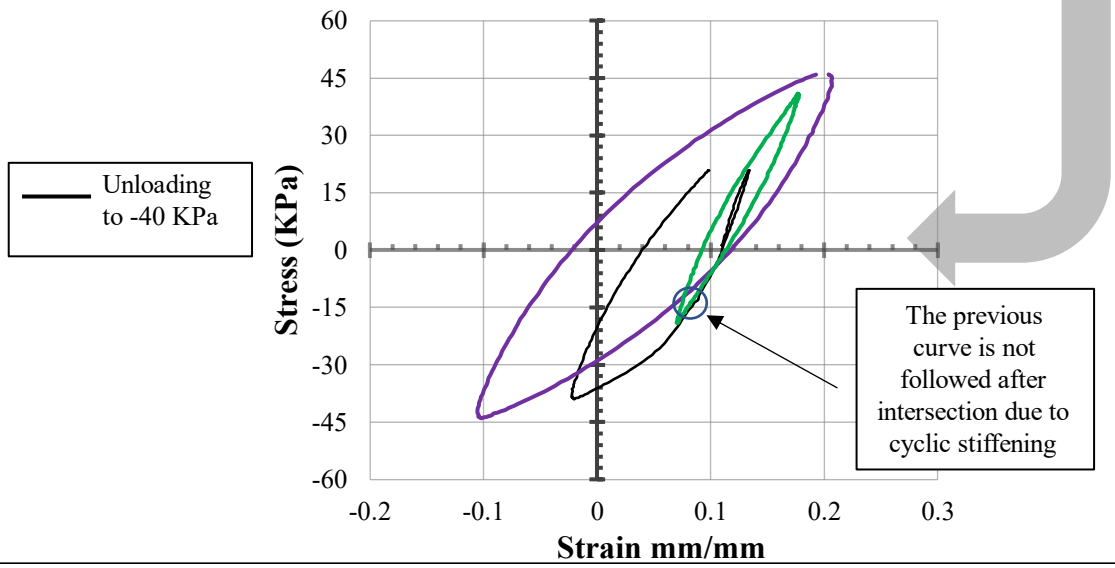

(c) Loading to 20 KPa then unloading to -40 KPa

Figure 5-30 Irregular cyclic loading for sample B to demonstrate the limitation of the fourth Masing criterion.

Thesis statements

6.1 Thesis #1

I have shown good agreement between the two testing methods (the Resonant Column and Torsional Simple Shear tests) in measuring the dynamic properties of dry sand. The two tests are interchangeable within the common measurement range of strains (10^{-2} - 10^{-1}) %. **I created subroutines in Visual Basic for Applications (VBA) in Excel for a faster and deeper analysis of the TOSS test results for both cyclic and irregular tests.** The subroutines calculate the shear modulus and damping ratio for each cycle to study the effect of the increasing number of cycles on the dynamic properties of soils in cyclic tests. By separating the loops in tests with irregular loading time history we can better identify the stress-strain path. The analysis includes applying the Ramberg-Osgood equation coupled with the Masing criteria to predict the shear stress-shear strain curves. **By implementing these subroutines, I demonstrated the limitations of the Masing criteria in predicting soil behavior under irregular loading histories due to the stiffening behavior. Initially, there was a good fit between the curves for the first few loops; however, as the number of cycles increased, especially at higher stress levels, the model began to drift away from the test results.**

6.2 Thesis #2

I have developed a three-dimensional finite element model on Midas GTS NX to simulate the TOSS test. This model is now able to simulate cyclic and irregular load TOSS tests. I used this model and irregular load TOSS test results to compare the Ramberg-Osgood and Hardin-Drnevich soil models. **(a) I found that the R-O model can obtain a good fit with the test results (R^2=99.99%), while the H-D model struggled to match the nonlinearity of the curve (R^2=99.48%). As a result, I have introduced a curvature parameter (*m)* to the H-D model, which better fits the test results (R^2=99.99%). (b) I also proved that the shear stress-shear strain curve will follow the extended Masing criteria when neglecting the effect of the stiffening behavior due to cyclic loading.**

6.3 Thesis #3

I applied Masing's theory to soil in the model created in Midas and found that the sample is non-uniform and not all material elements yield simultaneously, and a simple elasto-

plastic material model can produce complex nonlinear behavior when the properties are varied. **I developed an iterative method using solver in Excel and Midas to find a discrete distribution of the yield stresses of the elements that has a collective behavior that matches the results obtained from the TOSS test. I used this model with the discrete distribution of elements to study nonuniform samples with inclusions and voids.** I found that stiffness increased with the increasing percentage of inclusions in the specimen and a decrease in stiffness with the increasing percentage of voids in the sample.

6.4 Thesis #4

I measured the damping ratio using three different methods: Steady State Vibration (SSV), Free Vibration Decay (FVD), and damping in TOSS device from the hysteresis loops. Based on the results, **I recommend using the SSV method at very low strain amplitudes (below 0.005%) where the response curve is symmetrical and the FVD method's measurements are unreliable due to the noise created by the device when turning off the drive power. At medium strain levels, the two methods and the TOSS test results agree with each other. However, at higher strain amplitudes (above 0.03%) I recommend the FVD method to measure damping ratio due to the reduced accuracy of the SSV method. The SSV response curves are not symmetric anymore which compromises the use of the half-bandwidth method causing an overestimation in the damping ratio values.**

I investigated the effect of the shear stiffening behavior during cyclic loading in the TOSS test on the damping ratio. After exceeding the volumetric shear strain threshold, I observed a considerable decrease in the damping ratio, which is more evident in loose samples where damping can decrease by up to 64% after 100 cycles compared to 54% decrease in dense samples depending on the stress level of the applied cycles.

6.5 Thesis #5

I studied the stiffening behavior of dry sand due to cyclic loading in the TOSS test. **I showed the substantial effect of the stiffening behavior on the dynamic properties of soil and presented two equations that can be used to estimate the dynamic shear modulus (G_N) of dry Danube sand after *N* number of cycles at any shear stress (τ).**

$$\delta_G = \frac{G_N}{G_1} = t * \log(N) + 1 \qquad \text{Equation 6-1}$$

$$t = 0.822\left(\frac{\tau}{\tau_{\max}}\right)^2 - 0.11\frac{\tau}{\tau_{\max}} - 0.024 \qquad \text{Equation 6-2}$$

Where δ_G: is the stiffening index.

G_N: is the shear modulus after *N* cycls

G_1: is the shear modulus of the first cycles (on the backbone curve)

t: is the slope of (δ_G-1)-log(*N*) plot that represents the stiffening parameter.

The fit was obtained between *t* and the standardized shear stress ($\tau/\tau_{\max}$) with a coefficient of determination R^2=0.988.

6.6 Thesis #6

I investigated the limitations of the soil models coupled with the Masing criteria to simulate the stiffening behavior of soil. I found that the Masing criteria are only reliable when the stiffening behavior is not considered.

I introduced modifications to the Ramberg-Osgood and Hardin-Drnevich models coupled with the Masing criteria as follows:

Ramberg-Osgood model:

- The model parameters (C_b and R_b) for the backbone curve are higher than the model parameters for the unloading-reloading curves (*C* and *R*).
- I found a method to surpass the limitation in the second Masing criterion by finding the equation of the increase in the model parameter *R* with the increasing stress level for each sample.
- I simulated the stiffening and reduced damping behavior by decreasing the parameter *R* with increasing cycles.
- I introduced a stiffening parameter (*b*) to the model, which represents the slope of the log(δ_R)-log(*n*) plot, where δ_R is the ratio between the parameter *R* at the n^{th} half-cycle *(R_n)* and the first undegraded loop (R_1).
- The third Masing criterion is not valid due to the stiffening behavior. I replaced this criterion with a method to continue the shear stress-shear strain curve based on where the previously maximum shear stress is exceeded.
- I introduced a parameter (*k*) to the model to find the parameter (*R*) change due to any previous cyclic loading based on an equivalent number of cycles.

Hardin-Drnevich model:

- The model parameter (γ_{r_b}) for the backbone curve is higher than the model parameters for the unloading-reloading curves (γ_r).

- γ_{r} can be considered constant with the increasing strain level.
- I introduced a stiffening parameter (*f*) to the model, which represents the slope of the log($\delta_{\gamma_{\mathrm{r}}}$)-log(*n*) plot, where $\delta_{\gamma_{\mathrm{r}}}$is the ratio between the parameter γ_r at the n^{th} half-cycle (γ_{r_n}) and the first half-cycle (γ_{r_1}).
- I introduced a parameter (*s*) to the model to find the change in the parameter (γ_{r}) due to any previous cyclic loading.

I developed Excel worksheets with VBA subroutines to manage the curve fitting of the cyclic TOSS tests using the Generalized Reduced Gradient Method and worksheets to find the parameters I introduced to R-O and H-D models.

Summary and future research

In my dissertation I used the combined Resonant Column-Torsional Simple Shear device (RC-TOSS) to study the dynamic properties of dry sand and investigate the applicability and limitations of the soil models commonly used to simulate the dynamic behavior and predict the shear stress-shear strain curves. To acquire a deeper understanding of the dynamic properties of soil and methods to measure and model them, a thorough review of literature regarding dynamic soil modeling has been provided. 20 cyclic and irregular tests were conducted on three types of Danube sands to find the backbone curves and to study the stiffening behavior due to cyclic loading. Furthermore, damping ratio measurements were taken employing the SSV and FVD methods in the RC tests and from the hysteresis loops in the TOSS tests. Recommendations are presented on the utilization of these three methods depending on the range of the strain amplitude. A 3D Finite Element (FE) model is developed in Midas GTS NX to simulate the TOSS test, and a comparison between the Ramberg-Osgood model and the Hardin-Drnevich model is performed. The same FE model is further advanced to examine the nonuniformity of the sample and the effect of voids and inclusions by finding a discrete distribution of Tresca elastoplastic material properties in the sample that matches the test data. The limitation of the soil models and Masing criteria to simulate the stiffening behavior of sand are discussed, and modifications and new parameters to the RO and HD models are introduced along with the tools needed to calibrate the models using Visual Basic for Applications (VBA) in Excel.

Future studies could involve enhancing and refining the RC-TOSS device by enabling it to conduct strain-controlled tests, investigating the impact of anisotropic loading through the addition of vertical loads to the sample, improving the sealing of specimens, conducting tests on saturated samples, and measuring pore pressure. Moreover, the models presented can be integrated in FE software (e.g., Plaxis, Midas GTS) to be used in nonlinear site response analysis while taking into consideration the stiffening behavior of the soil.

References

Afifi, S. S. & Woods, R. D., 1971. Long -Term Pressure Effects on Shear Modulus of Soils. *Journal of the Soil Mechanics and Foundations Division, ASCE,* 97(10), pp. 1445-1460.

Ahmad, M. & Ray , R., 2023. Modelling of the Torsional Simple Shear Test with Randomized Tresca Model Properties in Midas GTS NX. *Geotechnical and Geological Engineering*, Volume 41, p. 1937–1946.

Ahmad, M. & Ray, R., 2021. Comparison between Ramberg-Osgood and Hardin-Drnevich soil models in Midas GTS NX. *Pollack Periodica,* 16(3), p. 52–57.

Ahmad, M. & Ray, R., 2021. *Numerical study of random material properties within a soil specimen.* Iasi, Romania, IOP Publishing Ltd, p. 7 pp.

Ahmad, M. & Ray, R., 2023. Damping of Dry Sand in Resonant Column-Torsional Simple Shear Device. *sustainability,* 15(14), p. 11060.

Ahmad, M. & Ray, R., 2023. The Dynamic Properties of Sand under Torsion: A Literature Review. *geotechnics,* 3(2), pp. 480-514.

Ahmad, M. & Ray, R., 2024. Modeling the Stiffening Behavior of Sand Subjected to Dynamic Loading. *geosciences,* 14(1), p. 26.

Alarcon-Guzman, A., Chameau, J., Leonards, G. A. & Frost, J. D., 1989. Shear Modulus and Cyclic Undrained Behavior of Sands. *Soils and Foundations,* 29(4), pp. 105-119.

Anderson, B. A., 1979. *Deformation characteristics of soft, high-plastic clays under dynamic loading conditions.* Gothenburg: Chalmers University of Technology.

Anderson, D. G. & Richart, F. E. J., 1976. "Effects of straining on shear modulus of clays. *Journal of the Geotechnical Engineering Division,* 102(9), pp. 975-987.

ASTM D4015, 1992. *Standard test methods for modulus and damping of soils by resonant-column method. Annual Book of ASTM Standards.* USA: ASTM International.

Bae, Y.-S., 2007. *MODELING SOIL BEHAVIOR IN LARGE STRAIN RESONANT COLUMN AND TORSIONAL SHEAR TESTS.* PhD dissertation ed. Logan,: Utah State University.

Baig, S., Picornell, M. & Nazarian, S., 1997. Low strain shear moduli of cemented sands. *Journal of Geotechnical and Geoenvironmental Engineering, ASCE,* 123(6), pp. 540-545.

Basas, V., Pantazopoulos, I. & Atmatzidis, D., 2020. Torsional and flexural resonant column testing of grouted sands. *Soil Dynamics and Earthquake Engineering,* Volume 139.

Benz, T., 2006. *Small strain stiffness of soils and its numerical consequences, PhD Dissertation.* s.l.:Universität Stuttgart Institut für Geotechnik.

Biarez, J. & Hicher, P., 1994. *Elementary Mechanics of Soil Behavior.* Balkema: ISBN : 9054101571 .

Carraro, J., Prezzi, M. & Salgado, R., 2009. Shear strength and stiffness of sands containing plastic or nonplastic fines. *Journal of Geotechnical and Geoenvironmental Engineering,* 135(9), pp. 1167-1178.

Chaudhary, S., Kuwano, J. & Hayano, Y., 2004. Measurement of quasi-elastic stiffness parameters of dense Toyoura sand in hollow cylinder apparatus and triaxial apparatus with bender elements. *Geotechnical Testing Journal,* 27(1), pp. 1-13.

Cherian, A. C. & Kumar, J., 2016. Effects of Vibration Cycles on Shear Modulus and Damping of Sand Using Resonant Column Tests. *Journal of Geotechnical and Geoenvironmental Engineering,* 142(12), pp. 1-6.

Chopra , A. K., 2007. *Dynamics of Structures, Theory and Applications to Earthquake Engineering.* 3rd ed ed. New Jersey: Prentice Hall.

Constantopoulos , I. V., Roesset, J. M. & Christian, J. T., 1973. *A Comparison of Linear and Exact Nonlinear Analyses of Soil Amplification.* s.l., Proceedings, Fifth World Conference on Earthquake Engineering, Paper No. 225.

Darendeli, B., 2001. Development of a new family of normalized modulus reduction and material damping curves. In: *PhD dissertation.* Austin, USA: University of Texas, pp. 1-362.

Darendeli, B., 2001. Development of a new family of normalized modulus reduction and material damping curves. In: *PhD dissertation.* University of Texas at Austin, USA: http://hdl.handle.net/2152/10396, pp. 1-362.

Das, S. & Bhowmik, D., 2017. *SMALL STRAIN DYNAMIC BEHAVIOR OF SAND AND SAND-CRUMB RUBBER MIXTURE IN DRY CONDITION.* Guwahati, India, Indian Geotechnical Conference 2017 GeoNEstAt.

Dobry, R., 1970. *Damping in soils: its hysteretic nature and the linear approximation,* s.l.: Massachusetts Institute of Technology.

Dobry, R. & Vucetic, M., 1987. *Dynamic properties and response of soft clay deposits. State of the art report.* Mexico City, Proc. Int. Symp. Geotech. Eng. Soft Soils.

Drnevich, V. P., 1967. *Effect of Strain History on the Dynamic Properties of Sand.* Ph.D. Dissertation ed. s.l.:University of Michigan.

Drnevich, V. P., Hardin, B. O. & Shippy, D. J., 1978. Modulus and damping of soils by the resonant col- umn method. Dynamic Geotechnical Testing. *ASTM STP 654, Dynamic Geo- technical Testing,* pp. 91-125.

Edil, T. B. & Luh, G. F., 1978. *Dynamic modulus and damping relationships for sands.* Pasadena, Calif, Proceedings ASCE Specialty Conference on Earthquake Engineering and Soil Dynamics.

Faccioli, E., Santayo, V. & Leone, J., 1973. *Microzonation criteria and seismic response studies for the city of Managua.* s.l., Earthqucake Engineering Research Institue Conference Proceedings, pp. 271-291.

Facciorusso, J., 2020. An archive of data from resonant column and cyclic torsional shear tests performed on Italian clays. *Earthquake Spectra,* 73(1), p. 545–562.

Fam, M. A., Cascante, G. & Dusseault, M. B., 2002. Large and Small Strain Properties of Sands Subjected to Local Void Increase. *Journal of Geotechnical and Geoenvironmental Engineering,* 12(128), pp. 1018-1025.

Fernandes, J. B., Rocha, B. P. & Giacheti, H. L., 2023. Maximum shear modulus and modulus degradation curves of an unsaturated tropical soil. *Soils and Rocks,* 46(2).

Finn, W. D. L., Lee, K. W. & Martin, G., 1977. An Effective Stress Model for Liquefaction. *Journal of the Geotechnical Engineering Division, ASCE,* 103(6), pp. 517-533.

Fioravante, V., 2000. Anisotropy of Small Strain Stiffness of Ticino and Kenya Sands from Seismic Wave Propagation Measured in Triaxial Testing. *Soils and Foundations,* 40(4), pp. 129-142.

Gabryś, K., Soból, E., Sas, W. & Szymański, A., 2018. Material damping ratio from free-vibration method. *Annals of Warsaw University of Life Sciences-SGGW Land Reclamation,* 50(2), pp. 83-97.

Georgiannou, V. N., Rampello, S. & Silvestri, F., 1991. *Static and dynamic measurements of undrained stiffness of natural overconsolidated clays.* Florence, Italy,, Proc., lOth European Conf. on Soil Mech. and Found. Engrg. A. A. Balkema,, pp. 91-95.

Guha, S., 1995. *Dynamic Characteristics of Old Bay Clay Deposits in the East San Francisco Bay Area.* s.l.:PhD dissertation, Graduate School, Purdue University, USA.

Hall, J. R. & Richart, F. E., 1963. Dissipation of Elastic Wave Energy in Granular Soils. *Journal of the Soil Mechanics and Foundations Division,* 89(6), pp. 27-56.

Hardin, B., 1965. The Nature of Damping in Sands. *Journal of the Soil Mechanics and Foundations Division,* 91(1), pp. 63-98.

Hardin, B. & Black, W., 1966. Sand stiffness under various triaxial stresses. *Journal of the Soil Mechanics and Foundations Division,* 92(2), pp. 27-42.

Hardin, B. & Drnevich, V., 1972. Shear modulus and damping in soils: Design equations and curves. *Journal of the Soil Mechanics and Foundations Division,* 98(7), pp. 667-692.

Hardin, B. O. & Music, J., 1965. *Apparatus for Vibration of Soil Specimens during the Triaxial Test, Instruments and Apparatus for Soil and Rock Mechanics,* s.l.: American Society for Testing and Materials.

Hardin, B. & Richart, F., 1963. Elastic wave velocities in granular soils. *Journal of the Soil Mechanics and Foundations Division,* 89(1), pp. 33-65.

Hoque, E. & Tatsuoka, F., 2000. Kinematic elasticity of a granular material. In: *In Proc. GeoEng2000, Melbourne.* s.l.:https://www.onepetro.org/conference-paper/ISRM-IS-2000-231.

Hoque, E. & Tatsuoka, F., 2004. Effects of stress ratio on small-strain stiffness during triaxial shearing. *Géotechnique,* 54(7), pp. 429-439.

Idriss, I. M., Dobry, R. & Singh, R. D., 1978. Nonlinear behavior of soft clays during cyclic loading. *Journal of the Geotechnical Engineering Division,* 104(12), pp. 1427-1447.

Idriss, I. M., Dobry, R. & Singh, R. D., 1978. Nonlinear behavior of soft clays during cyclic loading. In: *Journal of the Geotechnical Engineering Division 104:12.* s.l.:https://trid.trb.org/view.aspx?id=86207, pp. 1427-1447.

Im, J., Tran, T. P. A., Chang, I. & Cho, G.-C., 2017. Dynamic properties of gel-type biopolymer-treated sands evaluated by Resonant Column (RC) Tests. *Geomechanics and Engineering,* 12(5), pp. 815-830.

Isenhower, W. M., 1979. *Torsional Simple Shear / Resonant Column Properties of San Francisco Bay Mud.* M.S. Thesis ed. Austin, USA: University of Texas.

Ishihara, K., 1996. Soil Behavior in Earthquake Geotechnics. In: New York: Oxford University Press, pp. 33-39 ISBN 0-19-856224-1.

Ishimoto, M. & Iida, K., 1936. *Determination of Elastic Constants of Soils by means of Vibration Methods. Part 1, Young's Modulus,* s.l.: Bulletin of the Earthquake Research Institute, University of Tokyo 14: 632-657..

Iwasaki, T. & Tatsuoka, F., 1977. Effects of grain size and grading on dynamic shear moduli of sands. *Soils and Foundations,* 17(3), pp. 19-35.

Iwasaki, T., Tatsuoka, F. & Takagi, Y., 1978. Shear moduli of sands under cyclic torsional shear loading. *Soils & Foundations,* 18(1), pp. 39-50.

Jennings, P., 1965. Earthquake Response of a Yielding Structures. *Journal of Geotechnical Engineering Division,* 91(4), pp. 41-68.

Kagawa, T., 1992. Moduli and damping factors of soft marine clays. *Journal of Geotechnical Engineering,* 118(9), pp. 1360 - 1375.

Kallioglou, P., Tika, T. & Pitilakis, K., 2008. Shear Modulus and Damping Ratio of Cohesive Soils. *Journal of Earthquake Engineering,* 12(6), pp. 879-913.

Kallioglou, T., Papadopoulou, A. & Pitilakis, K., 2003. Shear modulus and damping of natural sands. In: *Deformation Characteristics of Geomaterials.* Proc. IS-Lyon: A.A. Balkema https://doi.org/ 10.1201/NOE9058096043.ch50, pp. 401-407.

Kim, D. S., Stokoe, K. H. & Hudson, W. R., 1991. *Deformational char- acteristics of soils at small to intermediate strains from cyclic tests,* Austin: Center for Transportation Research, Bureau of Engi- neering Research, Univ. of Texas, .

Kokusho, T., 1987. *In situ Dynamic Soil Properties and Their Evaluations.* Kyoto, Japan, Proc., Eighth Asian Regional Conference on Soil Mechanics and Foundation Engineering, pp. 215-240.

Kramer, S. L., 1996. *Geotechnical Earthquake Engineering.* ISBN-13: 978-0133749434 ed. New Jersey: Prentice Hall .

Kuwano, R. & Jardine, R., 2002. On the application of cross-anisotropic elasticity to granular materials at very small strains. In: *Géotechnique 52(10).* s.l.:https://doi.org/10.1680/geot.2002.52.10.727 , pp. 727-749.

Ladd, R. S., 1982. *Geotechnical laboratory testing program for study and eval- uation of liquefaction ground failure using stress and strain approaches: Heber Road site, October 15, 1979 Imperial Valley earthquake.* s.l.:Woodward- Clyde Consultants, Eastern Region, Wayne, N.J..

Lashin, I., Abdellaziz, M. & Karray, M., 2021. *Experimental assessment of shear modulus reduction curve for granular soils.* Niagara Falls, ON, Canada, Conference: GeoNiagara 2021, the 74th Canadian Geotechnical Conference.

Lin , M. L. & Chen, J. Y., 1991. *Degradation Behavior of Normally Consolidated Clay Under Cyclic Loading Condition.* St. Louis, Proc. 2nd Int. Conference on Recent Advances in Geotechnical Earthquake Engineering and Soil Dynamics, pp. 21-26.

Lin , M. L. & Chen, J. Y., 1991. *Degradation Behavior of Normally Consolidated Clay Under Cyclic Loading Condition.* St. Louis, Proc. 2nd Int. Conference on Recent Advances in Geotechnical Earthquake Engineering and Soil Dynamics, pp. 21-26.

Li, W. et al., 2018. Investigation on the dynamic shear modulus and damping ratio of steel slag sand mixtures. *Construction and Building Materials,* Volume 162, pp. 170-180.

Lo Presti, D. C. F. et al., 2000. *Modelling Of Hardening And Degradation Behavior Of Clays And Sands During Cyclic Loading.* Auckland, New Zealand, Proc. 12th World Conference on Earthquake Engineering, pp. 1-8.

Lo Presti, D. C. F. et al., 1997. Shear modulus and damping of soils. *Geotechnique,* 47(3), pp. 603-617.

Lo Presti, D. et al., 1993. Monotonic and cyclic loading behaviour of two sands at small strains. In: *Geotechnical Testing Journal 16(4).* s.l.:https://doi.org/10.1520/GTJ10281J, pp. 409-424.

Masing, G., 1926. Eigenspannungen und Verfestigung beim Messing. In: *Proc. 2nd Int. Congr. Appl. Mech.*. Zurich: s.n.

Matasovic, N. & Vucetic, M., 1993. Cyclic Characterization of Liquefiable Sands. *Journal of Geotechnical Engineering,* 119(11), pp. 1805-1822.

Meng, J., 2003. *The influence of loading frequency on dynamic soil properties, PhD dissertation.* Atlanta, USA: Georgia Institute of Technology.

MIDAS Information Technology Co., L., 2014. Midas GTS NX 2014 v2.1 Analysis Reference, Chapter 4. Materials. In: s.l.:http://midasgtsnx.com/, pp. 105-211.

Mog, K. & Anbazhagan, P., 2022. Evaluation of the damping ratio of soils in a resonant column using different methods. *Soils and Foundations,* 62(1).

Oztoprak, S. & Bolton, M., 2013. Stiffness of sands thourgh a laboratory test database. *Géotechnique,* 63(1), pp. 54-70.

Payan, M., Senetakis, K., Khoshghalb, A. & Khalili, N., 2016. Influence of particle shape on small-strain damping ratio of dry sands. *Geotechnique,* 66(7), pp. 610-616.

Pyke, R., 1979. Nonlinear soil models for irregular cyclic loadings. *Journal of the Geotechnical Engineering Division, 105(GT6),* 106(GT11), pp. 715-726.

Qian, X., Gray, D. H. & Woods, R. D., 1991. Resonant column tests on partially saturated sands. *Geotechnical Testing Journal,* 14(3), p. 266–275.

Qian, X., Gray, D. H. & Woods, R. D., 1993. Voids and Granulometry: Effects on Shear Modulus of Unsaturated Sands. *Journal of Geotechnical Engineering,* 119(2), p. 295–314.

Ramberg, W. & Osgood, W. R., 1943. *Description of stress strain curves by three parameters,* s.l.: National Advisory Committee for Aeronautics, Technical Note No. 902..

Ray, R. P., 1984. *Changes in shear modulus and damping in cohesionless soils due to repeated loading, PhD Dissertation.* s.l.:University of Michigan, USA.

Ray, R. & Woods, R., 1988. Modulus and damping due to uniform and variable cyclic loading. *Journal of Geotechnical Engineering,* 114(8), pp. 861-876.

Richart, F. E., Hall, J. R. & Woods, 1970. *Vibrations of soils and foundations,* Englewood Cliffs, N.J.: Prentice-Hall.

Rocha, B. P., Fernandes, J. & Giacheti, H. L., 2021. *Dynamic shear modulus and stiffness decay curves of a tropical sandy soil via laboratory and in situ tests.* Budapest, Hungary, 6th International Conference on Geotechnical and Geophysical Site Characterization.

Rosenblueth, E. & Herrera, I., 1964. On a kind of hysteretic damping. *Journal of the Engineering Mechanics Division,* 91(3), pp. 37-48.

Saxena, S. K. & Reddy, K. R., 1989. Dynamic Moduli and Damping Ratios for Monterey No. 0 Sand by Resonant Column Tests. *Soils and Foundations,* 29(2), pp. 37-51.

Senetakis, K., Anastasiadis, A. & Pitilakis, K., 2015. A comparison of material damping measurements in resonant column using the steady-state and free-vibration decay methods. *Soil Dynamics and Earthquake Engineering,* Volume 74, pp. 10-13.

Senetakis, K., Anastasiadis, A. & Pitilakis, K., 2012. Small strain shear modulus and damping ratio of quartz and volcanic sands. *Geotechnical Testing Journal,* 36(6), pp. 1-17.

Sherif, M. A. & Ishibashi, I., 1976. Dynamic shear modulus for dry sands. *Journal of the Geotechnical Engineering Division,* 102(11), p. 1171±1184.

Silver, M. L. & Seed, H. B., 1971. Volume changes in sands during cyclic loading. *Journal of the Soil Mechanics and Foundations Division,* 97(9), pp. 1171-1182.

Simonini, P. & Cola, S., 2000. Use of piezocone to predict maximum stiffness of Venetian soils. *Journal of Geotechnical and Geoenvironmental Engineering, ASCE,* 126(4), pp. 378-382.

Skelton, R. P., Maier, H. J. & Christ, H. J., 1997. The Bauschinger effect, Masing model and the Ramberg–Osgood. *Materials Science and Engineering,* 238(2), p. 377–390.

Stokoe, K. H. & Richart, F. E., 1973. *Shear moduli of soils, in-situ and from laboratory tests.* s.l., the 5Th World Conference in Earthquake Engineering, pp. 356-359.

Streeter, V. L., Benjamin Wylie , E. & Richart, F. E. J., 1974. Soil Motion Computation by Characteristics Method. *Journal of the,* 100(3), pp. 247-263.

Szilvágyi, Z., 2017. *Dynamic Soil Properties of Danube Sands, PhD dissertation.* Győr, Hungary: Széchenyi István University.

Szilvágyi, Z. et al., 2017. Ground Response Analyses in Budapest Based on Site Investigations and Laboratory Measurements. *International Journal of Environmental, Chemical, Ecological, Geological and Geophysical Engineering,* 11(4), pp. 307-317.

Tatsuoka, F. et al., 1979. Shear modulus and damping by drained tests on clean sand specimen reconstituted by various methods. *Soils and Foundations,* 19(1), pp. 39-54.

Tatsuoka, F. & Shibuya, S., 1992. Deformation characteristics of soils and rocks from field and laboratry tests. *Report of the Institute of Industrial Science, University of Tokyo; (Japan),* 37(1), pp. 101-190.

Valera , J. E. et al., 1978. *Study of Nonlinear Effects on One-Dimensional Earthquake Response,* Palo Alto, California: Report No. NP-865, Electric Power Research Institute, Palo Alto, Calif.

Vucetic, M., 1994. Cyclic threshold shear strains in soils. *Journal of Geotechnical Engineering 120,* 120(12), pp. 2208-2228.

Vucetic, M. & Dobry, R., 1991. Effect of soil plasticity on cyclic response. *Journal of Geotechnical Engineering,* 117(1), pp. 89-107.

Vucetic, M. & Dobry, R., 1991. Effect of soil plasticity on cyclic response. In: *Journal of Geotechnical Engineering, ASCE, Vol 117.* s.l.:https://doi.org/10.1061/ (ASCE)0733-9410(1991)117:1(89), pp. 89-107.

White, J. E., 1983. *Underground sound: applications of seismic waves.* Amestrdam, Netherlands: Elsevier.

Wichtmann, T., Navarrete Hernández, M. & Triantafyllidis, T., 2015. On the influence of a non-cohesive fines content on small strain stiffness, modulus degradation and damping of quartz sand. *Soil Dynamics and Earthquake Engineering,* 69(2), pp. 103-114.

Wichtmann, T. & Triantafyllidis, T., 2004. Influence of a cyclic and dynamic loading history on dynamic properties of dry sand, Part i: cyclic and dynamic torsional prestraining. *Soil Dynamics and Earthquake Engineering,* 24(2), pp. 127-147.

Wichtmann, T. & Triantafyllidis, T., 2009. Influence of the grain-size distribution curve of quartz sand on the small strain shear modulus Gmax. In: *Journal of the Geotechnical and Geoenvironmental Engineering 135(10).* s.l.:(ASCE)GT.1943-5606.0000096, pp. 1404-1418.

Woods, R. D., 1978. *Measurement of dynamic soil properties.* New York, Proc., ASCE Geotechnical Engineering Division Speciality Conf., Earthquake Engineering and Soil Dynamics, p. 91–178.

Wu, Q. et al., 2021. Dynamic shear modulus and damping ratio of rubber-sand mixtures with a wide range of rubber. *Materials Today Communications*, 27(March).

Xu, Z., Tao, Y. & Hernandez, L., 2021. Novel Methods for the Computation of Small-Strain Damping Ratios of Soils from Cyclic Torsional Shear and Free-Vibration Decay Testing. *Geotechnics*, 1(2), pp. 330-346.

Yang, Z., Wen, Y. & Kun, P., 2019. Previbration Signature on Dynamic Properties of Dry Sand. *Journal of Testing and Evaluation*, 47(3), pp. 1-27.

Yu, X., Yuan, X., Chen, Z. & Zhang, J., 2017. Resonant Column Test on the Frozen Silt Soil Modulus and Damping at Different Temperatures. *Periodica Polytechnica Civil Engineering*, 61(4), p. 762–769.

List of figures

List of symbols

G	Dynamic shear modulus
D	Damping ratio
G_{max}	Maximum shear modulus
V_s	Shear wave velocity
P	Density
γ_{tl}	The linear shear strain threshold
γ_{tv}	The volumetric threshold shearing strain
G_{sec}	Secant shear modulus
γ	Shear strain
C	Viscous damping coefficient
$\dot{u}$	Particle velocity
$\ddot{u}$	Particle acceleration
A_L	The area of the loop
A_T	The area of the triangle bounded by a straight line defining the secant modulus at the point of maximum strain
D_{min}	Small strain damping ratio
δ	Logarithmic decrement
N	Number of cycles
Z_1	First amplitude
Z_{1+N}	Amplitude after N cycles
ξ	Model damping ratio of a structure
$\Delta\omega$	The half-power bandwidth
f_1	The frequency below the resonance where the strain amplitude is P
f_2	The frequency above the resonance where the strain amplitude is P
P_{max}	Maximum amplitude (or resonant amplitude
f_r	Resonant frequency
P	The amplitude that equals ($P_{max}/\sqrt{2}$)
I	Sample polar moment of inertia
I_0	Free end mass polar moment of inertia
ω_n	Resonant frequency in torsion
L	Length of the sample
θ	Measured rotation
θ_{max}	Maximum rotation
h	Height of the section where the calculated point is located
r	The distance between the calculated point and the axis of the specimen

x	Length of the arc which a given point at the edge of the specimen during vibration
R	Radius of the tested cylindrical specimen
x_{A}	Displacement of an accelerometer mounted on the drive plate
l_{A}	Offset of accelerometer from the axis of the tested specimen
e	Void ratio
$F(e)$	The function of void ratio
A	Experimentally found coefficient for $F(e)$
a	Experimentally found coefficient for $F(e)$
n	Experimentally found coefficient for $F(e)$
$p^{'}$	Thew mean effective stress
p_{atm}	The atmospheric pressure
C_U	uniformity coefficient
FC	coefficient of fine particles
τ	Shear stress
$\tau_{\max}$	Maximum shear stress
α, C, R	Ramberg-Osgood curve fitting constants
$G_{\tan}$	Tangent shear modulus
γ_r	reference shear strain
γ_{i}	Shear strain at turning point
τ_i	Shear stress at turning point
E_0	Initial stiffness
σ_{eq}	Von Mises stress
$\varepsilon_{\mathrm{eq}}$	the equivalent deviatoric strain
ϑ	Poisson's ratio
a, b	Hyperbolic model fitting constants
$D_{\max}$	Maximum damping ratio
γ_{r}, m	Hardin-Drnevich model constants
D_i	Inner diameter of the specimen
D_o	Outer diameter of the specimen
d	Distance between proximitors
R_{ave}	Average radius of specimen
R_{in}	Inner radius of specimen
R_{out}	Outer radius of specimen
E	Elasticity modulus
σ_{y}	Yield stress
n	Number of yield elements

Z	Total number of elements
$\sigma_{\max}$	Maximum stress
y	The increase in stiffness in percent
x	The percentage of inclusions in the sample
d_{50}	Mean particle diameter
d_{10}	Eff particle diameter
$e_{\max}$	Maximum void ratio
$e_{\min}$	Minimum void ratio
w_{l}	Liquid limit for fines
w_{p}	Plastic limit for fines
I_{p}	Plastic index for fines
D_{r}	Relative density
φ	Angle of friction
δ_{G}	The stiffening index
t	Slope of stiffening index
δ_R	Stiffening index in RO model
b	Stiffening parameter in RO model
δ_γ	Inverse stiffening index in RO model
k	Slope of the inverse stiffening index in RO model
N_{eq}	Equivalent number of cycles
C'	Coefficient of exceeding the previous maximum shear stress in RO model
δ_{γ_r}	Stiffening index in HD model
f	Stiffening parameter in HD model
ω	Coefficient of exceeding the previous maximum shear strain in HD model
s	Slope of the inverse stiffening index in HD model

List of Publications

1. Ahmad, M. & Ray, R., 2021. Comparison between Ramberg-Osgood and Hardin-Drnevich soil models in Midas GTS NX. Pollack Periodica, 16(3), p. 52–57. DOI: https://doi.org/10.1556/606.2021.00353
2. Ahmad, M., Ray, R. Numerical study of random material properties within a soil specimen. IOP Conference Series: Materials Science and Engineering, Volume 1141, Computational Civil Engineering (CCE 2021) 27th-29th May 2021, Iasi, Romania 2021.
3. Ahmad, M. & Ray, R., 2023. Modelling of the Torsional Simple Shear Test with Randomized Tresca Model Properties in Midas GTS NX. Geotechnical and Geological Engineering, Volume 41, p. 1937–1946. DOI: https://doi.org/10.1007/s10706-023-02382-z
4. Ahmad, M. & Ray, R., 2023, The Dynamic Properties of Dry Sand in Torsion: A Literature Review, Geotechnics 2023, 3(2), 480-514. DOI:https://doi.org/10.3390/geotechnics3020027
5. Ahmad, M. & Ray, R., Damping of dry sand in RC-TOSS device, Sustainability 2023, 15(14), 11060. DOI: https://doi.org/10.3390/su151411060
6. Ahmad, M. & Ray, R., 2024 Modeling the Stiffening Behavior of Sand Subjected to Dynamic Loading, Geosciences, 14(1),26. DOI: https://doi.org/10.3390/geosciences14010026

Annex A - RC-TOSS measurement results

Test#1 measurement results (Sample A, Loose)

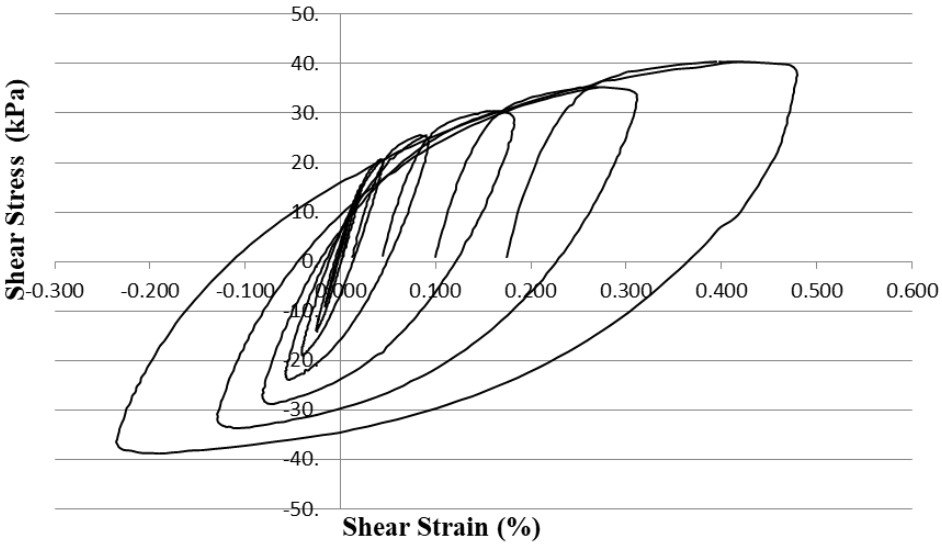

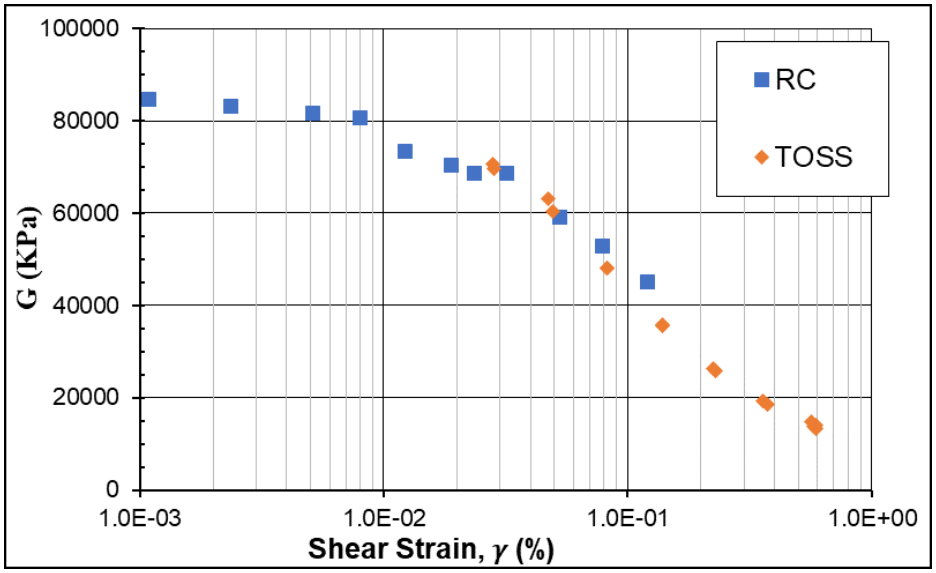

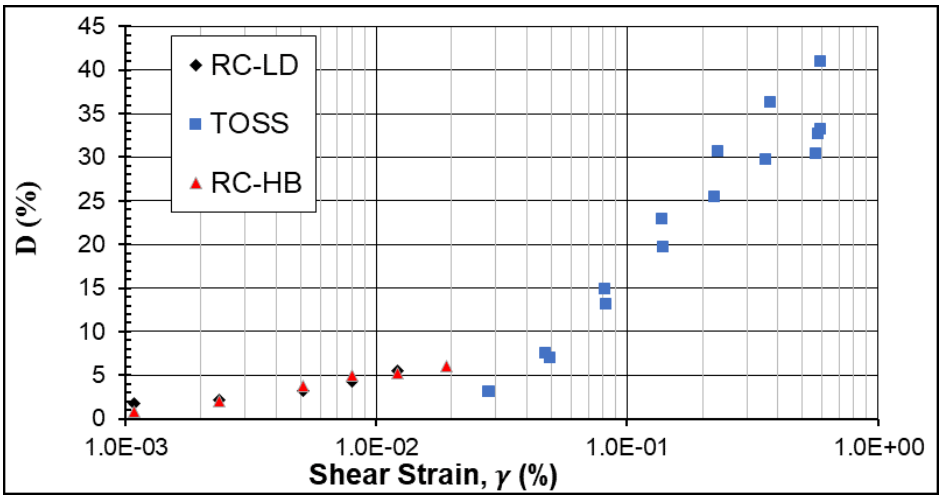

Test#2 measurement results (Sample A, Loose)

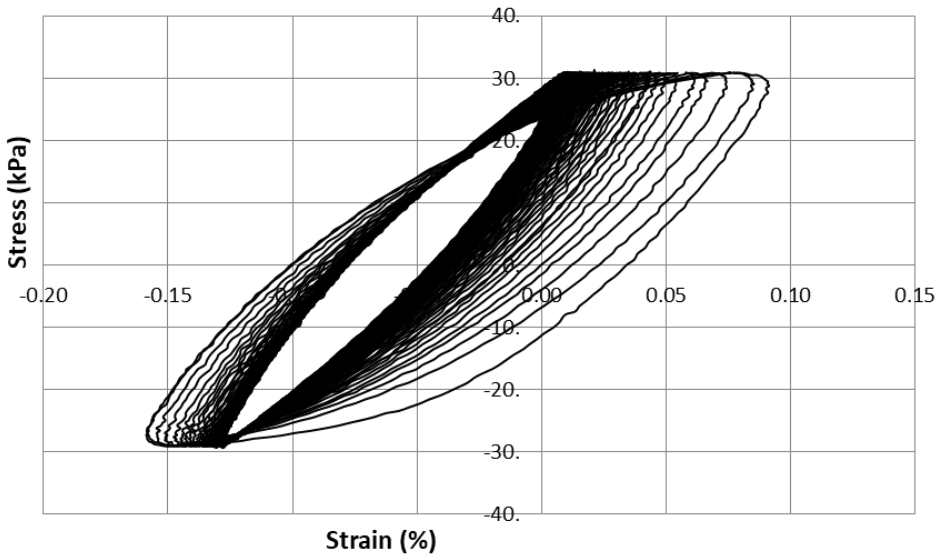

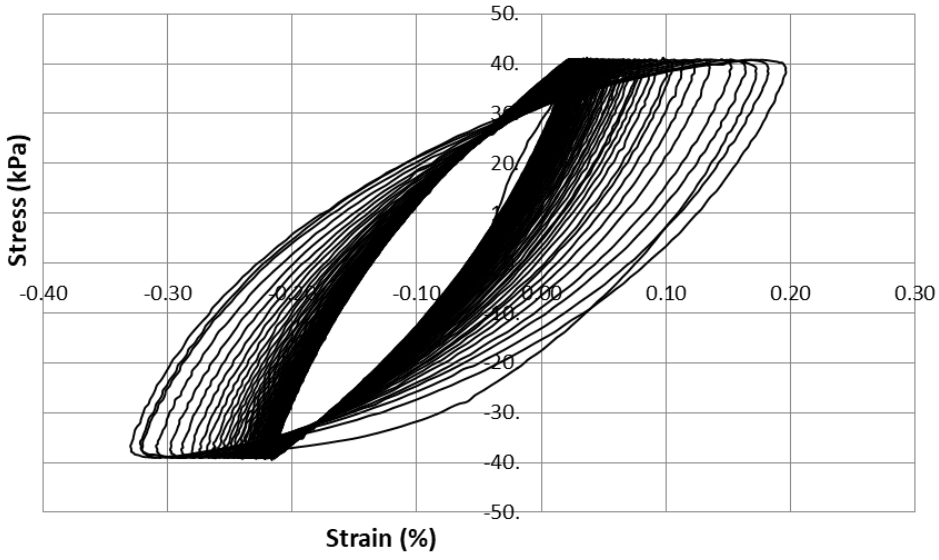

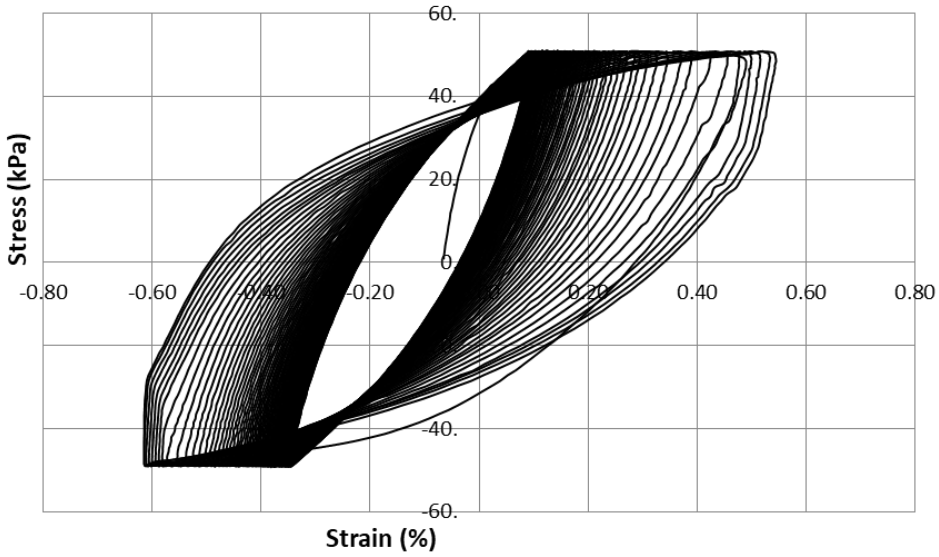
Stress (kPa)
60.
40.
20.
0.
-40.
-60.
-0.80
-0.60
-0.40
-0.20
0.20
0.40
0.60
0.80
Strain (%)

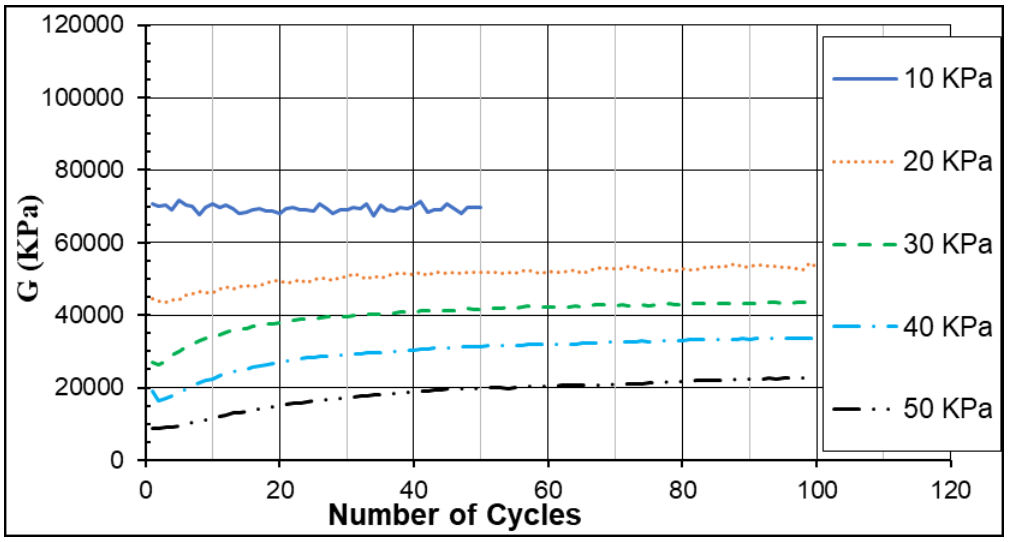
G (KPa)
120000
100000
80000
60000
40000
20000
0
0
20
40
60
80
100
120
Number of Cycles
10 KPa
20 KPa
30 KPa
40 KPa
50 KPa

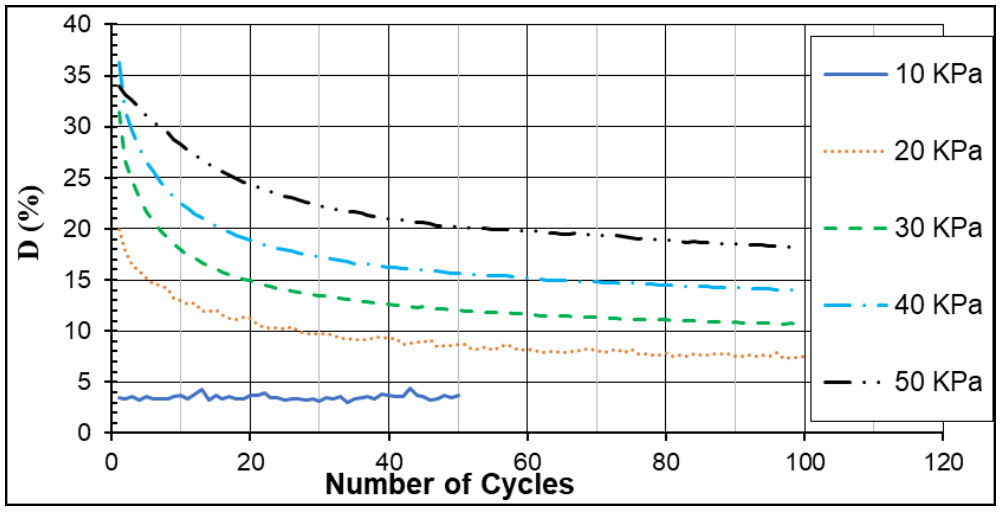
D (%)
40
35
30
25
20
15
10
5
0
0
20
40
60
80
100
120
Number of Cycles
10 KPa
20 KPa
30 KPa
40 KPa
50 KPa

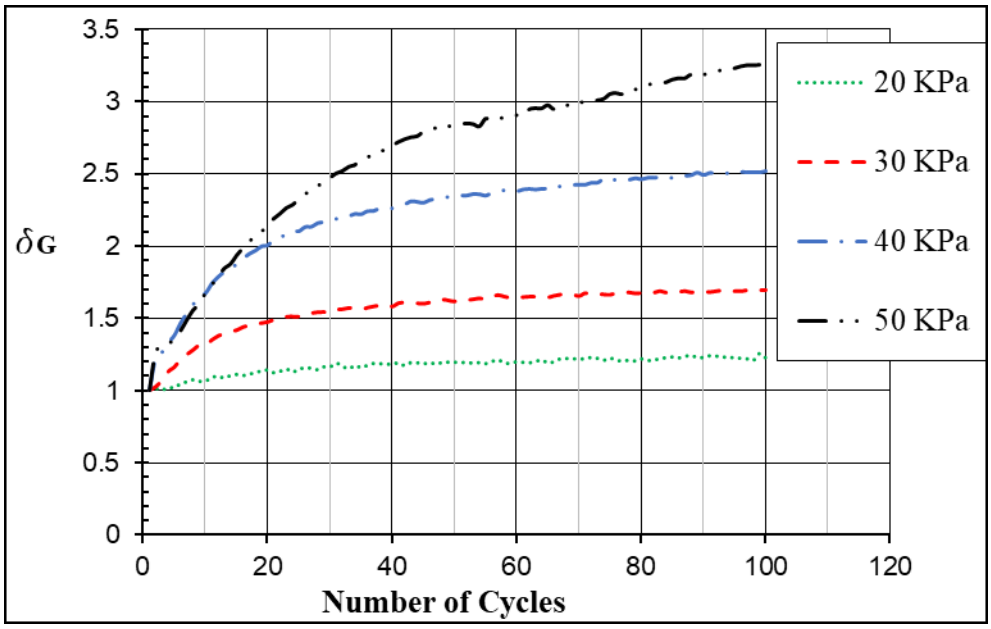

Test#3 measurement results (Sample A, Dense)

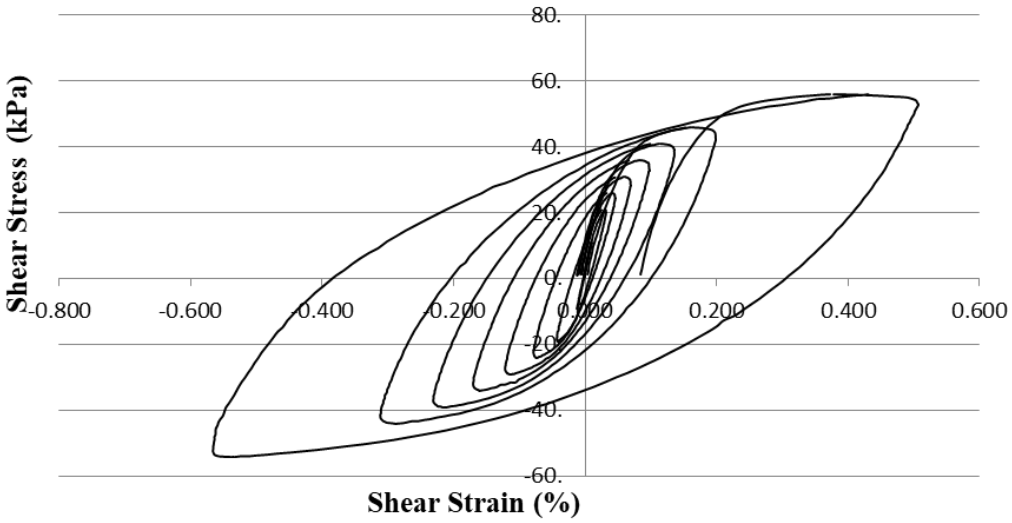

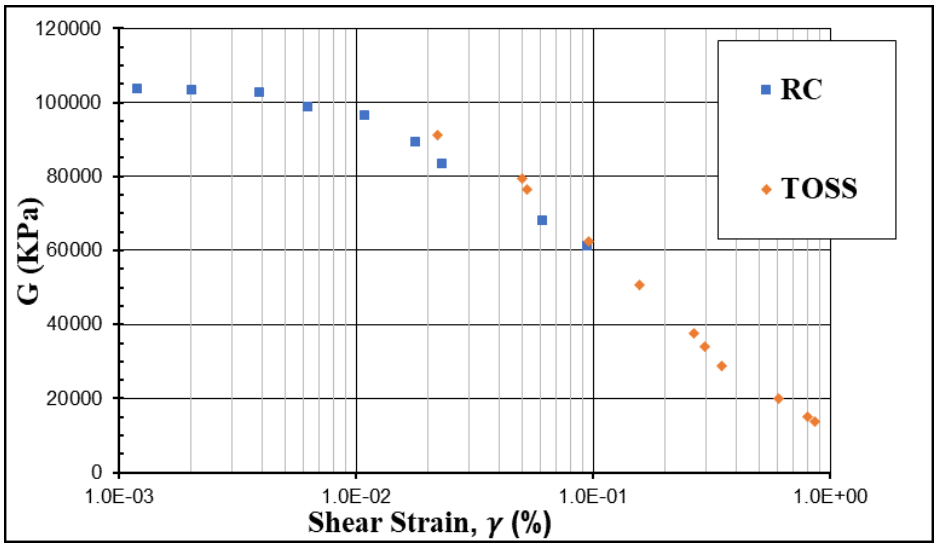

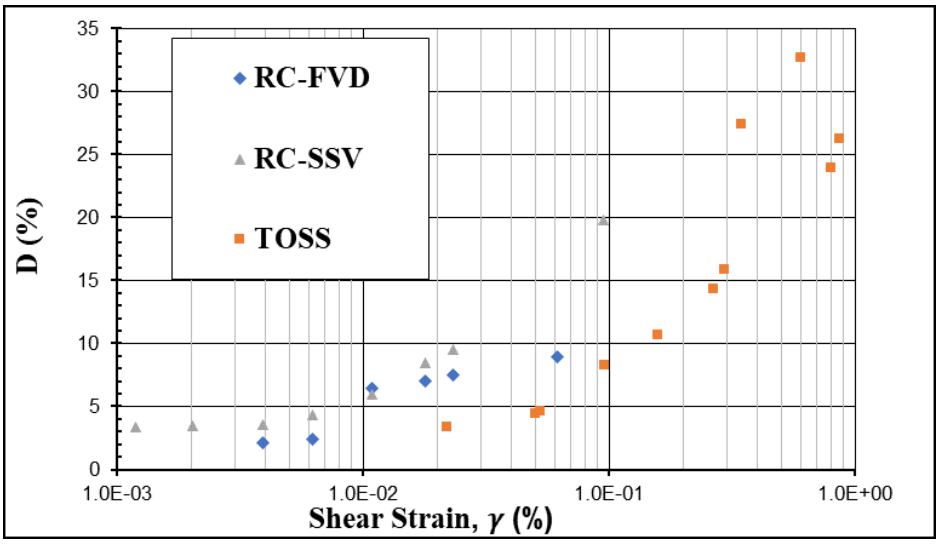

Test#4 measurement results (Sample A, Dense)

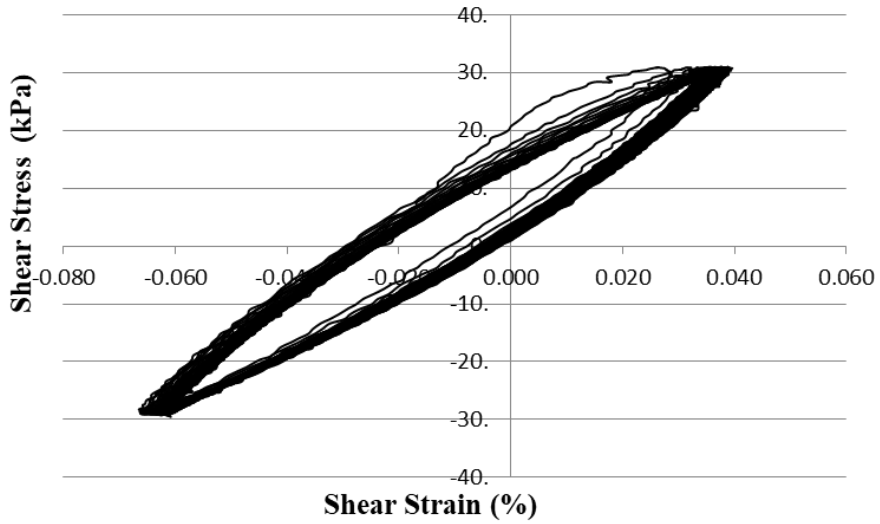

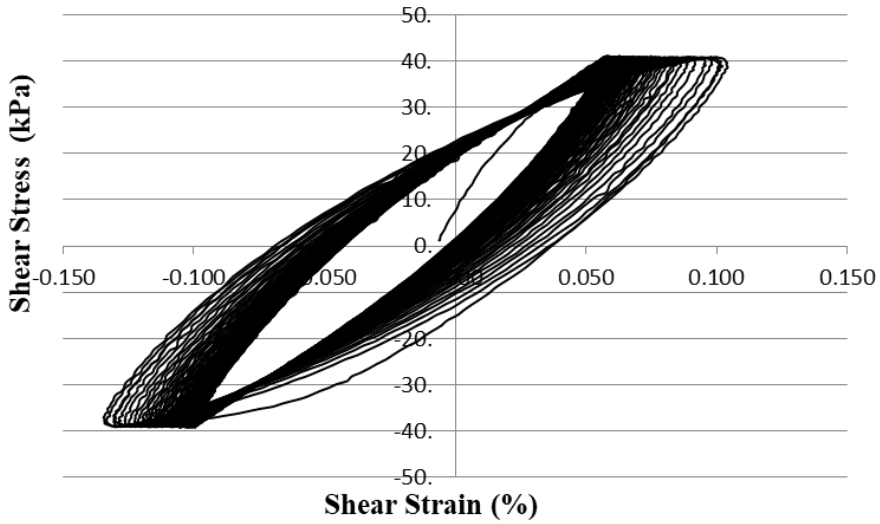

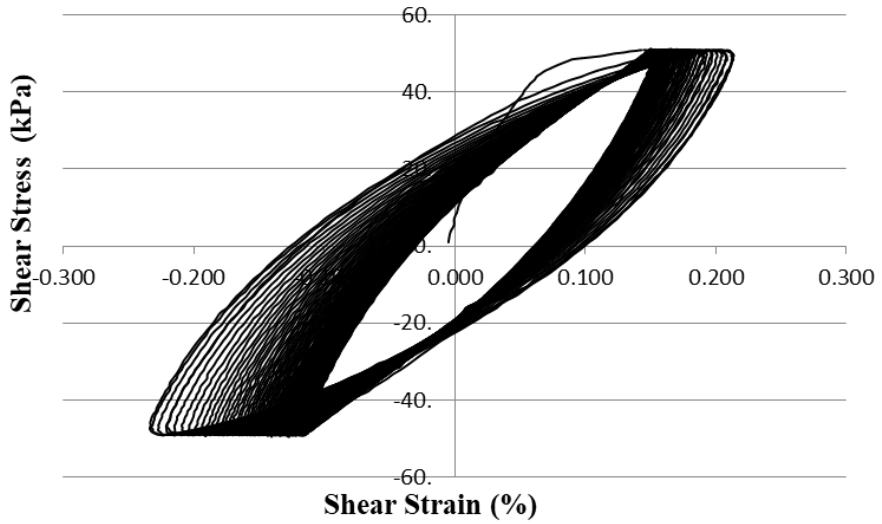
Shear Stress (kPa)
60.
40.
-0.300
-0.200
0.000
0.100
0.200
0.300
-20.
-40.
-60.
Shear Strain (%)

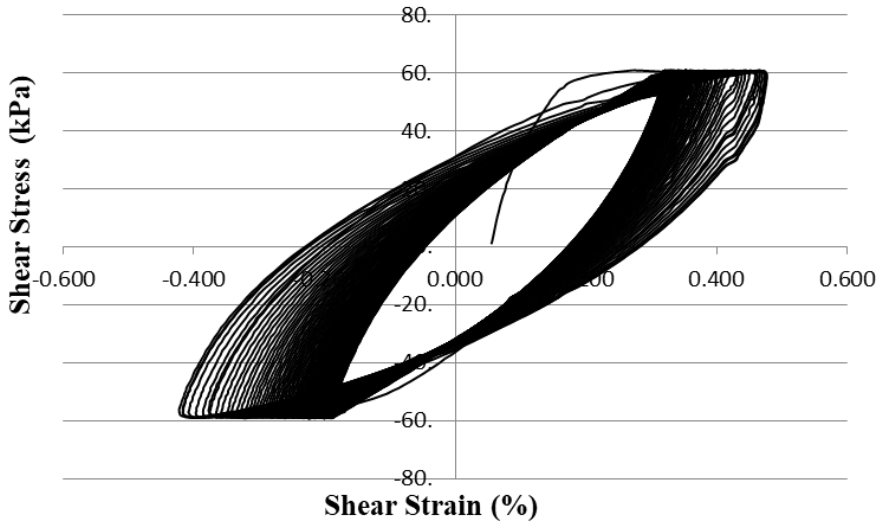
Shear Stress (kPa)
80.
60.
40.
-0.600
-0.400
0.000
0.400
0.600
-20.
-60.
-80.
Shear Strain (%)

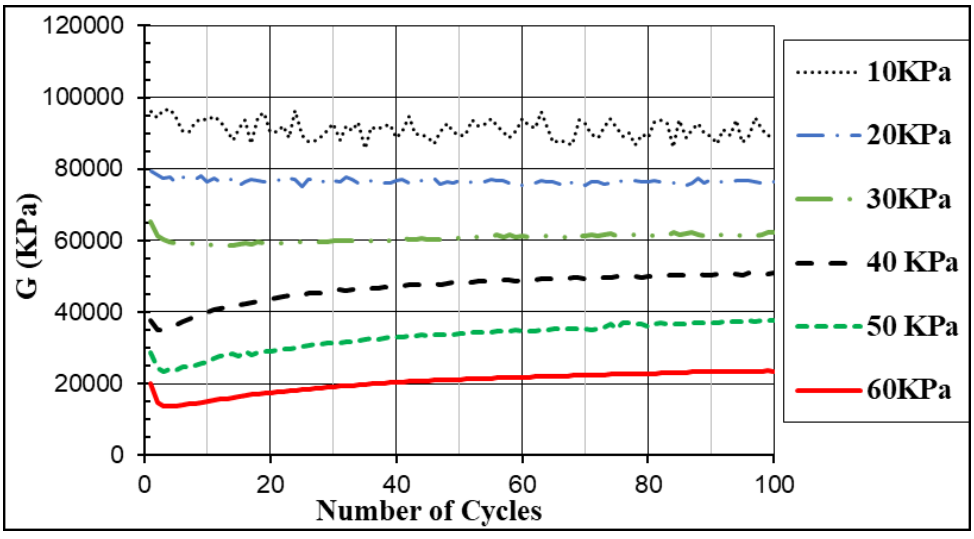
G (KPa)
120000
100000
80000
60000
40000
20000
0
0
20
40
60
80
100
Number of Cycles
10KPa
20KPa
30KPa
40 KPa
50 KPa
60KPa

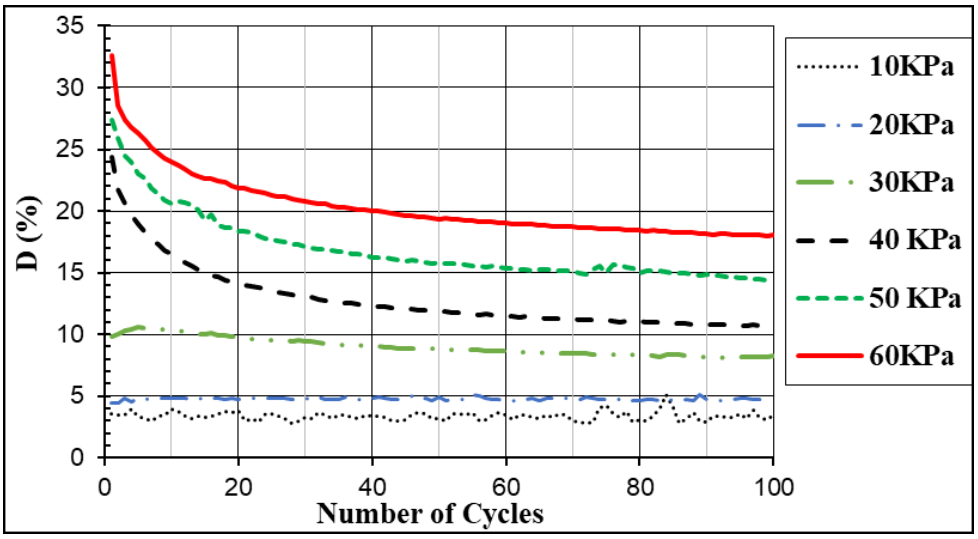

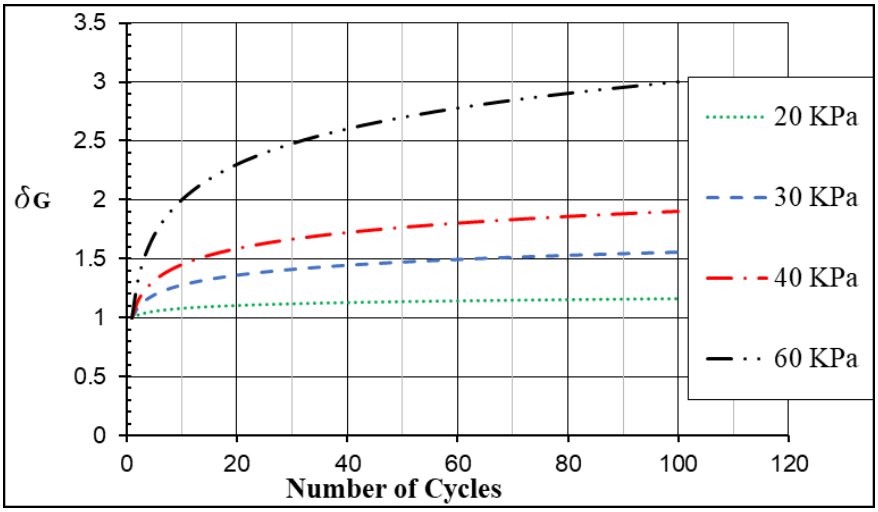

Test#5 measurement results (Sample B, Loose)

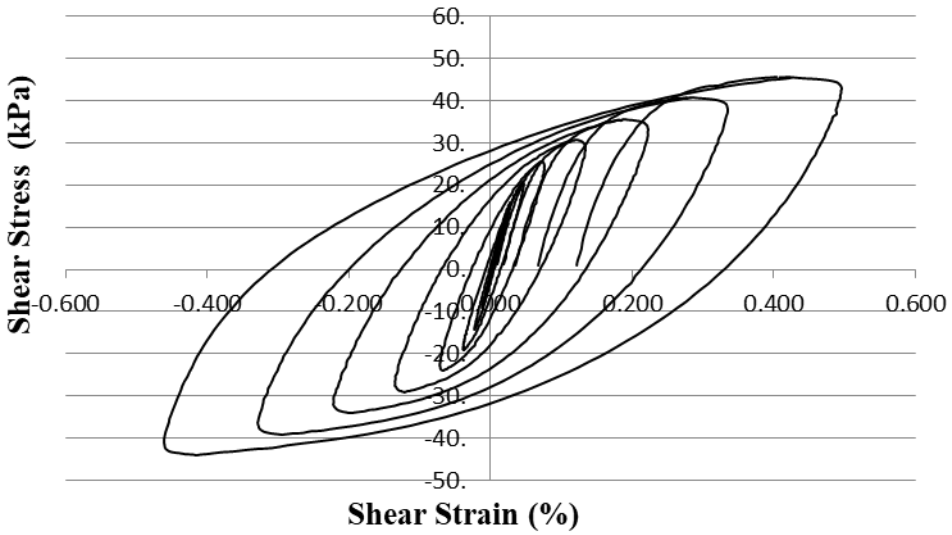

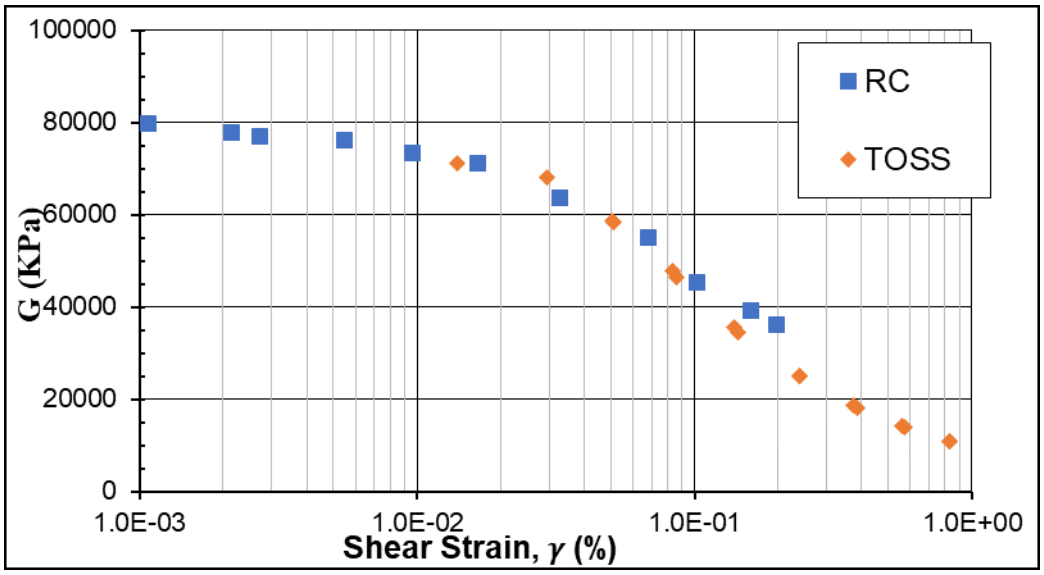

Test#6 measurement results (Sample B, Loose)

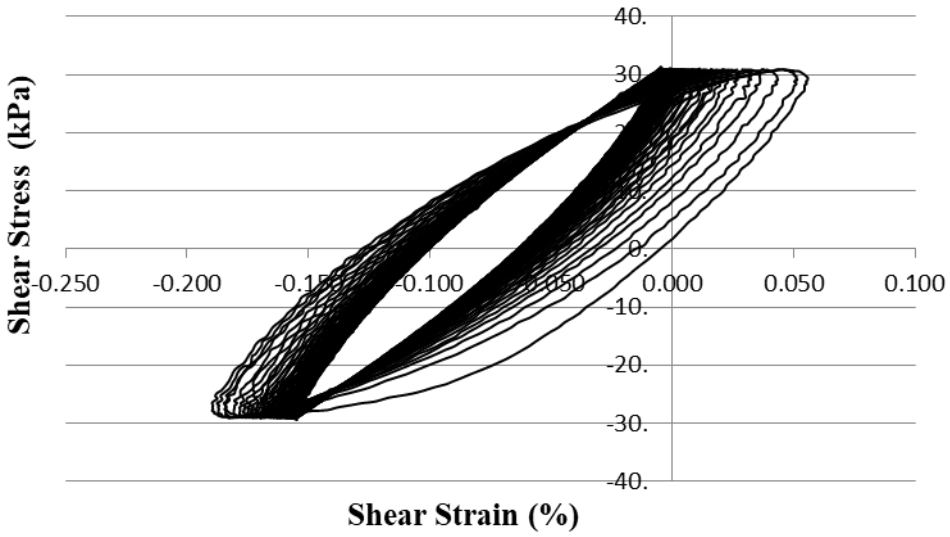

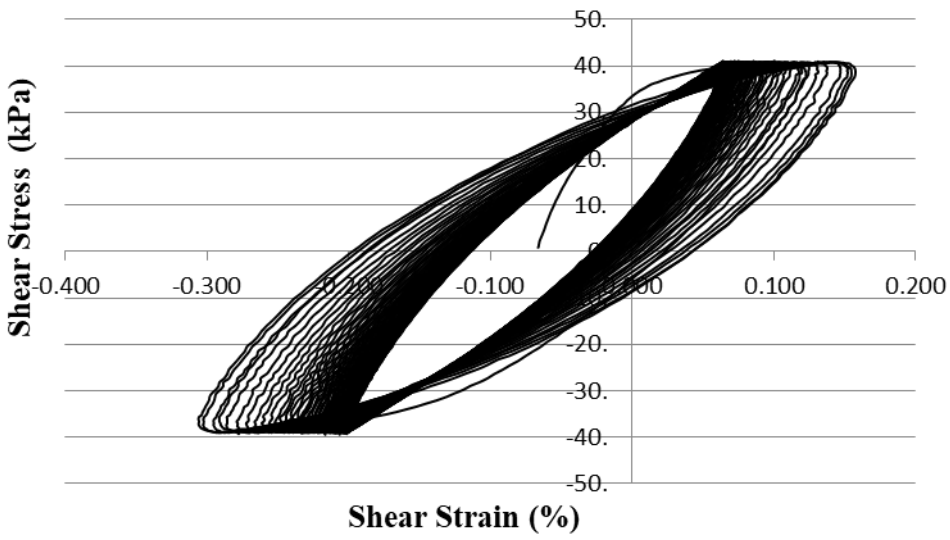
Shear Stress (kPa)
50.
40.
30.
10.
-20.
-30.
-40.
-50.
-0.400
-0.300
-0.100
0.100
0.200
Shear Strain (%)

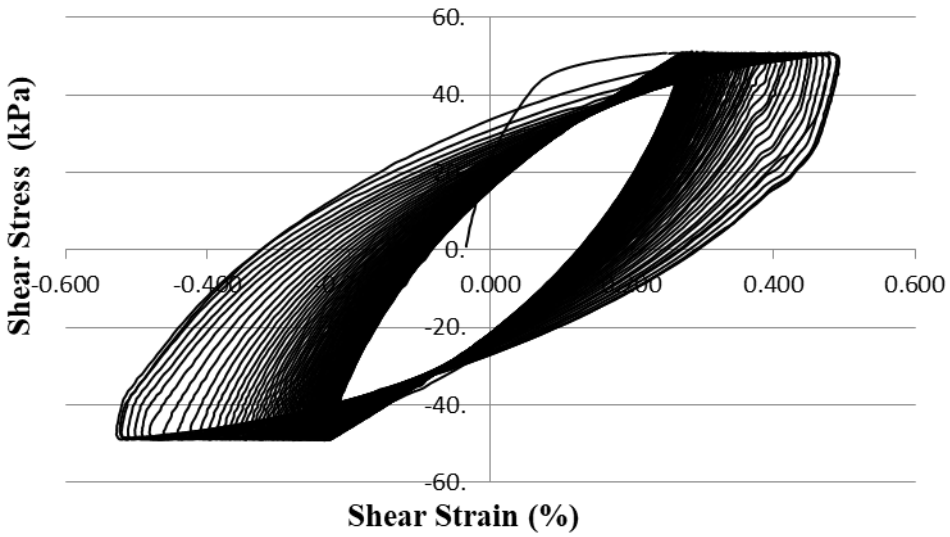
Shear Stress (kPa)
60.
40.
0.
-20.
-40.
-60.
-0.600
-0.400
0.000
0.400
0.600
Shear Strain (%)

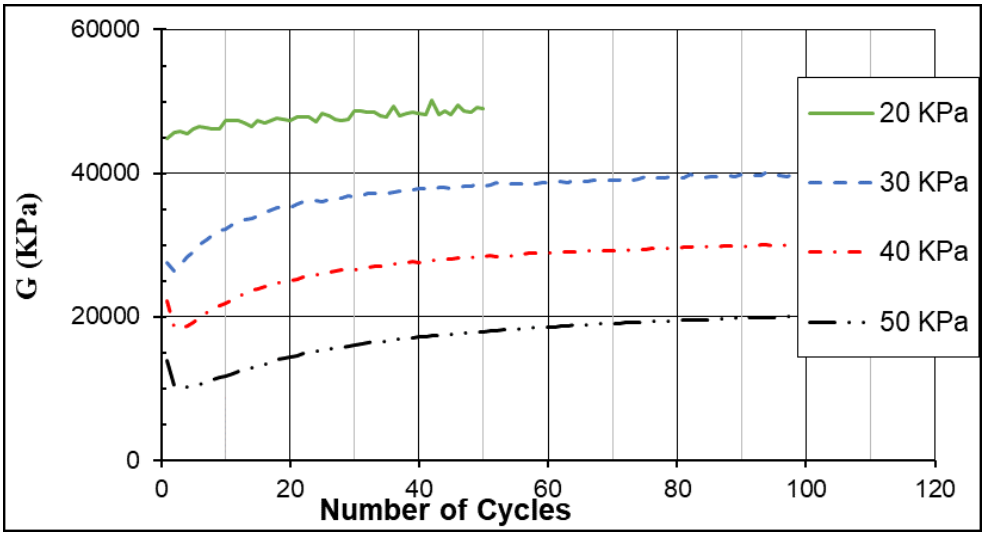
G (KPa)
60000
40000
20000
0
0
20
40
60
80
100
120
Number of Cycles
20 KPa
30 KPa
40 KPa
50 KPa

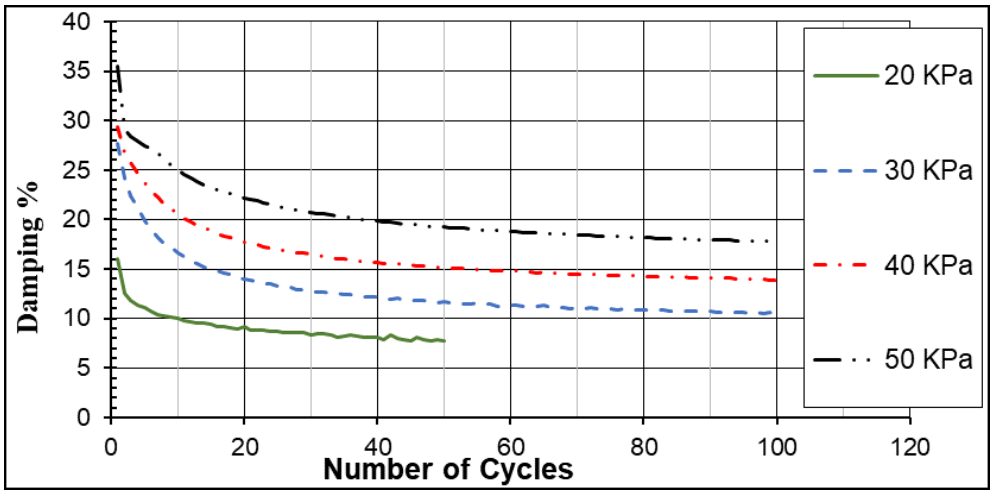

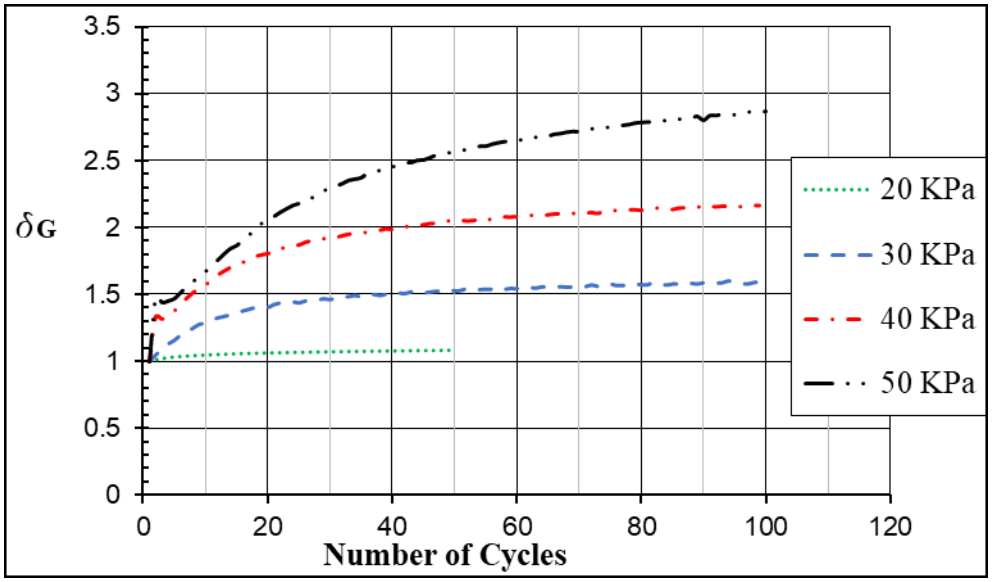

Test#7 measurement results (Sample B, Dense)

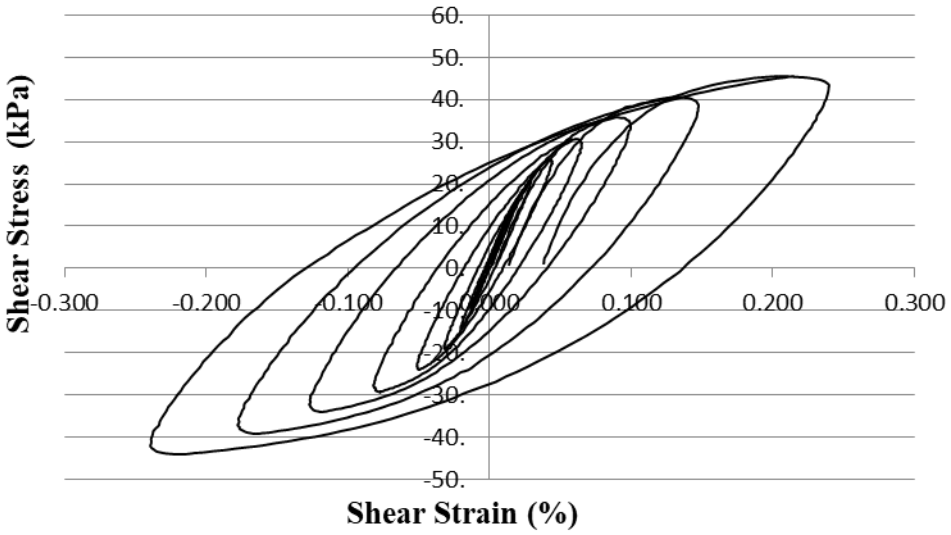

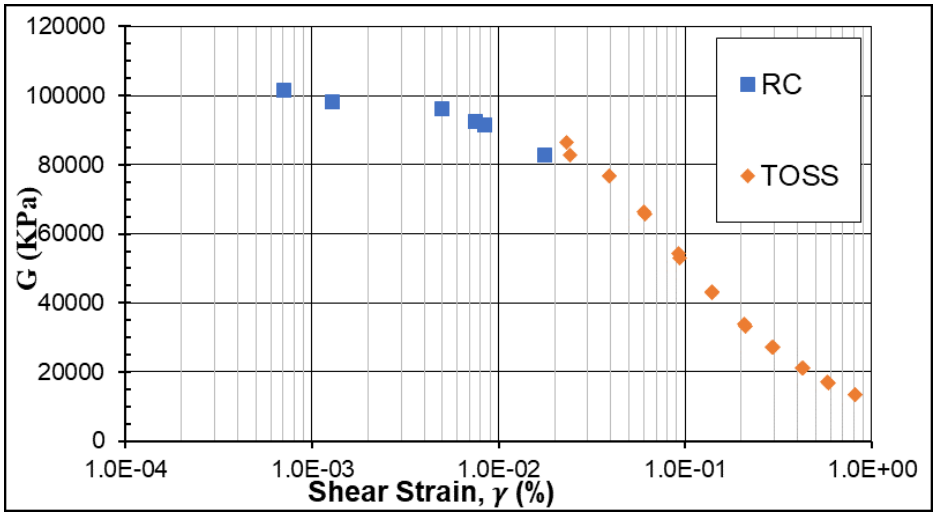

Test#8 measurement results (Sample B, Dense)

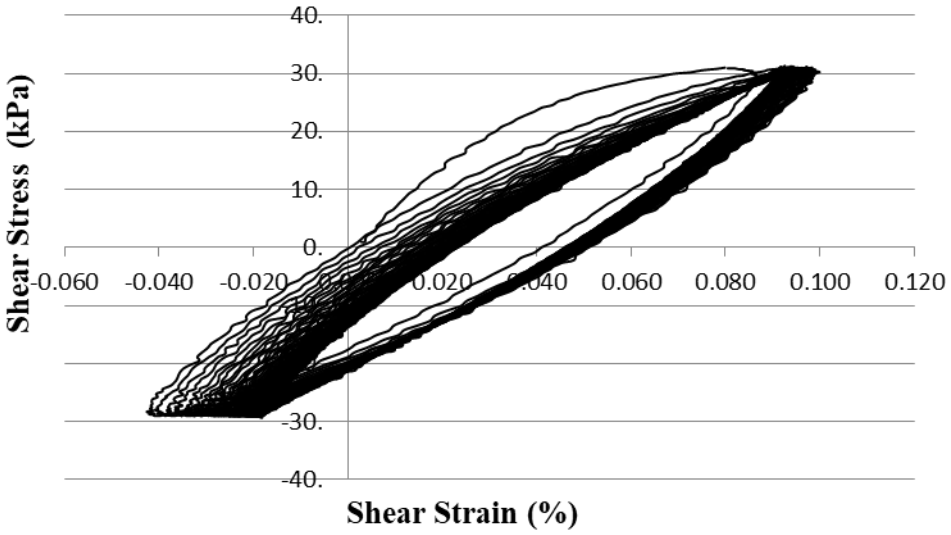

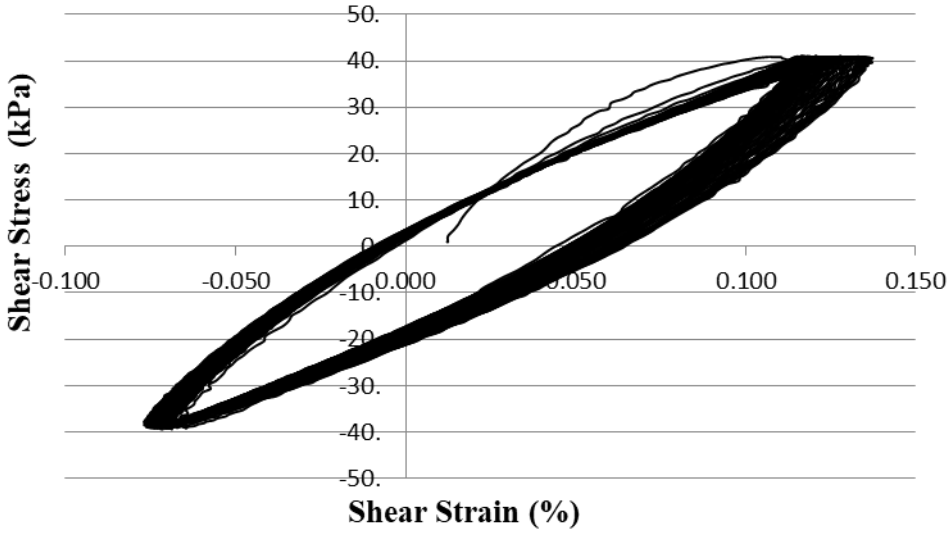
Shear Stress (kPa)
50.
40.
30.
20.
10.
0.
-10.
-20.
-30.
-40.
-50.
-0.100
-0.050
0.000
0.050
0.100
0.150
Shear Strain (%)

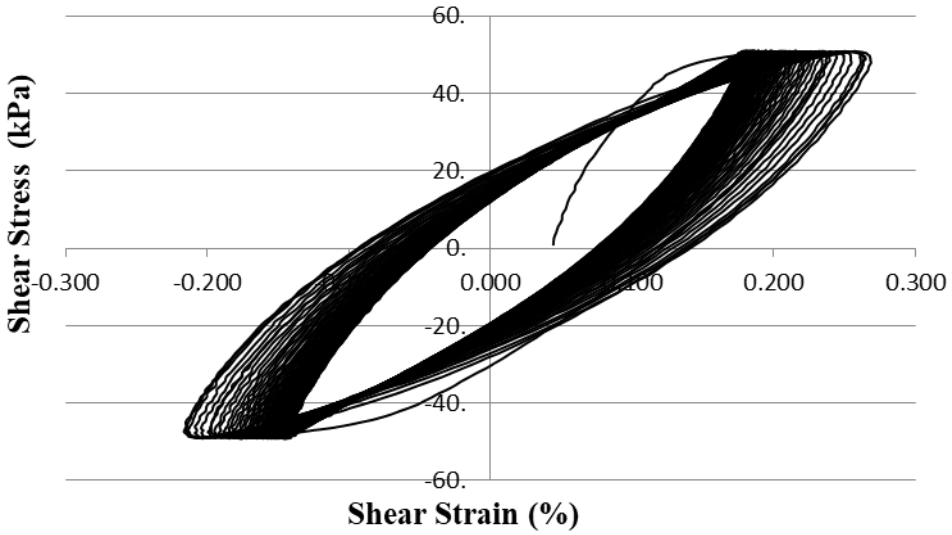
Shear Stress (kPa)
60.
40.
20.
0.
-20.
-40.
-60.
-0.300
-0.200
0.000
0.200
0.300
Shear Strain (%)

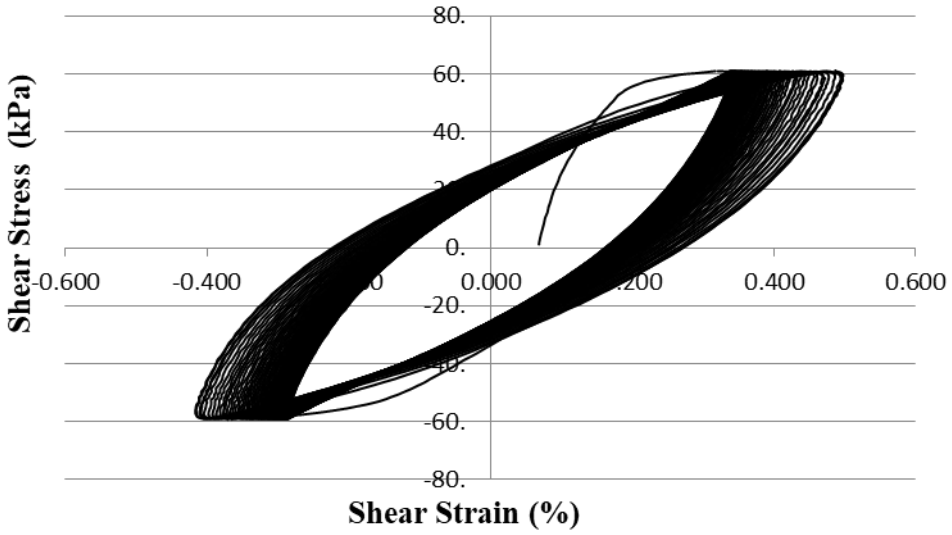
Shear Stress (kPa)
80.
60.
40.
0.
-20.
-60.
-80.
-0.600
-0.400
0.000
0.400
0.600
Shear Strain (%)

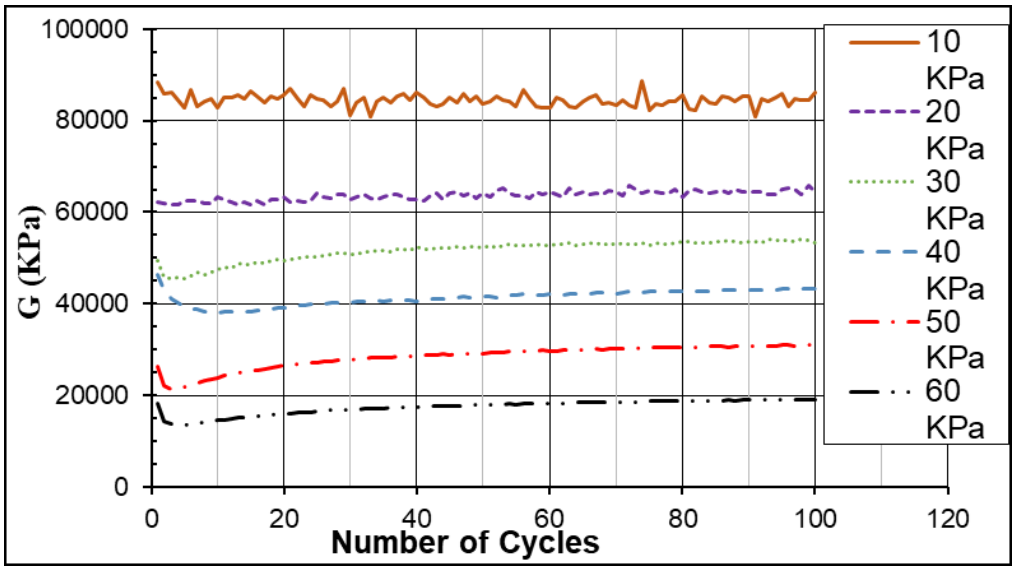
G (KPa)
100000
80000
60000
40000
20000
0
0
20
40
60
80
100
120
Number of Cycles
10 KPa
20 KPa
30 KPa
40 KPa
50 KPa
60 KPa

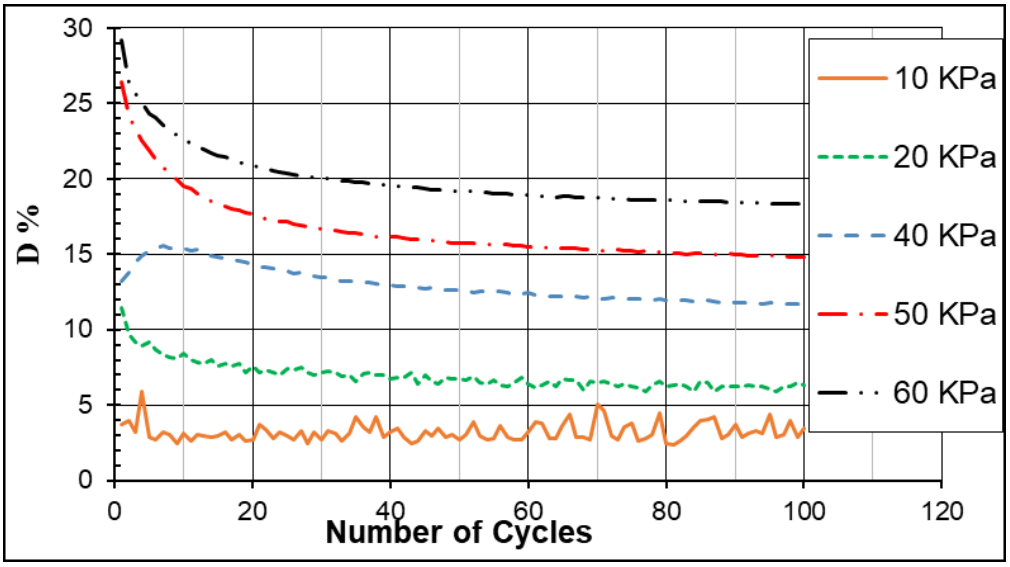
D %
30
25
20
15
10
5
0
0
20
40
60
80
100
120
Number of Cycles
10 KPa
20 KPa
40 KPa
50 KPa
60 KPa

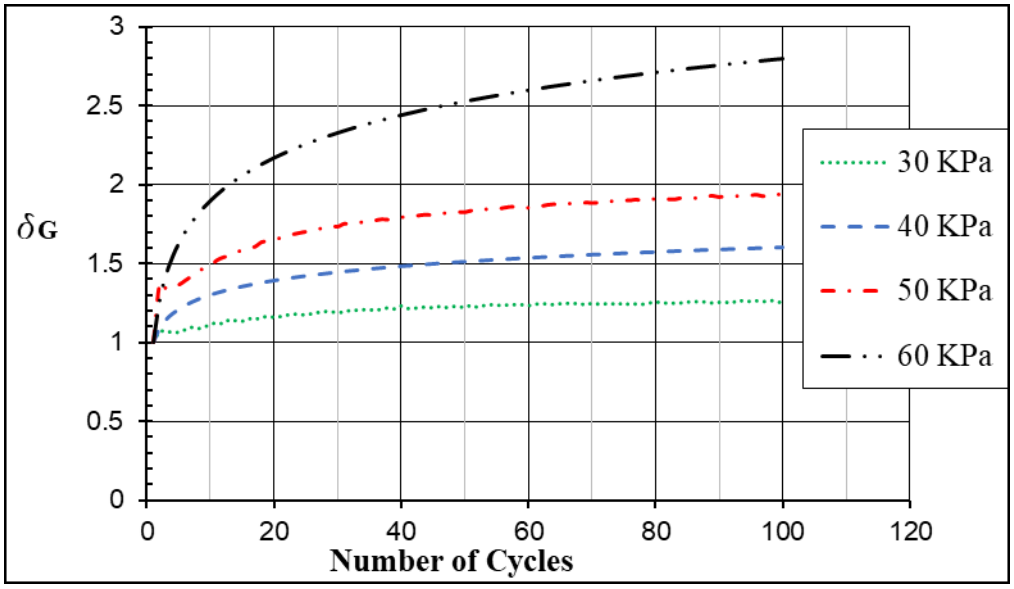
δG
3
2.5
2
1.5
1
0.5
0
0
20
40
60
80
100
120
Number of Cycles
30 KPa
40 KPa
50 KPa
60 KPa

Test#9 measurement results (Sample C, Loose)

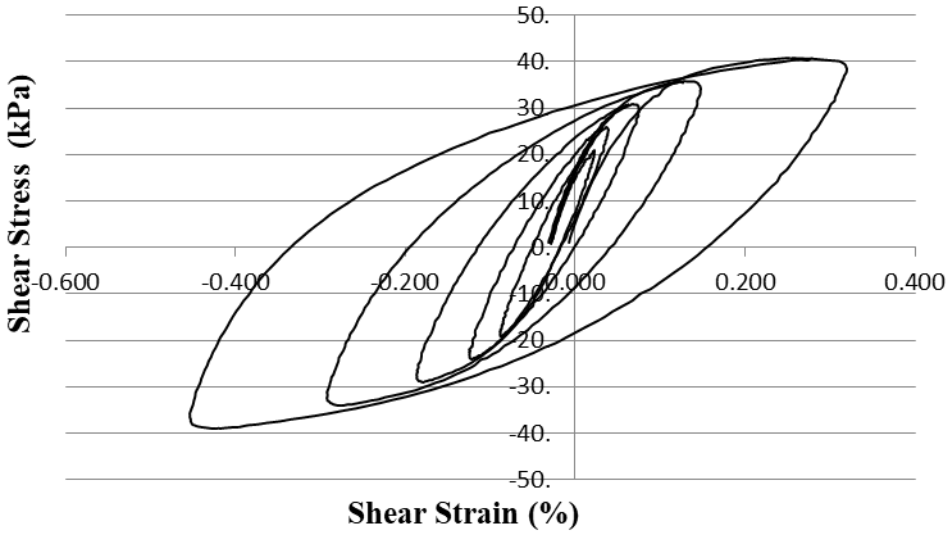

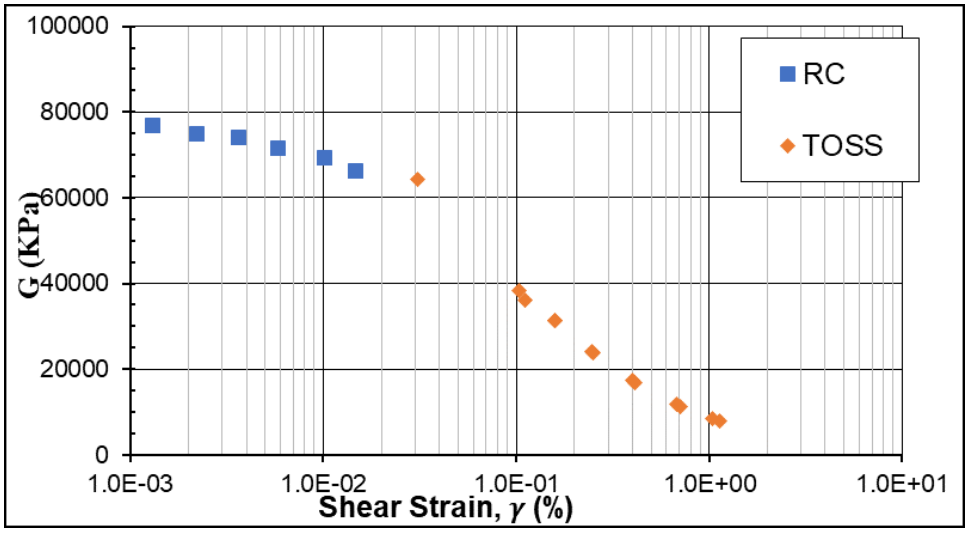

Test#10 measurement results (Sample C, Loose)

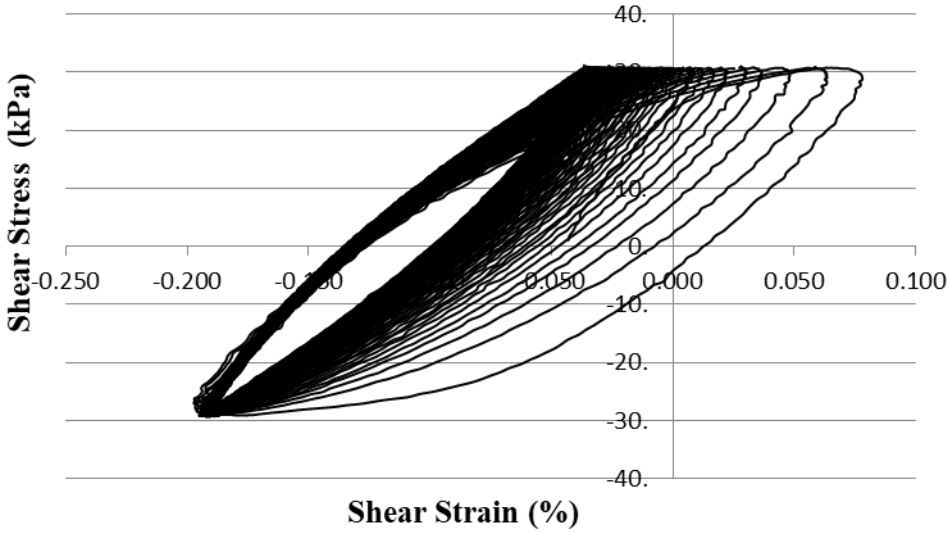

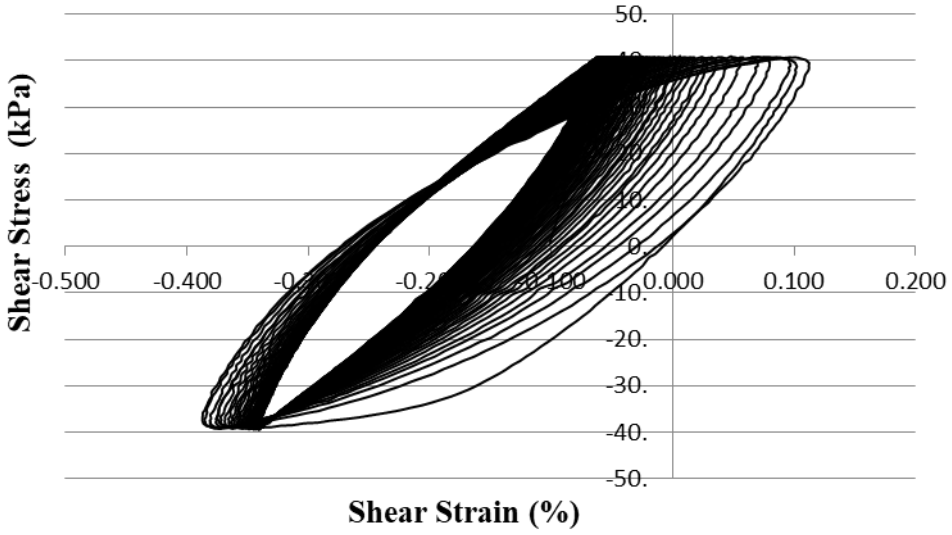
Shear Stress (kPa)
50.
10.
0.
-10.
-20.
-30.
-40.
-50.
-0.500
-0.400
0.000
0.100
0.200
Shear Strain (%)

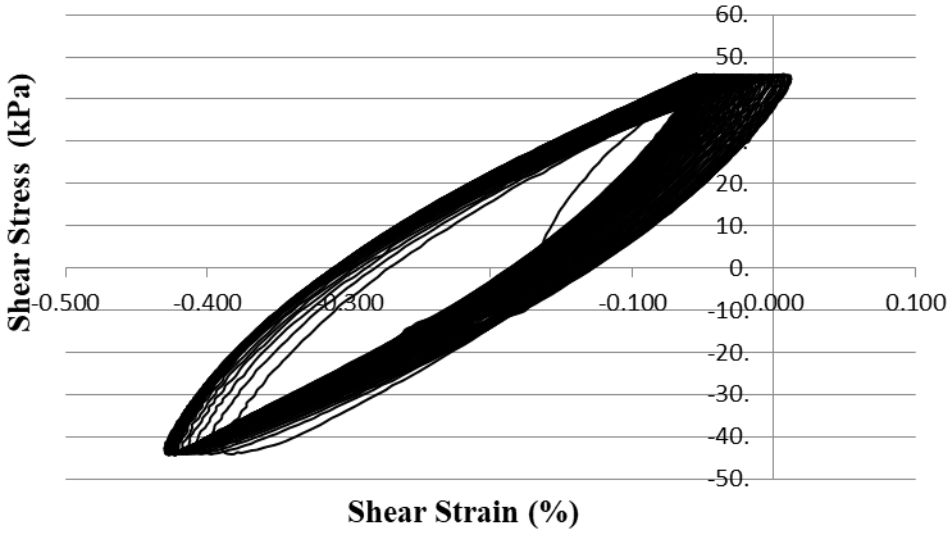
Shear Stress (kPa)
60.
50.
20.
10.
0.
-10.
-20.
-30.
-40.
-50.
-0.500
-0.400
-0.300
-0.100
0.000
0.100
Shear Strain (%)

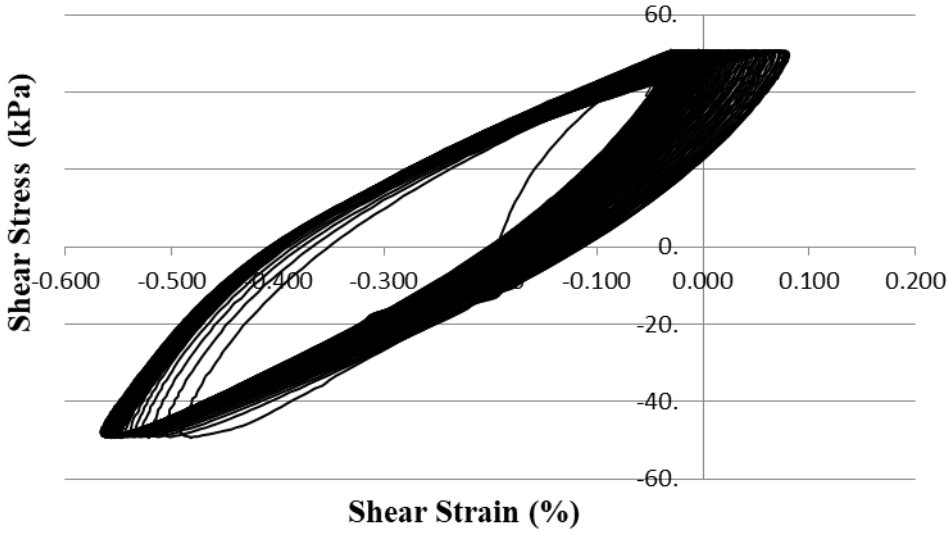
Shear Stress (kPa)
60.
0.
-20.
-40.
-60.
-0.600
-0.500
-0.400
-0.300
-0.100
0.000
0.100
0.200
Shear Strain (%)

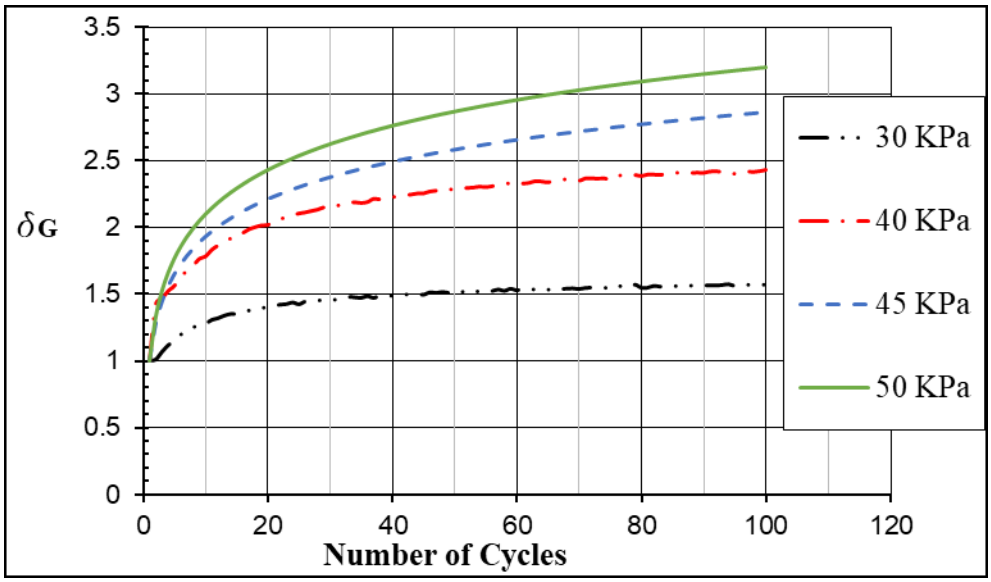

Test#11 measurement results (Sample C, Dense)

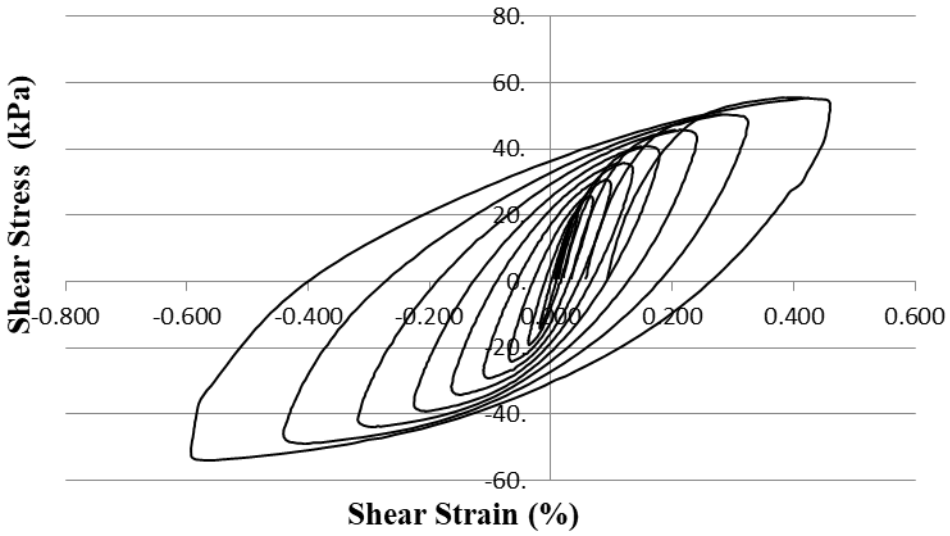

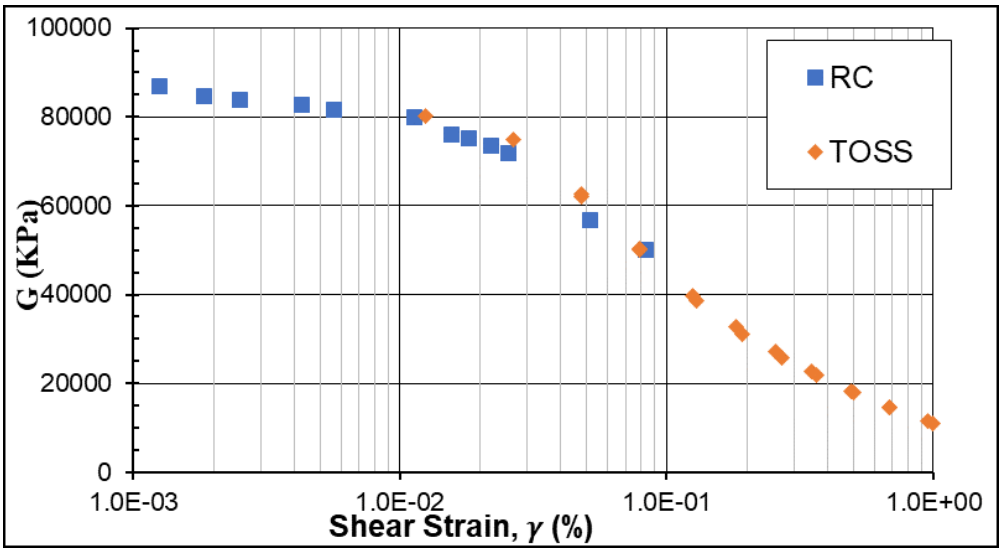

Test#12 measurement results (Sample C, Dense)

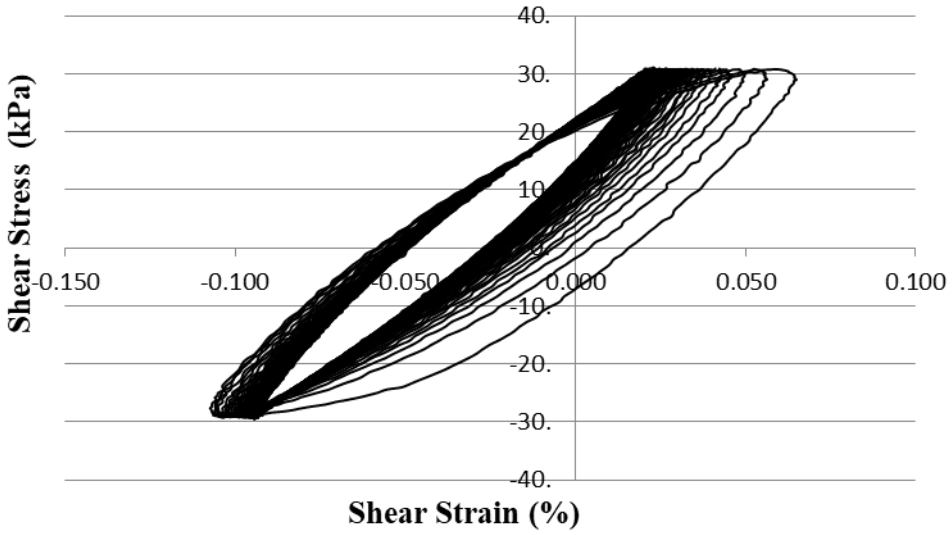

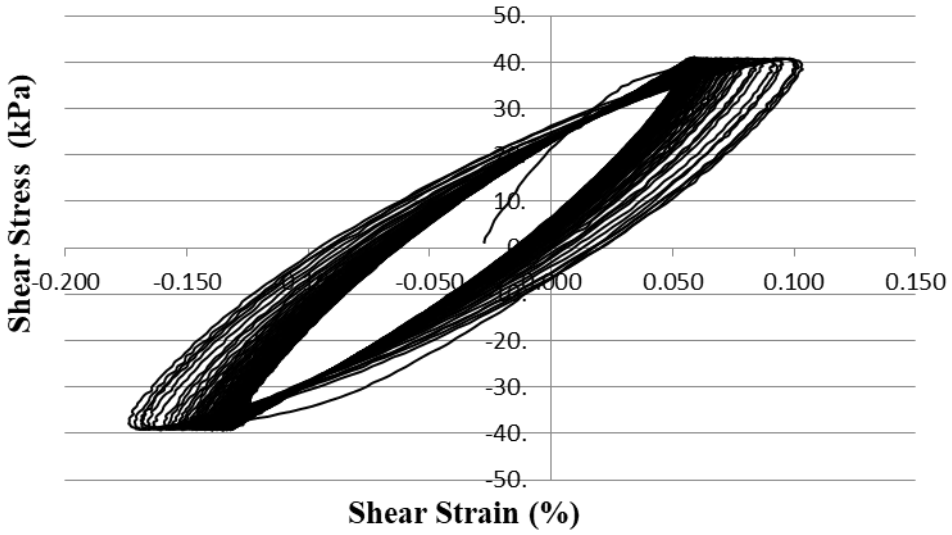

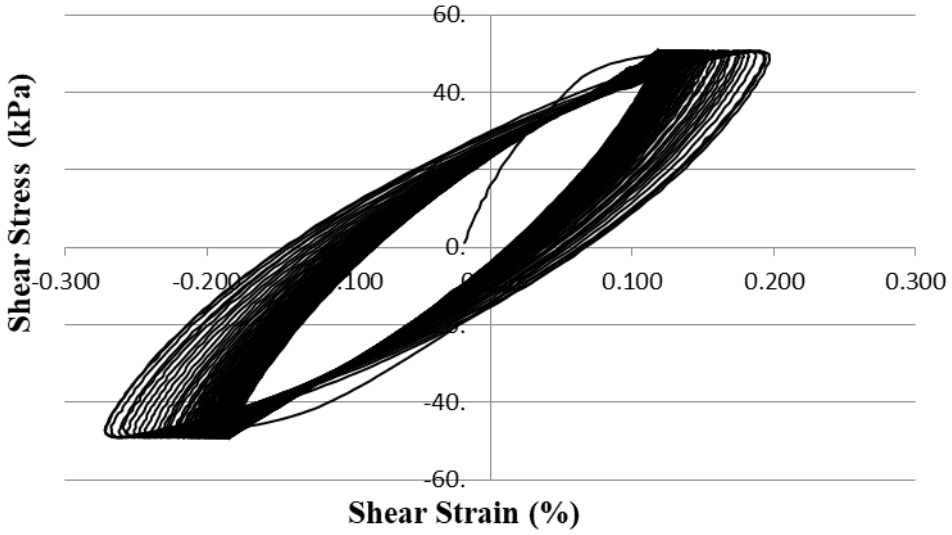

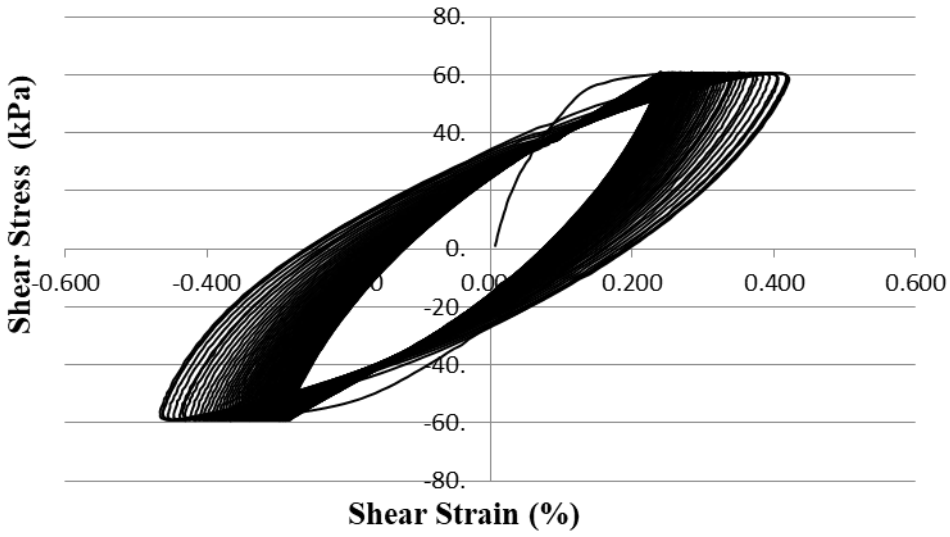
Shear Stress (kPa)
80.
60.
40.
0.
-20.
-40.
-60.
-80.
-0.600
-0.400
0.00
0.200
0.400
0.600
Shear Strain (%)

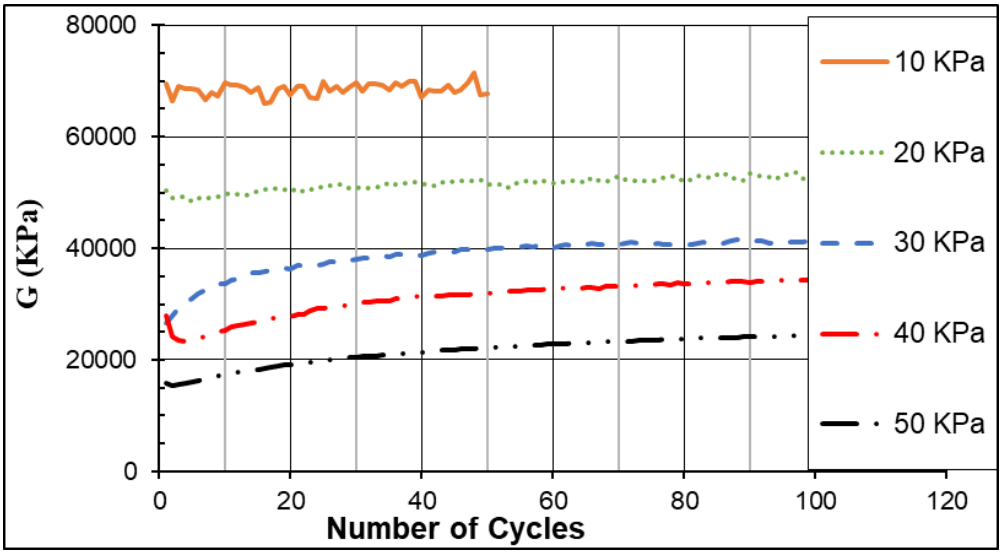
G (KPa)
80000
60000
40000
20000
0
0
20
40
60
80
100
120
Number of Cycles
10 KPa
20 KPa
30 KPa
40 KPa
50 KPa

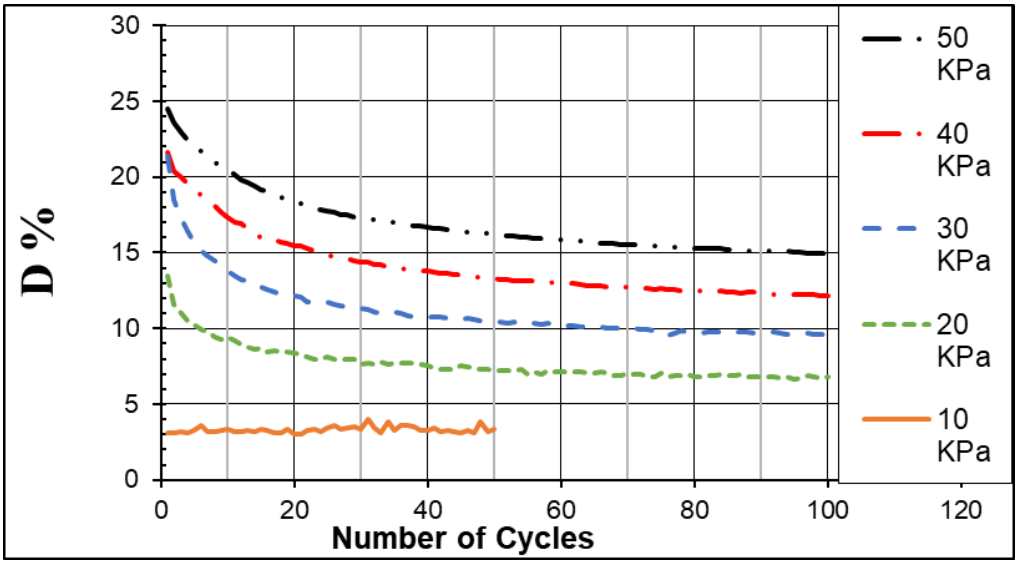
D %
30
25
20
15
10
5
0
0
20
40
60
80
100
120
Number of Cycles
50 KPa
40 KPa
30 KPa
20 KPa
10 KPa

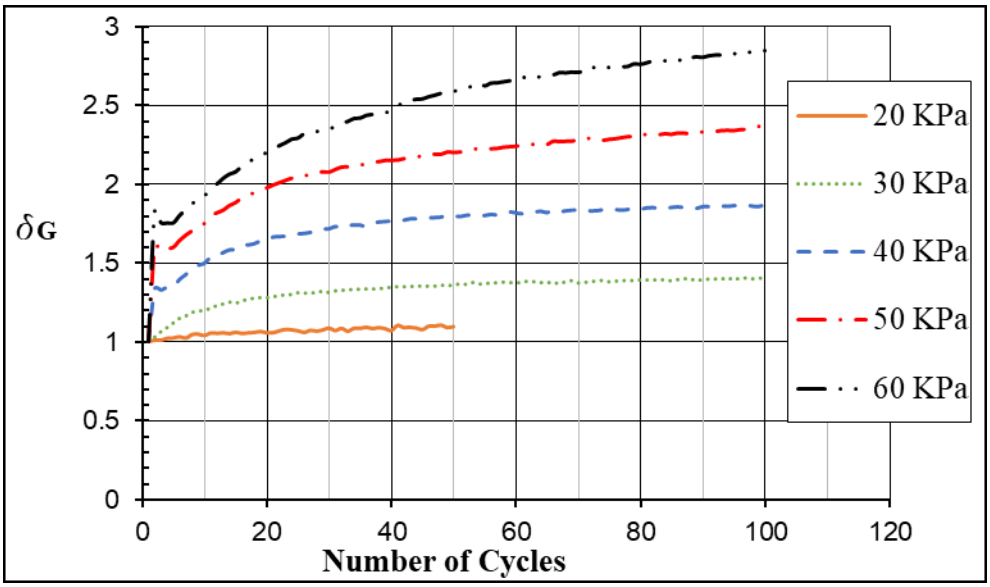
3
2.5
2
1.5
1
0.5
0
δG
0
20
40
60
80
100
120
Number of Cycles
20 KPa
30 KPa
40 KPa
50 KPa
60 KPa

Annex B - Developed Visual Basic codes

`This subroutine calculates the dynamic properties of a cyclic TOSS test for all cycles

```
Sub CycCal()

Dim Datasheet As Worksheet
Dim Calsheet As Worksheet
Dim i As Integer        'Counter for Row number
Dim j As Integer        'Counter for Column number
Dim k As Integer        'counter for cycle number
Dim n As Integer        ' counter to calculate the Gmax
Dim d As Integer        'counter to calculate the area
Dim Xav, Yav, up, down, G, a, b As Double   'To calculate Gmax
Dim taui1 As Single     'the starting and ending points of a cycle
Dim taui2 As Single
Dim gammai1 As Single
Dim gammai2 As Single
Dim tau1, tau2 As Single       'for damping calculations
Dim gamma1, gamma2 As Single
Dim gammaline1, gammaline2 As Single
Dim avgstreng As Single
Dim darea As Single
Dim cyclearea As Single
Dim damping As Single


'Setting the new summary sheet
Set Datasheet = ActiveSheet
Sheets.Add.Name = Datasheet.Name + "Cal"
Set Calsheet = ActiveSheet

Cells(1, 1) = "Cycle"
Cells(2, 1) = "#"
Cells(1, 2) = "Stress"
Cells(2, 2) = "KPa"
Cells(1, 3) = "Strain"
Cells(2, 3) = "mm/mm"
Cells(1, 4) = "Gsec"
Cells(2, 4) = "KPa"
Cells(1, 5) = "Gmax"
Cells(2, 5) = "Kpa"
Cells(1, 6) = "Cycle Area"
Cells(2, 6) = "mm2"
Cells(1, 7) = "AVGstrain"
Cells(1, 8) = "Damping"
Cells(2, 8) = "%"

'Properties Calculations
k = 1
For i = 0 To 8
   For j = 0 To 19
      If i = 0 And j = 0 Then GoTo 10
      If Datasheet.Cells(i * 204 + 2, 3 + j * 6).Value = "" Then GoTo 20
      Calsheet.Cells(k + 2, 1) = Datasheet.Cells(i * 204 + 2, 3 + j * 6)      'Obtain Number of cycle
      Calsheet.Cells(k + 2, 2) = (Datasheet.Cells(i * 204 + 4, 2 + j * 6) - Datasheet.Cells(i * 204 + 104, 2
+ j * 6)) / 2  'Stress level
```

```
            Calsheet.Cells(k + 2, 3) = (Datasheet.Cells(i * 204 + 4, 1 + j * 6) - Datasheet.Cells(i * 204 + 104, 1
+ j * 6)) / 100  'Strain level P-P
            Calsheet.Cells(k + 2, 4) = Calsheet.Cells(k + 2, 2) * 2 / Calsheet.Cells(k + 2, 3)   'Calculate Gsec

         'Calculate Gmax by finding the slope of the line of the first 32 datapoints
            G = 0
            Xav = 0
            Yav = 0
            a = 0
            b = 0
            up = 0
            down = 0
            For n = 1 To 32
               Yav = Yav + Datasheet.Cells(i * 204 + 3 + n, 2 + j * 6)
               Xav = Xav + Datasheet.Cells(i * 204 + 3 + n, 1 + j * 6)
            Next n
            Xav = Xav / (n - 1)
            Yav = Yav / (n - 1)
            For n = 1 To 32
               a = (Datasheet.Cells(i * 204 + 3 + n, 1 + j * 6) - Xav) * (Datasheet.Cells(i * 204 + 3 + n, 2 + j * 6)
- Yav)
               b = (Datasheet.Cells(i * 204 + 3 + n, 1 + j * 6) - Xav) ^ 2
               up = up + a
               down = down + b
            Next n
            G = up / down * 100
            Calsheet.Cells(k + 2, 5) = G

         'Claclulate cycle area
            taui1 = Datasheet.Cells(i * 204 + 4, 2 + j * 6)      'Maximum Stress
            taui2 = Datasheet.Cells(i * 204 + 103, 2 + j * 6)    'Minimum Stress
            gammai1 = Datasheet.Cells(i * 204 + 4, 1 + j * 6) / 100  'Maximum Strain
            gammai2 = Datasheet.Cells(i * 204 + 103, 1 + j * 6) / 100    'Minimum Strain
            avgstreng = AvgStrainEnergy(gammai1, taui1, gammai2, taui2)   'Average strain energy
            Calsheet.Cells(k + 2, 7) = avgstreng
         'The equation of the line that connects the two ende of the cycle
            cyclearea = 0
            For d = 1 To 199      'area for the unloading loop
               tau1 = Datasheet.Cells(i * 204 + d + 3, 2 + j * 6)
               gamma1 = Datasheet.Cells(i * 204 + d + 3, 1 + j * 6) / 100
               tau2 = Datasheet.Cells(i * 204 + d + 4, 2 + j * 6)
               gamma2 = Datasheet.Cells(i * 204 + d + 4, 1 + j * 6) / 100
               gammaline1 = ((tau1 - taui1) / (taui2 - taui1) * (gammai2 - gammai1)) + gammai1
               gammaline2 = ((tau2 - taui1) / (taui2 - taui1) * (gammai2 - gammai1)) + gammai1
               darea = Abs(((gammaline2 - gamma2) + (gammaline1 - gamma1)) / 2 * (tau2 - tau1))
               cyclearea = cyclearea + darea
            Next d
            Calsheet.Cells(k + 2, 6) = cyclearea
            damping = cyclearea / (4 * 3.14159265358979 * avgstreng) * 100
            Calsheet.Cells(k + 2, 8) = damping
            k = k + 1   'next cycle

      10       Next j
      Next i

      20 Rows("1:1").Insert Shift:=xlDown, CopyOrigin:=xlFormatFromLeftOrAbove
         Range("A1:H1").Merge
         ActiveCell.FormulaR1C1 = "Cyclic Test Summary"
         Range("A1:H1").Select
         With Selection.Font
```

```
    .Name = "Timesnewroman"
    .Size = 14
End With
Range("A2:H3").Select
With Selection.Font
    .Name = "Timesnewroman"
    .Size = 12
End With
Columns("F:F").ColumnWidth = 10.89
Columns("G:G").ColumnWidth = 10.33
Columns("H:H").ColumnWidth = 9.78
Range("A1:H3").Select
With Selection.Interior
    .Pattern = xlSolid
    .PatternColorIndex = xlAutomatic
    .ThemeColor = xlThemeColorLight2
    .TintAndShade = 0.599993896298105
    .PatternTintAndShade = 0
    Range("A1:H104").Select
Selection.Borders(xlDiagonalDown).LineStyle = xlNone
Selection.Borders(xlDiagonalUp).LineStyle = xlNone
With Selection.Borders(xlEdgeLeft)
    .LineStyle = xlContinuous
    .ColorIndex = 0
    .TintAndShade = 0
    .Weight = xlThin
End With
With Selection.Borders(xlEdgeTop)
    .LineStyle = xlContinuous
    .ColorIndex = 0
    .TintAndShade = 0
    .Weight = xlThin
End With
With Selection.Borders(xlEdgeBottom)
    .LineStyle = xlContinuous
    .ColorIndex = 0
    .TintAndShade = 0
    .Weight = xlThin
End With
With Selection.Borders(xlEdgeRight)
    .LineStyle = xlContinuous
    .ColorIndex = 0
    .TintAndShade = 0
    .Weight = xlThin
End With
With Selection.Borders(xlInsideVertical)
    .LineStyle = xlContinuous
    .ColorIndex = 0
    .TintAndShade = 0
    .Weight = xlThin
End With
With Selection.Borders(xlInsideHorizontal)
    .LineStyle = xlContinuous
    .ColorIndex = 0
    .TintAndShade = 0
    .Weight = xlThin
End With
With Selection
    .HorizontalAlignment = xlGeneral
    .VerticalAlignment = xlCenter
```

```
        .WrapText = False
        .Orientation = 0
        .AddIndent = False
        .IndentLevel = 0
        .ShrinkToFit = False
        .ReadingOrder = xlContext
    End With
    With Selection
        .HorizontalAlignment = xlCenter
        .VerticalAlignment = xlCenter
        .WrapText = False
        .Orientation = 0
        .AddIndent = False
        .IndentLevel = 0
        .ShrinkToFit = False
        .ReadingOrder = xlContext
    End With
    End With
    Range("A1").Select
```

'For damping calculation using the logaretmic decrement method

---

```
Sub Filter()
Dim min As Integer
Dim max As Integer

ActiveSheet.Range(Cells(4, 3), Cells(100000, 4)).Clear
min = Cells(1, 2).Value
max = Cells(2, 2).Value

ActiveSheet.Range(Cells(min + 4, 1), Cells(max + 4, 2)).Copy
Cells(4, 3).Select
ActiveSheet.Paste


End Sub
```

'Standard RO one-way formulation

```
Function gammaRO1(tau As Single, Gmax As Single, tmax As Single, Alpha As Single, C As Single, R As Single) As Single
  gammaRO1 = tau / Gmax * (1 + Alpha * Abs((tau / (C * tmax))) ^ (R - 1))
End Function
```

'Standard RO two-way formulation

```
Function GammaRO2(tau As Single, taui As Single, gami As Single, Gmax As Single, tmax As Single, Alpha As Single, C As Single, R As Single) As Single
  GammaRO2 = 2 * ((tau - taui) / (2 * Gmax) * (1 + Alpha * Abs(((tau - taui) / (2 * C * tmax))) ^ (R - 1))) + gami
End Function
```

'Function GammaROMidas is how Midas computes gamma from R-O formulation.

```
Function GammaROMidas(tau As Single, Gmax As Single, gamref As Single, Alpha As Single, beta As Single) As Single
 GammaROMidas = (tau + Alpha * Abs(tau) ^ beta * tau) / Gmax
End Function
```

'Function AvgStrainEnergy computes an averaged strain energy when the ends of a hysteresis loop are not symmetric. It draws a line from one end to the other and divides into two triangles at tau=0, one upward, one downward. This is because the gamma does not go through zero anymore. The bases of the triangles are a and b.

```
Function AvgStrainEnergy(gam1 As Single, tau1 As Single, gam2 As Single, tau2 As Single)
  Dim a As Single, b As Single
   b = (gam1 - gam2) / (1 - tau1 / tau2)
   a = gam1 - gam2 - b
   AvgStrainEnergy = 0.5 * (0.5 * Abs(tau1 * a) + 0.5 * Abs(tau2 * b))
End Function
```

'This subroutine does the curve fitting between the model and the testing results for all of the cycles to study the stiffening behavior.

```
Sub CurveFittingCyclic()

'Copy data to the a new sheet with two columns space for each cycle
Dim CyclesNum As Integer   'number of cycles
Dim Datasheet As Worksheet
Dim Calsheet As Worksheet
Dim Init As Single      'initial strain
Dim i As Integer
Dim j As Integer
Dim k As Integer
Dim m As Integer
Set Datasheet = ActiveSheet
Set Calsheet = ThisWorkbook.Sheets("CurveFitting")
Init = Datasheet.Cells(1, 2)
ThisWorkbook.Sheets("curveFitting").Activate

For i = 0 To 5


   For j = 0 To 19


   If Datasheet.Cells((i * 204) + 2, 6 * j + 3) = "" Then GoTo 10
    Calsheet.Cells(3, 2) = Datasheet.Cells((i * 204) + 2, 6 * j + 3)

      For k = 1 To 200


         Calsheet.Cells(k + 12, 1) = (Datasheet.Cells((i * 204) + (k + 3), 1 + j * 6) - Init) / 100
```

```
        Calsheet.Cells(k + 12, 2) = Datasheet.Cells((i * 204) + (k + 3), 2 + j * 6)

      Next k
    If i = 0 And j < 1 Then GoTo 20
       SolverOk SetCell:="$E$13", MaxMinVal:=2, ValueOf:=0, ByChange:="$B$9", Engine:= _
       1, EngineDesc:="GRG Nonlinear"
    SolverOk SetCell:="$E$13", MaxMinVal:=2, ValueOf:=0, ByChange:="$B$9", Engine:= _
      1, EngineDesc:="GRG Nonlinear"
    SolverSolve
    SolverOk SetCell:="$E$14", MaxMinVal:=2, ValueOf:=0, ByChange:="$G$9", Engine:= _
       1, EngineDesc:="GRG Nonlinear"
    SolverOk SetCell:="$E$14", MaxMinVal:=2, ValueOf:=0, ByChange:="$G$9", Engine:= _
      1, EngineDesc:="GRG Nonlinear"
    SolverSolve
    Calsheet.Cells((i * 19) + i + j + 12, 6) = Calsheet.Cells(3, 2)
    Calsheet.Cells((i * 19) + i + j + 12, 7) = Calsheet.Cells(7, 2)
    Calsheet.Cells((i * 19) + i + j + 12, 9) = Calsheet.Cells(9, 2)
    Calsheet.Cells((i * 19) + i + j + 12, 8) = Calsheet.Cells(9, 7)
    'Cells(5, 8) = Cells(212, 2)
    'Cells(5, 7) = Cells(212, 3)

20  Next j
'Cells(5, 8) = Cells(212, 2)
'Cells(5, 7) = Cells(212, 3)

Next i
10
End Sub
```

'Function TauHardinmod is my modified Hardin-Drnevich formulation.

```
Function TauHardinmod(gamma As Single, Gmax As Single, gamref As Single, m As Single) As Single

 TauHardinmod = (Gmax * gamma) / (1 + Abs((gamma / gamref) ^ m))
 End Function
```

'Function TauHardin2mod is my modified Hardin-Drnevich formulation for two-way loading.

```
 Function TauHardin2mod(gamma As Single, Gmax As Single, gamref As Single, tau1 As Single, gamma1 As Single, m As Single) As Single
TauHardin2mod = ((Gmax * (gamma - gamma1)) / (1 + (Abs((gamma - gamma1) / (2 * gamref))) ^ m)) + tau1

End Function
```

`This subroutine calculates divides the loops of an irregular TOSS test and calculates the dynamic properties.

```
Sub IrrTestAnalysis2()
Set datasheet = ThisWorkbook.Sheets("InputSheet")
'datacount = 1025
datacount = datasheet.Range("A2", Range("A2").End(xlDown)).Cells.Count
```

```
Dim tauraw(1 To 1000000) As Single
Dim gammaraw(1 To 1000000) As Single
'This section is for detecting the turning points and put each loop in a column in the tau and gamma matrices.
'The turning pont for each loop is also saved in the array taui and gammai.
'The number of data points is also saved in the array loopdatacount.


'read the input
For i = 1 To datacount
tauraw(i) = datasheet.Cells(i + 1, 1)
gammaraw(i) = datasheet.Cells(i + 1, 2)
Next i

j = 1
i = 0
For k = 1 To datacount
i = i + 1
tau(i, j) = tauraw(k)
gamma(i, j) = gammaraw(k)
        If j Mod 2 = 0 And tauraw(k + 1) > tauraw(k) Then
           taui(j) = tauraw(k)
           gammai(j) = gammaraw(k)
           loopdatacount(j) = i
           j = j + 1: i = 0
        ElseIf j Mod 2 <> 0 And tauraw(k + 1) < tauraw(k) Then
           taui(j) = tauraw(k)
           gammai(j) = gammaraw(k)
           loopdatacount(j) = i
           j = j + 1: i = 0
        End If

Next k
loopsNumber = j - 1



'Plot chart of divided loops

Dim xvalues() As Double 'the array that makes the strain values or x axis
Dim yvalues() As Double 'the array that makes the strain values or x axis
Dim cht As Chart
Set cht = Charts("chart1")
cht.ChartArea.Clear
With cht
   .ChartType = xlXYScatterLinesNoMarkers
   .Axes(xlValue, xlPrimary).HasTitle = True
   .Axes(xlValue, xlPrimary).AxisTitle.Caption = "Stress (KPa)"
   .Axes(xlValue, xlPrimary).AxisTitle.Font.Size = 24
   .Axes(xlCategory, xlPrimary).HasTitle = True
   .Axes(xlCategory, xlPrimary).AxisTitle.Caption = "Strain mm/mm"
   .Axes(xlCategory, xlPrimary).AxisTitle.Font.Size = 24
   .Axes(xlValue, xlPrimary).TickLabels.Font.Size = 18
   .Axes(xlCategory, xlPrimary).TickLabels.Font.Size = 18
   .Legend.Font.Size = 16
   'Change from matrix to an array for each of the loops in order to plot as an array
For j = 1 To loopsNumber
   ReDim xvalues(1 To loopdatacount(j))
   ReDim yvalues(1 To loopdatacount(j))
   For i = 1 To loopdatacount(j)
```

```
            xvalues(i) = gamma(i, j)
            yvalues(i) = tau(i, j)
        Next i
        .SeriesCollection.NewSeries
        .SeriesCollection(j).Format.Line.Weight = 3
        .FullSeriesCollection(j).Name = "Loop" & j
        .SeriesCollection(j).Values = yvalues
        .SeriesCollection(j).xvalues = xvalues
    Next j
    End With

    'Calculate the secant shear modulus for each loop
    ReDim gsec(loopsNumber) As Single
    ReDim strainpp(loopsNumber) As Single
    gsec(1) = (taui(1) - tau(1, 1)) / (gammai(1) - gamma(1, 1))
    strainpp(1) = gammai(1)
    For i = 2 To loopsNumber
        gsec(i) = (taui(i) - taui(i - 1)) / (gammai(i) - gammai(i - 1))
        strainpp(i) = gammai(i) - gammai(i - 1)
    Next i

    'Calculate damping for each of the loops
    Dim gammaline(1 To 500, 1 To 500) As Single 'the line that connects the two ends of the loop
    Dim darea(1 To 500, 1 To 500) As Single 'area of the trapazoids
    Dim halflooparea(1 To 500) As Single 'the total area between the loop and the straight line
    Dim avgstreng(1 To 500) As Single
    Dim damping(1 To 500) As Single

    'find the the straight line and average strain energy

    avgstreng(1) = AvgStrainEnergy(gamma(1, 1), tau(1, 1), gammai(1), taui(1))
    For i = 1 To loopdatacount(1)
        gammaline(i, 1) = ((tau(i, 1) - tau(1, 1)) / (taui(1) - tau(1, 1)) * (gammai(1) - gamma(1, 1))) + gam-
ma(1, 1)
    Next i
    For j = 2 To loopsNumber
        For i = 1 To loopdatacount(j)
        gammaline(i, j) = ((tau(i, j) - taui(j - 1)) / (taui(j) - taui(j - 1)) * (gammai(j) - gammai(j - 1))) + gam-
mai(j - 1)
        Next i
        avgstreng(j) = AvgStrainEnergy(gammai(j - 1), taui(j - 1), gammai(j), taui(j))
    Next j

    'Calculate the area between the curve and the straight line by dividing to trapazoids and summing there
areas.

    For j = 1 To loopsNumber
        For i = 2 To loopdatacount(j)
            darea(i, j) = ((gammaline(i, j) - gamma(i, j)) + (gammaline(i - 1, j) - gamma(i - 1, j))) / 2 * (tau(i, j) -
tau(i - 1, j))
            halflooparea(j) = halflooparea(j) + darea(i, j)
        Next i
        damping(j) = (2 * halflooparea(j)) / (4 * 3.14159265358979 * avgstreng(j)) * 100
    Next j

    'print the results in a seperate sheet
    Dim summsheet As Worksheet
    Set summsheet = ThisWorkbook.Sheets("summary")
    summsheet.Range("A4:XFD1048576").ClearContents
```

```
For j = 1 To loopsNumber
   summsheet.Cells(j + 3, 1).Value = j
   summsheet.Cells(j + 3, 2).Value = taui(j)
   summsheet.Cells(j + 3, 3).Value = gammai(j)
   summsheet.Cells(j + 3, 4).Value = gsec(j)
   summsheet.Cells(j + 3, 5).Value = strainpp(j)
   summsheet.Cells(j + 3, 6).Value = halflooparea(j)
   summsheet.Cells(j + 3, 7).Value = avgstreng(j)
   summsheet.Cells(j + 3, 8).Value = damping(j)

Next j

'print the loops to the "seperatedLoops" spreadsheet for further analysis
Dim printsheet As Worksheet
Set printsheet = ThisWorkbook.Sheets("SeperatedLoops")
printsheet.Cells.ClearContents
j = 1
Do Until j > (loopsNumber * 2)
printsheet.Cells(1, j).Value = "Loop" & j / 2 + 0.5
printsheet.Cells(2, j).Value = "Stress"
printsheet.Cells(2, j + 1).Value = "Strain"
j = j + 2
Loop
j = 1
Do Until j > (loopsNumber * 2)
   For i = 1 To loopdatacount(j / 2 + 0.5)
   printsheet.Cells(i + 2, j).Value = tau(i, j / 2 + 0.5)
   printsheet.Cells(i + 2, j + 1).Value = gamma(i, j / 2 + 0.5)
   Next i
   j = j + 2
Loop

End Sub
```

`This subroutine is a Ramberg-Osgood modeling for an irregular time history.

```
Sub ROMasing()

Dim taumax As Single
Dim gmax As Single
Dim alpha As Single
Dim C As Single
Dim R As Single
Dim gammaRO(1 To 500, 1 To 500) As Single ' Ramberg Osgood strains
Dim gammaiRO(1 To 500) As Single 'turning points of Ramber Osgood curves
Dim y As Integer 'counter for comoparing the curves
Dim gammamax As Single 'maximum strain so far
Dim z As Integer
Dim l As Integer

taumax = datasheet.Cells(3, 10)
gmax = datasheet.Cells(4, 10)
alpha = datasheet.Cells(5, 10)
C = datasheet.Cells(6, 10)
```

```
R = datasheet.Cells(7, 10)


'for the rest of the curves

For j = 1 To loopsNumber
   k = j - 1
   For i = 1 To loopdatacount(j)
      If k = 0 Then 'when the reloading curve intersects with the skeleton curve, no need to compare with previous anymore and it follow the skeleton curve
         gammaRO(i, j) = gammaRO1(tau(i, j), gmax, taumax, alpha, C, R)
         If gammaRO(i, j) > gammamax Then gammamax = gammaRO(i, j)
      ElseIf k = 1 Then 'when any unloading curve intersects with the first unloading curve, no need to compare it anymore
         gammaRO(i, j) = GammaRO2(tau(i, j), taui(k), gammaiRO(k), gmax, taumax, alpha, C, R)
         ElseIf i > 1 Then
            If gammaRO(i - 1, j) > gammamax Then 'when the loading curve exceeds the maximum strain
               gammaRO(i, j) = gammaRO1(tau(i, j), gmax, taumax, alpha, C, R)
               gammamax = gammaRO(i - 1, j)
            Else: GoTo 10
            End If
         Else
10       gammaRO(i, j) = GammaRO2(tau(i, j), taui(k), gammaiRO(k), gmax, taumax, alpha, C, R)
         l = k
         For z = l To 2 Step -2
         For y = 1 To loopdatacount(z - 1)
            If Abs(tau(i, j) - tau(y, z - 1)) < 0.4 And Abs(gammaRO(i, j) - gammaRO(y, z - 1)) < Abs(0.005 * gammaRO(i, j)) Then 'Tolerance 0.4 and 0.005 can be changed depending on the data set
               k = z - 2
               y = 1
            GoTo 50
            End If
         Next y
         Next z
         End If
50    Next i
   gammaiRO(j) = gammaRO(i - 1, j)
Next j



'printloops for RO Model
Dim ROsheet As Worksheet
Set ROsheet = ThisWorkbook.Sheets("RO")
ROsheet.Cells.ClearContents
j = 1
Do Until j > (loopsNumber * 2)
ROsheet.Cells(1, j).Value = "Loop" & j / 2 + 0.5
ROsheet.Cells(2, j).Value = "Stress"
ROsheet.Cells(2, j + 1).Value = "Strain"
j = j + 2
Loop
j = 1
Do Until j > (loopsNumber * 2)
   For i = 1 To loopdatacount(j / 2 + 0.5)
   ROsheet.Cells(i + 2, j).Value = tau(i, j / 2 + 0.5)
   ROsheet.Cells(i + 2, j + 1).Value = gammaRO(i, j / 2 + 0.5)
   Next i
   j = j + 2
```

```
Loop

'Plot chart of divided loops

Dim xvalues() As Double 'the array that makes the strain values or x axis
Dim yvalues() As Double 'the array that makes the strain values or x axis
Dim cht As Chart
Set cht = Charts("chartRO")
cht.ChartArea.Clear
With cht
   .ChartType = xlXYScatterLinesNoMarkers
   .Axes(xlValue, xlPrimary).HasTitle = True
   .Axes(xlValue, xlPrimary).AxisTitle.Caption = "Stress (KPa)"
   .Axes(xlValue, xlPrimary).AxisTitle.Font.Size = 24
   .Axes(xlCategory, xlPrimary).HasTitle = True
   .Axes(xlCategory, xlPrimary).AxisTitle.Caption = "Strain mm/mm"
   .Axes(xlCategory, xlPrimary).AxisTitle.Font.Size = 24
   .Axes(xlValue, xlPrimary).TickLabels.Font.Size = 18
   .Axes(xlCategory, xlPrimary).TickLabels.Font.Size = 18
   .Legend.Font.Size = 16
   'Change from matrix to an array for each of the loops in order to plot as an array
For j = 1 To loopsNumber
   ReDim xvalues(1 To loopdatacount(j))
   ReDim yvalues(1 To loopdatacount(j))
   For i = 1 To loopdatacount(j)

      xvalues(i) = gammaRO(i, j)
      yvalues(i) = tau(i, j)
   Next i
   .SeriesCollection.NewSeries
   .SeriesCollection(j).Format.Line.Weight = 3
   .FullSeriesCollection(j).Name = "Loop" & j
   .SeriesCollection(j).Values = yvalues
   .SeriesCollection(j).xvalues = xvalues
Next j
End With


End Sub
```

Annex C – Device calibration

Rotation/Voltage calibration

The voltage of the proximitors was set so it gives a reading of zero when the sensor is touching the target, and a voltage of 10v when the gap is at maximum range (about 2.5 mm) between the proxomitor and the target.

Rotational calibration is accomplished by loosely mounting the drive head on its calibrating rod, allowing it to rotate freely without wobbling (Figure C-1). A swing arm is used to rotate the drive head as it is pushed by a micrometer depth gage. The depth gage reading is converted to rotation and output voltages are read from the multimeter.

The distance between the targets and the calibrating rod is measured d_t=7.2 cm

Then the distance between the micrometer tip and the center of the calibrating rod is also recorded d_m=9.6 cm

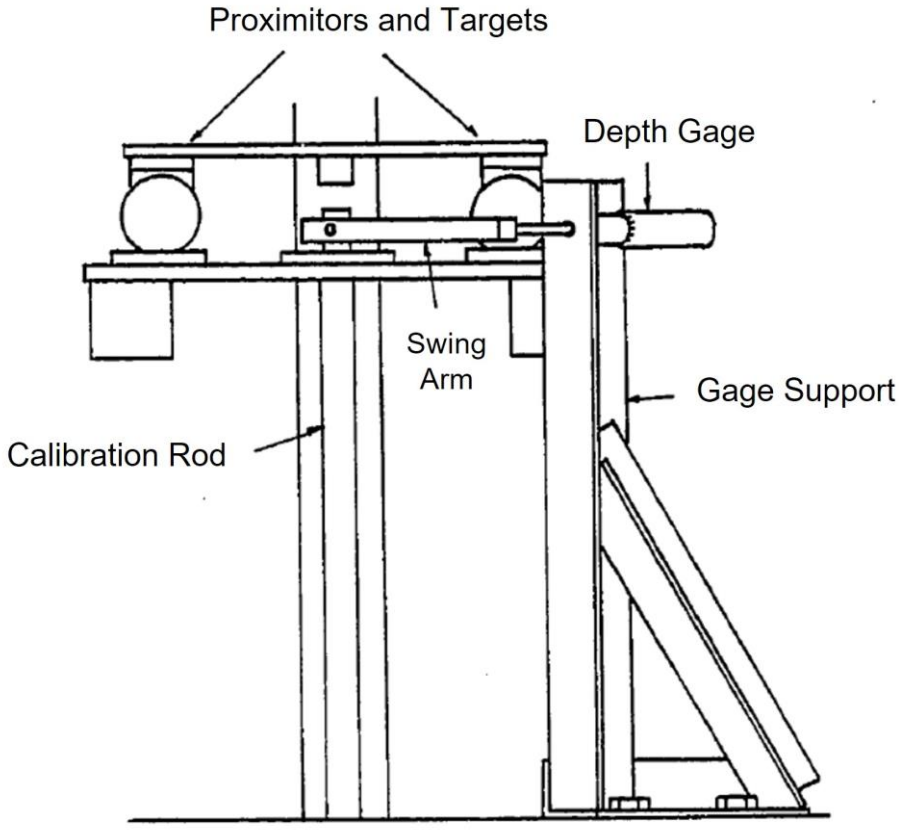

Figure C-11Rotational calibration set-up (Ray, 1984)

Reading of the voltage were recorded for every 0.25 mm increment on the micrometer and the gap between the proximitor and the target is calculated for every step from the following equation:

$$Gap = \frac{d_t}{d_m}(m_i - m_0) \qquad \text{Equation C-1}$$

Where m_i is the micrometer reading at that step and m_0 is the initial micrometer reading.

The relationship between the gap and voltage is plotted (Figure C-2) and an equation is fitted to be used in the TOSS testing program.

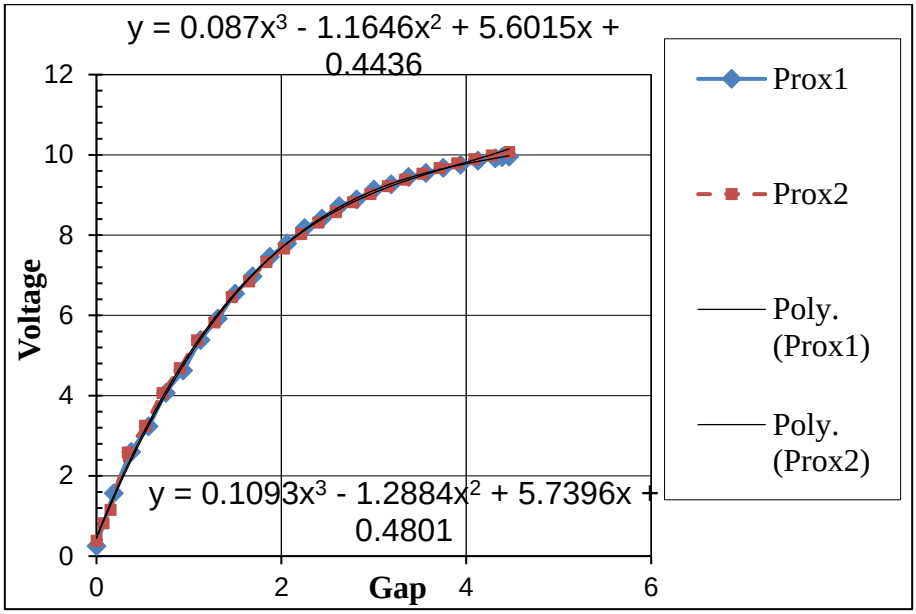

Figure C-2 Fitted equation for the Voltage x Gap relationship2

Polar mass moment of inertia:

The three-wire pendulum method employs a platform supported by three wires, which behaves as a rotational pendulum. When the drive head and top cap are placed onto the platform and the platform set into rotational motion, the governing equation of motion becomes:

$$j_{\text{device}} = \frac{gR_p^2}{4\pi^2 h}(m_d + m_p)T_{D+p}^2 - j_{\text{platform}} \qquad \text{Equation C-2}$$

Where, $m_d$is the mass of the device, T_{D+p} is the period of oscillation of device and platform, m_d is the mass of platform, g is the gravity acceleration, R_p is the radius of the platform, and h is the length of the pendulum wires.

The polar moment of inertia of the platform is given by:

$$j_{\text{platform}} = \left(\frac{R_p^2}{h}\right)\frac{m_p g T_p^2}{4\pi^2} \qquad \text{Equation C-3}$$

Where T_p is the period of the oscillation of the platform.

g=9.807 m/sec^2 m_p=0.4383 kg R_p=0.0899 m

h=0.8715 m m_d=1.0123 kg $m_{top\ ring}$=0.25369 kg

$m_{d+top\ ring}$=1.3047 kg T_p=1.3047 sec/cycle T_{D+p}=1.315 sec/cycle

$T_{ring+D+p}$= 1.2394 sec/cycle

From Equation C-3:

j_p=0.001718 kg.m^2

From Equation C-2:

j_d=0.00406 kg.m^2

j_{d+ring}=0.0043113 kg.m^2

Torque calibration

Once the factors for rotation are known and the spring constant of the calibration rod is determined, torque measurements are easy. It is assumed that the electrical current flowing through the drive coils is proportional to the torque developed.

The current delivered to the coils are measured and converted to a voltage. Calibration entails driving the device with the calibrating rod installed and measuring the deflection.

Measured values for current and deflection are plotted as shown in

The resonant column test conducted on the calibrating rod showed that its resonance period T_n=48.5 msec, giving an angular frequency of ω_n=129.55 rad/sec. Then the torque is calculated from the measured rotation and the mass polar moment of inertia obtained before. The torque vs measured voltage plot is shown in Figure C-3.

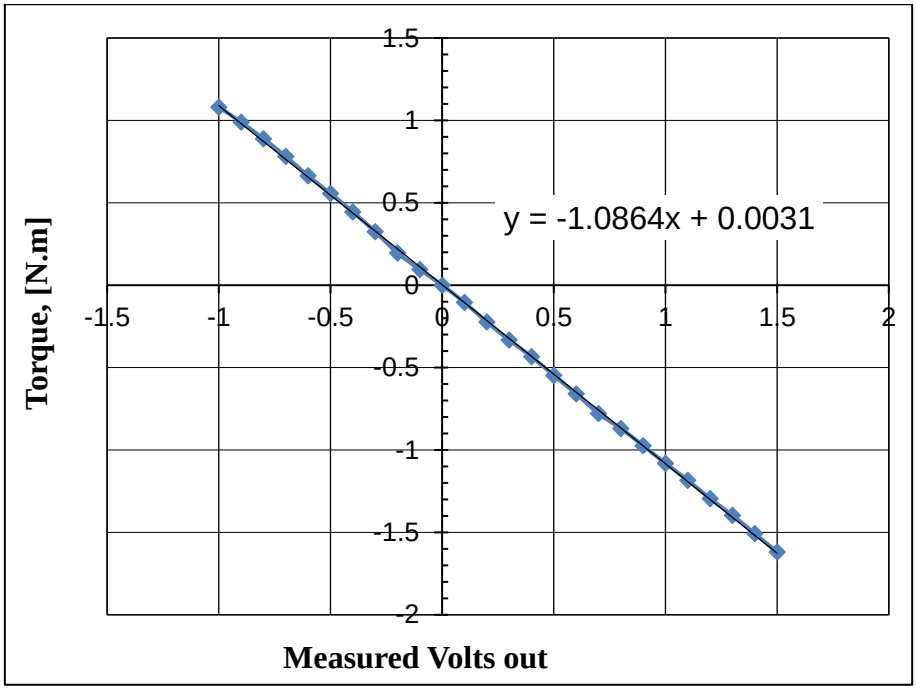

Figure C-3 Torque calibration plot.3